Pair correlation and continuum coupling effects on low-frequency modes of excitation in deformed neutron-rich nuclei

Kenichi Yoshida

January 2007

Abstract

The physics of nuclei far from the stability is one of the current frontiers in nuclear structure physics both theoretically and experimentally. The number of unstable nuclei experimentally accessible will remarkably increase when the next generation of radioactive-ion-beam facilities in all over the world start running. We then shall be able to study the properties not only of ground states but also of low-lying excited states of drip-line nuclei in the medium-mass region. In neutron-rich nuclei, new kinds of many-body correlation would emerge due to the presence of nearby continuum states; coupling among the bound, resonance and continuum states. Under the new environment, we expect emergence of collective modes unique in neutron-rich nuclei because low-lying collective motions are quite sensitive to the shell structure near the Fermi level and detail of the surface property. In studying such a possibility in neutron-rich nuclei, the effects of **nuclear deformation**, **pairing correlations** and **continuum coupling** are of main importance. In this Thesis, we study low-frequency modes of excitation in neutron-rich nuclei simultaneously taken into account these three effects based on the static and dynamic mean-field theory.

In order to study low-lying modes in neutron-rich nuclei paying attention to above three effects, we constructed a new computer code that carries out the deformed quasiparticle-random-phase approximation based on the coordinate-space Hartree-Fock-Bogoliubov formalism. Such calculations have scarcely done so far. Especially, the effect of nuclear deformation has been poorly investigated. In this Thesis, therefore, we concentrate on deformation effects, and discuss possible appearance of collective modes unique in deformed neutron-rich nuclei.

One of the unique features of low-lying excited state in drip-line nuclei is that the transition strength becomes extremely large due to the spatial extension of single-particle wave functions near the Fermi level, which are loosely bound or resonance states. However, the generation of collectivity is not directly connected to the enhancement of transition strength. Because spatial structures of single-particle wave functions near the Fermi level are quite different from each other, it is difficult to generate collectivity in the drip-line region. We have found that the pairing correlation is indispensable to create coherence among bound and resonance levels, and that the low-lying $K^\pi = 0^+$ mode in deformed neutron-rich nuclei is quite sensitive to the pair correlation, where the coupling between vibrations in the particle-hole and in the particle-particle channels brings forth the collective mode.

Contents

Chapter 1

Introduction

1.1 Exploration of unstable nuclei

At present, we know the existence of about 250 stable nuclei, about 50 naturally radioactive elements, and about 3000 unstable nuclei. Figure 1.1 shows the nuclear chart. The horizontal axis indicates the neutron number, while the vertical axis the proton number. This chart shows several thousands of nuclei that are expected to be bound. The black squares show the stable nuclei. The nuclei that have shorter half lives are represented by squares in lighter color. As shown in this figure, there are about 4000–7000 nuclei which are expected to be bound from several theoretical calculations but have not yet been discovered experimentally. Many of these nuclei are located in the neutron-rich region and they play an important role in explaining the nucleosynthesis mechanism beyond iron. It is considered that the rapid neutron capture process (r-process) synthesizes roughly 50% of all elements past the Fe-peak and all of the actinides [2].

The physics of nuclei located far from the beta stability line has been one of the most actively studied subjects in nuclear physics [3, 4, 5]. Thanks to the development of experimental techniques that provide radioactive ion (RI) beams, one can produce many nuclides that we know little about and can explore the terra incognita. Since the RI beam became available, a lot of novel structures unique in neutron-rich nuclei have been discovered in the light mass region of about $Z \leq 8$. One of the most striking features in neutron-rich nuclei is the existence of nuclei that have the "halo" structure [6]. In these nuclei, one or two neutrons extend far outside the distribution of protons. This phenomenon shows the breaking of similar distribution of protons and neutrons well known in stable nuclei. The halo is a purely quantal structure and this concept has now been extended to atomic and molecular physics [7]. Another phenomenon is the existence of the Borromean nuclei such as the two-neutron halo of ^{11}Li [8, 9], where any part of the subsystems (n-^{9}Li and n-n) is unbound whereas the total three-body system (n-n-^{9}Li) is bound. For the existence of such an exotic system, importance of pair correlations and emergence of di-neutron correlations have been pointed out [10, 11, 12, 13].

The number of unstable nuclei experimentally accessible will remarkably increase when the next generation of RI beam facilities, such as RIBF in RIKEN [14], start running. We then shall be able to study properties not only of the ground states but also of the low-lying excited states of drip-line nuclei in the medium-mass region. For heavier neutron-rich nuclei, we can expect, for instance, novel aspects of single-particle motion and many-body correlations in dilute systems, emergence of collective motion unique under the new environment.
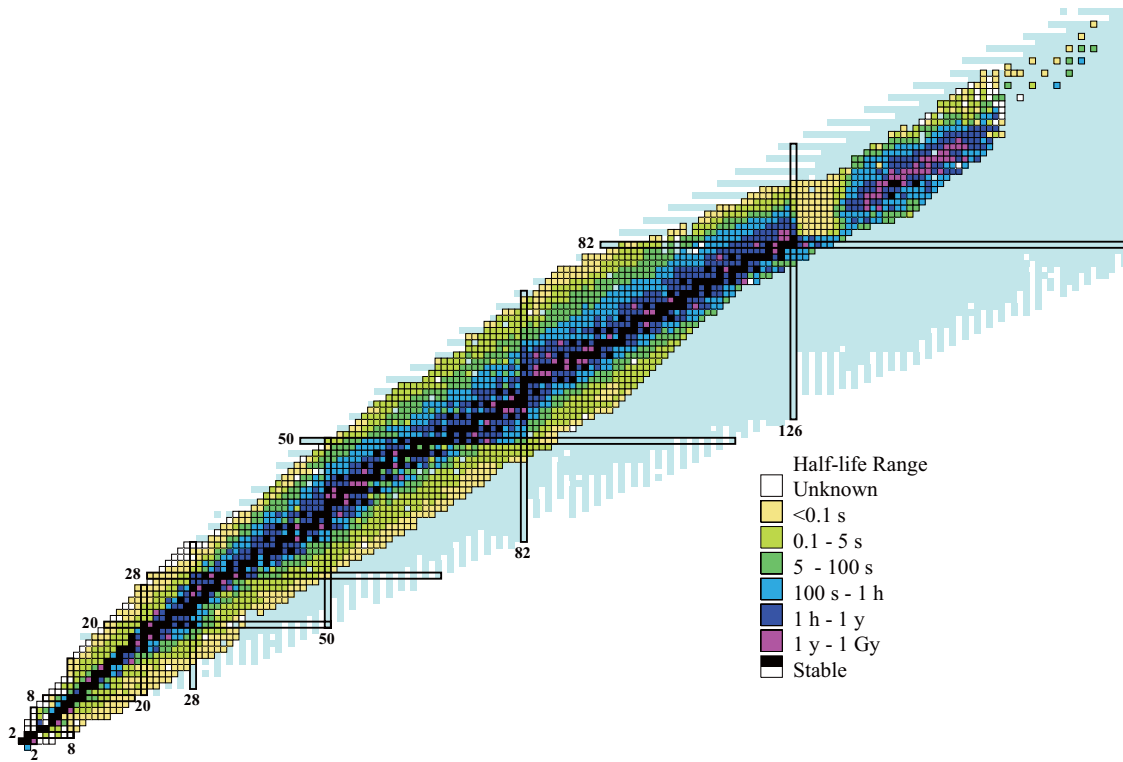
Figure 1.1: Nuclear chart as a function of neutron numbers (the horizontal axis) and proton numbers (the vertical axis). Each square corresponds to one nucleus, and darkness of the square represents its half life. The numbers 2, 8, 20, ... drawn in the figure are the "magic numbers". This figure is taken from LBNL Isotopes Project, Nuclear Structure Systematics Home Page[1].
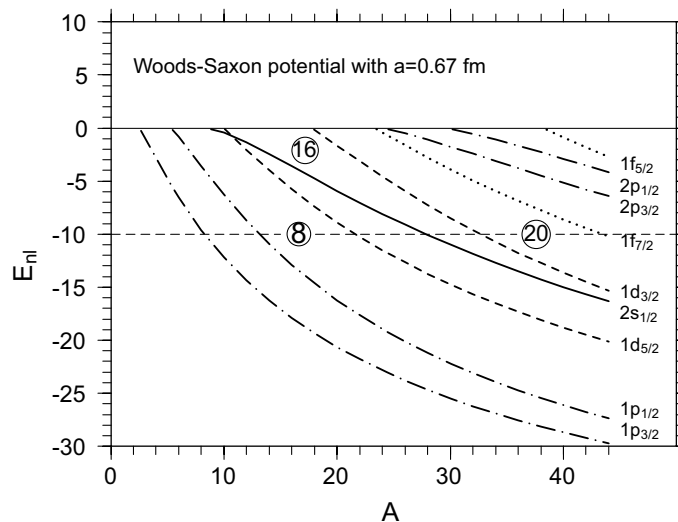
Figure 1.2: Single-particle energies for neutrons in the Woods-Saxon potential with standard parameters [23]. This figure is taken from [24].
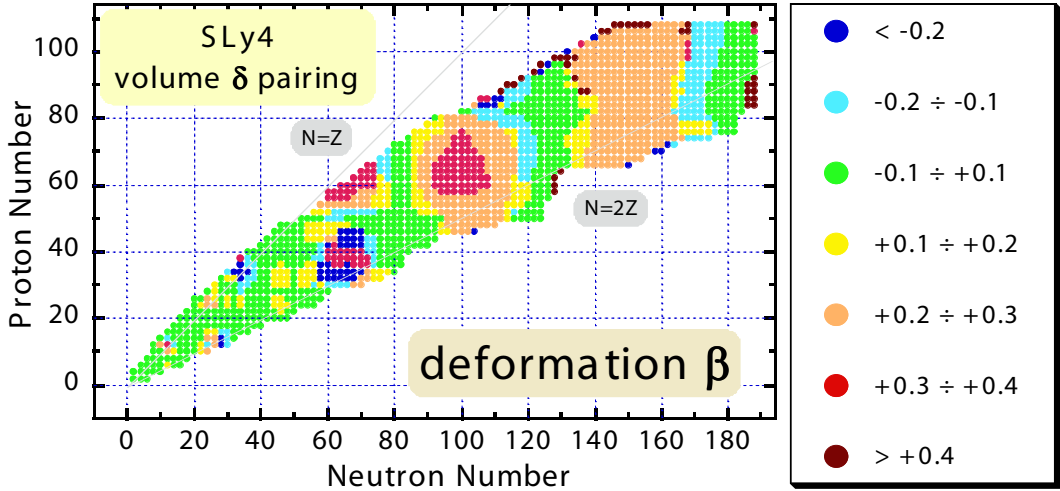
Figure 1.3: Quadrupole deformations β for all even-even particle-bound nuclei calculated by the Hartree-Fock-Bogoliubov plus particle-number projection method using the Skyrme SLy4 interaction for the particle-hole channel and the density-independent contact interaction for the particle-particle channel [26]. Blue and red circles correspond to oblate and prole deformations of the ground states, respectively.

1.2   Shell structures unique in neutron-rich nuclei

Single-particle motion in a mean-field potential is one of the most important concepts in many-body system, and $j - j$ coupling shell model [15, 16] has successfully described ground-state properties. Because the mean-field potential is determined self-consistently by the organizing nucleons, new aspects of single-particle motion are expected to appear in weakly bound systems. In light neutron-rich nuclei, the disappearance of the well-known magic number $N = 8$ has been reported from the observed low-lying excitation energy of the 2^+ state and large transition amplitude $B(E2)$ in ^{12}Be [17], and analysis of the mixing of the $1p_{1/2}$ and $2s_{1/2}$ orbitals in the ground-state wave function of ^{12}Be [18]. The disappearance of $N = 20$ magic number in ^{30}Ne [19] and ^{32}Mg [20, 21] has been envisaged by measuring the low-lying 2^+ level and large $B(E2)$ value. Instead of the disappearance of $N = 20$ shell closure in ^{30}Ne, the emergence of a new shell effect at $N = 16$ is discussed by the systematic analysis of neutron separation energies and interaction cross sections [22].

   In Fig. 1.2, we show single-particle energies for neutrons in the Woods-Saxon potential. It is seen that around $E_{nl} = -10$ MeV, which approximately corresponds to the Fermi level in stable nuclei, the neutron numbers $N = 8$ and 20 appear as shell gaps as is well known in stable nuclei. In contrast, the magic number $N = 8$ disappears for loosely binding region $E_{nl} = -2 \rightarrow 0$ MeV, and the neutron number $N = 16$ appears as a new magic number instead. According to this mean-field calculation, behavior of single-particle orbitals with small angular momentum, especially the $2s_{1/2}$ level, play an important role in changing the shell structure near the continuum threshold.

   The spin-orbit potential, which is crucial for creating the magic numbers above 20, is proportional to the derivative of the potential. In weakly bound nuclei where the potential diffuseness becomes large, the spin-orbit splitting and the shell closures will change in the
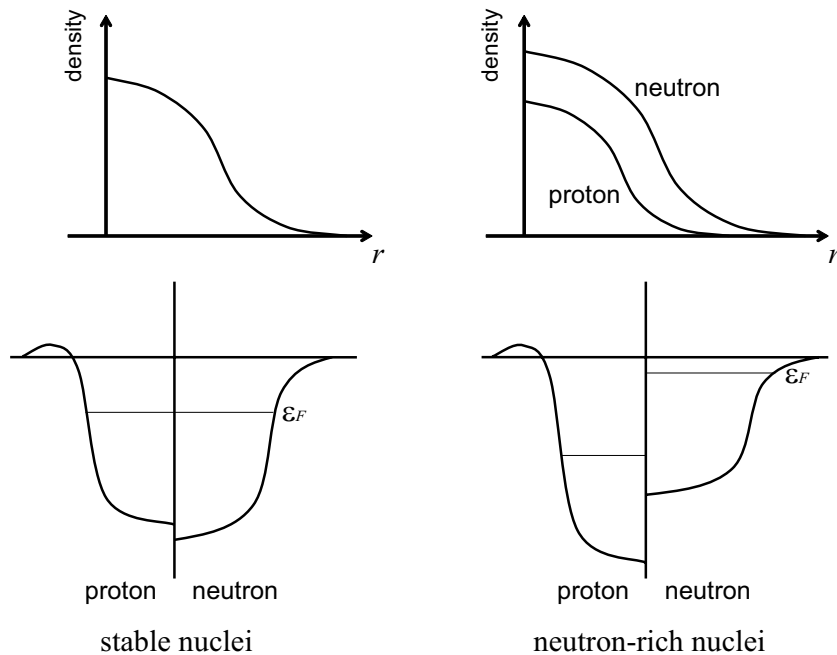
Figure 1.4: Schematic density distributions of stable nuclei and neutron-rich nuclei with neutron skins (the upper row), and mean-field potentials for neutrons and protons (the lower row).

medium-mass neutron-rich nuclei [25]. In Fig. 1.3, we show the quadrupole deformations of all even-even nuclei expected to be bound in the mean-field calculations [26]. This figure shows that new regions of deformation are expected in neutron-rich nuclei. For instance, we can see a domain of nuclear deformation, corresponding to the breaking of the shell closure at $N = 28$ in the neutron drip-line region.

Very recently, it became possible to access the region of $N = 28$ close to the neutron drip line. Four experimental results have been used to argue that the $N = 28$ shell closure is narrowed or collapsed in ^{42}Si as predicted by some theoretical calculations [27, 28, 29, 30, 31, 32, 33]: 1) a measurement of the lifetime of the β-decay of ^{42}Si [34], 2) the determination that ^{43}Si is bound [35], 3) a mass measurement of ^{42}Si [36], and 4) a measurement of the excited state of ^{40}Si [37]. On the other hand, in Refs [38, 39] they have argued that the proton subshell closure at $Z = 14$ would have a strong effect on the structure of ^{42}Si, which means that the proton closure at $Z = 14$ prevents ^{42}Si from being well deformed. Persisting the magic number $N = 28$ in ^{42}Si [40] and an evidence of strong subshell closure at $Z = 14$ in ^{42}Si [41] have been reported based on the measurement of two-proton knockout reaction cross sections.

Another unique structure in the medium-mass neutron-rich nuclei is emergence of the "neutron skin". The root-mean-square matter radii of Na isotopes were deduced from the interaction cross sections and the radii of neutrons were compared with those of protons for the first time along a chain of stable and unstable isotopes by Suzuki $et\ al.$ [42], and they obtained a monotonic increase in the neutron skin thickness as a neutron number increases. In Fig. 1.4, we show schematic density distributions of neutron-rich nuclei with the neutron

stable nuclei   neutron drip-line nuclei
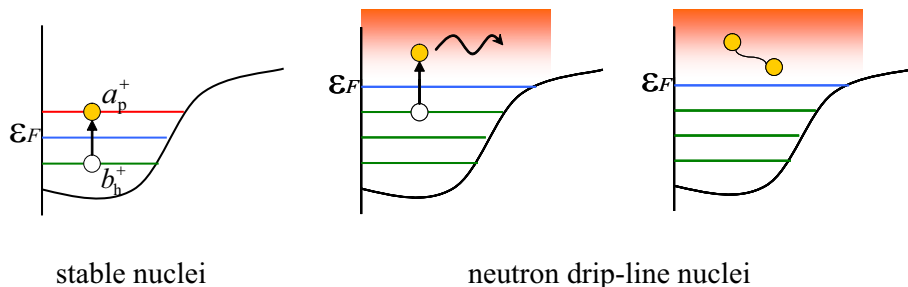
Figure 1.5: Schematic illustrations of particle-hole excitations in stable (*left*) and neutron-rich nuclei (*middle*), and two-neutron pair correlations in the continuum as one of the novel features in superfluid drip-line nuclei (*right*).

skin structure. Because the Fermi levels for neutrons and protons are quite asymmetric, the density distribution of neutrons extends outside that of protons. This phenomenon is different from the "neutron halo" in the sense that many neutrons take part in the formation of the skin structure, and would appear in many neutron-rich nuclei generically.

1.3 Collective motions under new extreme conditions

The collective vibrational mode of excitation can be described microscopically with the Random Phase Approximation (RPA) in which the excited state is written by superposition of particle-hole excitations [43]

$$|\text{vib.}\rangle = \sum_{\text{ph}} f_{\text{ph}} a_{\text{p}}^{\dagger} b_{\text{h}}^{\dagger} + g_{\text{ph}} b_{\text{h}} a_{\text{p}} |\text{gs.}\rangle, \tag{1.1}$$

where $a^{\dagger}, b^{\dagger}, a$ and b are creation and annihilation operators of particles and holes. In Fig. 1.5, we show schematic illustrations of particle-hole excitations in stable and neutron-rich nuclei. In stable nuclei, both particle and hole states are bound and their wave functions are spatially localized, whereas the particle can be easily excited into the continuum state in neutron-rich nuclei because the Fermi level for neutrons is shallow.

Because the low-frequency collective excitations are quite sensitive to the shell structure near the Fermi level and surface structure, we expect that new kinds of collective excitation emerge under new situations of nuclear structure. In order to quest for collective modes of excitation unique to unstable nuclei associated with new features such as neutron skins, many attempts have been made using the self-consistent RPA based on the Skyrme-Hartree-Fock (SHF) method [44, 45, 46] and the Quasiparticle-RPA (QRPA) including pairing correlations [47, 48, 49, 50, 51, 52]. A number of similar approaches using different mean fields have also been carried out [53, 54, 55, 56, 57, 58, 59, 60, 61]. (See Refs. [52, 58, 62] for extensive lists of references concerning the self-consistent RPA and mean-field calculations.) Most of these calculations, however, are restricted to spherical nuclei.

Quite recently, low-frequency RPA modes in deformed nuclei close to the neutron drip line have been investigated by several groups. The time-dependent Hartree-Fock method formulated in the three-dimensional coordinate space with a complex absorbing boundary condition was applied to low-frequency isovector dipole modes [63]. Possible appearance of

5

low-frequency octupole vibrations built on superdeformed states in neutron drip-line nuclei was discussed in Ref. [64] on the basis of the SHF plus mixed representation RPA [65, 66, 67] calculations. All of these calculations, however, did not take into account the pairing correlations. In Refs. [68, 69], low-lying Gamow-Teller β-decay strengths were investigated by means of the proton-neutron RPA using the SHF + BCS approximation. The gamma vibration in ^{38}Mg was studied using the QRPA with the BCS approximation on the basis of the response function formalism [70]. It should be noted that these calculations rely on the BCS approximation, which is inappropriate, because of the unphysical nucleon gas problem [71], for describing continuum coupling effects in drip-line nuclei.

The nature of pairing correlations in neutron drip-line nuclei is one of the most important subjects in the physics of unstable nuclei. One of the unique features of drip-line nuclei is that the pairing correlations take place not only among bound levels but also including continuum states (see Fig. 1.5). To describe this unique character of pairing, the coordinate-space Hartree-Fock-Bogoliubov (HFB) formalism is suitable [71, 72]. This has been widely used for the study of single-particle motion and shell structure near the continuum [25, 73, 74, 75]. Due to the pairing and continuum effects, spatial structures of quasiparticle wave functions near the chemical potential change significantly, which affects the properties of low-frequency excitation modes [76], and possible emergence of di-neutron correlations in the medium-mass neutron-rich nuclei both in the ground and in the excited states has been discussed [77].

1.4 Aim and outline of this thesis

In this thesis, based on the mean-field theory we study the effects of nuclear deformation, continuum coupling and pairing correlations on low-frequency excitation modes and investigate microscopic structure of excited states. In particular, we discuss the mechanism of emergence of collective modes unique in deformed neutron-rich nuclei paying attention to the existence of neutron skin structure and pairing correlations in the continuum. The methods that we use are explained in Chapter 2.

In order to clearly see effects of nuclear deformation and continuum coupling on low-frequency excitation modes in neutron drip-line nuclei, we investigate in Chapter 3 properties of octupole excitations built on superdeformed states in neutron-rich sulfur isotopes by means of the RPA based on the deformed Woods-Saxon potential in the coordinate-space mesh-representation. Discussions in this Chapter are based on Refs. [78, 79].

In Chapter 4, for the purpose of studying the effects of pairing correlation on the low-frequency vibrational modes in deformed nuclei near the neutron drip line, we have extended the above work to self-consistently include the pairing correlations, and constructed a new computer code that carries out the deformed QRPA calculation on the basis of the coordinate-space HFB formalism. We investigate low-frequency quadrupole vibrational modes with $K^\pi = 0^+$ and 2^+ in ^{36,38,40}Mg close to the neutron drip line. Discussions in this Chapter are based on Refs. [80, 81].

In Chapter 5, we apply the method presented in Chapter 4 for describing low-lying excited states in ^{34}Mg, and discuss the effect of nuclear deformation on properties of low-lying modes. We also discuss properties of low-lying $K^\pi = 0^+$ mode in ^{32}Ne. In order to see generic feature of soft $K^\pi = 0^+$ modes in deformed neutron-rich nuclei, we investigate in Chapter 6 properties of low-lying 0^+ modes in neutron-rich Cr and Fe isotopes around $N = 40$.

In Chapter 7, we study properties of single-particle resonances in a deformed system. In

neutron drip-line nuclei, the shell structure in the continuum is one of the key elements in understanding the emergence of new kinds of many-body correlation and collective mode. In order to study the resonance wave functions qualitatively, we introduce the Gamow state. We study the behavior of $s-$wave component of single-particle wave functions in a deformed potential around the continuum threshold. Discussions in this Chapter are based on Ref. [82].

In Chapters 3–7, we use the phenomenological potential for the mean field because the self-consistent calculations simultaneously taken into account the effects of nuclear deformation, continuum coupling and pairing correlations are very expensive, i.e., this kind of calculations require much computer memory and CPU time. In Chapter 8, we discuss the perspective to replace the phenomenological potential with the self-consistent potential based on the nuclear density-functional theory. As a first step towards description of excitation modes in deformed neutron-rich nuclei in a self-consistent manner, we construct a new computer mode that carries out the self-consistent HFB calculation in the cylindrical coordinate using the Skyrme effective interaction. Some results of such a self-consistent calculation are presented in this Chapter.

Finally, concluding remarks are given in Chapter 9.

Chapter 2

Microscopic theory of collective excitations in deformed neutron-rich nuclei

Single-particle motion in the mean field is a key concept of the many-body system in the sense that the mean-field approximation provides us with the classical picture of the quantal system such as deformation and superfluidity which is regarded as deformation in a gauge space. Correlations beyond the mean field is, however, essential to understand for instance the mechanism of emergence of coherent collective motions. The concept of single-particle motion keeps its importance in studying correlations beyond the mean field because it is a good starting point and a cornerstone of understanding the correlated many-body system by constructing the basis for treating many-body Hamiltonian.

In this chapter, we explain the mean-field theory and one of the methods we use in this thesis that goes beyond the static mean-field theory.

2.1   The Hartree-Fock and the Hartree-Fock-Bogoliubov method

2.1.1   The Hartree-Fock method

Let us consider a system of A Fermions at zero temperature. The Hartree-Fock (HF) approximation consists of assuming that the ground state $|\mathrm{HF}\rangle$ of the system is a Slater determinant composed of A orthonormal single-particle orbitals

$$|\mathrm{HF}\rangle = \prod_{i=1}^{A} c_i^\dagger |0\rangle, \tag{2.1}$$

where $c_\alpha^\dagger, c_\alpha$ are particle creation and annihilation operators associated with the orthonormal set $\{\varphi_\alpha(x)\}$, and $c_\alpha|0\rangle = 0$. We denote by x both space, spin and isospin coordinates of a particle: $x = (\boldsymbol{r}, \sigma, \tau)$.

Suppose that the Hamiltonian H of the system is the sum of a kinetic energy T and a two-body interaction V:

$$H = \sum_{\alpha\beta} t_{\alpha\beta} c_\alpha^\dagger c_\beta + \frac{1}{4} \sum_{\alpha\beta\gamma\delta} v_{\alpha\beta\gamma\delta} c_\alpha^\dagger c_\beta^\dagger c_\delta c_\gamma, \tag{2.2}$$

9

where the matrix element $v_{\alpha\beta\gamma\delta}$ is defined by

$$v_{\alpha\beta\gamma\delta} = \langle\alpha\beta|V|\gamma\delta - \delta\gamma\rangle \tag{2.3a}$$
$$= (\alpha\beta|V|\gamma\delta), \tag{2.3b}$$

and

$$<\alpha\beta|V|\gamma\delta> = \iint \mathrm{d}x\mathrm{d}x'\varphi_\alpha^*(x)\varphi_\beta^*(x')V(x,x\prime)\varphi_\gamma(x)\varphi_\delta(x'). \tag{2.4}$$

The expectation value of the Hamiltonian is

$$E[\varrho] = \langle\mathrm{HF}|H|\mathrm{HF}\rangle = \sum_{\alpha\beta} t_{\alpha\beta}\varrho_{\beta\alpha} + \frac{1}{2}\sum_{\alpha\beta\gamma\delta} v_{\alpha\beta\gamma\delta}\varrho_{\gamma\alpha}\varrho_{\delta\beta}$$
$$= \sum_i n_i t_{ii} + \frac{1}{2}\sum_{ij} v_{ijij}n_i n_j, \tag{2.5}$$

where we defined the single-particle density matrix associated with the state $|\mathrm{HF}\rangle$ as

$$\varrho_{ij} = \langle i|\varrho|j\rangle = \langle\mathrm{HF}|c_j^\dagger c_i|\mathrm{HF}\rangle, \tag{2.6}$$

and eigenvalues n_i of the density operator ϱ. *The necessary and sufficient condition for an antisymmetric state $|\mathrm{HF}\rangle$ to be a Slater determinant is that the single-particle density matrix ϱ satisfies the equation* [43, 83]

$$\varrho^2 = \varrho. \tag{2.7}$$

It follows that the eigenvalues n_i of the density operator ϱ are 0 or 1. Since $\mathrm{tr}\varrho = A$, there are A eigenvalues equal to 1, and all the others are 0. Therefore the Hartree-Fock energy can be written as

$$E^{\mathrm{HF}} = \sum_{i=1}^{A} t_i + \frac{1}{2}\sum_{ij}^{A} v_{ijij}. \tag{2.8}$$

Let us define the single-particle Hamiltonian h by the equation

$$h_{ij} = \frac{\delta E[\varrho]}{\delta\varrho_{ji}}. \tag{2.9}$$

This is evaluated from the energy functional (2.5):

$$h_{ij} = t_{ij} + \sum_{kl} v_{ikjl}\varrho_{lk}$$
$$= t_{ij} + \sum_{k} v_{ikik}n_k. \tag{2.10}$$

The variational equation under the constraint (2.7)

$$\delta[E[\varrho] - \mathrm{tr}\Lambda(\varrho^2 - \varrho)] = 0 \tag{2.11}$$

reads

$$\text{tr}(h - \varrho\Lambda - \Lambda\varrho + \Lambda)\delta\varrho = 0. \tag{2.12}$$

This equality should hold for any $\delta\varrho$, so that

$$h - \varrho\Lambda - \Lambda\varrho + \Lambda = 0. \tag{2.13}$$

Using the relation (2.7), one obtains the Hartree-Fock equation

$$[h, \varrho] = h\varrho - \varrho h = 0. \tag{2.14}$$

The equation (2.14) states that h and ϱ can be diagonalized simultaneously. One can therefore define the Hartree-Fock basis and convert (2.14) into an eigenvalue problem:

$$h_{kk'} = t_{kk'} + \sum_{i=1}^{A} v_{kik'i} = \epsilon_k \delta_{kk'}, \tag{2.15}$$

and one finds instead of (2.15)

$$-\frac{\hbar^2}{2m}\nabla^2\varphi_\alpha(x) + \sum_{i=1}^{A}\int \mathrm{d}x' \varphi_i^*(x')v(x',x)\{\varphi_i(x')\varphi_\alpha(x) - \varphi_a(x')\varphi_i(x)\} = \epsilon_\alpha\varphi_\alpha(x) \tag{2.16}$$

in the coordinate-space representation. This is called the coordinate-space HF equation.

2.1.2 The Hartree-Fock-Bogoliubov method

Next the HF method is extended to the Hartree-Fock-Bogoliubov (HFB) method in order to take into account the pair correlation. The HFB approximation assumes that the ground state $|\text{HFB}\rangle$ of the system is a product of quasiparticle annihilation operators

$$|\text{HFB}\rangle = \prod_{k=1}\beta_k|0\rangle, \tag{2.17}$$

where quasiparticle operators $\beta_k^\dagger, \beta_k$ are defined by the Bogoliubov transformation [43]

$$\beta_k^\dagger = \sum_l(U_{lk}c_l^\dagger + V_{lk}c_l), \tag{2.18a}$$

$$\beta_k = \sum_l(V_{lk}^*c_l^\dagger + U_{lk}^*c_l). \tag{2.18b}$$

An HFB vacuum is not an eigenstate of the particle number operator. One therefore imposes the condition that the average number of particles should be equal to the number of particles of the system,

$$\langle\text{HFB}|\hat{N}|\text{HFB}\rangle = \langle\text{HFB}|\sum_{i=1}^{A}c_i^\dagger c_i|\text{HFB}\rangle = \bar{A}, \tag{2.19}$$

and we minimize the the expectation value of the Hamiltonian

$$H' = H - \lambda N = \sum_{\alpha\beta}(t_{\alpha\beta} - \lambda\delta_{\alpha\beta})c_\alpha^\dagger c_\beta + \frac{1}{4}\sum_{\alpha\beta\gamma\delta}v_{\alpha\beta\gamma\delta}c_\alpha^\dagger c_\beta^\dagger c_\delta c_\gamma. \tag{2.20}$$

The Lagrange multiplier λ is called the chemical potential or the Fermi energy because it represents the increase of the energy $E' = \langle \mathrm{HFB}|H'|\mathrm{HFB}\rangle$ with respect to the change in the particle number

$$\lambda = \frac{dE'}{dN}. \tag{2.21}$$

The expectation value of the Hamiltonian H' in a quasiparticle vacuum is

$$E'[\varrho, \kappa, \kappa^*] = \langle \mathrm{HFB}|H'|\mathrm{HFB}\rangle = \sum_{\alpha\beta}(t_{\alpha\beta} - \lambda\delta_{\alpha\beta})\varrho_{\beta\alpha} + \frac{1}{2}\sum_{\alpha\beta\gamma\delta} v_{\beta\gamma\delta}\varrho_{\gamma\alpha}\varrho_{\delta\beta} + \frac{1}{4}\sum_{\alpha\beta\gamma\delta}\kappa^*_{\alpha\beta}v_{\alpha\beta\gamma\delta}\kappa_{\gamma\delta} \tag{2.22}$$

$$= E'[\mathscr{R}],$$

where we defined the single-particle density matrix ϱ_{ij} and pair density matrix κ_{ij} associated with the state $|\mathrm{HFB}\rangle$

$$\varrho_{ij} = \langle i|\varrho|j\rangle = \langle \mathrm{HFB}|c^\dagger_j c_i|\mathrm{HFB}\rangle = V^*V^T, \tag{2.23a}$$

$$\kappa_{ij} = \langle ij|\kappa\rangle = \langle \mathrm{HFB}|c_j c_i|\mathrm{HFB}\rangle = V^*U^T = -UV^\dagger, \tag{2.23b}$$

and the generalized density matrix $\mathscr{R}$

$$\mathscr{R} = \begin{pmatrix} \varrho & \kappa \\ -\kappa^* & 1 - \varrho^* \end{pmatrix}. \tag{2.24}$$

In the present case the following theorem holds [43, 83]: *The necessary and sufficient condition for an antisymmetric state* $|\mathrm{HFB}\rangle$ *to be a quasiparticle vacuum is that the generalized density matrix* $\mathscr{R}$ *satisfies the equation*

$$\mathscr{R}^2 = \mathscr{R}. \tag{2.25}$$

Let us define the single-particle Hamiltonian by the equation

$$h'_{ij} = \frac{\delta E'[\varrho, \kappa, \kappa^*]}{\delta\varrho_{ji}}, \tag{2.26}$$

and the pairing field by

$$\Delta_{ij} = \frac{\delta E'[\varrho, \kappa, \kappa^*]}{\delta\kappa^*_{ij}} = -\Delta_{ji}. \tag{2.27}$$

In the case where the energy functional is given by (2.22), the single-particle Hamiltonian and the pairing field are

$$h'_{ij} = \langle i|h'|j\rangle = t_{ij} - \lambda\delta_{ij} + \sum_{kl} v_{ikjl}\varrho_{lk} = h_{ij} - \lambda, \tag{2.28a}$$

$$\Delta_{ij} = \langle ij|\Delta\rangle = \frac{1}{2}\sum_{kl} v_{ijkl}\kappa_{kl}. \tag{2.28b}$$

The variation of the energy with respect to the matrix elements of ϱ, κ and κ^* reads

$$
\begin{aligned}
\delta E'[\varrho, \kappa, \kappa^*] &= \sum_{ij} \frac{\delta E'}{\delta \varrho_{ij}} \delta \varrho_{ij} + \frac{1}{2} \sum_{ij} \left[\frac{\delta E'}{\delta \kappa_{ij}^*} \delta \kappa_{ij}^* + \frac{\delta E'}{\delta \kappa_{ij}} \delta \kappa_{ij} \right], \\
&= \operatorname{tr} \left(h' \delta \varrho - \frac{1}{2} \Delta \delta \kappa^* - \frac{1}{2} \Delta^* \delta \kappa \right) \\
&= \frac{1}{2} \operatorname{tr} \mathscr{H} \delta \mathscr{R},
\end{aligned}
\tag{2.29}
$$

where we introduced the quasiparticle Hamiltonian

$$
\mathscr{H} = \begin{pmatrix} h' & \Delta \\ -\Delta^* & -h'^* \end{pmatrix} = \begin{pmatrix} h - \lambda & \Delta \\ -\Delta^* & -(h-\lambda)^* \end{pmatrix} = \mathscr{H}^\dagger.
\tag{2.30}
$$

Taking into account the constraint (2.25), the variational equation reads

$$
\delta[E'[\mathscr{R}] - \operatorname{tr}\Lambda(\mathscr{R}^2 - \mathscr{R})] = 0.
\tag{2.31}
$$

As in the case of the HF method, one obtains the HFB equation

$$
[\mathscr{H}, \mathscr{R}] = 0,
\tag{2.32}
$$

and introducing the quasiparticle basis, one can convert (2.32) to the eigenvalue problem

$$
\begin{pmatrix} h - \lambda & \Delta \\ -\Delta^* & -(h-\lambda)^* \end{pmatrix} \begin{pmatrix} U_k \\ V_k \end{pmatrix} = E_k \begin{pmatrix} U_k \\ V_k \end{pmatrix}.
\tag{2.33}
$$

2.1.3   The HFB in the coordinate-space representation

In neutron-rich nuclei, scattering of the pair into the continuum is one of the most important correlations uniquely appeared in the new region of nuclei. Such a continuum coupling effect can be described by means of the coordinate-space HFB method [71, 72].

Let us start by introducing the Bogoliubov transformation in the coordinate space,

$$
\psi^\dagger(\boldsymbol{r}\sigma) = \sum_k U_k^*(\boldsymbol{r}\sigma)\beta_k^\dagger + V_k(\boldsymbol{r}\sigma)\beta_k = \sum_k \varphi_{1,k}(\boldsymbol{r}\bar{\sigma})\beta_k^\dagger + \varphi_{2,k}^*(\boldsymbol{r}\sigma)\beta_k,
\tag{2.34a}
$$

$$
\psi(\boldsymbol{r}\sigma) = \sum_k U_k(\boldsymbol{r}\sigma)\beta_k + V_k^*(\boldsymbol{r}\sigma)\beta_k^\dagger = \sum_k \varphi_{1,k}^*(\boldsymbol{r}\bar{\sigma})\beta_k + \varphi_{2,k}(\boldsymbol{r}\sigma)\beta_k^\dagger,
\tag{2.34b}
$$

where the single-quasiparticle wave functions $\varphi_{1,k}(\boldsymbol{r}\sigma)$ and $\varphi_{2,k}(\boldsymbol{r}\sigma)$ satisfy the coordinate-space HFB equation given below. In the coordinate-space representation, one usually uses $\varphi_{1,k}(\boldsymbol{r}\sigma), \varphi_{2,k}(\boldsymbol{r}\sigma)$ instead of $U_k(\boldsymbol{r}\sigma), V_k(\boldsymbol{r}\sigma)$ for convenience of notation whereas $U_k(\boldsymbol{r}\sigma)$ and $V_k(\boldsymbol{r}\sigma)$ correspond directly to U, V matrices in the configuration-space HFB formalism explained above. The notation $\varphi(\boldsymbol{r}\bar{\sigma})$ is defined by $\varphi(\boldsymbol{r}\bar{\sigma}) \equiv -2\sigma\varphi(\boldsymbol{r} - \sigma)$.

The particle (normal) and pairing (abnormal) density matrices are defined as

$$
\varrho(\boldsymbol{r}\sigma, \boldsymbol{r}'\sigma') = \langle \mathrm{HFB}|\psi^\dagger(\boldsymbol{r}'\sigma')\psi(\boldsymbol{r}\sigma)|\mathrm{HFB}\rangle = \sum_k \varphi_{2,k}^*(\boldsymbol{r}'\sigma')\varphi_{2,k}(\boldsymbol{r}\sigma),
\tag{2.35a}
$$

$$
\tilde{\varrho}(\boldsymbol{r}\sigma, \boldsymbol{r}'\sigma') = \langle \mathrm{HFB}|\psi(\boldsymbol{r}'\bar{\sigma}')\psi(\boldsymbol{r}\sigma)|\mathrm{HFB}\rangle = -\sum_k \varphi_{1,k}^*(\boldsymbol{r}'\sigma')\varphi_{1,k}(\boldsymbol{r}\sigma),
\tag{2.35b}
$$

where the index k runs over all the states with positive energy E_k and $\varphi_k(\boldsymbol{r}\sigma) \equiv \varphi(E_k, \boldsymbol{r}\sigma)$.

For the time-reversal invariant state $|\text{HFB}\rangle$, both density matrices are time even and Hermitian [71]. Therefore, the pairing density matrix $\tilde{\varrho}(\boldsymbol{r}\sigma, \boldsymbol{r}'\sigma')$ is more convenient than the standard pairing tensor [43] $\kappa(\boldsymbol{r}\sigma, \boldsymbol{r}'\sigma') = 2\sigma'\tilde{\varrho}(\boldsymbol{r}\sigma, \boldsymbol{r}' - \sigma')$, which is asymmetric function in space-spin arguments.

Since the HFB state is an independent quasiparticle state, ϱ and $\tilde{\varrho}$ commute,

$$\varrho \cdot \tilde{\varrho} - \tilde{\varrho} \cdot \varrho = 0, \tag{2.36}$$

and fulfill the condition

$$\varrho \cdot \varrho + \tilde{\varrho} \cdot \tilde{\varrho} = \varrho, \tag{2.37}$$

where a product of operators in the coordinate-space representation is defined by

$$(\varrho \cdot \tilde{\varrho})(\boldsymbol{r}_1\sigma_1, \boldsymbol{r}_2\sigma_2) = \int d\boldsymbol{r} \sum_\sigma \varrho(\boldsymbol{r}\sigma_1, \boldsymbol{r}\sigma)\tilde{\varrho}(\boldsymbol{r}\sigma, \boldsymbol{r}_2\sigma_2). \tag{2.38}$$

Relations (2.36) and (2.37) are expressed using the generalized density

$$\mathcal{R} \cdot \mathcal{R} = \mathcal{R} \tag{2.39}$$

with

$$\mathcal{R} = \begin{pmatrix} \varrho & \tilde{\varrho} \\ \tilde{\varrho} & \delta(\boldsymbol{r} - \boldsymbol{r}')\delta_{\sigma\sigma'} - \varrho \end{pmatrix}. \tag{2.40}$$

Varying the energy expectation value $E = \langle \text{HFB}|H|\text{HFB}\rangle$ with respect to ϱ and $\tilde{\varrho}$, one obtains the HFB equation,

$$[\mathcal{H}, \mathcal{R}] = 0, \tag{2.41}$$

where

$$\mathcal{H} = \begin{pmatrix} h - \lambda & \tilde{h} \\ \tilde{h} & -h + \lambda \end{pmatrix}, \tag{2.42}$$

and h and $\tilde{h}$ are the particle and pairing field operators

$$h(\boldsymbol{r}\sigma, \boldsymbol{r}'\sigma') = \frac{\delta E}{\delta\varrho(\boldsymbol{r}'\sigma', \boldsymbol{r}\sigma)}, \tag{2.43a}$$

$$\tilde{h}(\boldsymbol{r}\sigma, \boldsymbol{r}'\sigma') = \frac{\delta E}{\delta\tilde{\varrho}(\boldsymbol{r}'\sigma', \boldsymbol{r}\sigma)}. \tag{2.43b}$$

We introduce the quasiparticle basis and convert (2.41) to the eigenvalue problem;

$$\int d\boldsymbol{r}' \sum_{\sigma'} \begin{pmatrix} h(\boldsymbol{r}\sigma, \boldsymbol{r}'\sigma') & \tilde{h}(\boldsymbol{r}\sigma, \boldsymbol{r}'\sigma') \\ \tilde{h}(\boldsymbol{r}\sigma, \boldsymbol{r}'\sigma') & -h(\boldsymbol{r}\sigma, \boldsymbol{r}'\sigma') \end{pmatrix} \begin{pmatrix} \varphi_1(E, \boldsymbol{r}'\sigma') \\ \varphi_2(E, \boldsymbol{r}'\sigma') \end{pmatrix} = \begin{pmatrix} E + \lambda & 0 \\ 0 & E - \lambda \end{pmatrix} \begin{pmatrix} \varphi_1(E, \boldsymbol{r}\sigma) \\ \varphi_2(E, \boldsymbol{r}\sigma) \end{pmatrix}. \tag{2.44}$$

This is called the coordinate-space HFB equation.

In order to see characteristic features of the coordinate-space HFB theory, following Ref. [71], we investigate the asymptotic solutions of Eq. (2.44) at $r \to \infty$. Since the nucleus has a finite volume, the fields $h(r\sigma, r'\sigma')$ and $\tilde{h}(r\sigma, r'\sigma')$ should vanish at large r, r' except for the kinetic energy. We thus write down the asymptotic equations for φ_1 and φ_2,

$$-\frac{\hbar^2}{2m}\nabla^2\varphi_1(E, r\sigma) = (\lambda + E)\varphi_1(E, r\sigma), \tag{2.45}$$

$$-\frac{\hbar^2}{2m}\nabla^2\varphi_2(E, r\sigma) = (\lambda - E)\varphi_2(E, r\sigma), \tag{2.46}$$

with the asymptotic solutions

$$\varphi_1(E, r\sigma) \sim \begin{cases} \cos(k_1 r + \delta_1) & \text{for } \lambda + E > 0 \\ \exp(-\kappa_1 r) & \text{for } \lambda + E < 0, \end{cases} \tag{2.47a}$$

$$\varphi_2(E, r\sigma) \sim \begin{cases} \cos(k_2 r + \delta_2) & \text{for } \lambda - E > 0 \\ \exp(-\kappa_2 r) & \text{for } \lambda - E < 0, \end{cases} \tag{2.47b}$$

with $k_1 = \sqrt{2m(\lambda + E)}/\hbar$, $\kappa_1 = \sqrt{-2m(\lambda + E)}/\hbar$, $k_2 = \sqrt{2m(\lambda - E)}/\hbar$ and $\kappa_2 = \sqrt{-2m(\lambda - E)}/\hbar$. For $\lambda > 0$, the entire spectrum is continuus, while for $\lambda < 0$, the spectrum is either continuus ($E > -\lambda$) or discrete ($E < -\lambda$). It has to be noted that the lower component φ_2 is always exponentialy decaying at infinity and the densities ϱ and $\tilde{\varrho}$ are thus always localized as far as the chemical potential is negative.

Next we show another feature of the coordinate-space HFB theory. Let us discuss the HF+BCS approximation to the HFB equation, in which one assumes the pairing field to be

$$\tilde{h}_{\text{BCS}}(r\sigma, r'\sigma') = -\Delta\delta(r - r')\delta_{\sigma\sigma'}, \tag{2.48}$$

where Δ is called the gap parameter. In this approximation, the pairing field is *not localized* to the region of small r and r', and thus the asymptotic properties of the solutions are different. The wave functions φ_1 and φ_2 are now proportional to the canonical-basis wave functions ψ_α,

$$\varphi_1(E_\alpha, r\sigma) = u_\alpha\psi_\alpha(r\sigma), \tag{2.49a}$$

$$\varphi_2(E_\alpha, r\sigma) = v_\alpha\psi_\alpha(r\sigma), \tag{2.49b}$$

which are eigenfunctions of the Hartree-Fock field h

$$\int dr' \sum_{\sigma'} h(r\sigma, r'\sigma')\psi_\alpha(r'\sigma') = \epsilon_\alpha\psi_\alpha(r\sigma), \tag{2.50}$$

where ϵ_α, u_α and v_α are related to E, Δ and λ by the usual BCS formulas [43]. The spectrum of the HF equation (2.50) is discrete for $\epsilon_\alpha < 0$ and continuus for $\epsilon_\alpha > 0$ and the wave functions are respectively localized and non-localized. The BCS densities are thus non-localized for weakly bound nuclei and the nucleus is surrounded by an unphysical nucleon gas. Therefore, in descriprion of the neutron-rich nuclei where the continuum coupling effect is important the BCS approximation breaks down and the coordinate-space HFB is the only method to treat the pair correlations and the continuum counpling effects simultaneously.

2.1.4   The HFB method in the cylindrical-coordinate representation

In this thesis, we study the nuclear defomation effects in addition to the pair correlations and the contitnuum coupling effects. We assume that the nucleus is symmetric with respect to the $z-$axis in the intrinsic frame of reference. We are going to follow the formulation given in Refs. [84, 85, 86]. In this case, the HFB Hamiltonian is invariant under rotation $\hat{R}_z$ about the $z-$axis,

$$[\mathscr{H}, \hat{R}_z] = 0. \tag{2.51}$$

It is advantageous to introduce the cilyndrical coordinates (ρ, z, ϕ). The rotation about the $z-$axis is generatred by the operator

$$\hat{R}_z(\phi) = \exp(-i\phi\hat{j}_z/\hbar). \tag{2.52}$$

This requirement is equivalent to

$$[\mathscr{H}, \hat{j}_z] = 0. \tag{2.53}$$

Thanks to the axial symmetry, it is possible to construct simultaneous eigenfunctions of the HFB Hamiltonian $\mathscr{H}$ and the $z-$component of the angular momentum $\hat{j}_z$,

$$\mathscr{H} \begin{pmatrix} \varphi_{1,i}(\rho, z, \phi, \sigma) \\ \varphi_{2,i}(\rho, z, \phi, \sigma) \end{pmatrix} = E_i \begin{pmatrix} \varphi_{1,i}(\rho, z, \phi, \sigma) \\ \varphi_{2,i}(\rho, z, \phi, \sigma) \end{pmatrix}, \tag{2.54a}$$

$$\hat{j}_z \begin{pmatrix} \varphi_{1,i}(\rho, z, \phi, \sigma) \\ \varphi_{2,i}(\rho, z, \phi, \sigma) \end{pmatrix} = \hbar\Omega_i \begin{pmatrix} \varphi_{1,i}(\rho, z, \phi, \sigma) \\ \varphi_{2,i}(\rho, z, \phi, \sigma) \end{pmatrix}, \tag{2.54b}$$

and the eigenfunctions are expressed in the spinor form

$$\varphi_i(\rho, z, \phi, \sigma) = \begin{pmatrix} \varphi_i^+(\rho, z)e^{i\Lambda_i^-\phi} \\ \varphi_i^-(\rho, z)e^{i\Lambda_i^+\phi} \end{pmatrix}, \tag{2.55}$$

where $\Lambda_i^\pm = \Omega_i \pm 1/2$. Since the angular denpendence is determined by Ω, we can define the Hamiltonian h that is uniquely defined by Ω, namely that is block diagonal in each Ω. Therefore we can write down the single quasiparticle Hamiltonian as

$$h(\rho, z, \phi) = \begin{pmatrix} h_{\uparrow\uparrow}(\rho, z) & e^{-i\phi}h_{\uparrow\downarrow}(\rho, z) \\ e^{i\phi}h_{\downarrow\uparrow}(\rho, z) & h_{\downarrow\downarrow}(\rho, z) \end{pmatrix}, \tag{2.56a}$$

$$\tilde{h}(\rho, z, \phi) = \begin{pmatrix} \tilde{h}_{\uparrow\uparrow}(\rho, z) & e^{-i\phi}\tilde{h}_{\uparrow\downarrow}(\rho, z) \\ e^{i\phi}\tilde{h}_{\downarrow\uparrow}(\rho, z) & \tilde{h}_{\downarrow\downarrow}(\rho, z) \end{pmatrix}. \tag{2.56b}$$

Inserting (2.56) into (2.44), we obtain the HFB equation in the cylindrical-coordinate representation for each Ω sector

$$\begin{pmatrix} h_{\uparrow\uparrow} - \lambda & h_{\uparrow\downarrow} & \tilde{h}_{\uparrow\uparrow} & \tilde{h}_{\downarrow\downarrow} \\ h_{\downarrow\uparrow} & h_{\downarrow\downarrow} - \lambda & \tilde{h}_{\downarrow\uparrow} & \tilde{h}_{\downarrow\downarrow} \\ \tilde{h}_{\uparrow\uparrow} & \tilde{h}_{\downarrow\uparrow} & -(h_{\uparrow\uparrow} - \lambda) & -h_{\uparrow\downarrow} \\ \tilde{h}_{\downarrow\uparrow} & \tilde{h}_{\downarrow\downarrow} & -h_{\downarrow\uparrow} & -(h_{\downarrow\downarrow} - \lambda) \end{pmatrix} \begin{pmatrix} \varphi_{1,i}^+ \\ \varphi_{1,i}^- \\ \varphi_{2,i}^+ \\ \varphi_{2,i}^- \end{pmatrix} = E_i \begin{pmatrix} \varphi_{1,i}^+ \\ \varphi_{1,i}^- \\ \varphi_{2,i}^+ \\ \varphi_{2,i}^- \end{pmatrix}. \tag{2.57}$$

2.2 The Random Phase Approximation and the Quasiparticle-RPA

The collective motions can be described by means of the time-dependent mean-field theory. In this thesis, we use the Random Phase Approximation (RPA) in order to take into account correlations beyond the mean field and study nuclear collective modes. The RPA was originally introduced to describe the plasma oscillation by Sawada in 1957 [87] and applied to the collective octupole vibration in closed-shell nuclei [88, 89] soon after the pioneering work of Sawada. The Quasiparticle-RPA (QRPA) including pairing correlations was formulated in 1960 by several authors [90, 91, 92, 93].

2.2.1 Linearization of the TDHF equation

The RPA is equaivalent to the small amplitude limit of the time-dependent mean-field theory.

The time-dependent Schrödinger equation for the many-body wave function $|\Psi(t)\rangle$

$$i\hbar\partial_t|\Psi(t)\rangle = H|\Psi(t)\rangle \tag{2.58}$$

is equaivalent to the time-denepdent variational principle

$$\delta\langle\Psi(t)|i\hbar\partial_t - H|\Psi(t)\rangle = 0. \tag{2.59}$$

The time-dependent Hartree-Fock (TDHF) theory assumes that the wave function $|\Psi(t)\rangle$ is a Slater determinant at any time.

Suppose that $|\Phi_0\rangle$ is a HF state at $t = 0$. One can define creation and annihilation operators of particles and holes associated with $|\Phi_0\rangle$,

$$c_\alpha^\dagger = (1 - n_\alpha)c_\alpha^\dagger + n_\alpha c_\alpha^\dagger = a_\alpha^\dagger + b_\alpha, \tag{2.60}$$

where

$$n_\alpha = \begin{cases} 1 & \text{for } \epsilon_\alpha \leq \epsilon_F \\ 0 & \text{for } \epsilon_\alpha > \epsilon_F. \end{cases} \tag{2.61}$$

The HF state is the vacuum for these particles and holes,

$$a_m|\Phi_0\rangle = 0, \quad b_i|\Phi_0\rangle = 0. \tag{2.62}$$

17

Using the particle and hole operators, the nuclear Hamiltonian (2.2) can be rewritten as

$$H = E_0 + H_0 + H_{int} \tag{2.63a}$$

$$E_0 = \langle H \rangle = \sum_i \left(\varepsilon_i - \frac{1}{2} \sum_j v_{ijij} \right) \tag{2.63b}$$

$$H_0 = \sum_\alpha \epsilon_\alpha : c_\alpha^+ c_\alpha := \sum_m \epsilon_m a_m^+ a_m - \sum_i \epsilon_i b_i^+ b_i \tag{2.63c}$$

$$H_{int} = \frac{1}{4} \sum_{\alpha\beta\gamma\delta} v_{\alpha\beta\gamma\delta} : c_\alpha^+ c_\beta^+ c_\delta c_\gamma := H_{pp} + H_{hh} + H_{ph} + H_V + H_Y \tag{2.63d}$$

$$H_{pp} = \frac{1}{4} \sum_{mnm'n'} v_{mnm'n'} a_m^+ a_n^+ a_{n'} a_{m'} \tag{2.63e}$$

$$H_{hh} = \frac{1}{4} \sum_{iji'j'} v_{iji'j'} b_i^+ b_j^+ b_{j'} b_{i'} \tag{2.63f}$$

$$H_{ph} = \sum_{mnij} v_{mjin} a_m^+ b_i^+ b_j a_n \tag{2.63g}$$

$$H_V = \frac{1}{4} \sum_{mnij} v_{mnij} (a_m^+ a_n^+ b_j^+ b_i^+ + a_m a_n b_j b_i) \tag{2.63h}$$

$$H_Y = \frac{1}{2} \left\{ \sum_{mnm'i} v_{mnm'i} (a_m^+ a_n^+ b_i^+ a_{m'} + a_{m'}^+ b_i a_n a_m) + \sum_{miji'} v_{mji'i} (a_m^+ b_i^+ b_{i'}^+ b_j + b_j^+ b_{i'} b_i a_m) \right\}. \tag{2.63i}$$

The time-dependent variational principle (2.59) reads

$$\frac{\partial}{\partial g_{mi}^*(t)} \langle \Phi(t) | i\hbar \partial_t - H | \Phi(t) \rangle = 0. \tag{2.64}$$

Suppose that $|\Phi(t)\rangle$ has a form of vibrational solution at time t

$$|\Phi(t)\rangle = e^{-iE_0 t/\hbar} e^{iG(t)} |\Phi_0\rangle \tag{2.65}$$

$$= e^{-iE_0 t/\hbar} \exp\left(\sum_{mi} \{ g_{mi}(t) a_m^\dagger b_i^\dagger - g_{mi}^*(t) b_i a_m \} \right) |\Phi_0\rangle, \tag{2.66}$$

where $e^{iG(t)}$ is a unitary operator.

Here we consider the solution

$$g_{mi}(t) = x_{mi} e^{-i\omega t} + y_{mi}^* e^{i\omega t}. \tag{2.67}$$

18

Evaluating the expectation value $\langle\Phi(t)|H|\Phi(t)\rangle$ up to the second order in $g_{mi}(t)$,

$$
\begin{aligned}
\langle\Phi(t)|H|\Phi(t)\rangle &= \langle\Phi_0|e^{-iG(t)}He^{iG(t)}|\Phi_0\rangle \\
&= E_0 + \sum_{mi}(\epsilon_m - \epsilon_i)g_{mi}(t)g_{mi}^*(t) + \sum_{mnij}v_{mjin}g_{mi}(t)g_{nj}^*(t) \\
&\quad + \frac{1}{2}\sum_{mnij}v_{mnij}g_{mi}(t)g_{nj}(t) + \frac{1}{2}\sum_{mnij}v_{mnij}g_{mi}^*(t)g_{nj}^*(t),
\end{aligned}
\tag{2.68a}
$$

$$
\langle\Phi(t)|i\hbar\partial_t|\Phi(t)\rangle = E_0 + \sum_{mi}g_{mi}^*(t)(i\hbar\partial_t)g_{mi}(t).
\tag{2.68b}
$$

One obtains the eigenvalue equation

$$
\hbar\omega x_{mi} = (\epsilon_m - \epsilon_i)x_{mi} + \sum_{nj}\{v_{mjin}x_{nj} + v_{mnij}y_{nj}\},
\tag{2.69a}
$$

$$
-\hbar\omega y_{mi} = (\epsilon_m - \epsilon_i)y_{mi} + \sum_{nj}\{v_{mjin}y_{nj} + v_{mnij}x_{nj}\}.
\tag{2.69b}
$$

This is written in a matrix form

$$
\sum_{nj}\begin{pmatrix} A_{minj} & B_{minj} \\ B_{minj}^* & A_{minj}^* \end{pmatrix}\begin{pmatrix} x_{nj} \\ y_{nj} \end{pmatrix} = \hbar\omega\begin{pmatrix} 1 & 0 \\ 0 & -1 \end{pmatrix}\begin{pmatrix} x_{mi} \\ y_{mi} \end{pmatrix},
\tag{2.70}
$$

where

$$
A_{minj} = (\epsilon_m - \epsilon_i)\delta_{mn}\delta_{ij} + v_{mjin},
\tag{2.71}
$$

$$
B_{minj} = v_{mnij}.
\tag{2.72}
$$

For the case of superfluid systems, one can derive the QRPA equation in a similar manner as the small amplitude limit of the TDHFB equation [83].

2.2.2 The equation-of-motion method

We discuss here an alternative method to derive the RPA equation, called the equation-of-motion method [95, 96, 97]. Let us strat with exact eigenstates of the Hamiltonian (2.2),

$$
H|\Psi_0\rangle = E_0|\Psi_0\rangle,
\tag{2.73a}
$$

$$
H|\Psi_\lambda\rangle = E_\lambda|\Psi_\lambda\rangle.
\tag{2.73b}
$$

We here introduce the creation and annihilation operators $\boldsymbol{O}_\lambda^\dagger, \boldsymbol{O}_\lambda$ satisfying

$$
\begin{cases} |\Psi_\lambda\rangle = \boldsymbol{O}_\lambda^\dagger|\Psi_0\rangle, \ \ |\Psi_0\rangle = \boldsymbol{O}_\lambda|\Psi_\lambda\rangle, \\ \boldsymbol{O}_\lambda|\Psi_0\rangle = 0. \end{cases}
\tag{2.74}
$$

It is easy to derive the equation of motion

$$
[H, \boldsymbol{O}_\lambda^\dagger]|\Psi_0\rangle = (E_\lambda - E_0)\boldsymbol{O}_\lambda^\dagger|\Psi_0\rangle,
\tag{2.75}
$$

or equivalently

$$
\langle\Psi_0|[\delta\boldsymbol{O}, [H, \boldsymbol{O}_\lambda^\dagger]]|\Psi_0\rangle = (E_\lambda - E_0)\langle\Psi_0|[\delta\boldsymbol{O}, \boldsymbol{O}_\lambda^\dagger]|\Psi_0\rangle.
\tag{2.76}
$$

Here we define the phonon operator and the approximated ground state $|\Psi_0^{\text{RPA}}\rangle$ as

$$O_\lambda^\dagger = \sum_{mi} f_{mi}^\lambda a_m^\dagger b_i^\dagger - g_{mi}^\lambda b_i a_m, \tag{2.77a}$$

$$O_\lambda |\Psi_0^{\text{RPA}}\rangle = 0. \tag{2.77b}$$

Taking $a_m^\dagger b_i^\dagger |\Psi_0^{\text{RPA}}\rangle$ and $b_i a_m |\Psi_0^{\text{RPA}}\rangle$ as a variation $\delta O |\Psi_0\rangle$, one obtains

$$\langle \Psi_0^{\text{RPA}}|[b_i a_m, [H, O_\lambda^\dagger]]|\Psi_0^{\text{RPA}}\rangle = \hbar\omega_\lambda \langle \Psi_0^{\text{RPA}}|[b_i a_m, O_\lambda^\dagger]|\Psi_0^{\text{RPA}}\rangle, \tag{2.78a}$$

$$\langle \Psi_0^{\text{RPA}}|[a_m^\dagger b_i^\dagger, [H, O_\lambda^\dagger]]|\Psi_0^{\text{RPA}}\rangle = \hbar\omega_\lambda \langle \Psi_0^{\text{RPA}}|[a_m^\dagger b_i^\dagger, O_\lambda^\dagger]|\Psi_0^{\text{RPA}}\rangle, \tag{2.78b}$$

where $\hbar\omega_\lambda$ is the excitation energy of the state $|\Psi_\lambda^{\text{RPA}}\rangle$.

In calculating the expectation values in Eq.(2.78), we replace $|\Psi_0^{\text{RPA}}\rangle$ by $|\Psi_0^{\text{HF}}\rangle$. This approximation is valid if the correlated state $|\Psi_0^{\text{RPA}}\rangle$ does not differ very much from $|\Psi_0^{\text{HF}}\rangle$. Under this approximation, Eq. (2.78) reads Eq. (2.69), where

$$\langle \Psi_0^{\text{RPA}}|b_i a_m|\Psi_\lambda^{\text{RPA}}\rangle \simeq \langle \Psi_0^{\text{HF}}|[b_i a_m, O_\lambda^\dagger]|\Psi_0^{\text{HF}}\rangle = x_{mi}^\lambda, \tag{2.79a}$$

$$\langle \Psi_0^{\text{RPA}}|a_m^\dagger b_i^\dagger|\Psi_\lambda^{\text{RPA}}\rangle \simeq \langle \Psi_0^{\text{HF}}|[a_m^\dagger b_i^\dagger, O_\lambda^\dagger]|\Psi_0^{\text{HF}}\rangle = y_{mi}^\lambda. \tag{2.79b}$$

The orthonormality of the one-phonon states $|\Psi_\lambda^{\text{RPA}}\rangle, |\Psi_{\lambda'}^{\text{RPA}}\rangle$ is satisfied by the condition;

$$\begin{aligned}
\langle \Psi_{\lambda'}^{\text{RPA}}|\Psi_\lambda^{\text{RPA}}\rangle &\simeq \sum_{mi}\sum_{nj}\{x_{nj}^{\lambda'*}\langle \Psi_0^{\text{HF}}|[b_j a_n, a_m^\dagger b_i^\dagger]|\Psi_0^{\text{HF}}\rangle x_{mi}^\lambda - y_{nj}^{\lambda'*}\langle \Psi_0^{\text{HF}}|[b_i a_m, a_n^\dagger b_j^\dagger]|\Psi_0^{\text{HF}}\rangle y_{mi}^\lambda\} \\
&= \sum_{mi} x_{mi}^{\lambda*}x_{mi}^{\lambda'} - y_{mi}^{\lambda*}y_{mi}^{\lambda'} \\
&= \delta_{\lambda\lambda'},
\end{aligned} \tag{2.80}$$

which gives the normalization of the amplitudes x_{mi}^λ and y_{mi}^λ.

2.2.3 Invariances and spurious solutions in the RPA

We introduce the generalized coordinates $\mathcal{Q}_\nu$ and momenta $\mathcal{P}_\nu$ [94] defined by

$$\mathcal{P}_\nu = \frac{\hbar}{i}\sqrt{\frac{M_\nu\omega_\nu}{\hbar}}\frac{1}{\sqrt{2}}(O_\nu - O_\nu^\dagger), \tag{2.81a}$$

$$\mathcal{Q}_\nu = \sqrt{\frac{\hbar}{M_\nu\omega_\nu}}\frac{1}{\sqrt{2}}(O_\nu + O_\nu^\dagger), \tag{2.81b}$$

where the numbers M_ν are arbitrary. The operators $\mathcal{P}_\nu, \mathcal{Q}_\nu$ fulfill the commutation relations

$$[\mathcal{P}_\nu, \mathcal{P}_{\nu'}] = [\mathcal{Q}_\nu, \mathcal{Q}_{\nu'}] = 0, \tag{2.82a}$$

$$[\mathcal{P}_\nu, \mathcal{Q}_{\nu'}] = \frac{\hbar}{i}\delta_{\nu\nu'}. \tag{2.82b}$$

The Hamiltonian H is now expressed in terms of these operators

$$H = E_{\text{RPA}} + \sum_\nu \left(\frac{1}{2M_\nu}\mathcal{P}_\nu^2 + \frac{M_\nu}{2}\omega_\nu^2 \mathcal{Q}_\nu^2\right) \tag{2.83}$$

in the RPA order with

$$E_{\text{RPA}} = E_{\text{HF}} - \sum_\nu \hbar\omega_\nu \sum_{mi} |y_{mi}^\nu|^2. \tag{2.84}$$

The operators $\mathscr{P}_\nu, \mathscr{Q}_\nu$ obey the equations of motion

$$[H, \mathscr{P}_\nu] = i\hbar\omega_\nu^2 M_\nu \mathscr{Q}_\nu, \tag{2.85a}$$

$$[H, \mathscr{Q}_\nu] = -\frac{i\hbar}{M_\nu} \mathscr{P}_\nu, \tag{2.85b}$$

which are written in a matrix representation as

$$\begin{pmatrix} A & B \\ B^* & A^* \end{pmatrix} \begin{pmatrix} P \\ -P^* \end{pmatrix} = i\hbar\omega_\nu^2 M_\nu \begin{pmatrix} Q \\ Q^* \end{pmatrix}, \tag{2.86a}$$

$$\begin{pmatrix} A & B \\ B^* & A^* \end{pmatrix} \begin{pmatrix} Q \\ -Q^* \end{pmatrix} = \frac{\hbar}{i} \frac{1}{M_\nu} \begin{pmatrix} P \\ P^* \end{pmatrix}. \tag{2.86b}$$

The vectors P, Q are determined by the condition (2.82b)

$$\begin{pmatrix} P^* & P \end{pmatrix}_\nu \begin{pmatrix} Q \\ -Q^* \end{pmatrix}_{\nu'} = \frac{\hbar}{i} \delta_{\nu\nu'}. \tag{2.87}$$

Let us assume that the Hamiltonian H is invariant under a continuous symmetry operation generated by a Hermitian one-body operator $\hat{P}$. The exact Hamiltonian commutes with $\hat{P}$:

$$[H, \hat{P}] = 0. \tag{2.88}$$

It is easily confirmed that $\hat{P}$ is a spurious solution of the RPA equation [83]

$$\langle \text{HF} | [\delta O, [H, \hat{P}] | \text{HF} \rangle = 0. \tag{2.89}$$

In the matrix representation, this is written as

$$\begin{pmatrix} A & B \\ B^* & A^* \end{pmatrix} \begin{pmatrix} P \\ -P^* \end{pmatrix} = 0. \tag{2.90}$$

The RPA equation (2.69) or (2.86) has this solution for the case in which the symmetry is broken by the HF solution; $[\varrho^{(0)}, \hat{P}] \neq 0$. Otherwise the matrix elements P_{mi} vanish identically. We can determine the constant M_0 for the spurious mode using Eqs.(2.86) and (2.87). This constant M_0 corresponds to the total mass of the nucleus $M_0 = Am$ and the moment of inertia $M_0 = \mathscr{J}$ for the case of breaking the translational and the rotational invariances, respectively.

2.2.4   The Quasiparticle-RPA equation

Next we present the explicit expression of the QRPA equation based on the coordinate-space HFB formalism. We redefine the RPA phonon operator as

$$O_\lambda^\dagger = \sum_{i<j} f_{ij}^\lambda \beta_i^\dagger \beta_j^\dagger - g_{ij}^\lambda \beta_{\bar{j}} \beta_{\bar{i}} = \sum_{i<j} f_{ij}^\lambda A_{ij}^\dagger - g_{ij}^\lambda A_{\bar{i}\bar{j}}, \tag{2.91}$$

where $\{ij\}$ runs over all two-quasiparticle combinations and $\bar{i}$ denotes the time-reversed state of i. The time-reversed state is defined by

$$\varphi_{\bar{i}}(\boldsymbol{r}\sigma) = \mathscr{T}\varphi_i(\boldsymbol{r}\sigma) = -2\sigma\varphi_i^*(\boldsymbol{r} - \sigma). \tag{2.92}$$

Here we introduce the Fermion bilinear operators $A_{ij}^\dagger = \beta_i^\dagger\beta_j^\dagger$ and $A_{ij} = \beta_j\beta_i$. These operators satisfy the following boson-like commutation relations

$$\langle\mathrm{HFB}|[A_{ij}^\dagger, A_{i'j'}^\dagger]|\mathrm{HFB}\rangle = \langle\mathrm{HFB}|[A_{ij}, A_{i'j'}]|\mathrm{HFB}\rangle = 0, \tag{2.93a}$$

$$\langle\mathrm{HFB}|[A_{ij}, A_{i'j'}^\dagger]|\mathrm{HFB}\rangle = \delta_{ii'}\delta_{jj'} - \delta_{ij'}\delta_{ji'} = \delta_{i'j'}^{ij}. \tag{2.93b}$$

The QRPA equation is written in a simple matrix form [96]

$$\sum_{\gamma\delta}\begin{pmatrix} A_{\alpha\beta\gamma\delta} & B_{\alpha\beta\gamma\delta} \\ B_{\alpha\beta\gamma\delta}^* & A_{\alpha\beta\gamma\delta}^* \end{pmatrix}\begin{pmatrix} f_{\gamma\delta}^\lambda \\ g_{\gamma\delta}^\lambda \end{pmatrix} = \hbar\omega_\lambda\begin{pmatrix} 1 & 0 \\ 0 & -1 \end{pmatrix}\begin{pmatrix} f_{\alpha\beta}^\lambda \\ g_{\alpha\beta}^\lambda \end{pmatrix}, \tag{2.94}$$

where

$$A_{\alpha\beta\gamma\delta} = \langle\mathrm{HFB}|[A_{\alpha\beta}, [H, A_{\gamma\delta}^\dagger]]|\mathrm{HFB}\rangle, \tag{2.95a}$$

$$B_{\alpha\beta\gamma\delta} = -\langle\mathrm{HFB}|[A_{\alpha\beta}, [H, A_{\bar{\gamma}\bar{\delta}}]]|\mathrm{HFB}\rangle. \tag{2.95b}$$

Explicit expressions of the matrix elements are

$$\begin{aligned}
A_{\alpha\beta\gamma\delta} &= (E_\alpha + E_\beta)\delta_{\alpha\gamma}\delta_{\beta\delta} \\
&+ \sum_{\sigma_1,\sigma_2,\sigma_1',\sigma_2'}\int d\boldsymbol{r}_1 d\boldsymbol{r}_2 d\boldsymbol{r}_1' d\boldsymbol{r}_2' \times \\
&\{U_\alpha^*(\boldsymbol{r}_1\sigma_1)U_\beta^*(\boldsymbol{r}_2\sigma_2)\bar{v}_{pp}(\boldsymbol{r}_1\sigma_1, \boldsymbol{r}_2\sigma_2; \boldsymbol{r}_1'\sigma_1', \boldsymbol{r}_2'\sigma_2')U_\gamma(\boldsymbol{r}_1'\sigma_1')U_\delta(\boldsymbol{r}_2'\sigma_2') \\
&+ V_\alpha^*(\boldsymbol{r}_1\sigma_1)V_\beta^*(\boldsymbol{r}_2\sigma_2)\bar{v}_{pp}(\boldsymbol{r}_1\sigma_1, \boldsymbol{r}_2\sigma_2; \boldsymbol{r}_1'\sigma_1', \boldsymbol{r}_2'\sigma_2')V_\gamma(\boldsymbol{r}_1'\sigma_1')V_\delta(\boldsymbol{r}_2'\sigma_2') \\
&- U_\alpha^*(\boldsymbol{r}_1\sigma_1)V_\gamma(\boldsymbol{r}_2\sigma_2)\bar{v}_{ph}(\boldsymbol{r}_1\sigma_1, \boldsymbol{r}_2\sigma_2; \boldsymbol{r}_1'\sigma_1', \boldsymbol{r}_2'\sigma_2')V_\beta^*(\boldsymbol{r}_1'\sigma_1')U_\delta(\boldsymbol{r}_2'\sigma_2') \\
&- V_\alpha^*(\boldsymbol{r}_1\sigma_1)U_\gamma(\boldsymbol{r}_2\sigma_2)\bar{v}_{ph}(\boldsymbol{r}_1\sigma_1, \boldsymbol{r}_2\sigma_2; \boldsymbol{r}_1'\sigma_1', \boldsymbol{r}_2'\sigma_2')U_\beta^*(\boldsymbol{r}_1'\sigma_1')V_\delta(\boldsymbol{r}_2'\sigma_2') \\
&+ U_\alpha^*(\boldsymbol{r}_1\sigma_1)V_\delta(\boldsymbol{r}_2\sigma_2)\bar{v}_{ph}(\boldsymbol{r}_1\sigma_1, \boldsymbol{r}_2\sigma_2; \boldsymbol{r}_1'\sigma_1', \boldsymbol{r}_2'\sigma_2')V_\beta^*(\boldsymbol{r}_1'\sigma_1')U_\gamma(\boldsymbol{r}_2'\sigma_2') \\
&+ V_\alpha^*(\boldsymbol{r}_1\sigma_1)U_\delta(\boldsymbol{r}_2\sigma_2)\bar{v}_{ph}(\boldsymbol{r}_1\sigma_1, \boldsymbol{r}_2\sigma_2; \boldsymbol{r}_1'\sigma_1', \boldsymbol{r}_2'\sigma_2')U_\beta^*(\boldsymbol{r}_1'\sigma_1')V_\gamma(\boldsymbol{r}_2'\sigma_2')\}, \tag{2.96}
\end{aligned}$$

$$\begin{aligned}
B_{\alpha\beta\gamma\delta} &= \sum_{\sigma_1,\sigma_2,\sigma_1',\sigma_2'}\int d\boldsymbol{r}_1 d\boldsymbol{r}_2 d\boldsymbol{r}_1' d\boldsymbol{r}_2' \times \\
&\{-U_\alpha^*(\boldsymbol{r}_1\sigma_1)U_\beta^*(\boldsymbol{r}_2\sigma_2)\bar{v}_{pp}(\boldsymbol{r}_1\sigma_1, \boldsymbol{r}_2\sigma_2; \boldsymbol{r}_1'\sigma_1', \boldsymbol{r}_2'\sigma_2')V_{\bar{\gamma}}^*(\boldsymbol{r}_1'\sigma_1')V_{\bar{\delta}}^*(\boldsymbol{r}_2'\sigma_2') \\
&- V_\alpha^*(\boldsymbol{r}_1\sigma_1)V_\beta^*(\boldsymbol{r}_2\sigma_2)\bar{v}_{pp}(\boldsymbol{r}_1\sigma_1, \boldsymbol{r}_2\sigma_2; \boldsymbol{r}_1'\sigma_1', \boldsymbol{r}_2'\sigma_2')U_{\bar{\gamma}}^*(\boldsymbol{r}_1'\sigma_1')U_{\bar{\delta}}^*(\boldsymbol{r}_2'\sigma_2') \\
&+ U_\alpha^*(\boldsymbol{r}_1\sigma_1)U_{\bar{\gamma}}^*(\boldsymbol{r}_2\sigma_2)\bar{v}_{ph}(\boldsymbol{r}_1\sigma_1, \boldsymbol{r}_2\sigma_2; \boldsymbol{r}_1'\sigma_1', \boldsymbol{r}_2'\sigma_2')V_\beta^*(\boldsymbol{r}_1'\sigma_1')V_{\bar{\delta}}^*(\boldsymbol{r}_2'\sigma_2') \\
&+ V_\alpha^*(\boldsymbol{r}_1\sigma_1)V_{\bar{\gamma}}^*(\boldsymbol{r}_2\sigma_2)\bar{v}_{ph}(\boldsymbol{r}_1\sigma_1, \boldsymbol{r}_2\sigma_2; \boldsymbol{r}_1'\sigma_1', \boldsymbol{r}_2'\sigma_2')U_\beta^*(\boldsymbol{r}_1'\sigma_1')U_{\bar{\delta}}^*(\boldsymbol{r}_2'\sigma_2') \\
&- U_\alpha^*(\boldsymbol{r}_1\sigma_1)U_{\bar{\delta}}^*(\boldsymbol{r}_2\sigma_2)\bar{v}_{ph}(\boldsymbol{r}_1\sigma_1, \boldsymbol{r}_2\sigma_2; \boldsymbol{r}_1'\sigma_1', \boldsymbol{r}_2'\sigma_2')V_\beta^*(\boldsymbol{r}_1'\sigma_1')V_{\bar{\gamma}}^*(\boldsymbol{r}_2'\sigma_2') \\
&- V_\alpha^*(\boldsymbol{r}_1\sigma_1)V_{\bar{\delta}}^*(\boldsymbol{r}_2\sigma_2)\bar{v}_{ph}(\boldsymbol{r}_1\sigma_1, \boldsymbol{r}_2\sigma_2; \boldsymbol{r}_1'\sigma_1', \boldsymbol{r}_2'\sigma_2')U_\beta^*(\boldsymbol{r}_1'\sigma_1')U_{\bar{\gamma}}^*(\boldsymbol{r}_2'\sigma_2')\}. \tag{2.97}
\end{aligned}$$

Using the wave functions φ_1 and φ_2, the solutions of the coordinate-space HFB equation, they are written as

$$
\begin{aligned}
A_{\alpha\beta\gamma\delta} = {} & (E_\alpha + E_\beta)\delta_{\alpha\gamma}\delta_{\beta\delta} \\
& + \sum_{\sigma_1,\sigma_2,\sigma_1',\sigma_2'} \int d\boldsymbol{r}_1 d\boldsymbol{r}_2 d\boldsymbol{r}_1' d\boldsymbol{r}_2' \times \\
& \{\varphi_{1,\alpha}(\boldsymbol{r}_1\bar{\sigma}_1)\varphi_{1,\beta}(\boldsymbol{r}_2\bar{\sigma}_2)\bar{v}_{pp}(\boldsymbol{r}_1\sigma_1,\boldsymbol{r}_2\sigma_2;\boldsymbol{r}_1'\sigma_1',\boldsymbol{r}_2'\sigma_2')\varphi_{1,\gamma}^*(\boldsymbol{r}_1'\bar{\sigma}_1')\varphi_{1,\delta}^*(\boldsymbol{r}_2'\bar{\sigma}_2') \\
& + \varphi_{2,\alpha}(\boldsymbol{r}_1\sigma_1)\varphi_{2,\beta}(\boldsymbol{r}_2\sigma_2)\bar{v}_{pp}(\boldsymbol{r}_1\sigma_1,\boldsymbol{r}_2\sigma_2;\boldsymbol{r}_1'\sigma_1',\boldsymbol{r}_2'\sigma_2')\varphi_{2,\gamma}^*(\boldsymbol{r}_1'\sigma_1')\varphi_{2,\delta}^*(\boldsymbol{r}_2'\sigma_2') \\
& - \varphi_{1,\alpha}(\boldsymbol{r}_1\bar{\sigma}_1)\varphi_{2,\gamma}^*(\boldsymbol{r}_2\sigma_2)\bar{v}_{ph}(\boldsymbol{r}_1\sigma_1,\boldsymbol{r}_2\sigma_2;\boldsymbol{r}_1'\sigma_1',\boldsymbol{r}_2'\sigma_2')\varphi_{2,\beta}(\boldsymbol{r}_1'\sigma_1')\varphi_{1,\delta}^*(\boldsymbol{r}_2'\bar{\sigma}_2') \\
& - \varphi_{2,\alpha}(\boldsymbol{r}_1\sigma_1)\varphi_{1,\gamma}^*(\boldsymbol{r}_2\bar{\sigma}_2)\bar{v}_{ph}(\boldsymbol{r}_1\sigma_1,\boldsymbol{r}_2\sigma_2;\boldsymbol{r}_1'\sigma_1',\boldsymbol{r}_2'\sigma_2')\varphi_{1,\beta}(\boldsymbol{r}_1'\bar{\sigma}_1')\varphi_{2,\delta}^*(\boldsymbol{r}_2'\sigma_2') \\
& + \varphi_{1,\alpha}(\boldsymbol{r}_1\bar{\sigma}_1)\varphi_{2,\delta}^*(\boldsymbol{r}_2\sigma_2)\bar{v}_{ph}(\boldsymbol{r}_1\sigma_1,\boldsymbol{r}_2\sigma_2;\boldsymbol{r}_1'\sigma_1',\boldsymbol{r}_2'\sigma_2')\varphi_{2,\beta}(\boldsymbol{r}_1'\sigma_1')\varphi_{1,\gamma}^*(\boldsymbol{r}_2'\bar{\sigma}_2') \\
& + \varphi_{2,\alpha}(\boldsymbol{r}_1\sigma_1)\varphi_{1,\delta}^*(\boldsymbol{r}_2\bar{\sigma}_2)\bar{v}_{ph}(\boldsymbol{r}_1\sigma_1,\boldsymbol{r}_2\sigma_2;\boldsymbol{r}_1'\sigma_1',\boldsymbol{r}_2'\sigma_2')\varphi_{1,\beta}(\boldsymbol{r}_1'\bar{\sigma}_1')\varphi_{2,\gamma}^*(\boldsymbol{r}_2'\sigma_2')\}, \quad (2.98)
\end{aligned}
$$

$$
\begin{aligned}
B_{\alpha\beta\gamma\delta} = {} & \sum_{\sigma_1,\sigma_2,\sigma_1',\sigma_2'} \int d\boldsymbol{r}_1 d\boldsymbol{r}_2 d\boldsymbol{r}_1' d\boldsymbol{r}_2' \times \\
& \{-\varphi_{1,\alpha}(\boldsymbol{r}_1\bar{\sigma}_1)\varphi_{1,\beta}(\boldsymbol{r}_2\bar{\sigma}_2)\bar{v}_{pp}(\boldsymbol{r}_1\sigma_1,\boldsymbol{r}_2\sigma_2;\boldsymbol{r}_1'\sigma_1',\boldsymbol{r}_2'\sigma_2')\varphi_{2,\bar{\gamma}}(\boldsymbol{r}_1'\sigma_1')\varphi_{2,\bar{\delta}}(\boldsymbol{r}_2'\sigma_2') \\
& - \varphi_{2,\alpha}(\boldsymbol{r}_1\sigma_1)\varphi_{2,\beta}(\boldsymbol{r}_2\sigma_2)\bar{v}_{pp}(\boldsymbol{r}_1\sigma_1,\boldsymbol{r}_2\sigma_2;\boldsymbol{r}_1'\sigma_1',\boldsymbol{r}_2'\sigma_2')\varphi_{1,\bar{\gamma}}(\boldsymbol{r}_1'\bar{\sigma}_1')\varphi_{1,\bar{\delta}}(\boldsymbol{r}_2'\bar{\sigma}_2') \\
& + \varphi_{1,\alpha}(\boldsymbol{r}_1\bar{\sigma}_1)\varphi_{1,\bar{\gamma}}(\boldsymbol{r}_2\bar{\sigma}_2)\bar{v}_{ph}(\boldsymbol{r}_1\sigma_1,\boldsymbol{r}_2\sigma_2;\boldsymbol{r}_1'\sigma_1',\boldsymbol{r}_2'\sigma_2')\varphi_{2,\beta}(\boldsymbol{r}_1'\sigma_1')\varphi_{2,\bar{\delta}}(\boldsymbol{r}_2'\sigma_2') \\
& + \varphi_{2,\alpha}(\boldsymbol{r}_1\sigma_1)\varphi_{2,\bar{\gamma}}(\boldsymbol{r}_2\sigma_2)\bar{v}_{ph}(\boldsymbol{r}_1\sigma_1,\boldsymbol{r}_2\sigma_2;\boldsymbol{r}_1'\sigma_1',\boldsymbol{r}_2'\sigma_2')\varphi_{1,\beta}(\boldsymbol{r}_1'\bar{\sigma}_1')\varphi_{1,\bar{\delta}}(\boldsymbol{r}_2'\bar{\sigma}_2') \\
& - \varphi_{1,\alpha}(\boldsymbol{r}_1\bar{\sigma}_1)\varphi_{1,\bar{\delta}}(\boldsymbol{r}_2\bar{\sigma}_2)\bar{v}_{ph}(\boldsymbol{r}_1\sigma_1,\boldsymbol{r}_2\sigma_2;\boldsymbol{r}_1'\sigma_1',\boldsymbol{r}_2'\sigma_2')\varphi_{2,\beta}(\boldsymbol{r}_1'\sigma_1')\varphi_{2,\bar{\gamma}}(\boldsymbol{r}_2'\sigma_2') \\
& - \varphi_{2,\alpha}(\boldsymbol{r}_1\sigma_1)\varphi_{2,\bar{\delta}}(\boldsymbol{r}_2\sigma_2)\bar{v}_{ph}(\boldsymbol{r}_1\sigma_1,\boldsymbol{r}_2\sigma_2;\boldsymbol{r}_1'\sigma_1',\boldsymbol{r}_2'\sigma_2')\varphi_{1,\beta}(\boldsymbol{r}_1'\bar{\sigma}_1')\varphi_{1,\bar{\gamma}}(\boldsymbol{r}_2'\bar{\sigma}_2')\}. \quad (2.99)
\end{aligned}
$$

In the HF limit, these matrix elements reduce to those in the RPA equation.

$$
\begin{aligned}
A_{minj} = {} & (\epsilon_m - \epsilon_i)\delta_{mn}\delta_{ij} \\
& + \sum_{\sigma_1,\sigma_2,\sigma_1',\sigma_2'} \int d\boldsymbol{r}_1 d\boldsymbol{r}_2 d\boldsymbol{r}_1' d\boldsymbol{r}_2' \phi_m^*(\boldsymbol{r}_1\sigma_1)\phi_j^*(\boldsymbol{r}_2\sigma_2)\bar{v}_{ph}(\boldsymbol{r}_1\sigma_1,\boldsymbol{r}_2\sigma_2;\boldsymbol{r}_1'\sigma_1',\boldsymbol{r}_2'\sigma_2')\phi_i(\boldsymbol{r}_1'\sigma_1')\phi_n(\boldsymbol{r}_2'\sigma_2')
\end{aligned}
$$
$$(2.100)$$

$$
B_{minj} = \sum_{\sigma_1,\sigma_2,\sigma_1',\sigma_2'} \int d\boldsymbol{r}_1 d\boldsymbol{r}_2 d\boldsymbol{r}_1' d\boldsymbol{r}_2' \phi_m^*(\boldsymbol{r}_1\sigma_1)\phi_{\bar{n}}^*(\boldsymbol{r}_2\sigma_2)\bar{v}_{ph}(\boldsymbol{r}_1\sigma_1,\boldsymbol{r}_2\sigma_2;\boldsymbol{r}_1'\sigma_1',\boldsymbol{r}_2'\sigma_2')\phi_i(\boldsymbol{r}_1'\sigma_1')\phi_{\bar{j}}(\boldsymbol{r}_2'\sigma_2')
$$
$$(2.101)$$

Here, $\bar{v}_{ph}$ and $\bar{v}_{pp}$ are the antisymmetrized two-body effective interactions. In Chapters 3–6, we use the Skyrme-type interaction without momentum-dependent terms [98],

$$
v(\boldsymbol{r}_1,\boldsymbol{r}_2) = \left[t_0(1 + x_0 P_\sigma) + \frac{1}{6}t_3(1 + x_3 P_\sigma)\varrho(\boldsymbol{r}_1)\right]\delta(\boldsymbol{r}_1 - \boldsymbol{r}_2) \quad (2.102)
$$

for the particle-hole channel. The anitisymmetrized interaction reads

$$
\begin{aligned}
\bar{v}_{ph}(1,2) = {} & t_0\left[\frac{3}{4} - \frac{1}{4}(1 + 2x_0)\boldsymbol{\tau}_1\cdot\boldsymbol{\tau}_2 - \frac{1}{4}(1 - 2x_0)\boldsymbol{\sigma}_1\cdot\boldsymbol{\sigma}_2 - \frac{1}{4}\boldsymbol{\sigma}_1\cdot\boldsymbol{\sigma}_2\boldsymbol{\tau}_1\cdot\boldsymbol{\tau}_2\right]\delta(\boldsymbol{r}_1 - \boldsymbol{r}_2) \\
& + \frac{t_3}{6}\left[\frac{3}{4} - \frac{1}{4}(1 + 2x_3)\boldsymbol{\tau}_1\cdot\boldsymbol{\tau}_2 - \frac{1}{4}(1 - 2x_3)\boldsymbol{\sigma}_1\cdot\boldsymbol{\sigma}_2 - \frac{1}{4}\boldsymbol{\sigma}_1\cdot\boldsymbol{\sigma}_2\boldsymbol{\tau}_1\cdot\boldsymbol{\tau}_2\right]\varrho(\boldsymbol{r}_1)\delta(\boldsymbol{r}_1 - \boldsymbol{r}_2)
\end{aligned}
$$
$$(2.103)$$

$$
= \begin{cases}
\left[\dfrac{t_0}{2}(1-x_0) + \dfrac{t_3}{12}(1-x_3)\varrho(\boldsymbol{r}_1) \right] \\
\qquad\qquad\qquad \times (1 - \boldsymbol{\sigma}_1 \cdot \boldsymbol{\sigma}_2)\delta(\boldsymbol{r}_1 - \boldsymbol{r}_2) \quad \text{for the n-n and p-p channels,} \\
\left[\dfrac{t_0(x_0+2)}{2} + \dfrac{t_0 x_0}{2}\boldsymbol{\sigma}_1 \cdot \boldsymbol{\sigma}_2 \right. \\
\left. \quad + \left(\dfrac{t_3(x_3+2)}{12} + \dfrac{t_3 x_3}{12}\boldsymbol{\sigma}_1 \cdot \boldsymbol{\sigma}_2 \right) \varrho(\boldsymbol{r}_1) \right] \delta(\boldsymbol{r}_1 - \boldsymbol{r}_2) \quad \text{for the n-p channel,}
\end{cases}
$$

$$(2.104)$$

where we neglect the rearrangement term [99] coming from the density dependence of the effective interactoin. When we take into account the rearrangement effect, the antisymmetrized interaction v_{ph} reads

$$
\bar{v}_{ph}(1,2) = t_0 \left[\frac{3}{4} - \frac{1}{4}(1+2x_0)\boldsymbol{\tau}_1 \cdot \boldsymbol{\tau}_2 - \frac{1}{4}(1-2x_0)\boldsymbol{\sigma}_1 \cdot \boldsymbol{\sigma}_2 - \frac{1}{4}\boldsymbol{\sigma}_1 \cdot \boldsymbol{\sigma}_2 \boldsymbol{\tau}_1 \cdot \boldsymbol{\tau}_2 \right] \delta(\boldsymbol{r}_1 - \boldsymbol{r}_2)
$$
$$
+ \left[\frac{3}{48}t_3(\alpha+2)(\alpha+1) - \frac{t_3}{24}(1+2x_3)\boldsymbol{\tau}_1 \cdot \boldsymbol{\tau}_2 - \frac{t_3}{24}(1-2x_3)\boldsymbol{\sigma}_1 \cdot \boldsymbol{\sigma}_2 - \frac{t_3}{24}\boldsymbol{\sigma}_1 \cdot \boldsymbol{\sigma}_2 \boldsymbol{\tau}_1 \cdot \boldsymbol{\tau}_2 \right]
$$
$$
\times \varrho^\alpha(\boldsymbol{r}_1)\delta(\boldsymbol{r}_1 - \boldsymbol{r}_2)
$$
$$
- \alpha \left[\frac{t_3}{24}(1+2x_3)(\varrho_\nu(\boldsymbol{r}_1) - \varrho_\pi(\boldsymbol{r}_1))(\tau_{1,z} + \tau_{2,z}) \right] \varrho^{\alpha-1}(\boldsymbol{r}_1)\delta(\boldsymbol{r}_1 - \boldsymbol{r}_2)
$$
$$
- \alpha(\alpha-1) \left[\frac{t_3}{48}(1+2x_3)(\varrho_\nu(\boldsymbol{r}_1) - \varrho_\pi(\boldsymbol{r}_1))^2 \right] \varrho^{\alpha-2}(\boldsymbol{r}_1)\delta(\boldsymbol{r}_1 - \boldsymbol{r}_2), \qquad (2.105)
$$

where α is the exponent of the density denpendence. We adopt the density-dependent power $\alpha = 1$ in the calculations of this thesis.

Chapter 3

Octupole excitations on superdeformed states in neutron drip-line nuclei – effects of continuum coupling and nuclear deformation

3.1 Introduction

In order to clearly see the effect of nuclear deformation on properties of low-frequency modes of excitation in neutron-rich nuclei, we study octupole excitations on superdeformed (SD) states in neutron drip-line nuclei. Because we would like to understand the effects of continuum coupling and nuclear deformation, we do not take into account the pairing correlation in this chapter.

Recently, Inakura *et al.*[64] investigated properties of negative-parity collective excitations built on SD states in neutron-rich sulfur isotopes by means of the mixed representation RPA [65, 66, 67] based on the SHF mean field, and found many low-energy modes possessing strongly enhanced isoscalar octupole transition strengths. They also studied excitation modes built on the SD states in the ^{40}Ca region with $N = Z$, for which the SD yrast states have been discovered in recent experiments [101, 102]. In the mixed representation RPA, the *particle* states are treated using the coordinate-mesh representation, while the HF basis is used for the *hole* states. This approach is fully self-consistent in that the same effective interaction is used in both the mean-field and RPA calculations. Also, it is unnecessary to introduce an upper cutoff with respect to the energies of the *particle* states. On the other hand, it is not easy in this method to identify microscopic particle-hole configurations generating individual RPA modes. Therefore, in this chapter, using the deformed Woods-Saxon potential and the conventional matrix formulation of the RPA, we have made a detailed analysis of the microscopic structure of octupole excitation modes built on the SD states in the ^{40}Ca region with $N = Z$ and the ^{50}S region close to the neutron drip line. In this approach, we can easily obtain a simple and transparent understanding of the particle-hole configurations generating the RPA eigenmodes.

This chapter is organized as follows. In the next section, the frameworks of the mean-

field and RPA calculations are described. In §3.3.1, the results of the RPA calculation for
the SD states in ^{32}S, ^{36}S and ^{40}Ca are presented and discussed. In §3.3.2, we present the
result for ^{50}S close to the neutron drip line and suggest that some low-lying states associated
with excitations of a single neutron from a loosely bound state to a resonance state acquire
extremely strong transition strengths. In §3.3.3, we discuss excitation modes in the oblately
deformed ^{40}Mg and suggest that the results obtained for ^{50}S are not restricted to the SD
states but are rather general phenomena. Conclusions are given in §3.4.

This work was reported in Refs. [78, 79].

3.2 Method of calculation

3.2.1 Mean-field calculation

We consider the single-particle motion in an axially symmetric deformed potential. Using
the standard notation, the Schrödinger equation is written

$$\left\{ -\frac{\hbar^2}{2m}\nabla^2 + V_{WS}f(\boldsymbol{r}) + V_{SO}\nabla f(\boldsymbol{r}) \cdot (\boldsymbol{\sigma} \times \boldsymbol{p}) + V_C(\boldsymbol{r})\frac{(1-\tau_3)}{2} \right\} \Phi_i = e_i\Phi_i. \tag{3.1}$$

The solutions to this equation take the following form:

$$\Phi_i(x) = \Phi_i(\boldsymbol{r},\sigma,\tau) = \chi_{q_i}(\tau)\left[\phi_i^+(\rho,z)e^{i\Lambda_i^-\varphi}\chi_{\frac{1}{2}}(\sigma) + \phi_i^-(\rho,z)e^{i\Lambda_i^+\varphi}\chi_{-\frac{1}{2}}(\sigma) \right]. \tag{3.2}$$

Here, $\Lambda_i^\pm = \Omega_i \pm 1/2$, where Λ_i and Ω_i are the z-components of the total and orbital angular
momenta, respectively, and (ρ,z,φ) are the cylindrical coordinates of $\boldsymbol{r} = (x,y,z)$:

$$x = \rho\cos\varphi, \quad y = \rho\sin\varphi, \quad z = z. \tag{3.3}$$

The subscript $q_i = +1/2$ $(-1/2)$ denotes neutrons (protons). In terms of the wave functions
given in (3.2), the nucleon density is given by

$$\varrho(\rho,z) = \sum_i [|\phi_i^+(\rho,z)|^2 + |\phi_i^-(\rho,z)|^2], \tag{3.4}$$

and the mean-square radii of protons and neutrons are calculated as

$$\langle r^2 \rangle_\tau = \frac{\int \rho\mathrm{d}\rho\mathrm{d}z r^2 \varrho_\tau(\rho,z)}{\int \rho\mathrm{d}\rho\mathrm{d}z \varrho_\tau(\rho,z)}, \tag{3.5}$$

where $r = \sqrt{\rho^2 + z^2}$ and $\tau = \pi$ or ν, with $\varrho_\pi(\rho,z)$ and $\varrho_\nu(\rho,z)$ being the proton and neutron
densities.

We employ the phenomenological Woods-Saxon potential

$$f(\boldsymbol{r}) = (1 + \exp[(r - R(\theta))/a])^{-1}, \tag{3.6}$$

$$R(\theta) = c(1 + \beta_2 Y_{20}(\theta)), \tag{3.7}$$

where c is determined by the volume conservation condition. Though an angle dependent
diffuseness parameter $a(\theta)$ is better for a more accurate calculation [103], we use a constant

$a = 0.67$ fm for simplicity. We also use the standard parameter values [23] for the central and spin-orbit potentials,

$$V_{WS} = -51 + 33\frac{N-Z}{A}\tau_3, \tag{3.8}$$

$$V_{SO} = \frac{1}{2}r_0^2\left(-22 + 14\frac{N-Z}{A}\tau_3\right), \tag{3.9}$$

with $r_0 = 1.27$ fm. The spin-orbit term is written

$$\hat{V}_{ls} = -\frac{1}{2}V_{SO}\left[\sigma_+ e^{-i\varphi}\left\{\frac{\partial f}{\partial\rho}\frac{\partial}{\partial z} - \frac{\partial f}{\partial z}\left(\frac{\partial}{\partial\rho} + \frac{\hat{l}_z}{\rho}\right)\right\}\right.$$
$$\left. + \sigma_- e^{i\varphi}\left\{-\frac{\partial f}{\partial\rho}\frac{\partial}{\partial z} + \frac{\partial f}{\partial z}\left(\frac{\partial}{\partial\rho} - \frac{\hat{l}_z}{\rho}\right)\right\} + \sigma_z 2\frac{\partial f}{\partial\rho}\frac{\hat{l}_z}{\rho}\right], \tag{3.10}$$

where $\sigma_{\pm} = \sigma_x \pm i\sigma_y$ and $\hat{l}_z = -i\partial/\partial\varphi$. For protons, we solve the Poisson equation, $\nabla^2 V_C(\boldsymbol{r}) = 4\pi e\varrho_\pi(\boldsymbol{r})$, to obtain the Coulomb potential V_C. In the present calculation, we approximate the proton density $\varrho_\pi(\boldsymbol{r})$ by a Woods-Saxon form.

We can rewrite the Schrödinger equation (3.1) in the matrix form

$$h\boldsymbol{\phi} = \begin{pmatrix} h_{\uparrow\uparrow} & h_{\uparrow\downarrow} \\ h_{\downarrow\uparrow} & h_{\downarrow\downarrow} \end{pmatrix}\begin{pmatrix} \phi_i^+(\rho,z) \\ \phi_i^-(\rho,z) \end{pmatrix} = e_i\begin{pmatrix} \phi_i^+(\rho,z) \\ \phi_i^-(\rho,z) \end{pmatrix}, \tag{3.11}$$

where

$$h_{\uparrow\uparrow} = -\frac{\hbar^2}{2m}\left[\frac{\partial^2}{\partial\rho^2} + \frac{1}{\rho}\frac{\partial}{\partial\rho} + \frac{\partial^2}{\partial z^2} - \left(\frac{\Lambda^-}{\rho}\right)^2\right] + V_{WS}f(\rho,z) - V_{SO}\frac{\partial f(\rho,z)}{\partial\rho}\frac{\Lambda^-}{\rho}, \tag{3.12a}$$

$$h_{\downarrow\downarrow} = -\frac{\hbar^2}{2m}\left[\frac{\partial^2}{\partial\rho^2} + \frac{1}{\rho}\frac{\partial}{\partial\rho} + \frac{\partial^2}{\partial z^2} - \left(\frac{\Lambda^+}{\rho}\right)^2\right] + V_{WS}f(\rho,z) + V_{SO}\frac{\partial f(\rho,z)}{\partial\rho}\frac{\Lambda^+}{\rho}, \tag{3.12b}$$

$$h_{\uparrow\downarrow} = -\frac{1}{2}V_{SO}\left[\frac{\partial f(\rho,z)}{\partial\rho}\frac{\partial}{\partial z} - \frac{\partial f(\rho,z)}{\partial z}\left(\frac{\partial}{\partial\rho} + \frac{\Lambda^+}{\rho}\right)\right], \tag{3.12c}$$

$$h_{\downarrow\uparrow} = -\frac{1}{2}V_{SO}\left[-\frac{\partial f(\rho,z)}{\partial\rho}\frac{\partial}{\partial z} + \frac{\partial f(\rho,z)}{\partial z}\left(\frac{\partial}{\partial\rho} - \frac{\Lambda^-}{\rho}\right)\right]. \tag{3.12d}$$

Because this equation possesses time-reversal symmetry, we know that if $\Phi_i = \{\phi_i^+, \phi_i^-, \Omega_i\}$ is a solution, then $\Phi_{\bar{i}} = \{-\phi_i^-, \phi_i^+, -\Omega_i\}$ is also a solution with the same eigenvalue e_i, and thus it is sufficient to solve it for positive Ω only. We also assume reflection symmetry with respect to the x-y plane. Then, the wave function $\phi^{\pm}$ possesses z-parity $\pi(-1)^{\Lambda^{\mp}}$ as a good quantum number (π being the parity), and therefore it is sufficient to consider only positive z.

We solve Eq. (3.11) directly in coordinate space. In comparison to the conventional method of using a deformed harmonic oscillator basis [104], this method is believed to be more effective in the treatment of spatially extended wave functions, like loosely bound states, resonant states and continuum states. The Hamiltonian matrix (3.11) is discretized by use of a coordinate mesh in the (ρ, z) plane. The mesh points are chosen as

$$\rho_i = \left(i - \frac{1}{2}\right)\Delta, \qquad i = 1, 2, \cdots N, \tag{3.13}$$

to avoid division by zero, where Δ represents the lattice mesh size. The mesh points in the z direction are taken as

$$z_j = (j-1)\Delta, \qquad j = 1, 2, \cdots M. \tag{3.14}$$

The boundary conditions are set as

$$\phi_{i,M} = \phi_{N,j} = 0, \tag{3.15}$$

where $\phi_{i,j} = \phi(\rho, z)$. We construct the discretized Hamiltonian matrix by use of the finite difference method for derivatives and then diagonalize the matrix to obtain the single-particle wave functions on the two-dimensional lattice. The kinetic energy term is evaluated using the 9-points formula; its explicit expression is given in Appendix A.

3.2.2 RPA calculation

Using the single-particle basis obtained in the previous subsection, we solve the RPA equation in the standard matrix formulation [43],

$$\sum_{p'h'} \begin{pmatrix} A_{php'h'} & B_{php'h'} \\ B^*_{php'h'} & A^*_{php'h'} \end{pmatrix} \begin{pmatrix} f^\lambda_{p'h'} \\ g^\lambda_{p'h'} \end{pmatrix} = \hbar\omega_\lambda \begin{pmatrix} 1 & 0 \\ 0 & -1 \end{pmatrix} \begin{pmatrix} f^\lambda_{ph} \\ g^\lambda_{ph} \end{pmatrix}, \tag{3.16}$$

where

$$A_{php'h'} = (e_p - e_h)\delta_{pp'}\delta_{hh'} + \bar{v}_{ph'hp'}, \qquad B_{php'h'} = \bar{v}_{pp'hh'}. \tag{3.17}$$

Here, the subscripts p and h denote the single-particle states above and below the Fermi energy (particles and holes), respectively. The antisymmetrized matrix elements of the residual interaction v are denoted $\bar{v}_{ph'hp'}$ and $\bar{v}_{pp'hh'}$. For v, we employ the Skyrme-type interaction [98] without momentum-dependent terms,

$$v(\boldsymbol{r}, \boldsymbol{r}') = \left[t_0(1 + x_0 P_\sigma) + \frac{1}{6}t_3(1 + x_3 P_\sigma)\varrho(\boldsymbol{r}) \right]\delta(\boldsymbol{r} - \boldsymbol{r}'), \tag{3.18}$$

with $t_0 = -1100$ MeV·fm^3, $t_3 = 16000$ MeV·fm^6, $x_0 = 0.5$, and $x_3 = 1.0$, P_σ being the spin exchange operator. Because our calculation is not self-consistent in the sense that the residual interaction is not related to the mean-field potential, we renormalize the residual interaction by multiplying it by a factor f to obtain the spurious modes at zero excitation energy: $v \to f \cdot v$.

The intrinsic matrix elements $\langle 0|Q_{3K}|\lambda\rangle$ of the octupole operator Q_{3K} between the excited state $|\lambda\rangle$ and the ground state $|0\rangle$ are given by

$$\langle 0|Q_{3K}|\lambda\rangle = \sum_{ph} \left(Q^{hp}_{3K} f^\lambda_{ph} + Q^{ph}_{3K} g^\lambda_{ph} \right) = \sum_{ph} M^{ph}_{3K}, \tag{3.19}$$

and

$$Q^{ph}_{3K} = 2\pi\delta_{K,\Omega_p - \Omega_h} \int \rho d\rho dz \left(\phi^+_p(\rho, z)\phi^+_h(\rho, z) + \phi^-_p(\rho, z)\phi^-_h(\rho, z) \right) Q_{3K}(\rho, z) \tag{3.20}$$

$$\equiv 2\pi\delta_{K,\Omega_p - \Omega_h} \int d\rho dz Q^{ph}_{3K}(\rho, z), \tag{3.21}$$

where $Q_{3K}(\rho, z) = Q_{3K}(\boldsymbol{r})e^{-iK\varphi} = r^3 Y_{3K}(\theta, \varphi)e^{-iK\varphi}$.

The isoscalar octupole strength function is

$$S^{\mathrm{IS}}(\omega) = \sum_\lambda |\langle 0|Q_{3K}^{\mathrm{IS}}|\lambda\rangle|^2 \delta(\hbar\omega - \hbar\omega_\lambda), \tag{3.22}$$

where $Q_{3K}^{\mathrm{IS}} = Q_{3K}^{\pi} + Q_{3K}^{\nu}$, and Q_{3K}^{π} and Q_{3K}^{ν} are the proton and neutron octupole operators. The reduced isoscalar octupole transition probability is defined by $B(Q^{\mathrm{IS}}3) = |\langle 0|Q_{3K}^{\mathrm{IS}}|\lambda\rangle|^2$. The reduced proton and neutron octupole transition probabilities, $B(E3)$ and $B(Q^{\nu}3)$, are obtained by replacing Q_{3K}^{IS} with eQ_{3K}^{π} and Q_{3K}^{ν}, respectively. Note that these quantities represent intrinsic transition strengths, and hence the appropriate Clebsh-Gordan coefficients should be multiplied to obtain transition probabilities in the laboratory frame [126].

3.2.3 Details of numerical calculation

We numerically solved the Schrödinger equation (3.11) in a rectangular box, using a lattice mesh size $\Delta = 0.5$ fm. The size of the box used was 2.5 (3.5) times the half density radii in the directions of the major and minor axes for ^{32,36}S and ^{40}Ca (^{50}S). The Bode's rule was used for the numerical integrations of the RPA matrix elements (see Appendix A). The deformation parameters β_2 were determined so as to approximately reproduce the shell structure near the Fermi level obtained in the SHF calculation by Inakura *et al.* [100]. Their values for protons and neutrons are not necessarily the same. The actual values of the box size used in the calculations are indicated in the figure captions for individual cases, together with the β_2 values adopted. The RPA matrix (3.17) was diagonalized with the cutoff at 30 MeV for the particle-hole excitation energy. In spherical systems, there is only one spurious $J^\pi = 1^-$ mode associated with the center-of-mass motion. In deformed systems, this mode splits into the $K^\pi = 0^-$ and 1^- modes. We find that, e.g., for ^{32}S, the factors $f_0 = 0.7545$ and $f_1 = 0.7723$ are needed to obtain the spurious $K^\pi = 0^-$ and $K^\pi = 1^-$ modes at zero energy. Using these f_0 and f_1 values, we obtain low-lying $K^\pi = 2^-$ states at 2.653 and 2.557 MeV, respectively. This difference of about 0.1 MeV indicates the magnitude of the numerical uncertainty caused by ignoring self-consistency in our calculation. In the following, we choose the factor f such that the excitation energy of the spurious $K^\pi = 1^-$ mode becomes zero.

3.3 Results and Discussion

3.3.1 The SD states in ^{32}S, ^{36}S and ^{40}Ca

We first discuss the result of the RPA calculation for the SD state in ^{32}S. Although the existence of the SD band in ^{32}S has been conjectured for a long time [105], it has not yet been observed, and this remains a great challenge: As discussed in Refs. [106, 107, 108, 109, 110], the SD local minimum in ^{32}S corresponds to the doubly closed shell configuration with respect to the SD magic number $Z = N = 16$. It involves two protons and two neutrons in the down-sloping single-particle levels originating from the $f_{7/2}$ shell (see Fig. 3.1). The calculated octupole transition strengths with $K^\pi = 2^-$ are displayed in Fig. 3.2. A prominent peak is seen at about 2.6 MeV with a strongly enhanced transition strength of about 23 Weisskopf units (1 W.u. $\simeq 61$ fm^6 for ^{32}S). There are no peaks representing strengths greater than 1 W.u. for other values of K in this energy region. As shown in Table 3.1, the major component of this RPA mode is the particle-hole excitation from the [211]1/2 state to
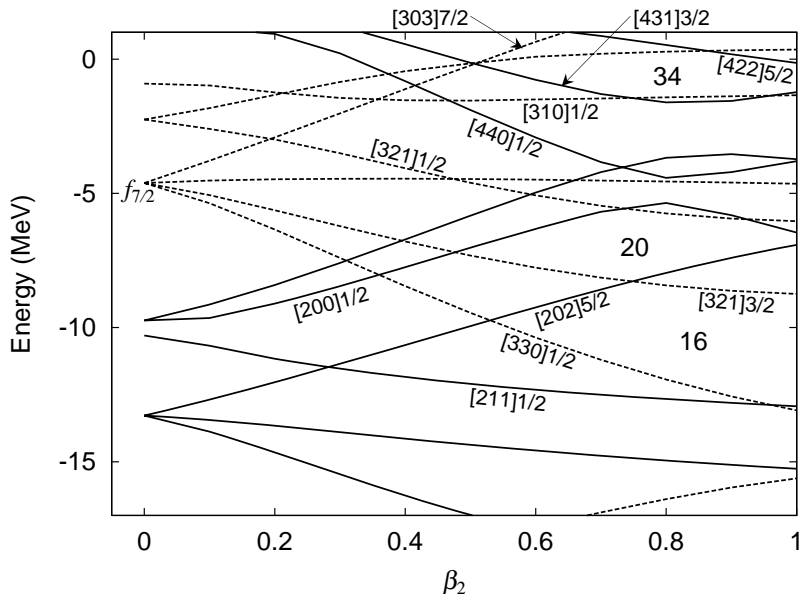
Figure 3.1: Neutron single-particle levels in the deformed Woods-Saxon potential, plotted as functions of the quadrupole deformation parameter β_2. The solid and dotted curves denote positive- and negative-parity levels, respectively. The SD magic numbers are $N = 16$, 20 and 34. They are responsible for the appearance of the SD states in ^{32}S, ^{36}S, ^{40}Ca and ^{50}S.

the [321]3/2 state. The proton and neutron excitations act coherently. Other particle-hole configurations also contribute coherently. Here we note that, although the RPA amplitude f_{ph} for the particle-hole excitation from the [330]1/2 state to the [202]5/2 state is appreciable, its contribution to the transition matrix element M_{32}^{ph} is very small. This can be understood from the asymptotic selection rules [111] for low-energy octupole transitions in the SD harmonic-oscillator potential with the axis ratio 2:1 :

$$Q_{30}: \quad \Delta N_{\rm sh} = 1, \ \Delta n_3 = 1, \ \Delta\Lambda = 0, \tag{3.23a}$$

$$Q_{31}: \quad \Delta N_{\rm sh} = 0, \ \Delta n_3 = 2, \ \Delta\Lambda = 1, \tag{3.23b}$$

$$Q_{32}: \quad \Delta N_{\rm sh} = 1, \ \Delta n_3 = 1, \ \Delta\Lambda = 2, \tag{3.23c}$$

$$Q_{33}: \quad \Delta N_{\rm sh} = 2, \ \Delta n_3 = 0, \ \Delta\Lambda = 3. \tag{3.23d}$$

Here, the shell quantum number is defined as $N_{\rm sh} = 2n_\perp + n_3$. These selection rules hold approximately also for the SD Wood-Saxon potential under consideration. Accordingly, the [330]1/2 $\rightarrow$ [202]5/2 octupole matrix element is very small, while that of the [211]1/2 $\rightarrow$ [321]3/2 excitation is large. Thus, the coherent proton and neutron excitations from the [211]1/2 hole state to the [321]3/2 particle state are the major origin of the large octupole transition strength for this RPA mode.

Next, let us discuss the result of the RPA calculation for the SD state in ^{40}Ca. As mentioned in §3.1, for this nucleus, the SD yrast band has been discovered in recent experiments [101, 102]. The SD shell gap at $Z = N = 20$ is associated with the $4p$-$4h$ excitation (for both protons and neutrons) from below the spherical closed shell to the $f_{7/2}$ shell. Figure 3.3 presents the calculated octupole transition strengths with $K^\pi = 1^-$. It is seen that there
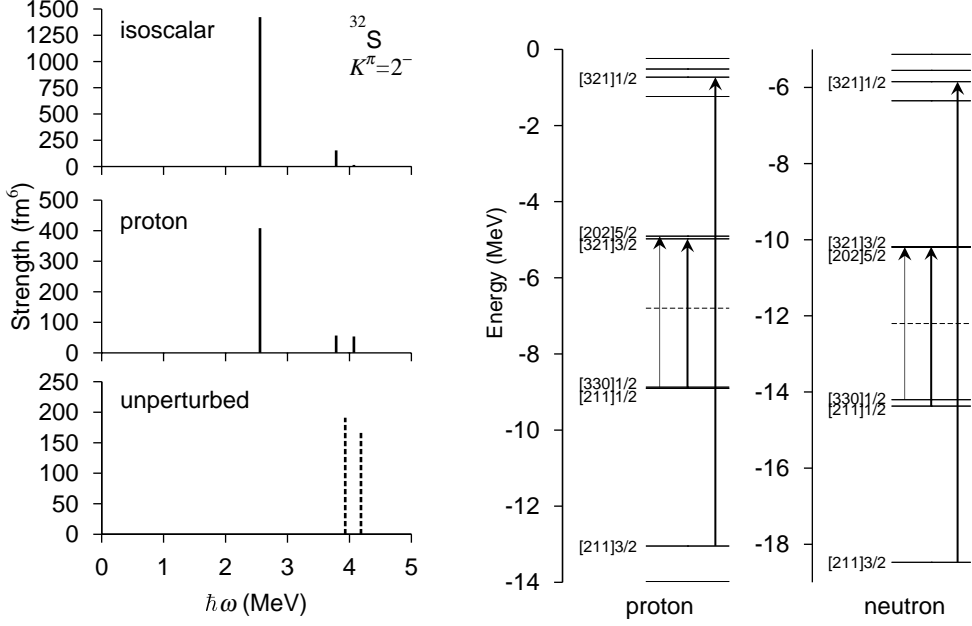
Figure 3.2: *Left*: The isoscalar and proton octupole strengths, $B(Q^{IS}3)$ and $B(E3)/e^2$, for the $K^\pi = 2^-$ excitations on the SD state in ^{32}S are plotted in the top and middle panels as functions of the excitation energy. These were obtained using an RPA calculation with $\beta_2 = 0.78$ for both protons and neutrons, using a box of size $\rho_{max} \times z_{max} = 8.25$ fm $\times 14.0$ fm. The unperturbed particle-hole strengths are also plotted with dashed lines in the bottom panel. *Right*: Particle-hole configurations generating the lowest $K^\pi = 2^-$ state at 2.6 MeV. Excitations satisfying the asymptotic selection rule Eq. (3.23) are indicated by thick arrows. The asymptotic quantum numbers $[Nn_3\Lambda]\Omega$ are displayed for pertinent levels. The Fermi surfaces for protons and neutrons are indicated by the dashed lines.

Table 3.1: RPA amplitudes for the 2^- state at 2.6 MeV in ^{32}S, calculated with $\beta_2 = 0.78$ for both protons and neutrons. It is characterized by $B(E3) = 408$ e^2fm^6, $B(Q^\nu 3) = 306$ fm^6, $B(Q^{IS}3) = 1422$ fm^6, and $\sum |g_{ph}|^2 = 1.86 \times 10^{-1}$. The single-particle levels are labeled with the asymptotic quantum numbers $[Nn_3\Lambda]\Omega$. Only components with $|f_{ph}| > 0.1$ are listed.

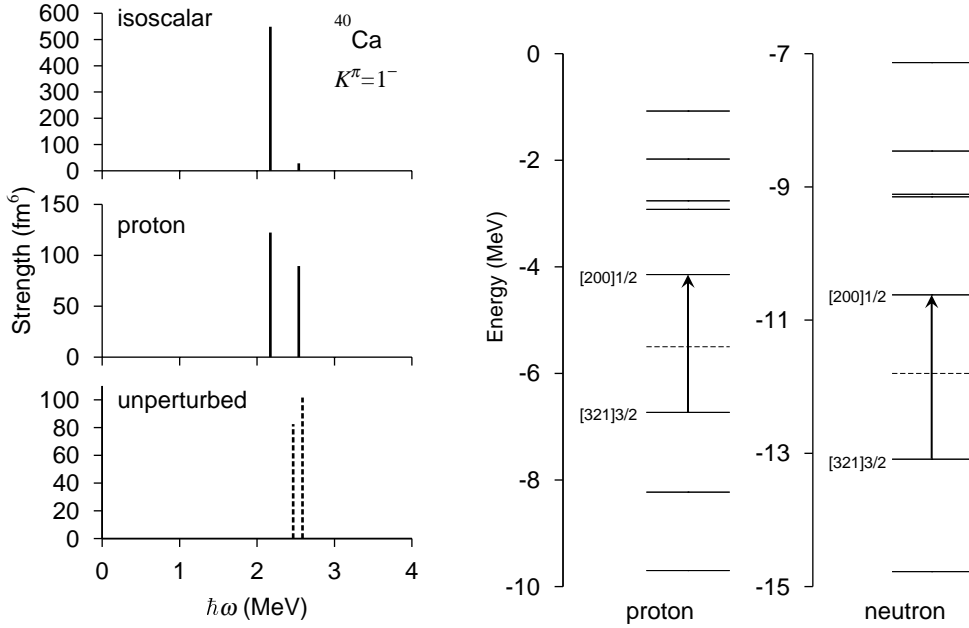| particle	hole	$\epsilon_p - \epsilon_h$ (MeV)	f_{ph}	Q_{32}^{ph} (fm^3)	M_{32}^{ph} (fm^3)
$\nu[202]5/2$	$\nu[330]1/2$	4.01	-0.293	-0.101	0.040
$\nu[321]3/2$	$\nu[211]1/2$	4.19	-0.631	-13.0	11.5
$\nu[321]1/2$	$\nu[211]3/2$	12.6	-0.141	-11.2	2.27
$\pi[202]5/2$	$\pi[330]1/2$	3.97	-0.282	-0.248	0.096
$\pi[321]3/2$	$\pi[211]1/2$	3.93	-0.733	-13.8	13.7
$\pi[321]1/2$	$\pi[211]3/2$	12.3	-0.138	-11.8	2.35

Figure 3.3: *Left*: The isoscalar and proton octupole strengths, $B(Q^{IS}3)$ and $B(E3)/e^2$, for the $K^\pi = 1^-$ excitations on the SD state in ^{40}Ca are plotted in the top and middle panels as functions of the excitation energy. These were obtained using an RPA calculation with $\beta_2 = 0.6$ for both protons and neutrons, using a box of size $\rho_{max} \times z_{max} = 8.25$ fm $\times 14.0$ fm. The unperturbed particle-hole strengths are also plotted with dashed lines in the bottom panel. *Right*: Particle-hole configurations generating the lowest $K^\pi = 1^-$ state at 2.2 MeV. The notation here is the same as in Fig. 3.2.

are no peaks representing strengths greater than 1.5 W.u. for other values of K in this energy region. There is a prominent peak at 2.2 MeV with an isoscalar strength of about 6 W.u. (1 W.u. $\simeq 95$ fm^6 for ^{40}Ca). As shown in Table 3.2, this RPA eigenstate consists of components from the coherent proton and neutron excitations from [321]3/2 to [200]1/2, which satisfy the asymptotic selection rule (3.23b).

The SD states in ^{32}S and ^{40}Ca are associated with the SD magic numbers $N = Z = 16$ and 20, respectively. It is thus interesting to consider the SD state in ^{36}S, which has $Z = 16$ and $N = 20$. Evidence for the existence of the SD band in this nucleus has been obtained from an SHF calculation [100]. The result of the RPA calculation is presented in Fig. 3.4, Table 3.3 and Table 3.4. There is a peak corresponding to $K^\pi = 1^-$ at 2.6 MeV with an isoscalar strength of about 3.4 W.u. and another peak corresponding to $K^\pi = 2^-$ at 3.9 MeV with an isoscalar strength of about 11 W.u. (1 W.u. $\simeq 77$ fm^6 for ^{36}S). The $K^\pi = 1^-$ peak is associated with the particle-hole excitation from [321]3/2 to [200]1/2, while the $K^\pi = 2^-$ peak corresponds to the [211]1/2 $\rightarrow$ [321]3/2 excitation. These particle-hole configurations are the same as for the $K^\pi = 1^-$ state in ^{40}Ca and the $K^\pi = 2^-$ in ^{32}S discussed above. However, in contrast to the $N = Z$ nuclei, ^{32}S and ^{40}Ca, the coherence of proton and neutron excitations is absent in the case of ^{36}S. Thus, these RPA modes in ^{36}S are dominated by specific particle-hole configurations, although appreciable amounts of other

Table 3.2: RPA amplitudes for the 1^- state at 2.2 MeV in ^{40}Ca, calculated with $\beta_2 = 0.6$ for both protons and neutrons. It is characterized by $B(E3) = 122 \ e^2\text{fm}^6$, $B(Q^\nu 3) = 153 \ \text{fm}^6$, $B(Q^{\text{IS}}3) = 549 \ \text{fm}^6$, and $\sum |g_{ph}|^2 = 4.69 \times 10^{-2}$. Only components with $|f_{ph}| > 0.1$ are listed.

particle	hole	$\epsilon_p - \epsilon_h$ (MeV)	f_{ph}	Q_{31}^{ph} (fm^3)	M_{31}^{ph} (fm^3)
$\nu[200]1/2$	$\nu[321]3/2$	2.46	0.836	9.08	8.87
$\pi[200]1/2$	$\pi[321]3/2$	2.59	0.568	10.1	7.06

Table 3.3: RPA amplitudes for the 1^- state 2.6 MeV in ^{36}S, calculated with $\beta_2 = 0.565$ and 0.685 for protons and neutrons, respectively. It is characterized by $B(E3) = 5.95 \ e^2\text{fm}^6$, $B(Q^\nu 3) = 189 \ \text{fm}^6$, $B(Q^{\text{IS}}3) = 262 \ \text{fm}^6$, and $\sum |g_{ph}|^2 = 9.18 \times 10^{-3}$. Only components with $|f_{ph}| > 0.03$ are listed.

particle	hole	$\epsilon_p - \epsilon_h$ (MeV)	f_{ph}	Q_{31}^{ph} (fm^3)	M_{31}^{ph} (fm^3)
$\nu[200]1/2$	$\nu[321]3/2$	2.71	-0.999	9.71	-10.5
$\nu[200]1/2$	$\nu[330]1/2$	6.11	-0.038	4.46	-0.22
$\pi[200]1/2$	$\pi[330]1/2$	5.23	-0.062	3.62	-0.28

Table 3.4: RPA amplitudes for the 2^- state 3.9 MeV in ^{36}S, calculated with $\beta_2 = 0.565$ and 0.685 for protons and neutrons, respectively. It is characterized by $B(E3) = 352 \ e^2\text{fm}^6$, $B(Q^\nu 3) = 97.0 \ \text{fm}^6$, $B(Q^{\text{IS}}3) = 819 \ \text{fm}^6$, and $\sum |g_{ph}|^2 = 3.52 \times 10^{-2}$. Only components with $|f_{ph}| > 0.1$ are listed.

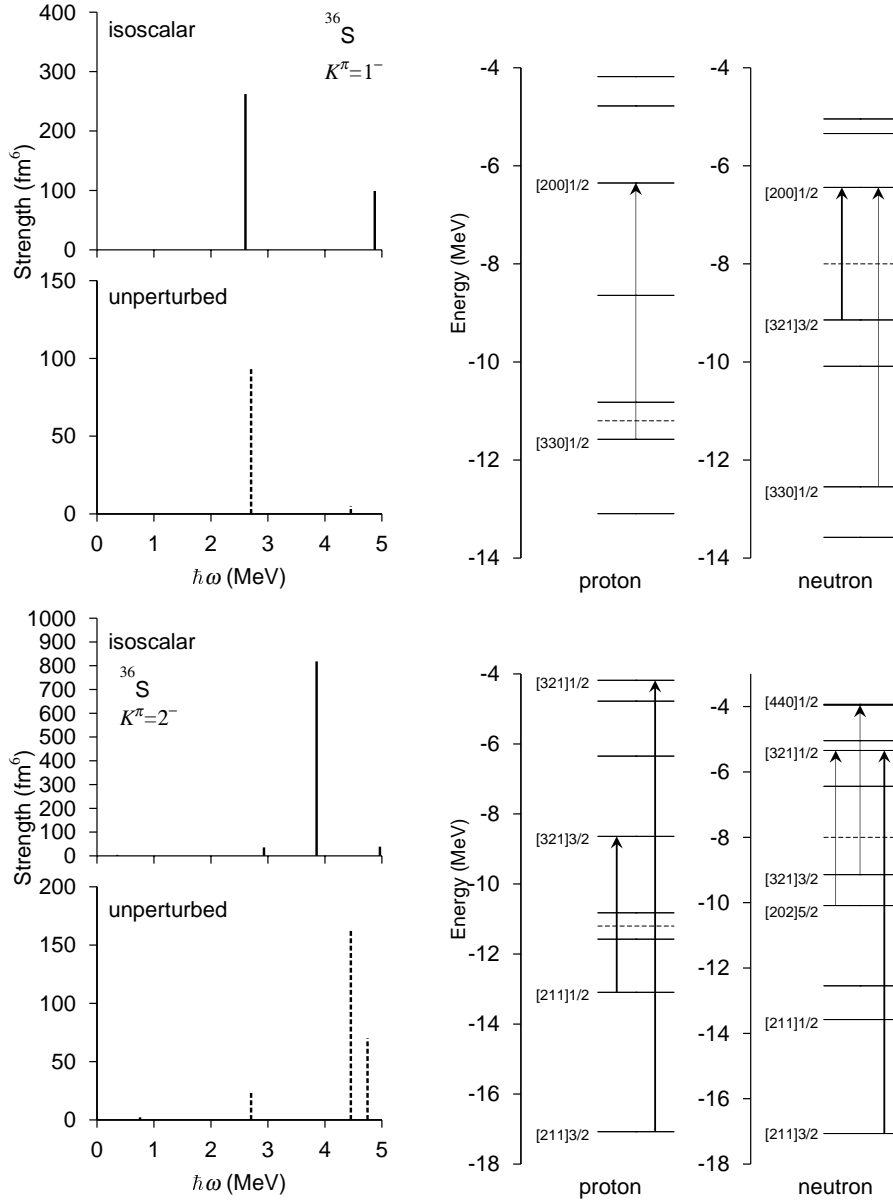| particle	hole	$\epsilon_p - \epsilon_h$ (MeV)	f_{ph}	Q_{32}^{ph} (fm^3)	M_{32}^{ph} (fm^3)
$\nu[321]1/2$	$\nu[202]5/2$	4.75	-0.141	-8.37	1.34
$\nu[440]1/2$	$\nu[321]3/2$	5.19	0.137	6.34	1.01
$\nu[321]1/2$	$\nu[211]3/2$	11.7	-0.114	-12.5	1.85
$\pi[321]3/2$	$\pi[211]1/2$	4.45	-0.970	-12.5	14.2
$\pi[321]1/2$	$\pi[211]3/2$	12.9	-0.101	-10.8	1.43

Figure 3.4: *Upper left*: The isoscalar octupole strength $B(Q^{IS}3)$ distribution for the $K^\pi = 1^-$ excitations on the SD state in ^{36}S is plotted in the top panel as a function of the excitation energy. This was obtained using an RPA calculation with $\beta_2 = 0.565$ and 0.685 for protons and neutrons, respectively, using a box of size $\rho_{max} \times z_{max} = 8.25$ fm $\times 14.0$ fm. The unperturbed particle-hole strength distribution is also plotted with dashed lines in the bottom panel. *Upper right*: Particle-hole configurations generating the lowest $K^\pi = 1^-$ state at 2.5 MeV. The notation is the same as in Fig. 3.2. *Lower left*: Same as above, but for the $K^\pi = 2^-$ excitations. *Lower right*: Same as above, but for the $K^\pi = 2^-$ excitation at 3.9 MeV.
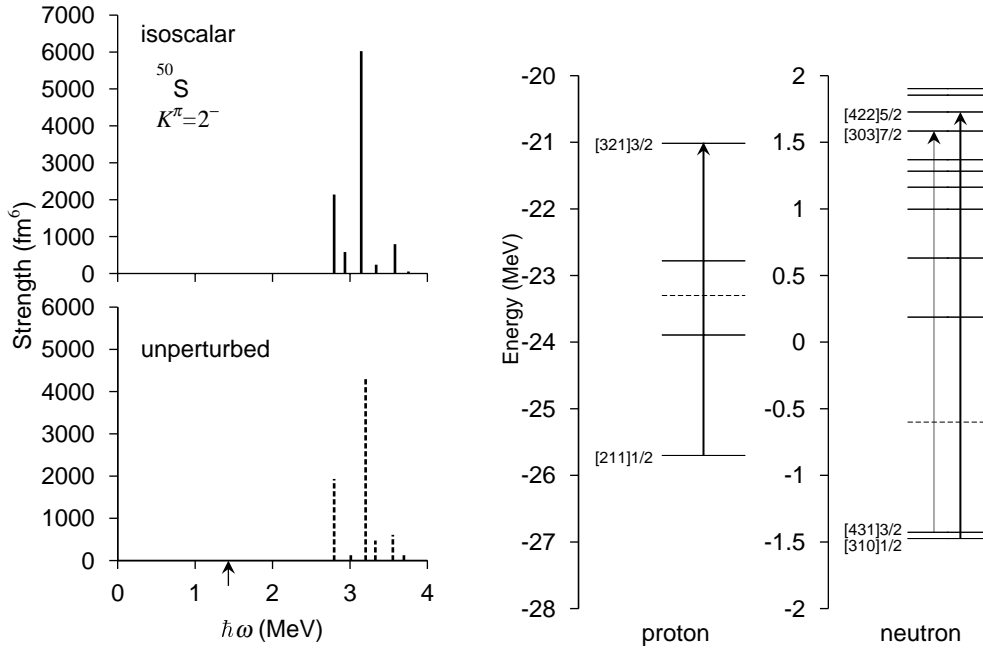
Figure 3.5: *Left*: The isoscalar octupole strength $B(Q^{\mathrm{IS}}3)$ distribution for the $K^\pi = 2^-$ excitations built on the SD state in ^{50}S is plotted in the top panel as a function of the excitation energy. This was obtained using an RPA calculation with $\beta_2 = 0.54$ and 0.73 for protons and neutrons, respectively, using a box of size $\rho_{\max} \times z_{\max} = 14.25$ fm $\times 22.0$ fm. The unperturbed particle-hole strengths are also plotted with dashed lines in the bottom panel. The arrow indicates the threshold energy, $E_{\mathrm{th}} = 1.4$ MeV. *Right*: Particle-hole configurations generating the lowest $K^\pi = 2^-$ state at 3.1 MeV. The notation here is the same as in Fig. 3.2.

particle-hole configurations collectively contribute to the $K^\pi = 2^-$ mode (see Table 3.4). The collectivity of these modes is apparently weak in comparison with the octupole vibrations built on the SD states in heavy nuclei [112, 113], because the number of particle-hole configurations contributing to the RPA modes is rather small in the nuclei under consideration. It should be mentioned, however, that transition strengths much larger than those in our results are obtained for these nuclei in the mixed representation RPA calculation carried out by Inakura *et al.* [64], where no cutoff is imposed in the particle-hole excitation energy. The major cause of this difference may be the rather severe energy cutoff in the present RPA calculation. (See Ref. [99] for a numerical analysis of the contributions from very high-lying particle-hole configurations to the transition strengths of the low-lying RPA modes.)

3.3.2 The SD state in ^{50}S

In this subsection, we discuss the result for ^{50}S, which is, according to the SHF calculations [28, 100], close to the neutron drip line. The existence of the SD band in this nucleus is suggested in Ref. [100]. The isoscalar octupole strength distribution with $K^\pi = 2^-$ calculated with the RPA is presented in Fig. 3.5. There are no peaks at any values of K in this energy region other than those corresponding to excitations to the discretized continuum. As we explain in detail below, the highest peak, at 3.1 MeV, with $K^\pi = 2^-$ is associated
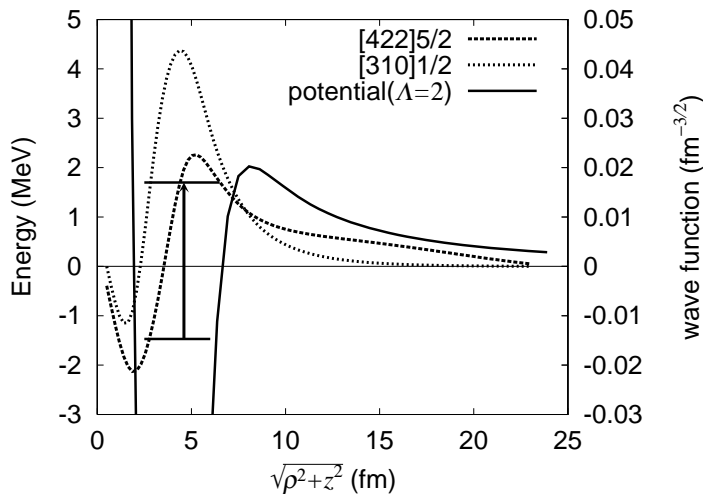
Figure 3.6: The neutron particle-hole excitation contributing to the strongly enhanced transition strength of the $K^\pi = 2^-$ state at 3.1 MeV in superdeformed ^{50}S. The particle and hole states are labeled by their asymptotic quantum numbers. Their wave functions are plotted by the dotted curves. The solid curve denotes the neutron single-particle potential including the centrifugal barrier for $\Lambda = 2$. The horizontal axis represents $\sqrt{\rho^2 + z^2}$ along the $\theta = 45°$ line.

with the excitation of a single neutron from the loosely bound [310]1/2 state to the resonance [422]5/2 state. We obtain a peak of similar nature but with a smaller strength at 2.9 MeV. It is associated with the excitation of a single neutron from the loosely bound [431]3/2 state to the resonance [303]7/2 state. This difference in strength between the two peaks can be understood from the asymptotic selection rule (3.23c): The former particle-hole excitation satisfies it, whereas the latter does not. On the other hand, the second highest peak, at 2.8 MeV, is due to a neutron excitation from the [431]3/2 state to a discretized continuum state with $\Omega^\pi = 1/2^-$.

We now discuss the microscopic structure of the $K^\pi = 2^-$ excitation at 3.1 MeV in detail. It has an extremely strong isoscalar strength of $B(Q^{IS}3) = 41$ W.u. and a weak electric strength of $B(E3) = 0.13$ W.u. (1 W.u. $\simeq 149$ fm^6 for ^{50}S). As shown in Table 3.5, the major component of this RPA mode is the [310]1/2 → [422]5/2 excitation of a neutron. Their wave functions are plotted in Fig. 3.6. Because the [310]1/2 state is loosely bound and the [422]5/2 state is a resonance state, their wave functions extend significantly outside of the half-density radius of this nucleus. Together with the fact that this particle-hole configuration satisfies the asymptotic selection rule (3.23c), the very extended spatial structures of their wave functions are the main reason why it has the extremely large transition strength.

This [422]5/2 state has an interesting property: Because the centrifugal barrier is angle dependent, it lies below the barrier along the z-axis and 0.2 MeV above it along the ρ-axis (see Fig. 3.7). To determine whether or not the resonance interpretation of this state is valid, we first examined the box size dependence of calculated single-particle energies. As shown in Fig. 3.8, the energy of the [422]5/2 state is found to be stable with respect to variation of the box size. We next evaluated the sum of the eigenphase, $\Delta(E) = \sum_a \delta_a(E)$, following the procedure of Ref. [114]. The eigenphase is obtained through eigenvalues of the S-matrix,

Table 3.5: RPA amplitudes for the 2^- state at 3.1 MeV in ^{50}S, calculated with $\beta_2 = 0.54$ and 0.73 for protons and neutrons, respectively. It is characterized by $B(E3) = 19.4\ e^2$fm^6, $B(Q^\nu 3) = 5359$ fm^6, $B(Q^{\mathrm{IS}}3) = 6023$ fm^6, and $\sum |g_{ph}|^2 = 6.42 \times 10^{-3}$. Only components with $|f_{ph}| > 0.1$ are listed.

particle	hole	$\epsilon_p - \epsilon_h$ (MeV)	f_{ph}	Q_{32}^{ph} (fm^3)	M_{32}^{ph} (fm^3)
$\nu[303]7/2$	$\nu[431]3/2$	3.01	0.133	-11.6	-1.49
$\nu[422]5/2$	$\nu[310]1/2$	3.20	0.967	65.7	66.1
$\pi[321]3/2$	$\pi[211]1/2$	4.69	-0.138	-12.4	2.26
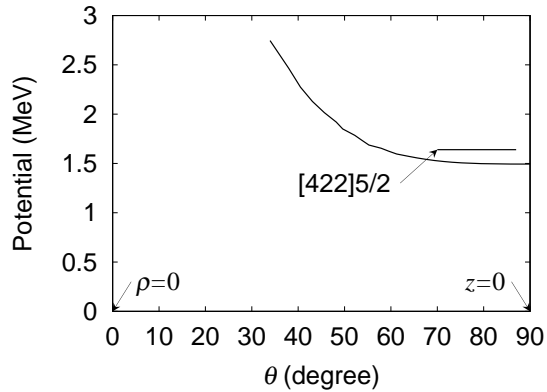
Figure 3.7: Angle dependence of the centrifugal barrier height for the $\Lambda = 2$ states in superdeformed ^{50}S. The z- and ρ-axes correspond to $\theta = 0°$ and $90°$, respectively.
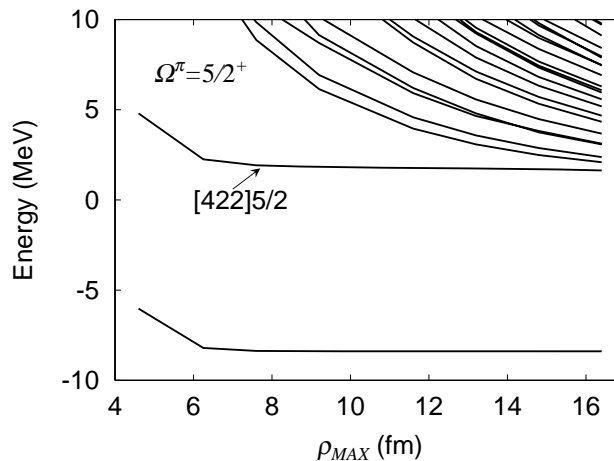
Figure 3.8: Box size dependence of single-particle levels with $\Omega^\pi = 5/2^+$ in superdeformed ^{50}S. The [422]5/2 level is stable with respect to variation of the box size.
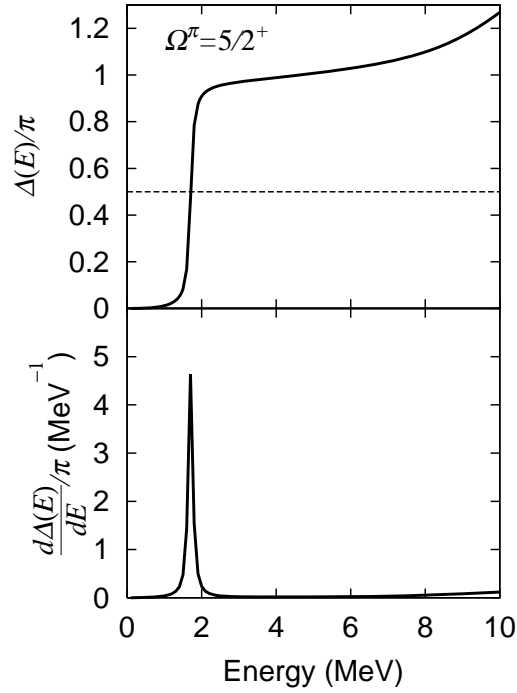
Figure 3.9: The eigenphase sum (upper panel) and its derivative (lower panel) for the $\Omega^{\pi} = 5/2^+$ state in superdeformed ^{50}S are plotted as functions of energy.
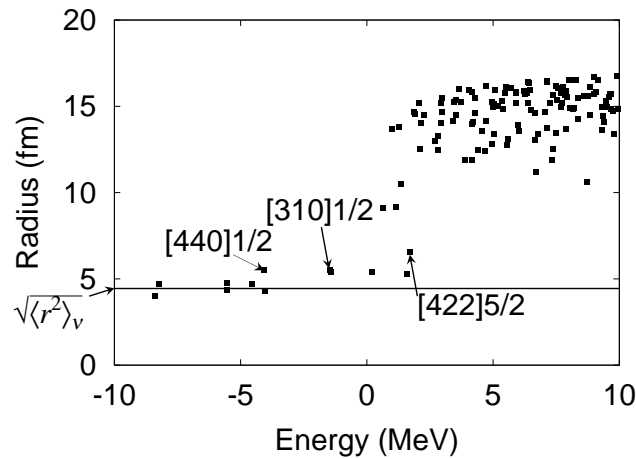
Figure 3.10: Root-mean-square radii $\sqrt{\langle r^2 \rangle}$ of neutron single-particle states in superdeformed ^{50}S, obtained in a calculation using a box of size $\rho_{max} \times z_{max} = 14.25$ fm $\times$ 22.0 fm. Here, the root-mean-square radius of neutrons $\sqrt{\langle r^2 \rangle_\nu}$ is 4.44 fm.

and their sum has the same energy dependence around a resonance as the phase shift in a spherical system [115],

$$\tan(\Delta(E) - \Delta_0(E)) = \frac{\Gamma}{2(E - E_R)},\tag{3.24}$$

where E_R and Γ denote the resonance energy and the total width, respectively. The sum of the background eigenphases, $\Delta_0(E)$, is considered a slowly-varying quantity. The result of this calculation, presented in Fig. 3.9, confirms that the [422]5/2 state can be regarded as a resonance. Its width is estimated to be about 0.14 MeV. Furthermore, we confirmed that the root-mean-square radius of this state is clearly distinguishable from those of discretized continuum states (see Fig. 3.10). In this figure, the root-mean-square radius of various single-particle states are plotted. We find that not only the resonance [422]5/2 state but also the weakly bound [310]1/2 state has a root-mean-square radius about 2 fm larger than the average value for neutrons, $\sqrt{\langle r^2 \rangle}_\nu = 4.44$ fm. This is because the low angular momentum $p_{1/2}$ component that has a spatially extended structure becomes dominant in such a $\Omega^\pi = 1/2^-$ neutron level as the binding energy approaches zero [116, 117].

In contrast to the peak at 3.1 MeV discussed above, the peak at 2.8 MeV corresponds to the excitation of the loosely bound [431]3/2 neutron to a discretized continuum state with $\Omega^\pi = 1/2^-$. Therefore, its position and height do not have definite physical meanings. In fact, these values change as the box size is varied. This peak even disappears when smaller boxes are used in the numerical calculation (see Fig. 3.11), whereas the peak position and the height associated with the [310]1/2 $\rightarrow$ [422]5/2 excitation is stable, as long as a box larger than $\rho_{\max} \times z_{\max} = 12.25$ fm $\times 20.0$ fm is used. We should also mention that the convergence of the numerical calculation is insufficient for the unperturbed strength of the [310]1/2 $\rightarrow$ [422]5/2 transition, because the root-mean-square radius of the [422]5/2 state still increases from 5.90 fm to 6.54 fm for a larger box, with $\rho_{\max} \times z_{\max} = 14.25$ fm $\times 22.0$ fm. Therefore, the calculated transition strength has only qualitative meaning.

Finally, let us make a comparison between the spatial distributions of the $K^\pi = 2^-$ octupole strength associated with individual particle-hole excitations on the SD state in the drip line nucleus ^{50}S and those in the stable nucleus ^{32}S. Figure 3.12 plots the spatial distribution functions $Q_{3K}^{ph}(\rho, z)$ for some major configurations generating the low-lying $K^\pi = 2^-$ modes in ^{32}S and ^{50}S. It is clear that the particle-hole excitations in ^{50}S have spatial distributions significantly extended outside of the nucleus, while those in ^{32}S are peaked around the surface region. This spatially extended structure brings about a strong enhancement of the octupole strength in ^{50}S. This can be regarded as one of the unique properties of excitation modes in nuclei close to the drip line. Note that this mechanism of transition strength enhancement is different from the threshold effect associated with the excitation of a loosely bound neutron into the non-resonant continuum [118].

3.3.3 The oblately deformed state in ^{40}Mg

To show that the strong enhancement of the transition strength for an excitation from a loosely bound state to a resonance state is not restricted to the SD states but expected to be a rather general phenomenon in nuclei close to the drip line, we present in this subsection another example of the RPA calculation for ^{40}Mg. According to the HFB calculations [26, 29], this nucleus is situated close to the neutron drip line and possesses both prolate and oblate local minima.
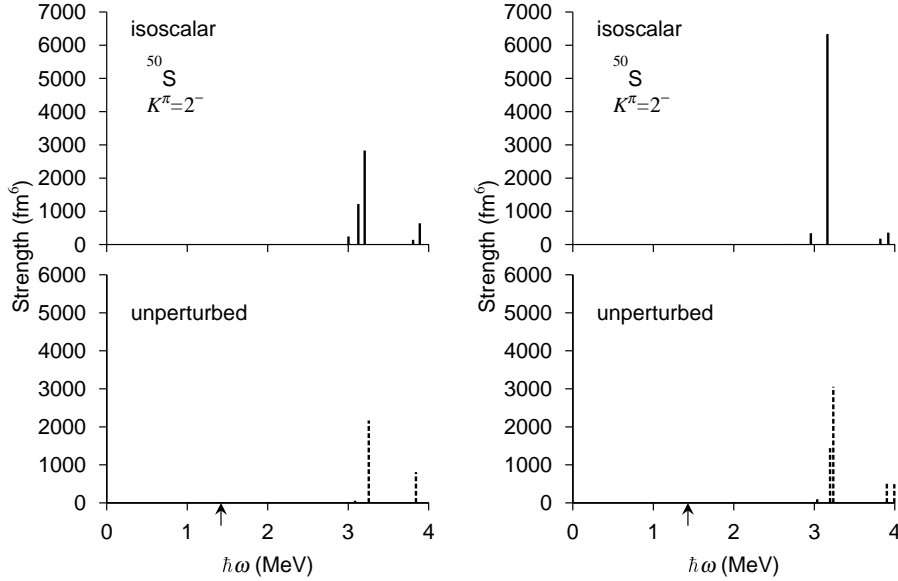
Figure 3.11: The isoscalar octupole strength $B(Q^{IS}3)$ distributions for the $K^\pi = 2^-$ excitations on the SD state in ^{50}S, obtained using an RPA calculation with $\beta_2 = 0.54$ and 0.73 for protons and neutrons, respectively, using a box of size $\rho_{max} \times z_{max} = 10.25$ fm $\times 16.0$ fm (left) and 12.25 fm $\times 20.0$ fm (right). The neutron root-mean-square radii $\sqrt{\langle r^2 \rangle_\nu}$ are 4.42 fm and 4.44 fm. The unperturbed particle-hole strengths are also plotted with dashed lines in the bottom panels. The arrows indicate the threshold energy, $E_{th} = 1.4$ MeV.

Table 3.6: RPA amplitudes for the 3^- state at 6.2 MeV in the oblately deformed ^{40}Mg, calculated with $\beta_2 = -0.2$ for both protons and neutrons. It is characterized by $B(E3) = 1.09\ e^2\text{fm}^6$, $B(Q^\nu 3) = 9280$ fm^6, $B(Q^{IS}3) = 9482$ fm^6, and $\sum |g_{ph}|^2 = 1.46 \times 10^{-3}$. The particle states other than the $\nu[404]9/2$ and $\nu[404]7/2$ resonances represent discretized continuum states. Only components with $|f_{ph}| > 0.1$ are listed.

particle	hole	$\epsilon_p - \epsilon_h$ (MeV)	f_{ph}	Q_{33}^{ph} (fm^3)	M_{33}^{ph} (fm^3)
$\nu\ 7/2^+$	$\nu[301]1/2$	5.84	-0.142	-56.0	7.81
$\nu\ 5/2^+$	$\nu[301]1/2$	5.92	0.156	49.6	7.58
$\nu\ 5/2^+$	$\nu[301]1/2$	6.06	0.211	-0.526	-0.109
$\nu[404]9/2$	$\nu[301]3/2$	6.24	0.909	-96.7	-89.5
$\nu\ 3/2^+$	$\nu[301]3/2$	6.45	0.171	-37.4	-6.51
$\nu[404]7/2$	$\nu[301]1/2$	6.52	0.160	-82.1	-13.3
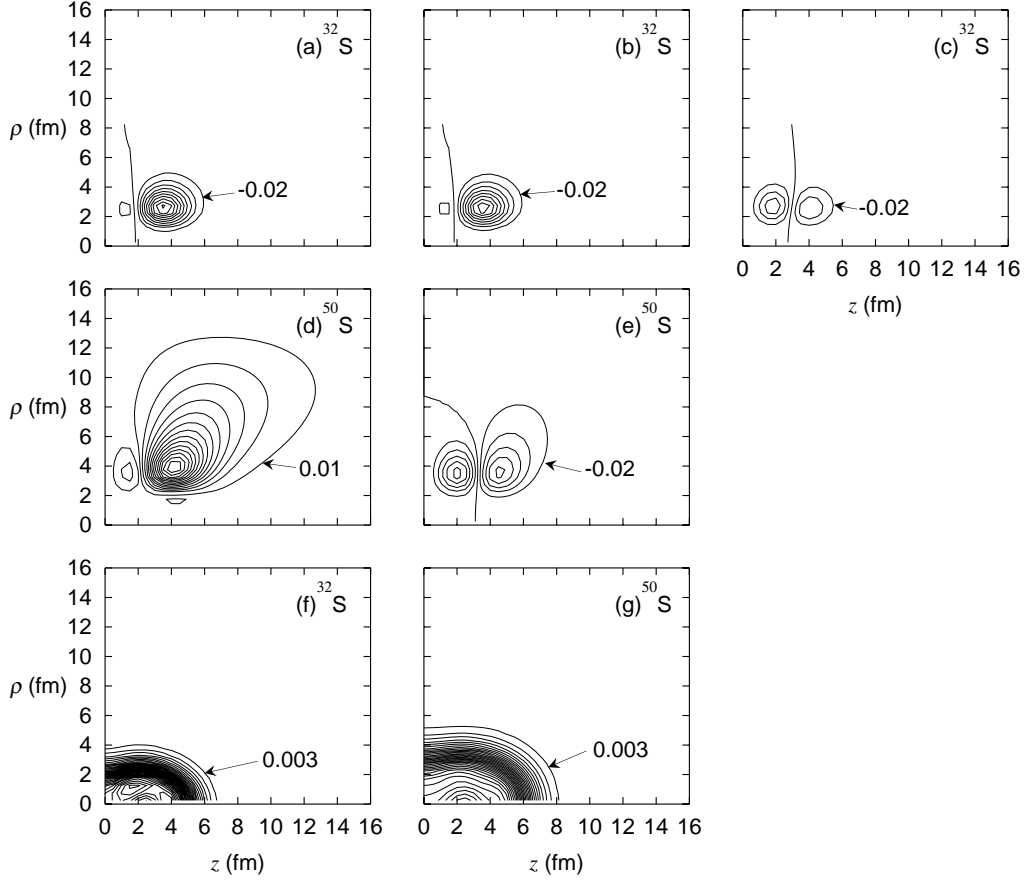
Figure 3.12: Spatial distribution functions $Q_{32}^{ph}(\rho, z)$ for some particle-hole excitations generating the low-lying $K^\pi = 2^-$ states in superdeformed ^{32}S and ^{50}S. The contour lines are plotted at intervals of 0.02 fm. The panels denoted (a), (b) and (c) correspond to the $[211]1/2 \rightarrow [321]3/2$, $[211]3/2 \rightarrow [321]1/2$, and $[330]1/2 \rightarrow [202]5/2$ excitations in ^{32}S, respectively, while (d) and (e) correspond to the $[310]1/2 \rightarrow [422]5/2$ and $[431]3/2 \rightarrow [303]7/2$ excitations in ^{50}S. The bottom panels, (f) and (g), display the neutron density distributions of the SD states in ^{32}S and ^{50}S, respectively. The contour lines are plotted at intervals of 0.003 fm^{-3}. The neutron root-mean-square radii, $\sqrt{\langle r^2 \rangle_\nu}$, are 3.49 and 4.44 fm for ^{32}S and ^{50}S, respectively.
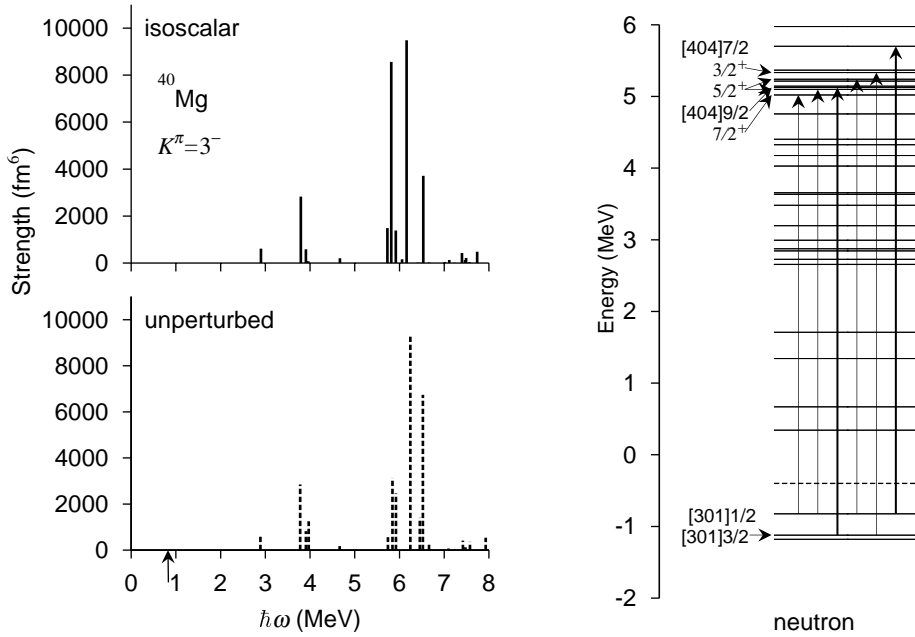
Figure 3.13: *Left*: The isoscalar octupole strength $B(Q^{IS}3)$ distribution for the $K^\pi = 3^-$ excitations on the oblate state in ^{40}Mg is plotted in the top panel as a function of the excitation energy. This was obtained using an RPA calculation with $\beta_2 = -0.2$ for both protons and neutrons, using a box of size $\rho_{\max} \times z_{\max} = 14.25$ fm $\times 12.0$ fm. The unperturbed particle-hole strengths are also plotted with dashed lines in the bottom panel. The arrow indicates the threshold energy $E_{\rm th} = 0.82$ MeV. *Right*: Particle-hole configurations of neutrons generating the $K^\pi = 3^-$ state at 6.2 MeV. The levels denoted [404]9/2 and [404]7/2 correspond to resonances, while other levels in the positive energy region represent discretized continuum states.
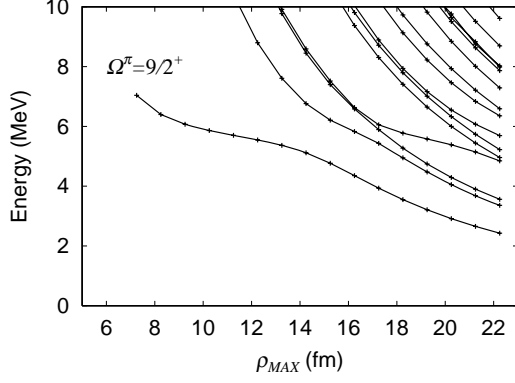
Figure 3.14: Box size dependence of single-particle levels with $\Omega^\pi = 9/2^+$ in the oblately deformed ^{40}Mg.
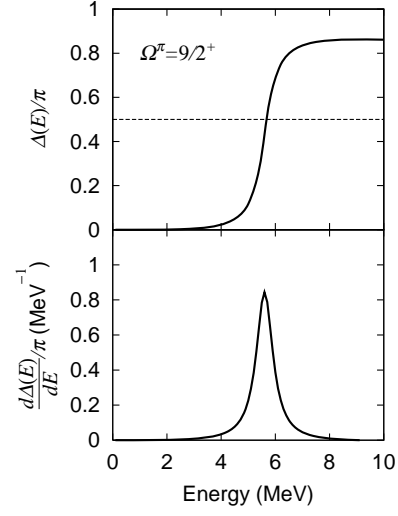
Figure 3.15: The eigenphase sum (upper panel) and its derivative (lower panel) for the $\Omega^\pi = 9/2^+$ state in the oblately deformed ^{40}Mg are plotted as functions of energy.
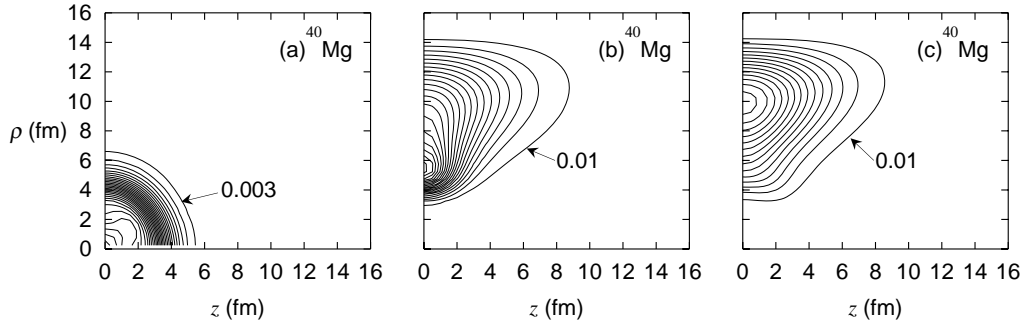
Figure 3.16: (a) The neutron density distribution of the oblately deformed state in ^{40}Mg. The contour lines are plotted at intervals of 0.003 fm^{-3}. The root-mean-square radius of neutrons, $\sqrt{\langle r^2 \rangle_\nu}$, is 4.06 fm. (b) Spatial distribution function $Q_{33}^{ph}(\rho, z)$ for the [301]3/2 → [404]9/2 excitation on the oblately deformed state in ^{40}Mg. The contour lines are plotted at intervals of 0.02 fm. (c) Same as (b), but for the [301]1/2 → [404]7/2 excitation.

Figure 3.13 displays the octupole transition strengths for the $K^\pi = 3^-$ excitations on the oblately deformed state in ^{40}Mg. Among several peaks in the isoscalar strength distribution, we can give a clear physical interpretation for the two prominent peaks at 6.2 and 6.6 MeV: The former is created by the excitation of a neutron from the loosely bound [301]3/2 state to the resonance [404]9/2 state, while the latter is from the loosely bound [301]3/2 state to the resonance [404]7/2 state. These resonance states are associated with the $g_{9/2}$ orbit, which has a high centrifugal barrier. Due to the spatially extended structure of this type of particle-hole excitation, they acquire extremely large transition strengths; the isoscalar octupole strength of the former (latter) is about 90 (39) W.u. (1 W.u. $\simeq 95$ fm^6 for ^{40}Mg). The major components of the RPA amplitudes of the $K^\pi = 3^-$ mode at 6.2 MeV are presented in Table 3.6. Other peaks in this figure are due to excitations to discretized continuum states; e.g., the peak at 3.8 (5.8) MeV is associated with the excitation from the [301]3/2 ([301]1/2) state to the discretized continuum Ω^π=3/2$^+$ (7/2$^+$) state. Therefore, their positions and peak heights do not have definite physical meanings. This conclusion was obtained by examining the box size dependence of single-particle energies and their eigenphase sums. Typical results of these calculations are presented in Figs. 3.14 and 3.15. The widths of the resonant [404]9/2 and [404]7/2 states are estimated to be about 0.8 and 1.2 MeV, respectively.

Finally, we show in Fig. 3.16 the spatial distribution functions $Q_{33}^{ph}(\rho, z)$ for the [301]3/2 $\rightarrow$ [404]9/2 and [301]1/2 $\rightarrow$ [404]7/2 excitations, together with the neutron density distribution of the oblately deformed state in ^{40}Mg. It is clearly seen that the strengths of these particle-hole excitations extend far from the nuclear surface. Furthermore, we notice that the peak positions of the two distributions, shown in (b) and (c), differ considerably. This can be regarded as the major reason that the two particle-hole configurations do not strongly mix with each other in the RPA eigenmodes, despite the fact that their unperturbed energies are fairy close (see Table 3.6). This is quite different from the familiar situations for low-frequency RPA modes in stable nuclei, in which the strength distribution functions of many particle-hole configurations have peaks near the nuclear surface and tend to mix with each other, generating collective vibrational modes.

3.4 Summary

By means of the RPA calculation based on the deformed Woods-Saxon potential in the coordinate-mesh representation, we have carried out a comparative study of octupole excitations built on the SD states in the ^{40}Ca region and those in ^{50}S. In the $N = Z$ stable nuclei, ^{32}S and ^{40}Ca, the enhancement of the octupole transition strength results from the coherence between the proton and neutron excitations. By contrast, in ^{50}S close to the neutron drip line, we have found that the low-lying state created by the excitation of a single neutron from a loosely bound low Ω state to a high Ω resonance state acquires an extremely large transition strength. We have made a detailed study of the spatial distributions of particle-hole transition strengths and confirmed that this enhancement of the strength is a natural consequence of the fact that these particle and hole wave functions extend significantly outside of the nuclear surface. To show that this kind of enhancement phenomenon is not restricted to the SD states, we have also presented another example for oblately deformed ^{40}Mg close to the neutron drip line.

The present calculation indicates that, as we approach the drip line, it becomes increasingly difficult to generate collective modes of excitation by coherent superpositions of many

particle-hole excitations. This is because the bound particle states disappear and individual resonance wave functions possess different spatial structures. It should be emphasized, however, that the pairing correlation is not taken into account in the present calculation. Quite recently, Yamagami showed [76] that collectivity emerges in nuclei close to the drip line, owing to the pairing anti-halo effect [122]: The self-consistent pairing correlation in the continuum brings about spatial localization of particle-hole excitations, which helps in generating the collective modes of excitation. Thus, it is an important next step to investigate how the results presented in this chapter are modified by the pairing correlation.

Chapter 4

Quadrupole vibrations in Mg isotopes close to the neutron drip line – further effects of pairing correlations

4.1 Introduction

The nature of pairing correlations in neutron drip-line nuclei is one of the most important subjects in the physics of unstable nuclei. One of the unique features of drip-line nuclei is that the pairing correlation takes place not only among bound levels but also including continuum states. To describe this unique character of pairing, the coordinate-space HFB formalism is suitable [71, 72]. Due to the pairing and continuum effects, spatial structure of quasiparticle wave functions near the chemical potential changes significantly, which affects the properties of low-frequency excitation modes in spherical neutron drip-line nuclei [76]. In order to study the effects of pairing on the low-frequency excitation modes in deformed nuclei near the neutron drip line, we have extended the work presented in the previous chapter to self-consistently include pairing correlations, and constructed a new computer code that carries out the deformed QRPA calculation on the basis of the coordinate-space HFB formalism.

The aim of this chapter is to carry out the deformed QRPA calculation for neutron drip-line nuclei and investigate the low-frequency quadrupole vibrational modes with $K^\pi = 0^+$ and 2^+ in ^{36,38,40}Mg close to the neutron drip line. According to the Skyrme-HFB calculations [26, 29] and Gogny-HFB calculation [33], these isotopes are well deformed. The shell-model calculation [39] also suggests that the ground state of ^{40}Mg is dominated by the neutron two-particle-two-hole components, which is consistent with the breaking of the $N = 28$ shell closure discussed in Ref. [119]. We investigate properties of low-frequency modes of excitation in these Mg isotopes simultaneously taking into account the deformed mean-field effects, the pairing correlations, and excitations into the continuum.

This chapter is organized as follows: In the next section, the framework of the mean-field and QRPA calculations is briefly described. In §4.3, results of the QRPA calculation for low-frequency quadrupole vibrations with $K^\pi = 0^+$ and 2^+ in ^{36,38,40}Mg are presented and discussed focusing our attention to the microscopic mechanism of emergence of collective modes in deformed superfluid nuclei close to the neutron drip line. Concluding remarks are

given in §4.4.

This work was reported in Refs. [80, 81].

4.2 Method

4.2.1 Mean-field calculation

In order to discuss simultaneously effects of nuclear deformation and pairing correlations including the continuum, we solve the HFB equation [71, 72, 84]

$$
\begin{pmatrix} h^\tau(\boldsymbol{r}\sigma) - \lambda^\tau & \tilde{h}^\tau(\boldsymbol{r}\sigma) \\ \tilde{h}^\tau(\boldsymbol{r}\sigma) & -(h^\tau(\boldsymbol{r}\sigma) - \lambda^\tau) \end{pmatrix} \begin{pmatrix} \varphi^\tau_{1,\alpha}(\boldsymbol{r}\sigma) \\ \varphi^\tau_{2,\alpha}(\boldsymbol{r}\sigma) \end{pmatrix} = E_\alpha \begin{pmatrix} \varphi^\tau_{1,\alpha}(\boldsymbol{r}\sigma) \\ \varphi^\tau_{2,\alpha}(\boldsymbol{r}\sigma) \end{pmatrix}
\tag{4.1}
$$

directly in the cylindrical-coordinate space assuming axial and reflection symmetry. In comparison to the conventional method of using a deformed harmonic oscillator basis, this method is more effective in the treatment of spatially extended wave functions, like loosely bound states, resonant states and continuum states. As is well known, when the quasiparticle energy E is greater than the absolute magnitude $|\lambda|$ of the chemical potential, the upper component $\varphi_1(\boldsymbol{r}\sigma)$ obeys the scattering-wave boundary condition, while the lower component $\varphi_2(\boldsymbol{r}\sigma)$ is always exponentially decaying at infinity.

For the mean-field Hamiltonian h, we employ the deformed Woods-Saxon potential with the parameters used in [78], except the isovector potential strength for which a slightly smaller value, 30 MeV in stead of 33 MeV, is adopted in order to describe ^{40}Mg as a drip-line nucleus in accordance with the Skyrme-HFB [26, 29] and Gogny-HFB calculations [33]. The pairing field is treated self-consistently by using the density-dependent contact interaction [10, 120],

$$
v_{pp}(\boldsymbol{r}, \boldsymbol{r}') = V_0 \frac{1 - P_\sigma}{2} \left[1 - \eta \left(\frac{\varrho^{\mathrm{IS}}(\boldsymbol{r})}{\varrho_0} \right) \right] \delta(\boldsymbol{r} - \boldsymbol{r}'),
\tag{4.2}
$$

with $V_0 = -450$ MeV·fm^3 and $\varrho_0 = 0.16$ fm^{-3}, where $\varrho^{\mathrm{IS}}(\boldsymbol{r})$ denotes the isoscalar density and P_σ is the spin exchange operator. The pairing force strength V_0 is chosen such that the average pairing gap roughly agrees with the systematics (see Table 4.1). For the parameter η, which represents density dependence, we use $\eta = 1.0$ (surface type). Sensitivity of calculated results to the parameter η will be examined in §4.3.4. The pairing Hamiltonian is then given by

$$
\tilde{h}^\tau(\boldsymbol{r}) = \frac{V_0}{2} \left[1 - \eta \left(\frac{\varrho^{\mathrm{IS}}(\boldsymbol{r})}{\varrho_0} \right) \right] \tilde{\varrho}^\tau(\boldsymbol{r}).
\tag{4.3}
$$

The normal (particle) and abnormal (pairing) densities are given by

$$
\varrho^\tau(\rho, z) = \sum_\alpha \sum_{\sigma=\pm 1/2} |\varphi^\tau_{2,\alpha}(\rho, z, \sigma)|^2,
\tag{4.4}
$$

$$
\tilde{\varrho}^\tau(\rho, z) = -\sum_\alpha \sum_{\sigma=\pm 1/2} \varphi^\tau_{1,\alpha}(\rho, z, \sigma)\varphi^\tau_{2,\alpha}(\rho, z, \sigma)
\tag{4.5}
$$

and the mean-square radii of protons and neutrons are calculated as

$$
\langle r^2 \rangle_\tau = \frac{\int \rho \, \mathrm{d}\rho \, \mathrm{d}z \, r^2 \varrho^\tau(\rho, z)}{\int \rho \, \mathrm{d}\rho \, \mathrm{d}z \, \varrho^\tau(\rho, z)},
\tag{4.6}
$$

Table 4.1: Ground state properties of ^{36,38,40}Mg obtained by the deformed WS-HFB calculation with $\beta_2 = 0.28$. Chemical potentials, average pairing gaps, and root-mean-square radii for protons and neutrons are listed.

nucleus	λ_π (MeV)	$\langle\Delta_\pi\rangle$ (MeV)	$\sqrt{\langle r^2\rangle_\pi}$ (fm)	λ_ν (MeV)	$\langle\Delta_\nu\rangle$ (MeV)	$\sqrt{\langle r^2\rangle_\nu}$ (fm)
^{36}Mg	-20.0	0.0	3.06	-2.09	1.93	3.74
^{38}Mg	-23.0	0.0	3.08	-1.15	2.05	3.86
^{40}Mg	-25.1	0.0	3.10	-0.41	2.15	3.99

where $\boldsymbol{r} = (\rho, z)$, $r = \sqrt{\rho^2 + z^2}$ and $\tau=\pi$ or ν; $\varrho^\pi(\rho,z)$ and $\varrho^\nu(\rho,z)$ being the proton and neutron densities. The average gaps are defined by [121, 122, 123, 124]

$$\langle\Delta_\tau\rangle = - \int \mathrm{d}\boldsymbol{r}\,\tilde\varrho^\tau(\boldsymbol{r})\tilde h^\tau(\boldsymbol{r})/\int \mathrm{d}\boldsymbol{r}\,\tilde\varrho^\tau(\boldsymbol{r}). \tag{4.7}$$

We construct the discretized Hamiltonian matrix by use of the finite difference method for derivatives and then diagonalize the matrix to obtain the quasiparticle wave functions on the two-dimensional lattice consisting of the cylindrical coordinates ρ and z. The kinetic energy term and the spin-orbit potential are evaluated using the 9-point formula. Because the time-reversal symmetry and the reflection symmetry with respect to the $x-y$ plane are assumed, we have only to solve for positive Ω and positive z. We use the lattice mesh size $\Delta\rho = \Delta z = 0.8$ fm and the box boundary condition at $\rho_{\max} = 10.0$ fm and $z_{\max} = 12.8$ fm. The quasiparticle energy is cut off at 50 MeV and the quasiparticle states up to $\Omega^\pi = 13/2^\pm$ are included. This model space is larger than that used in Ref. [81]. It is certainly desirable to use a larger box for a better evaluation of matrix elements involving spatially very extended quasiparticle wave functions. This improvement remains as a future task, however.

We impose the condition on the convergence of the pairing energy as $|(E_{pair}^{(i)} - E_{pair}^{(i-1)})/E_{pair}^{(i)}| < 10^{-5}$, where i denotes the iteration number and the pairing energy is defined by [74]

$$E_{pair} = \frac{1}{2}\sum_{\tau=\pi,\nu}\int \mathrm{d}\boldsymbol{r}\,\tilde\varrho^\tau(\boldsymbol{r})\tilde h^\tau(\boldsymbol{r}). \tag{4.8}$$

We use the same deformation parameter $\beta_2 = 0.28$ in the Woods-Saxon potential for both neutrons and protons. This parameter is chosen to approximately reproduce the $Q-$moments calculated in Ref. [29]. We checked that properties of the QRPA modes do not change significantly when the deformation parameter is varied around $\beta_2 \sim 0.3$.

4.2.2 Quasiparticle-RPA calculation

Using the quasiparticle basis obtained in the previous subsection, we solve the QRPA equation in the standard matrix formulation [96]

$$\sum_{\gamma\delta}\begin{pmatrix} A_{\alpha\beta\gamma\delta} & B_{\alpha\beta\gamma\delta} \\ B_{\alpha\beta\gamma\delta} & A_{\alpha\beta\gamma\delta} \end{pmatrix}\begin{pmatrix} f^\lambda_{\gamma\delta} \\ g^\lambda_{\gamma\delta} \end{pmatrix} = \hbar\omega_\lambda\begin{pmatrix} 1 & 0 \\ 0 & -1 \end{pmatrix}\begin{pmatrix} f^\lambda_{\alpha\beta} \\ g^\lambda_{\alpha\beta} \end{pmatrix}. \tag{4.9}$$

This method is convenient to analyze microscopic structures of the QRPA eigenmodes in comparison with other RPA formalisms based on the Greens function method. Namely, individual two-quasiparticle components, $(\alpha\beta), (\gamma\delta)$, etc., constituting the QRPA mode λ are directly represented by the amplitudes $f_{\gamma\delta}^\lambda$ and $g_{\gamma\delta}^\lambda$, whereas an additional procedure is needed to obtain them in the latter method [125].

The residual interactions in the particle-particle channel appearing in the QRPA matrices A and B are self-consistently treated using the density-dependent contact interaction (4.2). On the other hand, for residual interactions in the particle-hole channel, we use the Skyrme-type interaction [98]

$$v_{ph}(\boldsymbol{r}, \boldsymbol{r}') = \left[t_0(1 + x_0 P_\sigma) + \frac{t_3}{6}(1 + x_3 P_\sigma)\varrho^{\text{IS}}(\boldsymbol{r}) \right] \delta(\boldsymbol{r} - \boldsymbol{r}'), \qquad (4.10)$$

with $t_0 = -1100$ MeV·fm³, $t_3 = 16000$ MeV·fm⁶, $x_0 = 0.5$, and $x_3 = 1.0$. Because the deformed Wood-Saxon potential is used for the mean-field, we renormalize the residual interaction in the particle-hole channel by multiplying a factor f_{ph} to get the spurious $K^\pi = 1^+$ mode (representing the rotational mode) at zero energy ($v_{ph} \to f_{ph} \cdot v_{ph}$). This factor is found to be 0.380, 0.376 and 0.374 for ^{36}Mg, ^{38}Mg, and ^{40}Mg, respectively. It is desirable to carry out the QRPA calculation by using a model space which is consistent with that adopted in the HFB calculation. It requires, however, excessively demanding computer memory, so that we cut the model space by $E_\alpha + E_\beta \leq 30$ MeV. Accordingly, we need another self-consistency factor f_{pp} for the particle-particle channel. We determine this factor such that the spurious $K^\pi = 0^+$ mode associated with the number fluctuation appears at zero energy ($v_{pp} \to f_{pp} \cdot v_{pp}$). This factor is found to be 1.536 for $^{36-40}$Mg. The dimension of the QRPA matrix is about 3700 for the $K^\pi = 0^+$ modes in ^{40}Mg. We checked accuracy of the numerical calculation by applying our procedure to quadrupole excitations of the spherical nucleus ^{24}O and comparing the result with that of the continuum QRPA calculation by Matsuo [47] which exactly fulfills the energy-weighted sum-rule. It turned out that, although the overall structure of the strength distribution was well reproduced, the energy-weighted sum-rule value was underestimated by 14% due to the truncation of the model space. This shortcoming should be overcome in future by enlarging the QRPA model space.

In terms of the nucleon annihilation and creation operators in the coordinate representation, $\hat{\psi}(\boldsymbol{r}\sigma)$ and $\hat{\psi}^\dagger(\boldsymbol{r}\sigma)$, the quadrupole operator is represented as $\hat{Q}_{2K} = \sum_\sigma \int \mathrm{d}\boldsymbol{r} r^2 Y_{2,-K}(\hat{r}) \times \hat{\psi}^\dagger(\boldsymbol{r}\sigma)\hat{\psi}(\boldsymbol{r}\sigma)$. The intrinsic matrix elements $\langle\lambda|\hat{Q}_{2K}|0\rangle$ of the quadrupole operator between the excited state $|\lambda\rangle$ and the ground state $|0\rangle$ are given by

$$\langle\lambda|\hat{Q}_{2K}|0\rangle = \sum_{\alpha\beta} Q_{2K,\alpha\beta}^{(\text{uv})}(f_{\alpha\beta}^\lambda + g_{\alpha\beta}^\lambda) = \sum_{\alpha\beta} M_{2K,\alpha\beta}^{(\text{uv})}, \qquad (4.11)$$

where

$$Q_{2K,\alpha\beta}^{(\text{uv})} \equiv 2\pi\delta_{K,\Omega_\alpha+\Omega_\beta} \int \mathrm{d}\rho\mathrm{d}z Q_{2K,\alpha\beta}^{(\text{uv})}(\rho, z), \qquad (4.12)$$

with

$$Q_{2K,\alpha\beta}^{(\text{uv})}(\rho, z) = \rho\{\varphi_{1,\alpha}(\rho, z, \uparrow)\varphi_{2,\beta}(\rho, z, \downarrow) - \varphi_{1,\alpha}(\rho, z, \downarrow)\varphi_{2,\beta}(\rho, z, \uparrow)$$
$$- \varphi_{1,\beta}(\rho, z, \uparrow)\varphi_{2,\alpha}(\rho, z, \downarrow) + \varphi_{1,\beta}(\rho, z, \downarrow)\varphi_{2,\alpha}(\rho, z, \uparrow)\}Q_{2K}(\rho, z). \quad (4.13)$$
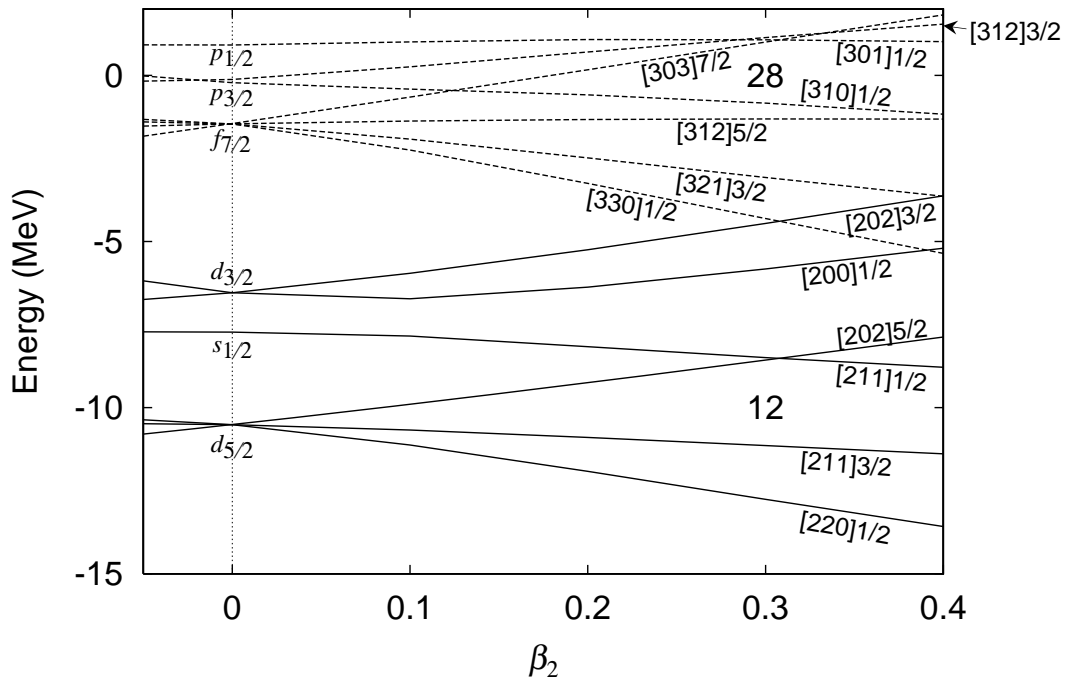
Figure 4.1: Single-particle energies in the deformed WS potential for neutrons in ^{40}Mg, plotted as functions of the quadrupole deformation parameter β_2. Solid and dotted lines denote positive- and negative-parity levels, respectively. Single-particle levels are labeled with the asymptotic quantum numbers $[Nn_3\Lambda]\Omega$.

Here $Q_{2K}(\rho, z) = Q_{2K}(\boldsymbol{r})e^{iK\phi} = r^2 Y_{2,-K}(\theta, \phi)e^{iK\phi}$.

We calculate the transition strength functions

$$S^{\mathrm{IS}}(\omega) = \sum_\lambda |\langle\lambda|\hat{Q}^{\mathrm{IS}}_{2K}|0\rangle|^2 \delta(\hbar\omega - \hbar\omega_\lambda) \tag{4.14}$$

for isoscalar quadrupole operators $\hat{Q}^{\mathrm{IS}}_{2K} = \hat{Q}^{\pi}_{2K} + \hat{Q}^{\nu}_{2K}$, and use notations $B(Q^\tau 2) = |\langle\lambda|\hat{Q}^\tau_{2K}|0\rangle|^2$ for transition strengths and $M_\tau = \langle\lambda|\hat{Q}^\tau_{2K}|0\rangle$ for transition matrix elements ($\tau = \pi, \nu$, IS). Note that these quantities are defined in the intrinsic coordinate frame associated with the deformed mean field, so that appropriate Clebsh-Gordan coefficients should be multiplied to obtain transition probabilities in the laboratory frame [126]. For instance, a factor 1/5 should be multiplied for obtaining the transition strength $B(E2; 2^+_1 \to 0^+_\beta)$ from the 2^+_1 state to the 0^+_β state, while the factor is unity for obtaining the transition strength $B(E2; 0^+_{\mathrm{gs}} \to 2^+_\beta)$ from the ground state to the 2^+_β state built on the excited $K^\pi = 0^+$ state. Here, 2^+_1 denotes the 2^+ member of the ground-state rotational band, while 0^+_β and 2^+_β indicate the rotational band members associated with the $K^\pi = 0^+$ intrinsic excitations.

4.3   Results and Discussion

4.3.1   Some features of calculated results

The single-particle shell structure around the Fermi surface for neutrons in ^{36,38,40}Mg exhibits an interesting feature. Figure 4.1 shows the single-particle energy diagram for the WS potential as a function of deformation parameter β_2. As β_2 increases, a level crossing between the up-sloping [303]7/2 level and the down-sloping [310]1/2 level takes place, and a deformed shell gap is formed at $N = 28$ around $\beta_2 = 0.3$. This deformed closed shell approximately corresponds to the $(f_{7/2})^{-2}(p_{3/2})^2$ configuration in the spherical shell model representation. The highest occupied level in this deformed closed shell is situated very near to the continuum threshold, so that there is no bound level above it. However, neutron particle-hole excitations may take place into resonance levels like [303]7/2, [301]1/2 [312]3/2 lying just above the continuum threshold. In fact, as we shall discuss below, these resonance levels participate in the pairing correlations and play an important role in generating low-frequency collective modes of excitation in ^{36,38,40}Mg. Thus, ^{40}Mg and its neighboring isotopes provide an interesting situation to investigate collective modes unique in unstable nuclei near the neutron drip line. The resonance character of these levels just above the continuum threshold is confirmed by means of the eigenphase-sum method (see Appendix).

Results of the deformed WS plus HFB calculation for the ground state properties of ^{36,38,40}Mg are listed in Table 4.1. Calculated values of the average pairing gap for neutrons are rather close to the value estimated in terms of the conventional systematics [23] $\Delta_{\mathrm{syst}} \simeq 12/\sqrt{A} \simeq 1.9$MeV. On the other hand, the average pairing gaps for protons vanish. As shown in this table, the neutron root-mean-square radius increases as approaching the neutron drip line, while the proton root-mean-square radius remains almost constant. This means that the neutron skin structure emerges in these nuclei; the difference between the neutron and proton radii in ^{40}Mg is about 0.9 fm.

Results of the QRPA calculation for quadrupole transition strengths are displayed in Fig. 4.2. We see prominent peaks at about 3 MeV for both the $K^\pi = 0^+$ and 2^+ excitations. Their strengths are much larger than the single-particle strengths indicating collective character of these excitations. The strength of the lowest $K^\pi = 2^+$ excitation gradually increases as approaching the neutron drip line, while the lowest $K^\pi = 0^+$ excitations in ^{36}Mg and ^{40}Mg seem to be split into two peaks in the case of ^{38}Mg. In the following, we make an extensive analysis on microscopic structure of these low-frequency collective excitations.

4.3.2 $K^\pi = 0^+$ modes

We first discuss the $K^\pi = 0^+$ excitation modes in ^{40}Mg. The QRPA transition strengths are compared with unperturbed two-quasiparticle strengths in Fig. 4.3 . A prominent peak is seen at about 3.2 MeV in the QRPA strength distribution; it possesses an enhanced strength of about 22 Weisskopf unit (1 W.u. $\simeq 8.1$ fm^4 for ^{40}Mg). From the QRPA amplitudes listed in Table 4.2, it is clear that this collective mode is generated by coherent superposition of neutron excitations of both particle-hole and particle-particle types. In Fig. 4.3, the QRPA strengths are also compared with the strengths without the dynamical pairing effects, i.e., the result of QRPA calculation ignoring the residual pairing interactions. One immediately notice that the transition strength to the lowest excited state is drastically reduced when the dynamical pairing effects are ignored.
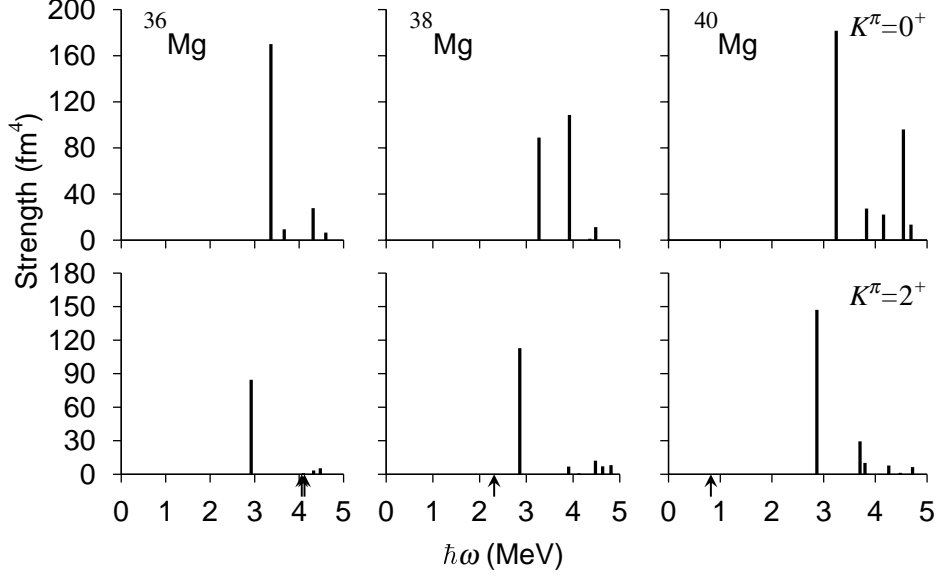
Figure 4.2: Isoscalar quadrupole transition strengths $B(Q^{\mathrm{IS}}2)$ for the $K = 0^+$ excitations (upper panel) and the $K = 2^+$ excitations (lower panel) built on the prolately deformed ground states of ^{36,38,40}Mg. The arrows beside the abscissa axes indicate the neutron threshold energies, $E_{\mathrm{th}} = 4.06$ MeV (one-quasiparticle (1qp) continuum; $|\lambda| + \min E_\alpha$), 4.12 MeV (two quasiparticle (2qp) continuum; $2|\lambda|$) for ^{36}Mg, 2.31 MeV (2qp continuum) for ^{38}Mg and 0.82 MeV (2qp continuum) for ^{40}Mg. The QRPA calculations are made by using the surface-type pairing interaction and $\beta_2 = 0.28$ for both protons and neutrons.

Table 4.2: QRPA amplitudes of the $K^\pi = 0^+$ mode at 3.2 MeV in ^{40}Mg. This mode has $B(E2) = 3.4$ e^2fm^4, $B(Q^\nu 2)=136$ fm^4, and $B(Q^{\mathrm{IS}}2) = 182$ fm^4. The single-particle levels are labeled with the asymptotic quantum numbers $[Nn_3\Lambda]\Omega$ of the dominant components of the wave functions. Only components with $|f_{\alpha\beta}|^2 - |g_{\alpha\beta}|^2 > 0.01$ are listed.

	α	β	$E_\alpha + E_\beta$ (MeV)	$|f_{\alpha\beta}|^2 - |g_{\alpha\beta}|^2$	$Q_{20,\alpha\beta}^{(\mathrm{uv})}$ (fm^2)	$M_{20,\alpha\beta}^{(\mathrm{uv})}$ (fm^2)
(a)	$\nu[310]1/2$	$\nu[310]1/2$	3.54	0.438	6.36	4.27
(b)	$\nu[301]1/2$	$\nu[310]1/2$	3.93	0.067	-2.57	0.925
(c)	$\nu[312]3/2$	$\nu[312]3/2$	3.99	0.280	-2.03	1.08
(d)	$\nu[301]1/2$	$\nu[301]1/2$	4.32	0.027	0.992	-0.176
(e)	$\nu[303]7/2$	$\nu[303]7/2$	5.76	0.077	-3.39	0.966
(f)	$\nu[321]3/2$	$\nu[321]3/2$	7.15	0.011	3.23	0.396
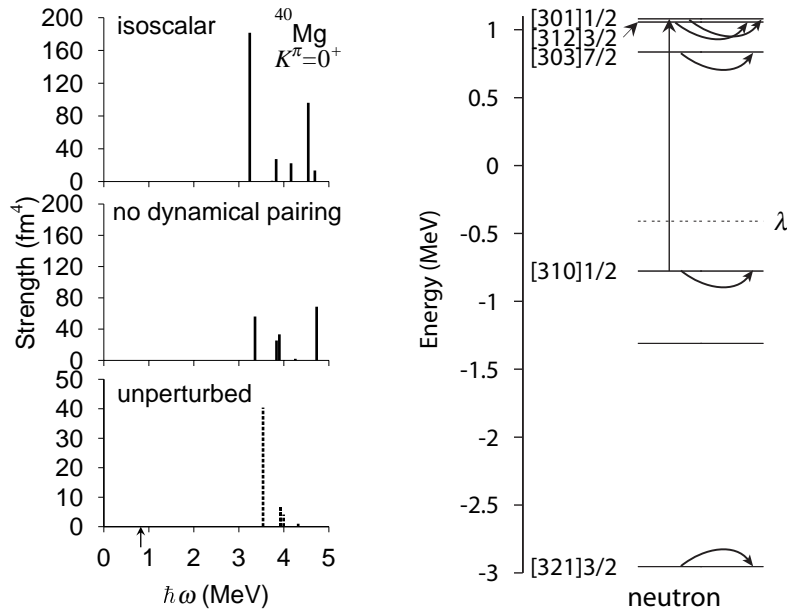
Figure 4.3: *Left*: Isoscalar quadrupole transition strengths $B(Q^{\mathrm{IS}}2)$ for the $K^{\pi} = 0^{+}$ excitations in ^{40}Mg. Results of the QRPA calculation with and without including the dynamical pairing effects are plotted in the upper and middle panels, respectively, while unperturbed two-quasiparticle strengths are shown in the lower panel. Notice that different scale is used for the unperturbed strengths. The arrow beside the abscissa axis indicates the neutron threshold energy $2|\lambda| = 0.82$ MeV. *Right*: Two-quasiparticle excitations generating the lowest $K^{\pi} = 0^{+}$ mode at 3.2 MeV. The single-particle levels for the deformed WS potential are labeled with the asymptotic quantum numbers $[Nn_3\Lambda]\Omega$. The chemical potential λ is indicated by the dashed line.
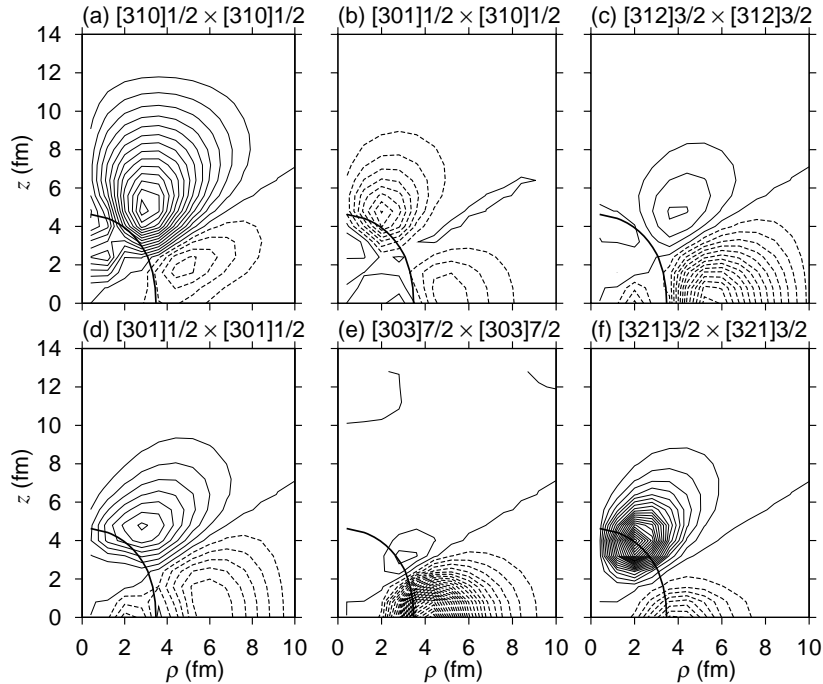
Figure 4.4: Spatial distribution functions $Q_{20,\alpha\beta}^{(uv)}(\rho, z)$ for some two-quasiparticle excitations generating the lowest $K^{\pi} = 0^+$ mode in ^{40}Mg. The contour lines are plotted at intervals of 0.002. The solid and dashed lines represent positive and negative quantities, respectively. The thick solid line indicates the neutron half-density radius; $\varrho_{\nu}(0)/2 \sim 0.045$fm^{-3}.

Let us discuss the reason why the lowest $K^{\pi} = 0^+$ mode acquires eminently large transition strength. There are two points to understand this mechanism: 1) existence of unperturbed two-quasiparticle configurations possessing large transition strengths, and 2) effect of residual interactions producing coherence among various two-quasiparticle configurations.

To examine the first point, we plot in Fig. 4.4 spatial distributions of the quadrupole transition amplitudes for major two-quasiparticle configurations generating the lowest $K^{\pi} = 0^+$ mode. We see that they are notably extended beyond the half-density radius. This is a situation similar to that encountered in Ref. [78], where a neutron excitation from a loosely bound state to a resonance state brings about very large transition strength. We also note that the transition strength associated with the $\nu[301]1/2 \otimes \nu[310]1/2$ configuration is much enhanced although it should be hindered if the selection rule $\Delta N = 2$ for the asymptotic quantum numbers [126] is applied. This selection rule is broken for matrix elements associated with loosely bound states, because their radial wave functions are spatially extended and quite different from those of the the harmonic oscillator potential.

Concerning the second point, we have found that the dynamical pairing plays an especially important role. This point is easily seen by comparing the QRPA calculations with and without the dynamical pairing effects, which are shown in Fig. 4.3. It is apparent that the prominent lowest peak disappears when the dynamical paring effects are ignored. We can say that the coherent superpositions among the particle-hole, particle-particle and hole-hole excitations are indispensable for the emergence of this mode. The importance of the coupling between the (particle-hole type) β vibration and the (particle-particle and hole-hole type)
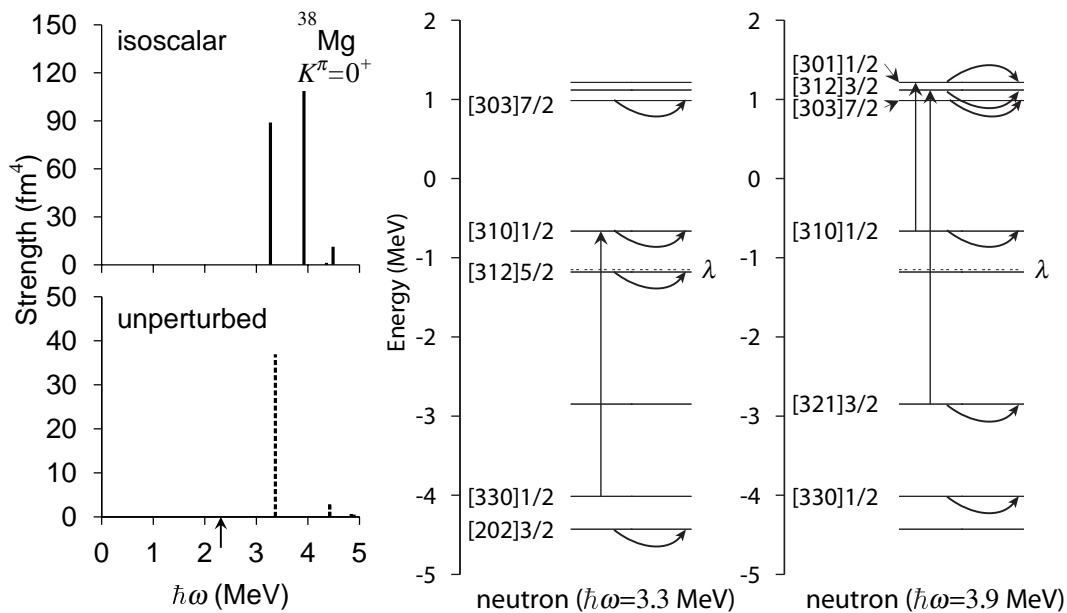
Figure 4.5: *Left*: Isoscalar quadrupole transition strengths $B(Q^{\mathrm{IS}}2)$ for the $K^{\pi} = 0^{+}$ excitations in ^{38}Mg are plotted in the upper panel, while unperturbed two-quasiparticle strengths are shown in the lower panel. The arrow beside the abscissa axis indicates the neutron threshold energy $2|\lambda| = 2.31$ MeV. *Right*: Two-quasiparticle excitations generating the low-lying $K^{\pi} = 0^{+}$ modes at 3.3 MeV and 3.9 MeV.

pairing vibration has been well known in stable deformed nuclei [126]. A new feature of the $K^{\pi} = 0^{+}$ mode in neutron drip-line nuclei under discussion is that this coupling takes place among two-quasiparticle configurations that are loosely bound or resonances, so that their transition strengths are strikingly enhanced. In addition, as seen in Fig. 4.4, their spatial structures (peak positions and distribution) are rather similar with each other. This is a favorable situation to generate coherence among them [76]. The importance of dynamical pairing effects in generating soft dipole excitations has been demonstrated by Matsuo et al. [77] for spherical unstable nuclei near the neutron drip line.

Next we discuss the $K^{\pi} = 0^{+}$ excitations in ^{38}Mg and ^{36}Mg. The quadrupole transition strengths calculated for ^{38}Mg are presented in Fig. 4.5, which exhibits two peaks below 4 MeV. The major two-quasiparticle excitations generating these peaks are illustrated in the middle and right panels of this figure. Their QRPA amplitudes are listed in Tables 4.3 and 4.4. From these Tables, it is seen that the peak at 3.3 MeV is mainly generated by the particle-particle type $\nu[310]1/2 \otimes \nu[310]1/2$ and $\nu[312]5/2 \otimes \nu[312]5/2$ excitations, while the peak at 3.9 MeV is mainly associated with the particle-hole type $\nu[301]1/2 \otimes \nu[310]1/2$ and $\nu[312]3/2 \otimes \nu[321]3/2$ excitations.

The quadrupole transition strengths calculated for ^{36}Mg are displayed in Fig. 4.6. We notice a prominent peak at about 3.4 MeV below the one-neutron threshold energy (4.1 MeV), which possesses a strongly enhanced transition strength of about 24 W.u. (1 W.u. $\simeq 7.1$ fm^{4} for ^{36}Mg). This peak exhibits a clear character of collective vibration: As seen from Table 4.5, this collective mode is created by coherent neutron excitations. Its main components are the particle-hole type $\nu[310]1/2 \otimes \nu[330]1/2$ and $\nu[301]1/2 \otimes \nu[310]1/2$ excitations and the particle-

Table 4.3: QRPA amplitudes of the $K^\pi = 0^+$ mode at 3.3 MeV in ^{38}Mg. This mode has $B(E2) = 1.67 \ e^2$fm^4, $B(Q^\nu 2)$=66.3 fm^4, $B(Q^{\text{IS}}2)$=89.0 fm^4, and $\sum |g_{\alpha\beta}|^2 = 2.32 \times 10^{-2}$. Only components with $|f_{\alpha\beta}|^2 - |g_{\alpha\beta}|^2 > 0.01$ are listed.

	α	β	$E_\alpha + E_\beta$ (MeV)	$|f_{\alpha\beta}|^2 - |g_{\alpha\beta}|^2$	$Q^{(\text{uv})}_{20,\alpha\beta}$ (fm^2)	$M^{(\text{uv})}_{20,\alpha\beta}$ (fm^2)
(a)	$\nu[310]1/2$	$\nu[310]1/2$	3.37	0.673	6.08	5.25
(b)	$\nu[312]5/2$	$\nu[312]5/2$	4.84	0.146	0.821	-0.293
(c)	$\nu[310]1/2$	$\nu[330]1/2$	5.35	0.023	-3.59	0.769
(d)	$\nu[303]7/2$	$\nu[303]7/2$	6.35	0.066	-2.64	0.614
(e)	$\nu[202]3/2$	$\nu[202]3/2$	7.82	0.021	-1.29	0.149

Table 4.4: QRPA amplitudes of the $K^\pi = 0^+$ mode at 3.9 MeV in ^{38}Mg. This mode has $B(E2) = 4.72 \ e^2$fm^4, $B(Q^\nu 2)$=68.1 fm^4, $B(Q^{\text{IS}}2)$=109 fm^4, and $\sum |g_{\alpha\beta}|^2 = 2.71 \times 10^{-2}$. Only components with $|f_{\alpha\beta}|^2 - |g_{\alpha\beta}|^2 > 0.01$ are listed.

	α	β	$E_\alpha + E_\beta$ (MeV)	$|f_{\alpha\beta}|^2 - |g_{\alpha\beta}|^2$	$Q^{(\text{uv})}_{20,\alpha\beta}$ (fm^2)	$M^{(\text{uv})}_{20,\alpha\beta}$ (fm^2)
(a)	$\nu[310]1/2$	$\nu[310]1/2$	3.37	0.037	6.08	1.34
(b)	$\nu[301]1/2$	$\nu[310]1/2$	4.42	0.258	1.67	-1.20
(c)	$\nu[312]3/2$	$\nu[312]3/2$	4.90	0.048	0.716	0.169
(d)	$\nu[312]3/2$	$\nu[321]3/2$	5.47	0.250	-3.04	-2.20
(e)	$\nu[301]1/2$	$\nu[301]1/2$	5.47	0.018	0.802	0.131
(f)	$\nu[321]3/2$	$\nu[321]3/2$	6.04	0.058	1.66	-0.411
(g)	$\nu[303]7/2$	$\nu[303]7/2$	6.35	0.084	-2.64	-0.853
(h)	$\nu[330]1/2$	$\nu[330]1/2$	7.33	0.099	4.57	-1.48

Table 4.5: QRPA amplitudes of the $K^\pi = 0^+$ mode at 3.4 MeV in ^{36}Mg. This mode has $B(E2) = 8.1 \ e^2$fm^4, $B(Q^\nu 2)$=104 fm^4, $B(Q^{\text{IS}}2)$=170 fm^4, and $\sum |g_{\alpha\beta}|^2 = 3.91 \times 10^{-2}$. Only components with $|f_{\alpha\beta}|^2 - |g_{\alpha\beta}|^2 > 0.01$ are listed.

	α	β	$E_\alpha + E_\beta$ (MeV)	$|f_{\alpha\beta}|^2 - |g_{\alpha\beta}|^2$	$Q^{(\text{uv})}_{20,\alpha\beta}$ (fm^2)	$M^{(\text{uv})}_{20,\alpha\beta}$ (fm^2)
(a)	$\nu[310]1/2$	$\nu[310]1/2$	4.06	0.071	5.80	-1.58
(b)	$\nu[321]3/2$	$\nu[321]3/2$	4.48	0.098	4.60	-1.61
(c)	$\nu[312]5/2$	$\nu[312]5/2$	4.87	0.227	0.714	0.347
(d)	$\nu[310]1/2$	$\nu[330]1/2$	4.91	0.211	-3.08	-2.11
(e)	$\nu[301]1/2$	$\nu[310]1/2$	5.69	0.033	2.02	-0.511
(f)	$\nu[330]1/2$	$\nu[330]1/2$	5.76	0.116	3.98	-1.50
(g)	$\nu[202]3/2$	$\nu[202]3/2$	5.79	0.046	-1.47	-0.271
(h)	$\nu[303]7/2$	$\nu[303]7/2$	7.67	0.049	-1.82	-0.411
(i)	$\pi[211]1/2$	$\pi[220]1/2$	6.44	0.054	-0.251	-0.599
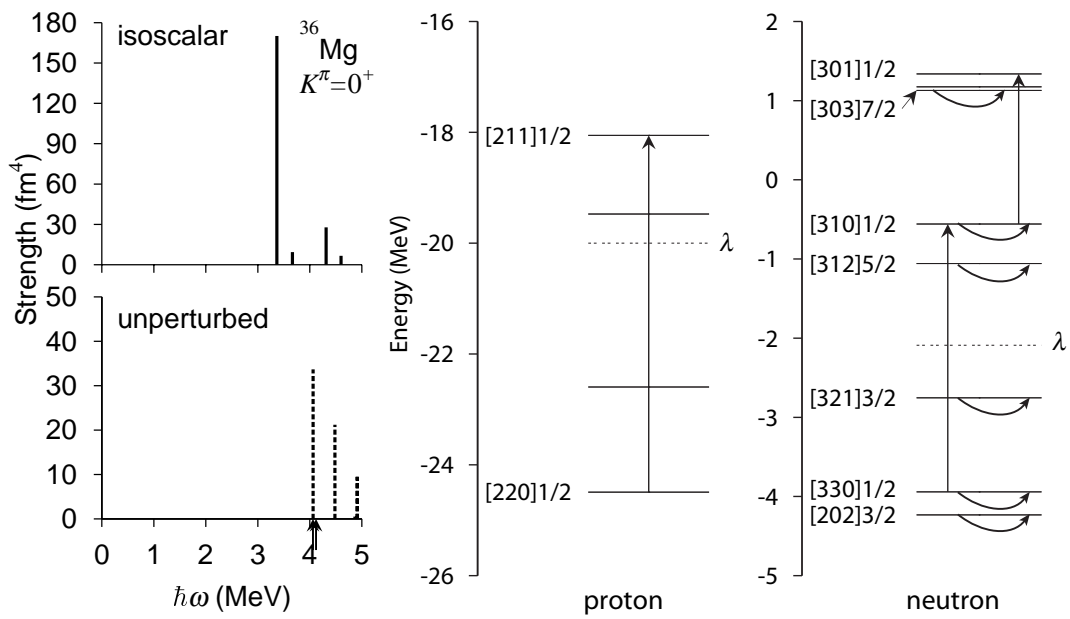
Figure 4.6: *Left*: Isoscalar quadrupole transition strengths $B(Q^{\text{IS}}2)$ for the $K^{\pi} = 0^+$ excitations in ^{36}Mg are plotted in the upper panel, while unperturbed two-quasiparticle strengths are shown in the lower panel. The arrows beside the abscissa axis indicate the neutron threshold energy $E_{\text{th}} = 4.06$ MeV (1qp continuum) and 4.12 MeV (2qp continuum). *Right*: Two-quasiparticle excitations generating the lowest $K^{\pi} = 0^+$ mode at 3.4 MeV in ^{36}Mg.
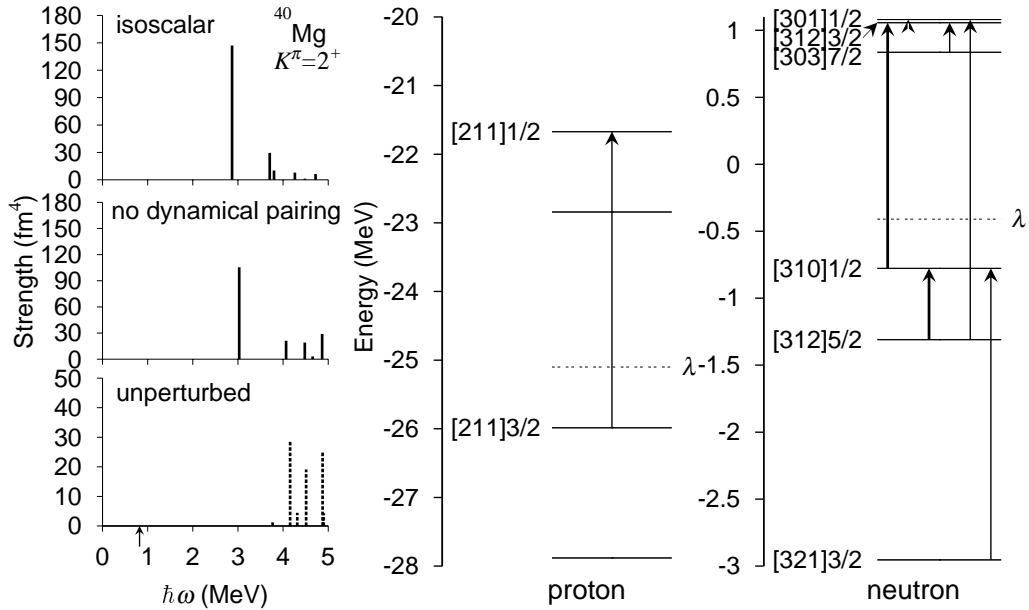
Figure 4.7: *Left*: Isoscalar quadrupole transition strengths $B(Q^{\mathrm{IS}}2)$ for the $K^\pi = 2^+$ excitations in ^{40}Mg. Results of the QRPA calculation with and without including the dynamical pairing effects are plotted in the upper and middle panels, respectively, while unperturbed two-quasiparticle strengths are shown in the lower panel. Notice that different scale is used for the unperturbed strengths. The arrow beside the abscissa axis indicates the neutron threshold energy $2|\lambda| = 0.82$ MeV. *Right*: Two-quasiparticle excitations generating the lowest $K^\pi = 2^+$ mode at 2.9 MeV. Two-quasiparticle excitations satisfying the asymptotic selection rule for the γ vibration ($\Delta N = 0, \Delta n_3 = 0, \Delta\Lambda = 2$) are drawn by thick arrows.

particle type $\nu[312]5/2 \otimes \nu[312]5/2$ and $\nu[321]3/2 \otimes \nu[321]3/2$ excitations. These particle-particle type and particle-hole type excitations are coherently superposed to generate this collective neutron mode.

4.3.3 $K^\pi = 2^+$ modes

Let us now turn to the $K^\pi = 2^+$ excitation modes. The quadrupole transition strengths calculated for ^{40}Mg are displayed in Fig. 4.7. We notice a prominent peak at about 2.8 MeV which possesses strongly enhanced transition strength of about 19 W.u. The QRPA amplitudes of this excitation are listed in Table 4.6. From this Table, we see that this peak represents a collective excitation consisting of a coherent superposition of the proton particle-hole excitation from the [211]3/2 level to the [211]1/2 level and a number of neutron two-quasiparticle excitations. Similarly to the $K^\pi = 0^+$ excitation modes discussed in the previous subsection, the asymptotic selection rule ($\Delta N = 0, \Delta n_3 = 0, \Delta\Lambda = 2$) well known for the γ vibrations is violated for the neutron excitations, because these levels are loosely bound or resonances and their quasiparticle wave functions are significantly extended outside of the nucleus. On the other hand, proton particle-hole excitations satisfy the selection rule because they are deeply bound. We also show in Fig. 4.7 the result of QRPA calculation where the residual pairing interaction is turned off. Comparing with the full QRPA result,

Table 4.6: QRPA amplitudes of the $K^\pi = 2^+$ mode at 2.9 MeV in ^{40}Mg. This mode has $B(E2) = 11.7\ e^2\text{fm}^4$, $B(Q^\nu 2)$=75.7 fm^4, $B(Q^{\text{IS}}2)$=147 fm^4, and $\sum |g_{\alpha\beta}|^2 = 6.73\times10^{-2}$. Only components with $|f_{\alpha\beta}|^2 - |g_{\alpha\beta}|^2 > 0.01$ are listed. The label $\nu 1/2^-$ denotes a discretized non-resonant continuum state.

	α	β	$E_\alpha + E_\beta$ (MeV)	$|f_{\alpha\beta}|^2 - |g_{\alpha\beta}|^2$	$Q^{(\text{uv})}_{22,\alpha\beta}$ (fm^2)	$M^{(\text{uv})}_{22,\alpha\beta}$ (fm^2)
(a)	$\nu[312]3/2$	$\nu[310]1/2$	3.77	0.013	1.22	-0.145
(b)	$\nu[301]1/2$	$\nu[312]3/2$	4.16	0.098	-5.37	-1.75
(c)	$\nu[310]1/2$	$\nu[312]5/2$	4.51	0.085	-4.37	-1.34
(d)	$\nu[312]3/2$	$\nu[303]7/2$	4.88	0.011	-5.03	-0.454
(e)	$\nu[301]1/2$	$\nu[312]5/2$	4.90	0.016	-2.07	-0.296
(f)	$\nu[310]1/2$	$\nu[321]3/2$	5.34	0.047	-2.67	-0.663
(g)	$\nu 1/2^-$	$\nu[312]5/2$	6.96	0.015	1.93	-0.298
(h)	$\nu 1/2^-$	$\nu[321]3/2$	7.28	0.018	1.46	-0.265
(i)	$\pi[211]1/2$	$\pi[211]3/2$	4.32	0.596	-2.11	-2.02

we see that the transition strength is reduced about 30%. Thus, the dynamical pairing effect is important, though its effect is weaker than for the $K^\pi = 0^+$ mode. This is because the $K^\pi = 2^+$ mode consists of both proton and neutron excitations and the pairing is effective only for neutrons.

The quadrupole transition strengths calculated for ^{38}Mg and ^{36}Mg are displayed in Figs. 4.8 and 4.9, respectively. For each case, we see a prominent peak at about 2.9 MeV which possesses strongly enhanced transition strength (about 15 W.u. and 12 W.u. for ^{38}Mg and ^{36}Mg, respectively). The QRPA amplitudes of these modes are listed in Tables 4.7 and 4.8. These modes possess essentially the same microscopic structure as the collective $K^\pi = 2^+$ mode in ^{40}Mg discussed above. They also correspond to the γ vibrational mode obtained in the previous QRPA calculation [70] for ^{38}Mg. In our calculation, however, the collectivity of these modes remains almost the same even if we use different deformations for protons and neutrons, differently from Ref. [70].

4.3.4 Dependence on pairing interaction

In this subsection, we examine sensitivity of the low-frequency $K^\pi = 0^+$ and 2^+ modes on the density dependence of the pairing interaction. For this purpose, we repeated the HFB and QRPA calculations using pairing interactions with density dependence different from the surface type ($\eta = 1.0$ in Eq. (4.2)); i.e., the mixed type ($\eta = 0.5$) and the volume type ($\eta = 0.0$). Since the result for the mixed-type pairing is intermediate between those for the surface-type and the volume-type, we show in Fig. 4.10 only the quadrupole transition strengths obtained using the volume-type pairing interaction. In this calculation, the pairing interaction strength $V_0 = -215.0$ MeV·fm^3 is chosen to yield approximately the same average pairing gaps as those for the surface type. Comparing with the results obtained using the surface-type pairing, shown in Fig. 4.2, we see that the transition strengths for the $K^\pi = 0^+$ collective modes are appreciably reduced, while those for the $K^\pi = 2^+$ collective modes are almost the same. We have checked that, although the strengths are reduced, the microscopic
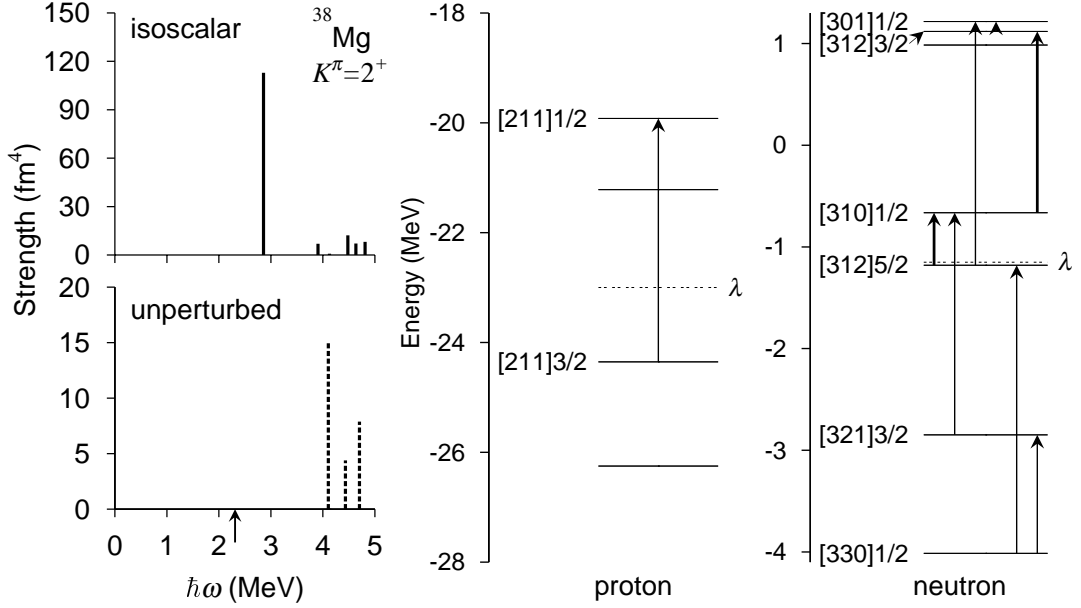
Figure 4.8: *Left*: Isoscalar quadrupole transition strengths $B(Q^{IS}2)$ for the $K^\pi = 2^+$ excitations in ^{38}Mg are plotted in the upper panel, while unperturbed two-quasiparticle strengths are shown in the lower panel. The arrow beside the abscissa axis indicates the neutron threshold energy $2|\lambda| = 2.31$ MeV. *Right*: Two-quasiparticle excitations generating the lowest $K^\pi = 2^+$ mode at 2.9 MeV in ^{38}Mg.

Table 4.7: QRPA amplitudes of the $K^\pi = 2^+$ mode at 2.9 MeV in ^{38}Mg. This mode has $B(E2) = 11.2\ e^2\text{fm}^4$, $B(Q^\nu 2) = 53.0\ \text{fm}^4$, $B(Q^{IS}2) = 113\ \text{fm}^4$, and $\sum |g_{\alpha\beta}|^2 = 6.95 \times 10^{-2}$. Only components with $|f_{\alpha\beta}|^2 - |g_{\alpha\beta}|^2 > 0.01$ are listed.

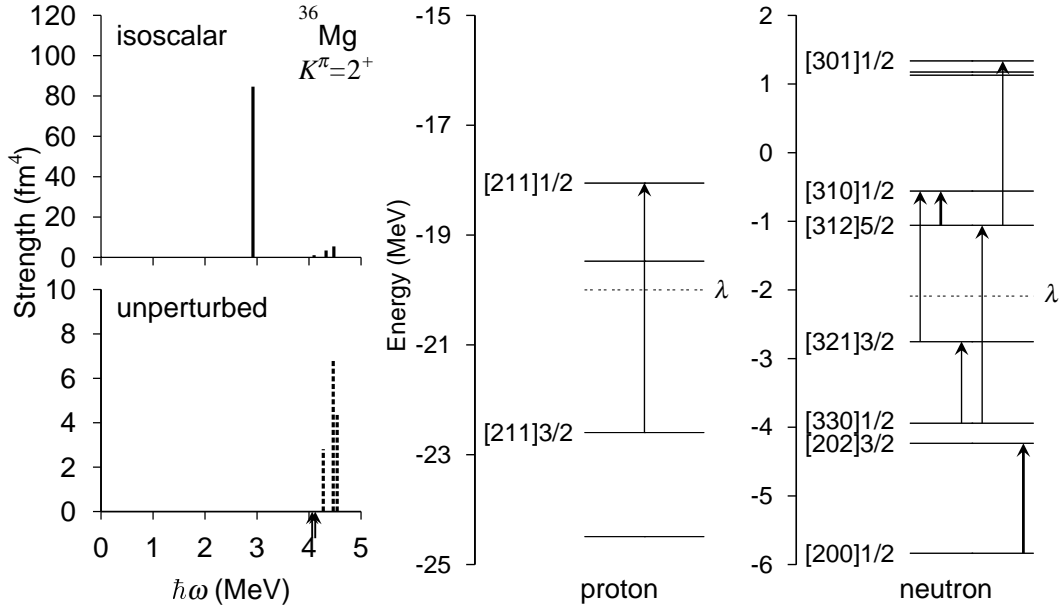|	α	β	$E_\alpha + E_\beta$ (MeV)	$|f_{\alpha\beta}|^2 - |g_{\alpha\beta}|^2$	$Q^{(uv)}_{22,\alpha\beta}$ (fm^2)	$M^{(uv)}_{22,\alpha\beta}$ (fm^2)
(a)	$\nu[310]1/2$	$\nu[312]5/2$	4.10	0.146	-3.89	-1.54
(b)	$\nu[312]3/2$	$\nu[310]1/2$	4.13	0.016	-0.221	-0.032
(c)	$\nu[310]1/2$	$\nu[321]3/2$	4.70	0.108	2.81	-1.05
(d)	$\nu[301]1/2$	$\nu[312]5/2$	5.15	0.010	1.81	-0.204
(e)	$\nu[301]1/2$	$\nu[312]3/2$	5.18	0.031	-3.58	-0.690
(f)	$\nu[312]5/2$	$\nu[330]1/2$	6.08	0.017	-1.42	-0.239
(g)	$\nu[321]3/2$	$\nu[330]1/2$	6.68	0.029	1.61	-0.344
(h)	$\pi[211]1/2$	$\pi[211]3/2$	4.43	0.541	-2.09	-1.94

Figure 4.9: *Left*: Isoscalar quadrupole transition strengths $B(Q^{\text{IS}}2)$ for the $K^\pi = 2^+$ excitations in ^{36}Mg are plotted in the upper panel, while unperturbed two-quasiparticle strengths are shown in the lower panel. The arrows beside the abscissa axis indicate the threshold energies 4.06 MeV (1qp continuum) and 4.12 MeV (2qp continuum). *Right*: Two-quasiparticle excitations generating the lowest $K^\pi = 2^+$ mode at 2.9 MeV.

Table 4.8: QRPA amplitudes of the $K^\pi = 2^+$ mode at 2.9 MeV in ^{36}Mg. This mode has $B(E2) = 10.6\ e^2\text{fm}^4$, $B(Q^\nu 2)=35.3$ fm^4, $B(Q^{\text{IS}}2)=84.6$ fm^4, and $\sum |g_{\alpha\beta}|^2 = 7.06 \times 10^{-2}$. Only components with $|f_{\alpha\beta}|^2 - |g_{\alpha\beta}|^2 > 0.01$ are listed. The columns (f) and (f′) are assigned the same configuration, because we obtain two discretized continuum states associated with the $\nu[200]1/2$ level for which $E > |\lambda|$.

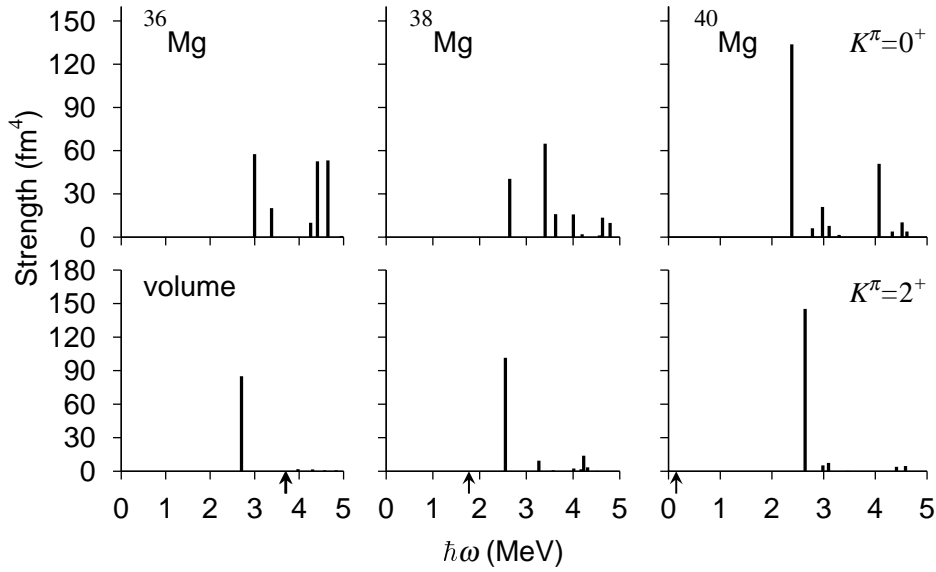|	α	β	$E_\alpha + E_\beta$ (MeV)	$|f_{\alpha\beta}|^2 - |g_{\alpha\beta}|^2$	$Q^{(\text{uv})}_{22,\alpha\beta}$ (fm^2)	$M^{(\text{uv})}_{22,\alpha\beta}$ (fm^2)
(a)	$\nu[310]1/2$	$\nu[321]3/2$	4.27	0.087	1.68	0.552
(b)	$\nu[310]1/2$	$\nu[312]5/2$	4.46	0.045	-2.62	0.551
(c)	$\nu[321]3/2$	$\nu[330]1/2$	5.12	0.165	2.51	1.20
(d)	$\nu[312]5/2$	$\nu[330]1/2$	5.31	0.034	-1.36	0.305
(e)	$\nu[301]1/2$	$\nu[312]5/2$	6.09	0.011	1.66	0.202
(f)	$\nu[202]3/2$	$\nu[200]1/2$	6.90	0.010	-2.633	0.270
(f′)	$\nu[202]3/2$	$\nu[200]1/2$	7.23	0.013	0.981	0.136
(g)	$\pi[211]1/2$	$\pi[211]3/2$	4.54	0.547	-2.09	1.87

Figure 4.10: Isoscalar quadrupole transition strengths $B(Q^{\mathrm{IS}}2)$ for the $K = 0^+$ excitations (upper panel) and the $K = 2^+$ excitations (lower panel) built on the prolately deformed ground states of ^{36,38,40}Mg. The QRPA calculations are made in the same way as in Fig. 4.2, except that the volume-type pairing interaction is used here. The arrows indicate the neutron threshold energies; 3.69 MeV (1qp continuum) and 3.71 MeV (2qp continuum) for ^{36}Mg, 1.77 MeV (2qp continuum) for ^{38}Mg, and 0.15 MeV (2qp continuum) for ^{40}Mg.

structure of these collective modes are basically the same as discussed above on the basis of the results of calculation using the surface-type pairing interaction. Thus, we can say that the quadrupole transition strengths for the low-frequency $K^\pi = 0^+$ collective modes are especially sensitive to the density dependence of the pairing interaction. Such a sensitivity has been stressed also in Refs. [47, 50, 77] in their continuum QRPA calculations for $E1$ and $E2$ strength functions in neutron-rich spherical nuclei.

4.4 Summary

We have carried out the QRPA calculations on the basis of the deformed WS plus HFB mean field in the coordinate representation, and obtained the low-frequency $K^\pi = 0^+$ and 2^+ collective modes in deformed ^{36,38,40}Mg close to the neutron drip line. It has been shown that these modes possess very strong isoscalar quadrupole transition strengths. One of the reasons of this enhancement is that the quasiparticle wave functions participating in these collective excitations have spatially extended structure. The other reason is that the residual pairing interactions, in addition to the particle-hole type residual interactions, enhance the collectivity of these modes. The result of the present calculation suggests that the low-frequency $K^\pi = 0^+$ collective mode is a particularly sensitive indicator of the nature of pairing correlations in nuclei close to the neutron drip line.

This calculation should be regarded as an exploratory work toward understanding low-frequency collective modes of excitation in unstable nuclei close to the neutron drip line. It is certainly desirable to improve the treatment of the continuum at least in the following points.
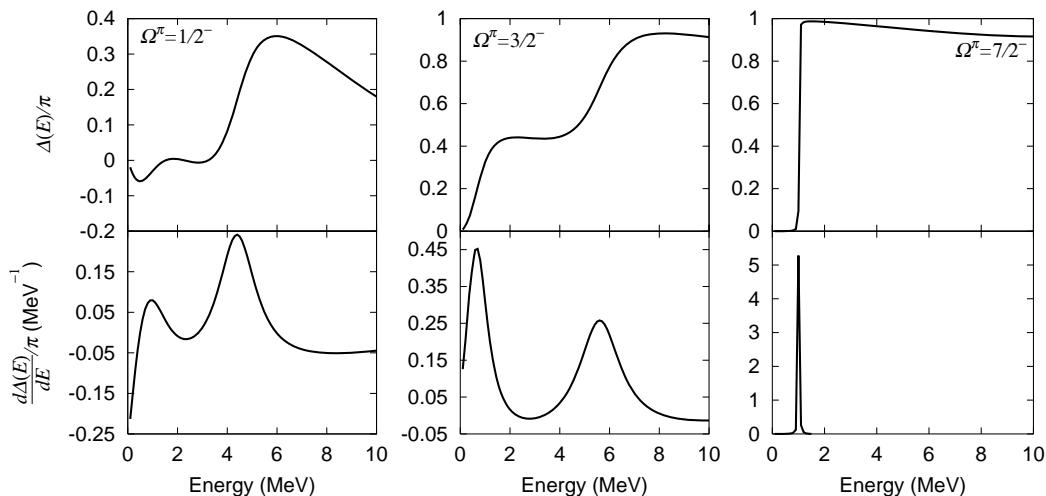
Figure 4.11: The eigenphase sum (upper panel) and its derivative (lower panel) for the $\Omega^\pi = 1/2^-, 3/2^-$ and $7/2^-$ states in ^{40}Mg are plotted as functions of energy.

First, one may try to use a smaller mesh size and a larger box by implementing an adaptive coordinate method [63]. Second, one may try to take into account the width of resonance by employing Gamow states as basis of the QRPA calculation [129, 130, 131, 132]. The result of the present work indicates that calculations using such an improved framework will be very interesting and worthwhile. We plan to attack this subject in future.

Appendix: Eigenphase sum for single-particle resonance states

We examine properties of three single-particle states in the continuum, which play a key role in generating the low-lying excitations modes in ^{36,38,40}Mg. The resonance energy and width in a deformed potential can be estimated using the eigenphase sum $\Delta(E)$. It is defined in terms of the eigenvalues of the scattering matrix (S-matrix) as

$$(U^\dagger SU)_{aa'} = e^{2i\delta_a(E)}\delta_{aa'}, \quad \Delta(E) = \sum_a \delta_a(E). \tag{4.15}$$

We evaluate the eigenphase sum for three states following the procedure of Ref. [114]. The resonance energy and width are identified with the peak energy of $\frac{1}{\pi}d\Delta(E)/dE$ and its FWHM, respectively [127, 128]. This evaluation is in good correspondence with another definition of the resonance; the Gamow state in a deformed potential [82] which represents the pole of the S−matrix in the complex momentum plane, as shown in chapter 7.

The result of this calculation, presented in Fig.4.11, indicates that the [301]1/2 and [312]3/2 states can be regarded as resonances with rather large widths; their energies are $0.53 − i0.46$ (MeV) and $0.42 − i0.33$ (MeV), respectively. On the other hand, the [303]7/2 state is evaluated as a narrow resonance with energy $0.44 − i0.0005$ (MeV). Obviously, the small width is due to its high centrifugal barrier.

Chapter 5

Low-lying excitation modes in neutron-rich ^{34}Mg region

5.1   introduction

Presently, the breaking of $N=20$ spherical magic number and striking enhancements of $B(E2; 0_1^+ \rightarrow 2_1^+)$ in ^{32}Mg and ^{34}Mg are under lively discussions in connection with onset of the quadrupole deformation, the pairing correlation and the continuum coupling effects. In order to get clear understanding of the nature of quadrupole deformation and pairing correlations in these nuclei, it is strongly desired to explore, both experimentally and theoretically, excitation spectra of these nuclei.

According to the recent experiments at MSU [133] by intermediate Coulomb excitations and at RIKEN [134] by proton inelastic scattering reactions at intermediate energy, the excitation energy of the 2_1^+ state in ^{34}Mg are 659 keV and 685 keV, respectively. Furthermore, the RIKEN experiment by fragmentation reactions reported the excitation energy 660 keV and 2120 keV for the 2_1^+ and 4_1^+ states, respectively [135]. In Fig. 5.1, we show the systematics of the excitation energy ratio $E(4^+)/E(2^+)$ as a function of the proton number for the $N = 22$ isotones. The energy ratio of ^{34}Mg is close to 3.3 corresponding to the rotational limit, while that of Si, S and Ar is close to 2 corresponding to the vibrational limit. These experiments
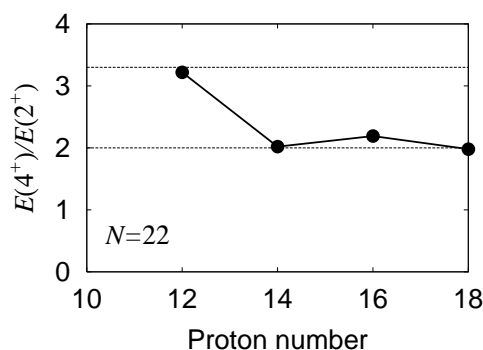

Figure 5.1: Systematics of the $E(4^+)$ to $E(2^+)$ ratio for Mg, Si, S and Ar isotones with $N = 22$. Experimental values are taken from Refs. [135, 136] and ENSDF [137].
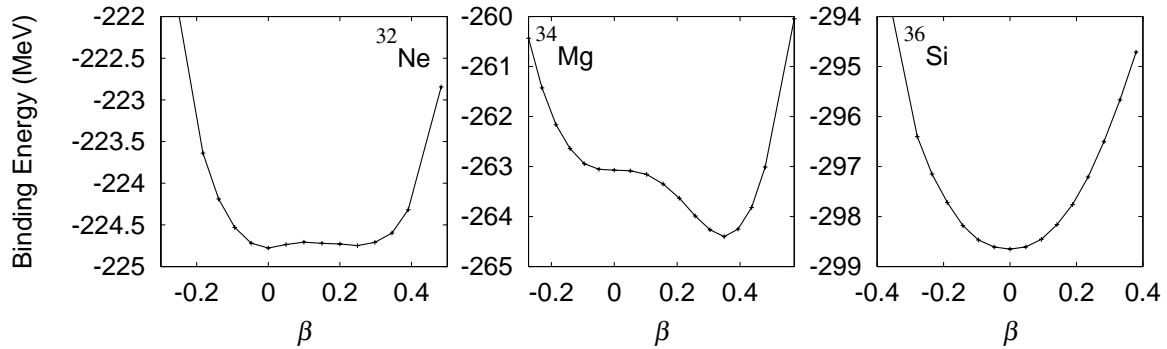
Figure 5.2: Potential energy surfaces for the $N = 22$ isotones, ^{32}Ne, ^{34}Mg and ^{36}Si, plotted as functions of deformation parameter β_2. These are calculated by using the HFBTHO code [138] with the SkM* interaction and the surface-type pairing with $V_0 = -418$ MeV·fm^3, where the particle number projection is not performed.

thus suggest that ^{34}Mg is well deformed.

In Fig. 5.2, we show the potential energy surfaces calculated with HFBTHO code [138] for the $N = 22$ isotones, ^{32}Ne, ^{34}Mg and ^{36}Si, as functions of the quadrupole deformation parameter β_2 using the Skyrme effective interaction (SkM* interaction) for the particle-hole channel and the surface-type delta interaction with $V_0 = -418$ MeV·fm^3 for the particle-particle channel. We have no experimental data on the low-lying excited states in ^{32}Ne. According to this calculation, this nucleus has minima at spherical and prolately deformed states which are very shallow. For ^{34}Mg, we can see a clear minimum at prolately deformed state and it is consistent with the experimental situation. And we obtained a spherical minimum in ^{36}Si, which is also consistent with experiments.

In order to study the effect of nuclear deformation on properties of low-lying excited state in ^{34}Mg, in this chapter, we carry out the QRPA calculation simultaneously taken into account the deformation of the mean field, pairing correlation and coupling to the continuum.

This chapter is organized as follows: In the next section, we explain the method for estimating the moment of inertia microscopically. In §5.3, results of the QRPA calculation for low-frequency quadrupole and octupole vibrations in ^{34}Mg are presented, and the result for the low-lying $K^\pi = 0^+$ mode in ^{32}Ne is also presented. Summary is given in §5.4.

5.2 Method

In order to investigate properties of low-frequency mode of excitation in deformed neutron-rich nuclei, we perform the deformed QRPA calculation based on the coordinate-space HFB formalism as presented in the previous chapter. The method we use in this chapter is same as in the previous chapter. For the residual interaction in the particle-hole channel, we take into the rearrangement effect (2.105). Furthermore, we estimate moments of inertia using the spurious solution of the RPA equation (2.86)

$$\begin{pmatrix} A & B \\ B^* & A^* \end{pmatrix} \begin{pmatrix} J_x \\ -J_x^* \end{pmatrix} = 0 \tag{5.1a}$$
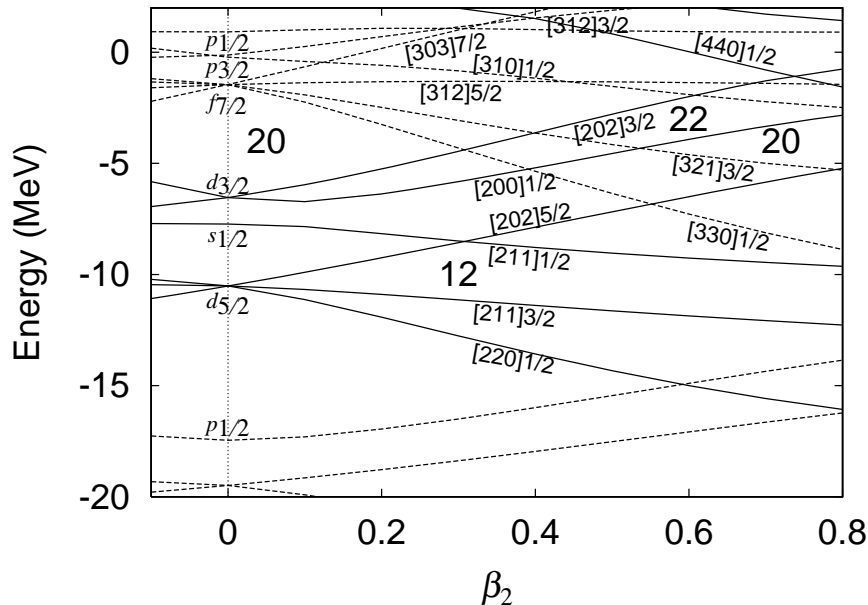
Figure 5.3: Single-particle energies in the deformed WS potential for neutrons, plotted as functions of the quadrupole deformation parameter β_2. Solid and dotted lines denote positive- and negative-parity levels, respectively. Single-particle levels are labeled with the asymptotic quantum numbers $[Nn_3\Lambda]\Omega$.

$$\begin{pmatrix} A & B \\ B^* & A^* \end{pmatrix} \begin{pmatrix} \Theta \\ -\Theta^* \end{pmatrix} = \frac{\hbar}{i} \frac{1}{\mathscr{J}_{\mathrm{TV}}} \begin{pmatrix} J_x \\ J_x^* \end{pmatrix}. \tag{5.1b}$$

When we use the phase convention that the matrix element J_x is pure imaginary, the moment of inertia can be calculated

$$\mathscr{J}_{\mathrm{TV}} = 2\hbar^2 \sum_{\alpha\beta\alpha'\beta'} (J_x)^*_{\alpha\beta}(A-B)^{-1}_{\alpha\beta\alpha'\beta'}(J_x)_{\alpha'\beta'}. \tag{5.2}$$

5.3 Results

In Fig. 5.3, the single-particle energy diagram for the WS potential is shown as a function of deformation parameter β_2. At around $\beta_2 = 0.3$, the deformed shell gap is formed at $N = 22$. Here the up-sloping level $[202]3/2$ and the down-sloping levels $[330]1/2$ and $[321]3/2$ play a role in creating the deformed gap.

Results of the deformed WS plus HFB calculation for the ground state properties of ^{34}Mg and ^{32}Ne are listed in Table 5.1. We determined the parameters for deformation and the pairing strength so that the calculated moment of inertia is consistent with the experimental data. In Fig. 5.4, we show the calculated levels obtained by the present scheme together with the experimental data. As shown in this figure, the 2^+_1 and 4^+_1 states are well reproduced with reasonable parameters, where we assume the rotation-vibration model [139]

$$E(I, K) = \hbar\omega_{\mathrm{RPA}} + \frac{\hbar^2}{2\mathscr{J}_{\mathrm{TV}}}(I(I+1) - K^2), \tag{5.3}$$

Table 5.1: Ground state properties of ^{34}Mg and ^{32}Ne obtained by the deformed WS-HFB calculation with $\beta_2 = 0.4$ and $V_0 = -400$ MeV·fm^3 for the pairing interaction. Chemical potentials, average pairing gaps, and root-mean-square radii for protons and neutrons are listed.

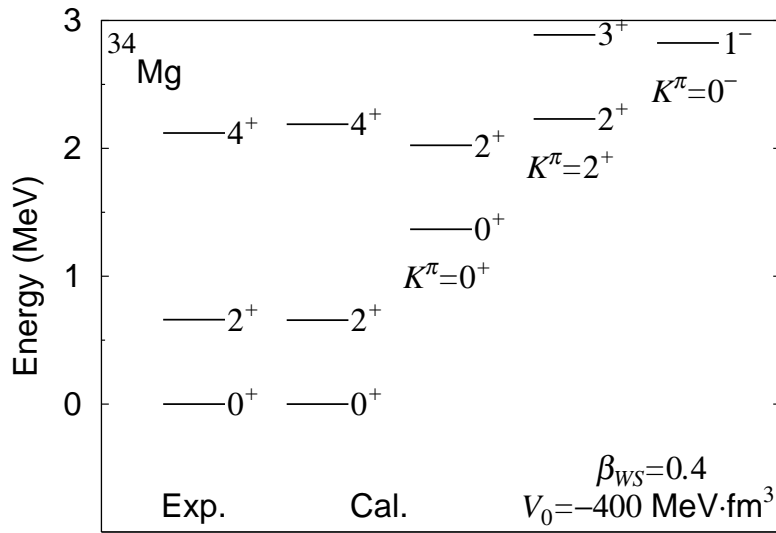| nucleus	λ_π (MeV)	$\langle\Delta_\pi\rangle$ (MeV)	$\sqrt{\langle r^2\rangle_\pi}$ (fm)	$\beta_{2,\pi}$	λ_ν (MeV)	$\langle\Delta_\nu\rangle$ (MeV)	$\sqrt{\langle r^2\rangle_\nu}$ (fm)	$\beta_{2,\nu}$
^{34}Mg	-20.0	0.0	3.08	0.45	-3.20	1.28	3.67	0.35
^{32}Ne	-25.1	0.0	2.92	0.45	-0.636	1.48	3.83	0.33

Figure 5.4: *Left*: Excited 2^+ and 4^+ states in ^{34}Mg [135]. *Right*: Calculated levels using $\beta_{\text{WS}} = 0.4$ and $V_0 = -400$ MeV·fm^3. Here, we assume the rotation-vibration model for the energy of each state.
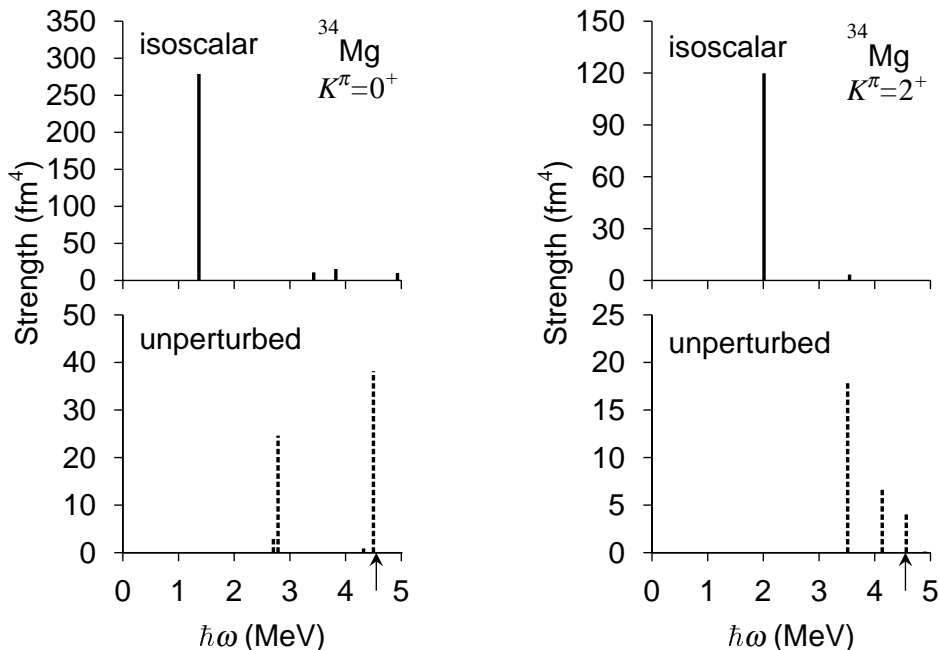
Figure 5.5: Isoscalar transition strengths for the $K^\pi = 0^+$ and 2^+ modes of quadrupole vibration in ^{34}Mg (the upper panel), and the transition strengths of unperturbed 2qp excitations (the lower panel) at prolately deformation with $\beta_{\mathrm{WS}} = 0.4$ for both neutrons and protons. The threshold energy, 4.55 MeV is indicated by the arrows. We obtained the self-consistency factors as $f_{pp} = 1.367$ and $f_{ph} = 0.742$.

where the vibration phonon and the moment of inertia are calculated microscopically. The measured reduced transition probability $B(E2; 0_1^+ \rightarrow 2_1^+)$ is 541(102) e^2fm^4 [133], and the calculated $B(E2 \uparrow)$ is 412 e^2fm^4.

5.3.1 Quadrupole vibrations

In Fig. 5.5, we show strength distributions for the $K^\pi = 0^+$ and 2^+ states in ^{34}Mg. For both the $K^\pi = 0^+$ and 2^+ states, we can see prominent peaks at around 2 MeV. The intrinsic transition strength for the $K^\pi = 0^+$ state is about 43 Weisskopf unit (1 W.u. $\simeq 6.5$ fm^4 for ^{34}Mg). From the QRPA amplitude listed in Table. 5.2, it is clear that this $K^\pi = 0^+$ state is created by coherent excitations of neutron pairs.

In order to understand the mechanism of generating the soft $K^\pi = 0^+$ mode in a deformed nucleus, we show here a simple model by Bohr and Mottelson [126]. Let us consider the case where only two $\lambda\bar{\lambda}$ components are present in the wave functions both of the ground 0_{gs}^+ and of the excited 0_2^+ states;

$$|0_{\mathrm{gs}}^+\rangle = \frac{a}{\sqrt{a^2 + b^2}}|\lambda_1\bar{\lambda}_1\rangle + \frac{b}{\sqrt{a^2 + b^2}}|\lambda_2\bar{\lambda}_2\rangle \tag{5.4a}$$

$$|0_2^+\rangle = -\frac{b}{\sqrt{a^2 + b^2}}|\lambda_1\bar{\lambda}_1\rangle + \frac{a}{\sqrt{a^2 + b^2}}|\lambda_2\bar{\lambda}_2\rangle. \tag{5.4b}$$

Table 5.2: QRPA amplitudes for the 0^+ state at 1.37 MeV in ^{34}Mg. This mode has $B(E2) = 15.9$ e^2fm^4, $B(Q^\nu 2)$=162 fm^4, $B(Q^{\mathrm{IS}}2)$=279 fm^4, and $\sum |g_{\alpha\beta}|^2 = 0.14$. The single-particle levels are labeled with the asymptotic quantum numbers $[Nn_3\Lambda]\Omega$. Only components with $f^2_{\alpha\beta} - g^2_{\alpha\beta} > 0.01$ are listed.

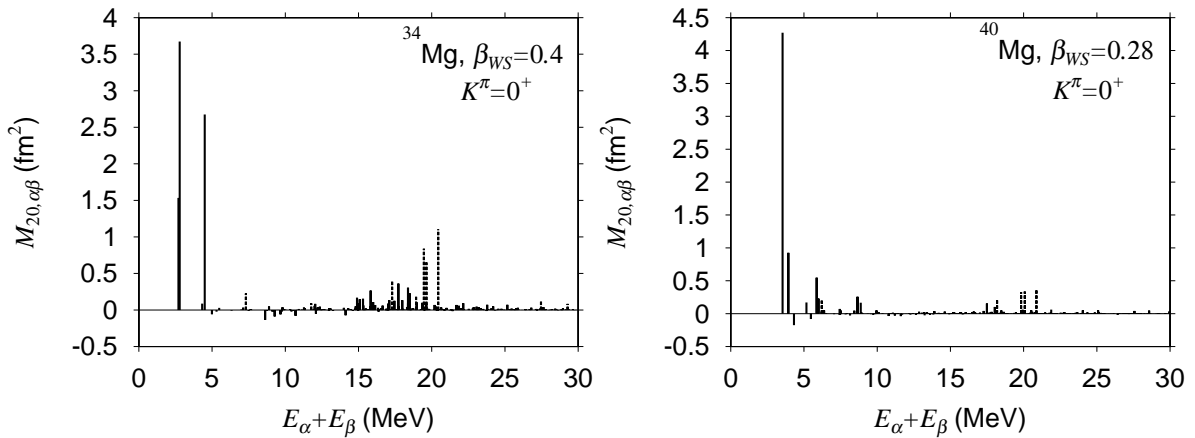| α	β	$E_\alpha + E_\beta$ (MeV)	$f^2_{\alpha\beta} - g^2_{\alpha\beta}$	$Q^{(\mathrm{uv})}_{20,\alpha\beta}$ (fm^2)	$M^{(\mathrm{uv})}_{20,\alpha\beta}$ (fm^2)
$\nu[202]3/2$	$\nu[202]3/2$	2.79	0.471	4.962	3.673
$\nu[330]1/2$	$\nu[330]1/2$	2.70	0.326	-1.815	1.534
$\nu[321]3/2$	$\nu[321]3/2$	4.50	0.134	6.177	2.676

Figure 5.6: Matrix elements $M^{(\mathrm{uv})}_{20,\alpha\beta}$ of 2qp excitations generating the lowest $K^\pi = 0^+$ state in ^{34}Mg and ^{40}Mg. Solid and dashed lines indicate 2qp excitations of neutron and proton, respectively.

The matrix element of r^2Y_{20} is then

$$\langle 0_{\mathrm{gs}}^+|r^2Y_{20}|0_2^+\rangle = \frac{2ab}{a^2+b^2}[\langle\lambda_1|r^2Y_{20}|\lambda_1\rangle - \langle\lambda_2|r^2Y_{20}|\lambda_2\rangle] \tag{5.5}$$

and the transition matrix element becomes proportional to the difference in the quadrupole moments of the individual orbitals composing the 0^+ states. In the case that the quadrupole moment of the orbitals has opposite sign each other, this matrix element becomes large. As the number of components increases, the wave function becomes more complicated but the general principle remain the same.

In the present case, the wave functions of the 0_{gs}^+ and 0_2^+ states are described by a lot of 2qp combinations in the QRPA. The main components generating the lowest 0^+ state are $[202]3/2\overline{[202]3/2}$ and $[330]1/2\overline{[330]1/2}$, which are up-sloping and down-sloping levels with opposite quadrupole moments. Therefore, the transition matrix element becomes enhanced. Furthermore, many other 2qp excitations coherently participate to generate the lowest 0^+ state as shown in the left panel in Fig. 5.6.

As discussed in the previous chapter, in ^{40}Mg we obtained the soft $K^\pi = 0^+$ mode possessing the extremely large transition strength. This enhancement mostly comes from the fact that the quasiparticle wave functions generating this mode have a spatially extended structure due to the strong effect of coupling to the continuum states. Also in the present case, the continuum coupling effect is important. The different feature of the soft $K^\pi = 0^+$ states in ^{34}Mg and ^{40}Mg is the coupling between the motion of neutrons and protons. In Fig. 5.6, we show the structure of $K^\pi = 0^+$ state in ^{40}Mg together with that in ^{34}Mg. We can see that there are appreciable contributions of 2qp excitations around 20 MeV for the $K^\pi = 0^+$ state in ^{34}Mg. They are mostly the $2\hbar\omega$ excitations of proton and can be identified as; $\pi[211]3/2 \to \pi[431]3/2$ (at 19.5 MeV), $\pi[101]3/2 \to \pi[321]3/2$ (at 17.3 MeV), $\pi[110]1/2 \to \pi[330]1/2$ (at 19.6 MeV) and $\pi[220]1/2 \to \pi[440]1/2$ (at 20.4 MeV). This analysis indicates that the obtained soft $K^\pi = 0^+$ mode is mainly generated by neutron 2qp excitations near the Fermi level (coupling between β vibration and pairing vibration) and coupling to the high-lying $2\hbar\omega$ excitations brings about further enhancement of the transition strength.

The pair correlation is indispensable for generation of the soft $K^\pi = 0^+$ mode in deformed nuclei. In order to clearly see unique features of pairing in a deformed system, we show strength distributions for the two-neutron pair transition in Fig. 5.7. We show in this figure two kinds of strength for pair transition, one is the monopole-pair transition and another the quadrupole-pair transition;

$$\hat{P}_{00}^\dagger = \int dr\hat{\psi}^\dagger(\boldsymbol{r}\uparrow)\hat{\psi}^\dagger(\boldsymbol{r}\downarrow), \tag{5.6a}$$

$$\hat{P}_{20}^\dagger = \int dr r^2Y_{20}(\hat{r})\hat{\psi}^\dagger(\boldsymbol{r}\uparrow)\hat{\psi}^\dagger(\boldsymbol{r}\downarrow). \tag{5.6b}$$

For the quadrupole-pair transition, the strengths at 1.37 MeV are enhanced compared with the unperturbed ones, whereas we cannot see a peak for the monopole-pair transition. We can say that the quadrupole pairing plays an important role in generating the soft $K^\pi = 0^+$ mode in deformed nuclei.

The excited 0^+ state in ^{34}Mg is predicted also by the shell model calculation [140]. In Fig. 5.8, we show the level structure of ^{34}Mg calculated by the Monte Carlo Shell Model [141].
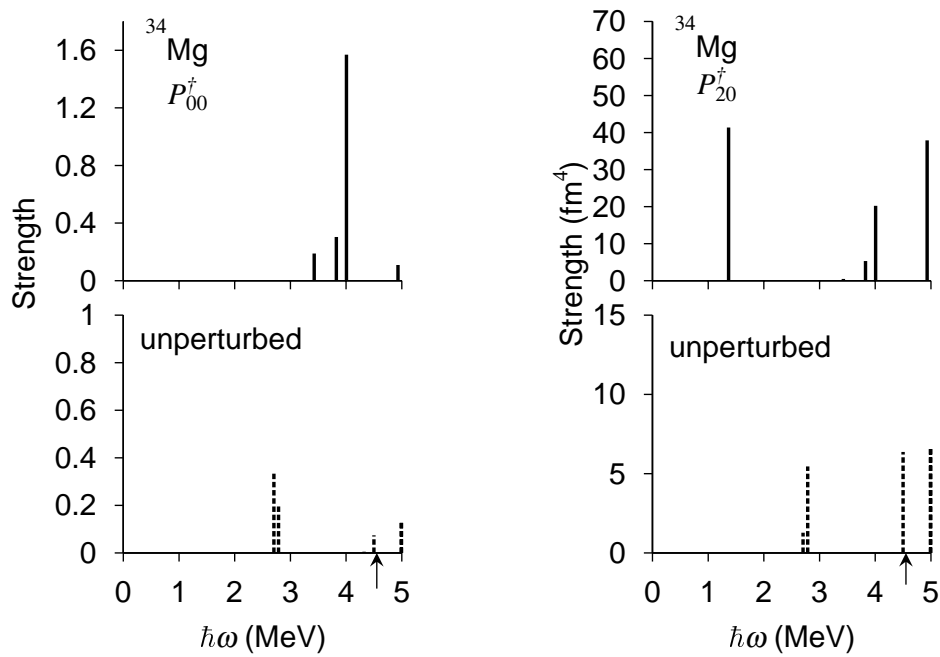
Figure 5.7: Strength distributions of the pair transition for the $K^\pi = 0^+$ mode in ^{34}Mg. The strengths for the monopole- and quadrupole-pair transition are shown in the left and right panels, respectively.
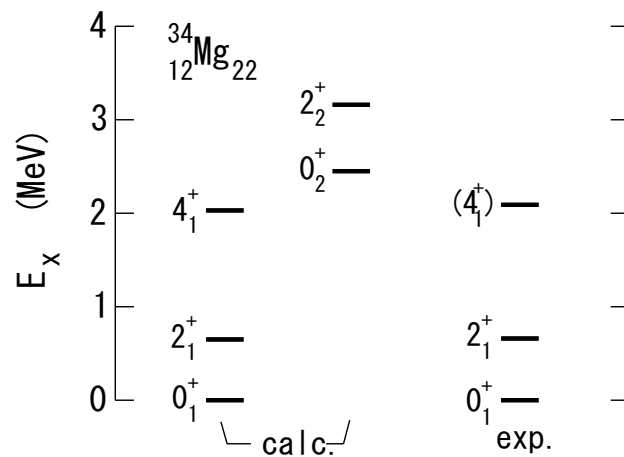

Figure 5.8: Level structure of ^{34}Mg calculated by the Monte Carlo Shell Model. This figure is taken from Ref. [140].

Table 5.3: QRPA amplitudes for the 2^+ state at 2.01 MeV in ^{34}Mg. This mode has $B(E2) = 6.28 \ e^2$fm^4, $B(Q^\nu 2)$=71.3 fm^4, $B(Q^{\text{IS}}2)$=120 fm^4, and $\sum |g_{\alpha\beta}|^2 = 0.105$.

α	β	$E_\alpha + E_\beta$ (MeV)	$f^2_{\alpha\beta} - g^2_{\alpha\beta}$	$Q^{(\text{uv})}_{22,\alpha\beta}$ (fm^2)	$M^{(\text{uv})}_{22,\alpha\beta}$ (fm^2)
$\nu[202]3/2$	$\nu[200]1/2$	3.51	0.647	4.228	-4.166
$\nu[310]1/2$	$\nu[321]3/2$	4.14	0.164	2.620	-1.375
$\nu[312]5/2$	$\nu[310]1/2$	5.39	0.019	-1.275	-0.217
$\nu[200]1/2$	$\nu[202]5/2$	7.16	0.023	-1.847	-0.345
$\pi[211]1/2$	$\pi[211]3/2$	4.57	0.096	-2.067	-1.060

Although the excitation energies of 0^+_2 and 2^+_2 states are slightly different from our results, their 0^+_2 state might have a similar structure to our soft $K^\pi = 0^+$ mode.

In Table. 5.3, we show the QRPA amplitude for the lowest $K^\pi = 2^+$ state in ^{34}Mg. As in ^{36,38,40}Mg, the $\pi[211]1/2 \otimes \pi[211]3/2$ excitation is one of the main components for generating the $\gamma-$vibration. Because this proton excitation satisfies the selection rule for the $\gamma-$vibration, the transition matrix element is large. In addition to this proton excitation, many neutron excitations coherently generate this $K^\pi = 2^+$ mode. This structure is quite similar to that of the $K^\pi = 2^+$ mode in ^{36,38,40}Mg.

5.3.2 Octupole vibrations

In Fig. 5.9, we show the isoscalar strength distributions for the $K^\pi = 0^-, 1^-$ and 2^- modes of octupole vibration in ^{34}Mg. For the $K^\pi = 0^-$ and 1^- states, we obtained prominent peaks with about 30 W.u. at around 3 MeV (1 W.u. $\simeq 67$ fm^6 for ^{34}Mg). We did not obtain excited states possessing enhanced transition strengths below 5 MeV for the $K^\pi = 3^-$ mode.

In Fig. 5.10, we show the structures of the lowest and the second lowest $K^\pi = 0^-$ states in ^{34}Mg. The lowest excited state at 2.6 MeV with $K^\pi = 0^-$ has 2230 fm^6 in intrinsic isoscalar transition strength. This state is generated mainly by the $\nu[202]3/2 \otimes \nu[321]3/2$ excitation whose component is about 90.4% and its excitation energy is 2.74 MeV. We can see another peak at 4.8 MeV possessing 4017 fm^6. This state is created mainly by the $\nu[310]1/2 \otimes \nu[200]1/2$ and $\nu[330]1/2 \otimes \nu[200]1/2$ excitations whose components are 69.7% and 8.12%, respectively. Although these two states are created by single-particle excitations dominantly, many 2qp excitations coherently participate in generating these modes as shown in Fig. 5.10, which brings about the enhancement of the transition strengths. It is noted that the lowest 2qp excitation of $\nu[202]3/2 \otimes \nu[321]3/2$ is in and out of phase to the other 2qp excitations in these two states at 2.6 and 4.8 MeV.

In Table. 5.4, we show the QRPA amplitude generating the lowest $K^\pi = 1^-$ state at 3.1 MeV. The main component is the $\nu[321]3/2 \otimes \nu[200]1/2$ excitation. Furthermore, many 2qp excitations also participate in generating this state. Though the contribution of 2qp excitations other than the $\nu[321]1/2 \otimes \nu[200]1/2$ excitation is small, these 2qp excitations coherently generate this $K^\pi = 1^-$ state as shown in Fig. 5.11.

Neutron numbers $N = 20$ and 22 are known to be superdeformed magic numbers, which correspond to the existence of superdeformed (SD) states in ^{40}Ca [101, 102] and ^{44}Ti [142]. In Fig. 5.3, we can see a deformed shell gap at around $\beta_2 = 0.6$ for $N = 22$ and at around
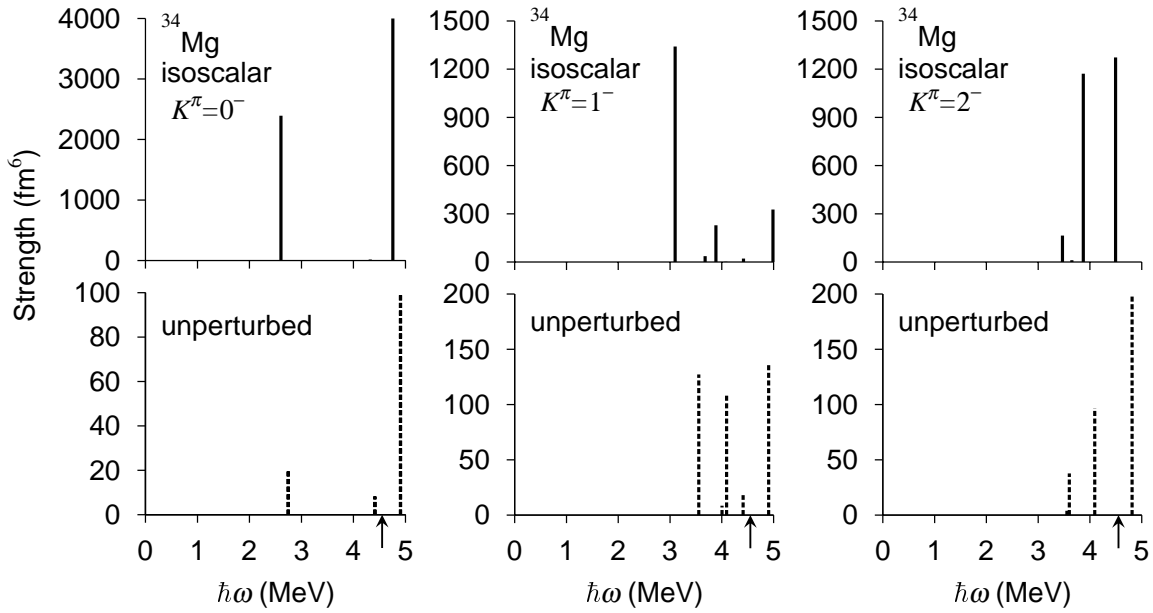
Figure 5.9: Isoscalar transition strengths for the $K^{\pi} = 0^-, 1^-$ and 2^- modes of octupole vibration in ^{34}Mg (the upper panel), and the transition strengths of unperturbed 2qp excitations (the lower panel). We obtained the self-consistency factors as $f_{pp} = 1.367$ and $f_{ph} = 0.751$.
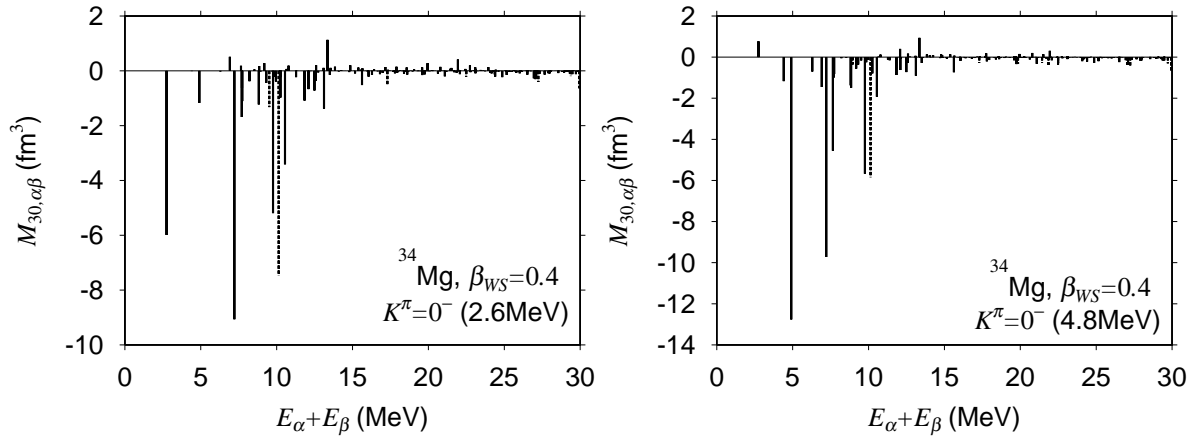
Figure 5.10: Matrix elements $M_{30,\alpha\beta}^{(\text{uv})}$ of 2qp excitations generating the low-lying $K^{\pi} = 0^-$ states at 2.6 MeV and 4.8 MeV in ^{34}Mg. Solid and dashed lines indicate 2qp excitations of neutron and proton, respectively.

Table 5.4: QRPA amplitudes for the 1^- state at 3.09 MeV in ^{34}Mg. This mode has $B(E3) = 34.4\ e^2$fm^6, $B(Q^\nu 3)$=946 fm^6, $B(Q^{\mathrm{IS}}3)$=1341 fm^6, and $\sum |g_{\alpha\beta}|^2 = 1.52 \times 10^{-2}$. Only components with $f_{\alpha\beta}^2 - g_{\alpha\beta}^2 > 0.01$ are listed.

α	β	$E_\alpha + E_\beta$ (MeV)	$f_{\alpha\beta}^2 - g_{\alpha\beta}^2$	$Q_{31,\alpha\beta}^{(\mathrm{uv})}$ (fm^3)	$M_{31,\alpha\beta}^{(\mathrm{uv})}$ (fm^3)
$\nu[321]3/2$	$\nu[200]1/2$	3.56	0.709	-11.28	-9.796
$\nu[202]3/2$	$\nu[330]1/2$	3.60	0.031	0.134	-0.025
$\nu[202]3/2$	$\nu[312]5/2$	4.00	0.015	-2.922	-0.382
$\nu[310]1/2$	$\nu[202]3/2$	4.09	0.160	10.47	-4.467
$\nu[310]1/2$	$\nu[200]1/2$	4.90	0.027	11.72	-2.186
$\nu[321]3/2$	$\nu[202]5/2$	6.39	0.025	10.11	-1.868
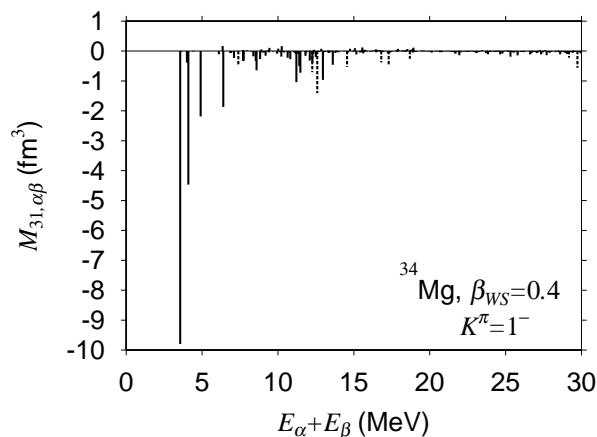
Figure 5.11: Matrix elements $M_{31,\alpha\beta}^{(\mathrm{uv})}$ of 2qp excitations generating the low-lying $K^\pi = 1^-$ state at 3.1 MeV in ^{34}Mg.

Table 5.5: QRPA amplitudes for the 1^- state at 2.60 MeV in ^{34}Mg for $\beta_{\mathrm{WS}} = 0.6$. This mode has $B(E3) = 38.5\ e^2$fm^6, $B(Q^\nu 3)$=1046 fm^6, $B(Q^{\mathrm{IS}}3)$=1486 fm^6, and $\sum |g_{\alpha\beta}|^2 = 1.26 \times 10^{-2}$. Only components with $f_{\alpha\beta}^2 - g_{\alpha\beta}^2 > 0.01$ are listed.

α	β	$E_\alpha + E_\beta$ (MeV)	$f_{\alpha\beta}^2 - g_{\alpha\beta}^2$	$Q_{31,\alpha\beta}^{(\mathrm{uv})}$ (fm^3)	$M_{31,\alpha\beta}^{(\mathrm{uv})}$ (fm^3)
$\nu[310]1/2$	$\nu[200]1/2$	3.01	0.238	13.67	7.141
$\nu[200]1/2$	$\nu[321]3/2$	3.06	0.648	-10.71	8.702
$\nu[202]3/2$	$\nu[310]1/2$	3.73	0.066	6.679	1.670
$\nu[321]3/2$	$\nu[202]5/2$	5.64	0.021	7.405	1.117
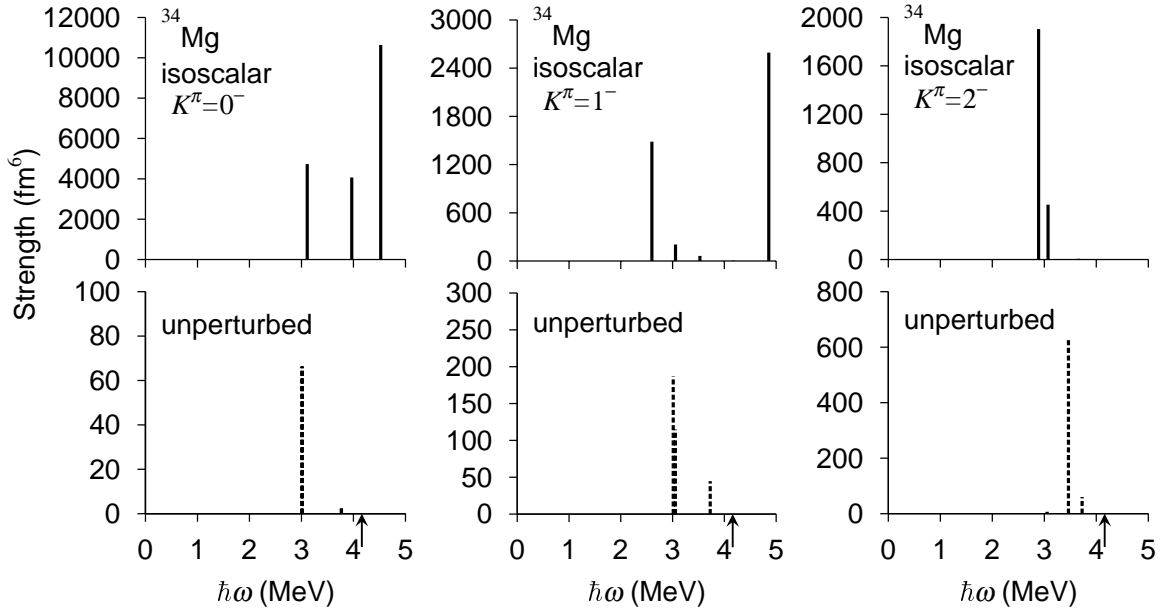
Figure 5.12: The same as Fig. 5.9 except for the deformation parameter $\beta_{\mathrm{WS}} = 0.6$. The threshold energy, 4.16 MeV is indicated by the arrows. We obtained the self-consistency factors as $f_{pp} = 1.369$ and $f_{ph} = 0.763$.

Table 5.6: QRPA amplitudes for the 2^- state at 2.89 MeV in ^{34}Mg for $\beta_{\mathrm{WS}} = 0.6$. This mode has $B(E3) = 23.0$ e^2fm^6, $B(Q^\nu 3)$=1493 fm^6, $B(Q^{\mathrm{IS}}3)$=1904 fm^6, and $\sum |g_{\alpha\beta}|^2 = 1.74 \times 10^{-2}$. Only components with $f_{\alpha\beta}^2 - g_{\alpha\beta}^2 > 0.01$ are listed.

α	β	$E_\alpha + E_\beta$ (MeV)	$f_{\alpha\beta}^2 - g_{\alpha\beta}^2$	$Q_{32,\alpha\beta}^{(\mathrm{uv})}$ (fm^3)	$M_{32,\alpha\beta}^{(\mathrm{uv})}$ (fm^3)
$\nu[200]1/2$	$\nu[321]3/2$	3.06	0.256	-2.639	1.343
$\nu[312]5/2$	$\nu[200]1/2$	3.47	0.653	25.16	22.07
$\nu[202]3/2$	$\nu[310]1/2$	3.73	0.035	-7.767	1.500
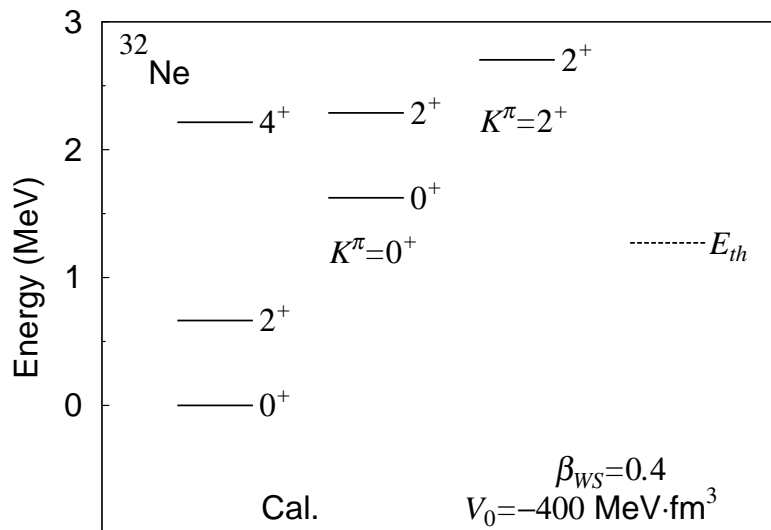
Figure 5.13: Calculated levels using $\beta_{\mathrm{WS}} = 0.4$ and $V_0 = -400$ MeV·fm³. The threshold energy, 1.27 MeV is indicated by E_{th}.

$\beta_2 = 0.7$ for $N = 20$. On top of these SD states, possible appearance of octupole excitations is discussed in Ref. [64]. Because the nucleus ^{34}Mg under discussion has the neutron number $N = 22$, let us study low-lying octupole excitations built on the SD state of this nucleus.

In Fig. 5.12, we show the isoscalar strength distributions for the $K^\pi = 0^-, 1^-$ and 2^- modes of octupole vibration in ^{34}Mg at $\beta_{\mathrm{WS}} = 0.6$. For $K^\pi = 1^-$ and 2^-, we obtained prominent peaks at around 3 MeV below the neutron threshold, and several excited states with large transition strengths for $K^\pi = 0^-$. The lowest $K^\pi = 0^-$ state at 3.1 MeV possessing 4729 fm⁶ is created mainly by the $\nu[310]1/2 \otimes \nu[200]1/2$ excitation, whose contribution is 88%. We show in Tables. 5.5,5.6, the QRPA amplitudes for the lowest $K^\pi = 1^-$ and 2^- states. From analysis of these three state, we found that they are generated by one or two 2qp excitations dominantly. As in the case of octupole excitations built on the normal deformed state, many other 2qp excitations coherently participate in creating these states, which brings about the enhancement of the transition strengths.

5.3.3 Excited states in ^{32}Ne

As shown in Fig. 5.2, ^{32}Ne has a minimum at prolately deformed state. This local minimum, however, is very shallow. Let us assume here that ^{32}Ne has a static deformation of $\beta_2 = 0.4$ as in ^{34}Mg, and perform the QRPA calculation and investigate properties of low-frequency excitation mode.

In Fig. 5.13, we show the levels below 3 MeV obtained by the present procedure. ^{32}Ne is a drip-line nucleus according to the calculations with the standard parameter set for the Woods-Saxon potential [23] and the Skyrme SLy4 interaction [26]. The chemical potential is -0.64 MeV in the present calculation. The neutron threshold energy thus is $2|\lambda| = 1.27$ MeV, indicated in Fig. 5.13 by a dotted line. Therefore, both the $K^\pi = 0^+$ and 2^+ states are embedded in the continuum.

Figure 5.14 shows the strength distributions of isoscalar quadrupole, monopole- and
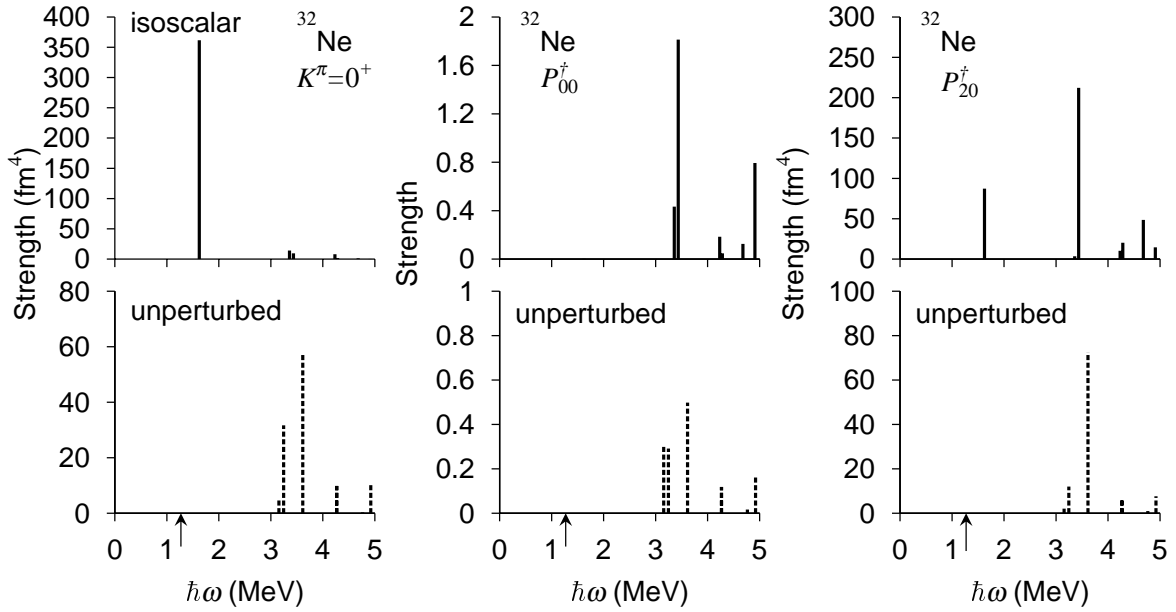
Figure 5.14: Isoscalar quadrupole and neutron-pair transition strengths for the $K^{\pi} = 0^{+}$ mode are shown together with the unperturbed 2qp transition strengths. The threshold energy, 1.27 MeV is indicated by the arrows. We obtained the self-consistency factors as $f_{pp} = 1.41$ and $f_{ph} = 0.795$.

Table 5.7: QRPA amplitudes for the 0^{+} state at 1.62 MeV in ^{32}Ne. This mode has $B(E2) = 13.6\ e^{2}$fm^{4}, $B(Q^{\nu}2)=235$ fm^{4}, $B(Q^{\mathrm{IS}}2)=362$ fm^{4}, and $\sum |g_{\alpha\beta}|^{2} = 0.14$. Only components with $f_{\alpha\beta}^{2} - g_{\alpha\beta}^{2} > 0.01$ are listed. The state without label represents a non-resonant continuum state.

α	β	$E_{\alpha} + E_{\beta}$ (MeV)	$f_{\alpha\beta}^{2} - g_{\alpha\beta}^{2}$	$Q_{20,\alpha\beta}^{\mathrm{(uv)}}$ (fm^{2})	$M_{20,\alpha\beta}^{\mathrm{(uv)}}$ (fm^{2})
$\nu[202]3/2$	$\nu[202]3/2$	3.16	0.433	-2.229	1.877
$\nu[321]3/2$	$\nu[321]3/2$	3.25	0.223	5.627	3.174
$\nu[310]1/2$	$\nu[310]1/2$	3.61	0.047	7.558	1.852
$\nu[310]1/2$	$\nu[330]1/2$	4.27	0.052	-3.133	1.292
$\nu[330]1/2$	$\nu[330]1/2$	4.92	0.081	3.198	1.165
$\nu1/2-$	$\nu[330]1/2$	5.74	0.020	-0.016	0.005

quadrupole-pair transitions for the $K^\pi = 0^+$ mode. We obtained a prominent peak at 1.62 MeV which has a large transition strength, 362 fm^4, in intrinsic quadrupole transition strength. Table 5.7 lists the QRPA amplitudes for this state. This state has a similar structure to the lowest state in ^{34}Mg: This mode is created by the pair vibration associated mainly with the up-sloping $(\nu[202]3/2)^2$ and the down-sloping $(\nu[321]3/2)^2$ levels which have opposite signs in the quadrupole moments. Furthermore, the quadrupole pairing is indispensable for the enhancement of the transition strength.

5.4 Summary

We have studied properties of low-frequency mode of excitation in ^{34}Mg by means of the deformed QRPA based on the coordinate-space HFB method. We found that the lowest $K^\pi = 0^+$ mode has a interesting property: The $K^\pi = 0^+$ mode is generated mainly by the pair vibration and the quadrupole pairing plays an important role in the enhancement of the transition strength. This feature is not restricted to ^{34}Mg. We found the similar soft $K^\pi = 0^+$ mode in ^{32}Ne. For generation of this soft $K^\pi = 0^+$ mode, it is crucial that the shell structure around the Fermi level has the following character; orbitals both of up-sloping and of down-sloping are existing. Therefore, the excited 0^+ state is a good indicator for studying the pair correlation and the nuclear deformation in neutron-rich nuclei.

Furthermore, in ^{34}Mg, we obtained the low-lying negative-parity state possessing large transition strength. However the collectivity is smaller than the positive-parity vibrational states.

Chapter 6

Soft $K^{\pi} = 0^+$ modes in neutron-rich chromium and iron isotopes around $N = 40$

6.1 Introduction

The subshell closure at 40 created by the gap between $1g_{9/2}$ and $2p_{1/2}, 1f_{5/2}$ orbitals has attracted much attention [119] for several reasons. The proton-rich $N = Z$ nucleus ^{80}Zr lies in the center of the well-deformed $A \simeq 80$ region [143]. A shell gap at 40 is again appeared in deformation region (see Fig. 6.2), and the shell effect of protons and neutrons coherently stabilize the nucleus deformed. On the other hand, the existence of $N = 40$ subshell closure was suggested experimentally for the neutron-rich nucleus ^{68}Ni [144]. This is because a weakening of the spin-orbit surface term for neutron-rich nuclei since their surface is expected to be more diffuse [25], which enlarges the gap of $N = 40$. The strength of this subshell closure and its persistence for $Z < 28$ determine the waiting point for the r-process at ^{64}Cr [145], which is considered to be a progenitor of ^{68}Ni.

The half-life measurement at CERN/ISOLDE have deduced that the neutron-rich ^{66}Fe is deformed with a quadrupole deformation $\beta_2 \sim 0.26$ [146]. Since the Cr isotopes lie at mid proton $1f_{7/2}$ shell, protons could additionally destabilize the nucleus and favor deformation. Recent measurement of the first excited 2^+ state in neutron-rich Cr isotopes [147] indicates that the deformation develops towards $N = 40$, as shown in Fig. 6.1. The calculated excitation energies by the shell model using different model spaces [148] are also plotted in this figure. Calculations labeled by fp, fpg and $fpgd$ correspond to the model space with full $pf-$shell, ^{48}Ca as a core and $\{2p_{3/2}, 1f_{5/2}, 2p_{1/2}, 1g_{9/2}\}$, and ^{54}Ca as a core and $\{1f_{5/2}, 2p_{1/2}, 1g_{9/2}, 2d_{5/2}\}$, respectively. The $pf-$shell calculation gives a good description of the experimental data up to $N = 36$. The drop in the excitation energy beyond $N = 36$ requires the inclusion of the upper orbits, implying the onset of deformation.

The deformation region near the shell closure gives a favorable situation for the emergence of the soft $K^{\pi} = 0^+$ mode discussed in the previous chapters because many orbitals with opposite quadrupole moments are crossing around the Fermi level. Since the excited 0^+ state is quite sensitive to pairing correlations and deformation, we study in this chapter properties of low-lying 0^+ state in neutron-rich Cr and Fe isotopes with $N \simeq 40$ region. In order to investigate properties of low-frequency mode of excitation in these isotopes, we perform the
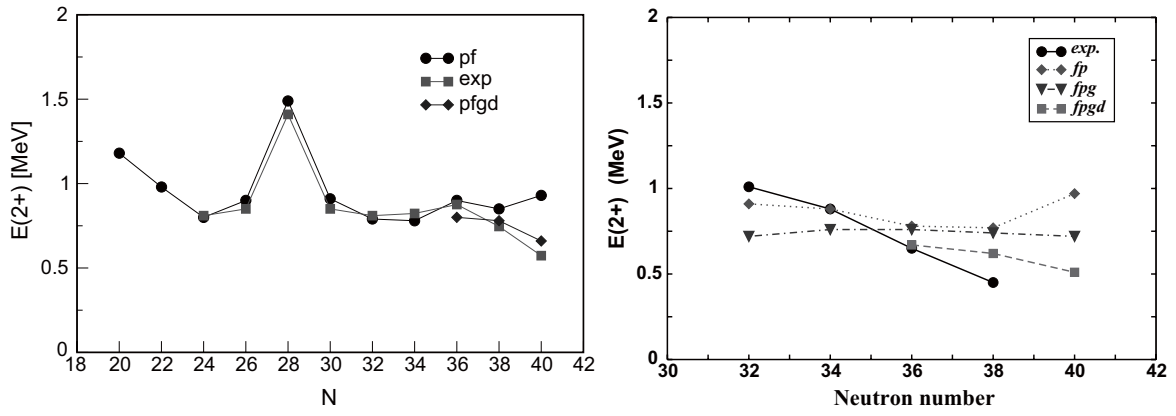
Figure 6.1: *Left*: Excitation energies of the 2^+ state in Fe isotopes, taken from Ref. [148]. *Right*: Excitation energies of the 2^+ state in Cr isotopes, taken from Ref. [147].
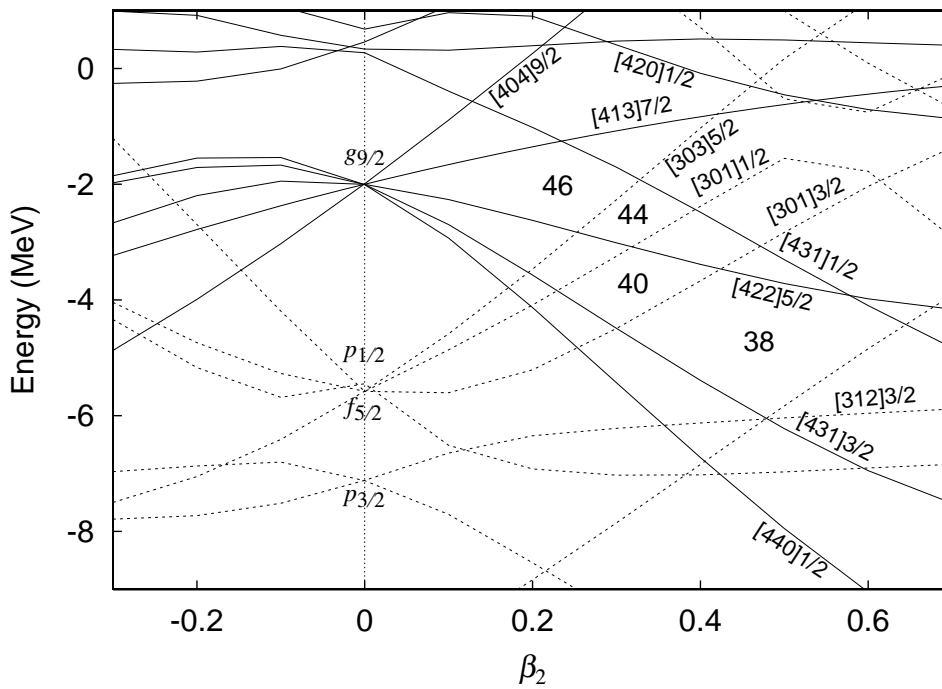
Figure 6.2: Neutron single-particle energies for ^{64}Cr in the Woods-Saxon potential as functions of deformation parameter β_2.
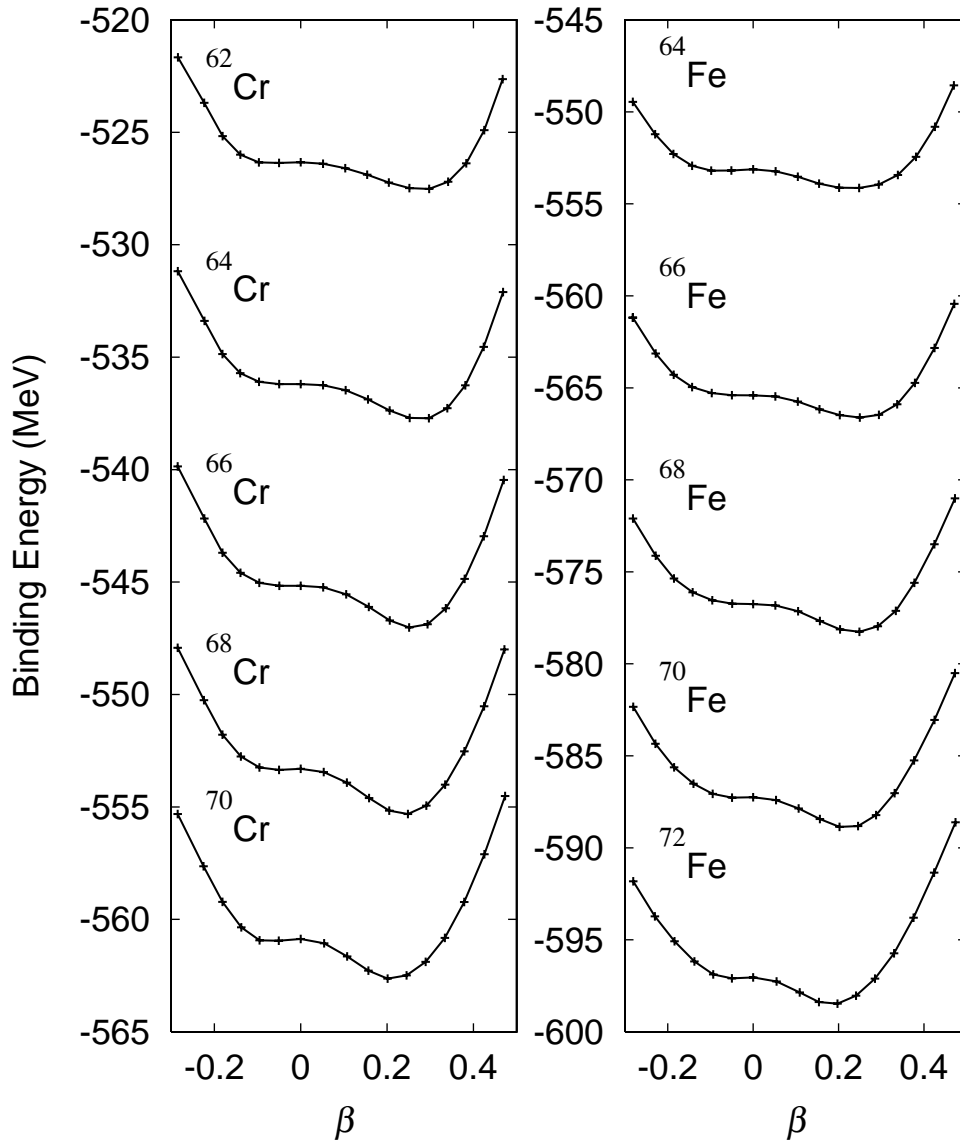
Figure 6.3: Potential energy surfaces for neutron-rich chromium and iron isotopes with $N \simeq$ 40 calculated by using the `HFBTHO` code [138]. The Skyrme SkM* interaction and the surface-type delta pairing interaction with $V_0 = -418$ MeV·fm^3 are employed, where the particle number projection is not performed.

Table 6.1: Ground-state properties of $^{62-70}$Cr and $^{62-72}$Fe obtained by the deformed WS-HFB calculation with $\beta_2 = 0.3$ and $V_0 = -420$ MeV·fm^3 for the pairing interaction. Chemical potentials, average pairing gaps, root-mean-square radii and quadrupole deformations for protons and neutrons are listed.

nucleus	λ_π (MeV)	$\langle\Delta_\pi\rangle$ (MeV)	$\sqrt{\langle r^2\rangle_\pi}$ (fm)	$\beta_{2,\pi}$	λ_ν (MeV)	$\langle\Delta_\nu\rangle$ (MeV)	$\sqrt{\langle r^2\rangle_\nu}$ (fm)	$\beta_{2,\nu}$
^{62}Cr	-16.2	0.0	3.69	0.323	-4.58	1.29	4.15	0.301
^{64}Cr	-17.4	0.0	3.70	0.325	-3.92	1.37	4.23	0.294
^{66}Cr	-18.6	0.0	3.71	0.327	-3.28	1.42	4.30	0.283
^{68}Cr	-19.7	0.0	3.73	0.329	-2.68	1.44	4.36	0.274
^{70}Cr	-20.9	0.0	3.74	0.330	-2.09	1.42	4.43	0.271
^{64}Fe	-13.2	0.0	3.78	0.309	-5.85	1.13	4.13	0.312
^{66}Fe	-14.5	0.0	3.79	0.311	-5.14	1.19	4.20	0.304
^{68}Fe	-15.6	0.0	3.78	0.312	-4.47	1.28	4.27	0.290
^{70}Fe	-16.8	0.0	3.81	0.314	-3.85	1.30	4.33	0.278
^{72}Fe	-17.9	0.0	3.83	0.316	-3.23	1.27	4.39	0.272

deformed QRPA calculation based on the coordinate-space HFB formalism. The method we use in this chapter is same as in the previous chapters.

6.2 Results and Discussion

In Fig. 6.2, we show neutron single-particle energies for ^{64}Cr as functions of deformation parameter β_2 using a deformed Woods-Saxon potential. In prolately deformation region around $\beta_2 \simeq 0.3$, we can see deformation shell gaps of $N = 38 - 46$. For creation of these shell gaps, the $\nu[431]1/2$ orbit coming from $2d_{5/2}$, $\nu[440]1/2$ from $1g_{9/2}$ and $\nu[301]3/2$ from $2p_{3/2}$ play an important role. Figure 6.3 shows the calculated potential energy surfaces for neutron-rich Cr and Fe isotopes around $N = 40$ using HFBTHO [138]. We used the Skyrme effective interaction SkM* for the particle-hole channel and the surface-type delta interaction for the particle-particle channel, where the particle number projection was not performed. We can see that the deformation well develops in these nuclei at around $\beta_2 = 0.2 \sim 0.3$, which is consistent with the recent experiments [146, 147].

Table. 6.1 lists ground-state properties of $^{62-70}$Cr and $^{64-72}$Fe obtained by the deformed WS-HFB calculation. We set the deformation parameter $\beta_2 = 0.3$ for the Woods-Saxon potential. In these nuclei, the root-mean-square radii for neutrons are about $0.4 - 0.7$ fm larger than those for protons. The neutron skin structure well develops in this calculation. The pairing gap for protons vanishes, whereas that for neutrons is finite for all nuclei in this region.

We next discuss properties of low-lying $K^\pi = 0^+$ mode in $^{62-70}$Cr and $^{64-72}$Fe isotopes. Figure 6.4 shows the isoscalar quadrupole transition strengths for the $K^\pi = 0^+$ mode. We can see a prominent peak at around 1 MeV in all nuclei under discussion. Because 1 Weisskopf unit is $14.6-17.1$ fm^4 for $^{62-70}$Cr and $15.2-17.8$ fm^4 for $^{64-72}$Fe, all low-lying states obtained here have extremely enhanced transition strengths. In ^{72}Fe, for instance, the strength becomes about 141 W.u. in the intrinsic isoscalar transition strength, and $B(E2; 0_2^+ \rightarrow 2_1^+)$ about 9.3
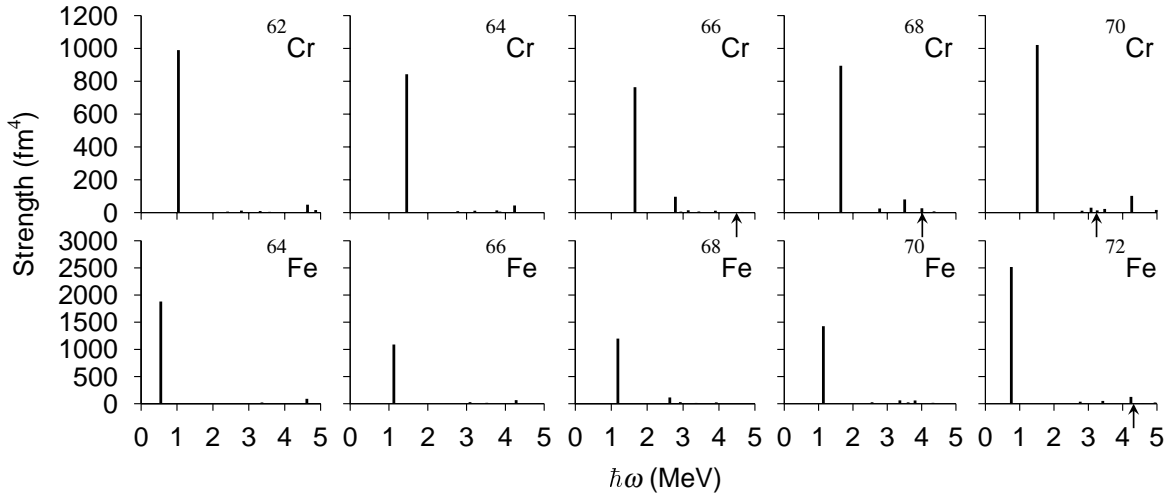
Figure 6.4: Isoscalar quadrupole transition strengths for $K^\pi = 0^+$ mode in $^{62-70}$Cr and $^{64-72}$Fe.

Table 6.2: QRPA amplitudes for the 0^+ state at 1.04 MeV in ^{62}Cr. This mode has $B(E2) = 57.5\ e^2$fm^4, $B(Q^\nu 2)$=570 fm^4, $B(Q^{IS}2)$=990 fm^4, and $\sum |g_{\alpha\beta}|^2 = 0.139$. The single-particle levels are labeled with the asymptotic quantum numbers $[Nn_3\Lambda]\Omega$. Only components with $|f_{\alpha\beta}^2 - g_{\alpha\beta}^2| > 0.01$ are listed.

	α	β	$E_\alpha + E_\beta$ (MeV)	$f_{\alpha\beta}^2 - g_{\alpha\beta}^2$	$Q_{20,\alpha\beta}^{(uv)}$ (fm^2)	$M_{20,\alpha\beta}^{(uv)}$ (fm^2)
(a)	$\nu[301]3/2$	$\nu[301]3/2$	2.13	0.385	-3.105	-2.190
(b)	$\nu[431]3/2$	$\nu[431]3/2$	2.78	0.133	7.235	-3.611
(c)	$\nu[440]1/2$	$\nu[440]1/2$	3.20	0.300	9.276	-7.062
(d)	$\nu[301]1/2$	$\nu[301]1/2$	3.36	0.079	-2.171	-0.727
(e)	$\nu[303]5/2$	$\nu[303]5/2$	5.51	0.028	-1.519	-0.336

W.u.

In Tables 6.2-6.11, we show the QRPA amplitudes for the lowest 0^+ state in these nuclei. The mechanism of generating these states are same as in ^{34}Mg: These states are mainly generated by neutron-pair vibrations, where 2qp excitations of time-reversed states coherently create the low-lying 0^+ state. The coherence comes from the fact that the 2qp excitations around the Fermi level have positive- and negative-quadrupole matrix elements in the level-crossing region.

Figure 6.4 shows the following feature: The transition strength of the lowest state becomes large at $N = 38$ and 46. The 2qp excitations of $(\nu[440]1/2)^2$ and $(\nu[431]1/2)^2$ whose quadrupole transition matrix element are large have an appreciable contribution to generate the 0^+ state in ^{62}Cr$_{38}$, ^{64}Fe$_{38}$ and ^{70}Cr$_{46}$, ^{72}Fe$_{46}$, respectively.

Furthermore, the transition strengths for quadrupole-pair creation become much enhanced, whereas those for monopole-pair creation are small. One example is shown in Fig. 6.5.

Table 6.3: QRPA amplitudes for the 0^+ state at 1.46 MeV in ^{64}Cr. This mode has $B(E2) = 44.9$ e^2fm^4, $B(Q^\nu 2)$=499 fm^4, $B(Q^{IS}2)$=843 fm^4, and $\sum |g_{\alpha\beta}|^2 = 0.098$. Only components with $|f_{\alpha\beta}^2 - g_{\alpha\beta}^2| > 0.01$ are listed.

	α	β	$E_\alpha + E_\beta$ (MeV)	$f_{\alpha\beta}^2 - g_{\alpha\beta}^2$	$Q_{20,\alpha\beta}^{(uv)}$ (fm^2)	$M_{20,\alpha\beta}^{(uv)}$ (fm^2)
(a)	$\nu[301]3/2$	$\nu[301]3/2$	2.60	0.082	-2.843	-1.007
(b)	$\nu[301]1/2$	$\nu[301]1/2$	2.65	0.181	-3.108	-1.661
(c)	$\nu[431]3/2$	$\nu[431]3/2$	3.07	0.336	7.044	-4.397
(d)	$\nu[422]5/2$	$\nu[422]5/2$	3.48	0.028	3.220	-0.429
(e)	$\nu[440]1/2$	$\nu[440]1/2$	3.88	0.258	9.178	-5.330
(f)	$\nu[303]5/2$	$\nu[303]5/2$	4.40	0.033	-2.131	-0.642

Table 6.4: QRPA amplitudes for the 0^+ state at 1.66 MeV in ^{66}Cr. This mode has $B(E2) = 38.4$ e^2fm^4, $B(Q^\nu 2)$=460 fm^4, $B(Q^{IS}2)$=764 fm^4, and $\sum |g_{\alpha\beta}|^2 = 0.108$. Only components with $|f_{\alpha\beta}^2 - g_{\alpha\beta}^2| > 0.01$ are listed.

	α	β	$E_\alpha + E_\beta$ (MeV)	$f_{\alpha\beta}^2 - g_{\alpha\beta}^2$	$Q_{20,\alpha\beta}^{(uv)}$ (fm^2)	$M_{20,\alpha\beta}^{(uv)}$ (fm^2)
(a)	$\nu[301]1/2$	$\nu[301]1/2$	2.42	0.227	-3.707	2.263
(b)	$\nu[422]5/2$	$\nu[422]5/2$	3.14	0.225	3.826	1.679
(c)	$\nu[303]5/2$	$\nu[303]5/2$	3.55	0.039	-2.819	1.059
(d)	$\nu[431]1/2$	$\nu[431]1/2$	3.63	0.111	7.772	2.428
(e)	$\nu[431]3/2$	$\nu[431]3/2$	3.71	0.231	6.271	2.988
(f)	$\nu[440]1/2$	$\nu[440]1/2$	5.10	0.066	3.683	8.620

Table 6.5: QRPA amplitudes for the 0^+ state at 1.65 MeV in ^{68}Cr. This mode has $B(E2) = 42.1$ e^2fm^4, $B(Q^\nu 2)$=549 fm^4, $B(Q^{IS}2)$=894 fm^4, and $\sum |g_{\alpha\beta}|^2 = 0.113$. Only components with $|f_{\alpha\beta}^2 - g_{\alpha\beta}^2| > 0.01$ are listed.

	α	β	$E_\alpha + E_\beta$ (MeV)	$f_{\alpha\beta}^2 - g_{\alpha\beta}^2$	$Q_{20,\alpha\beta}^{(uv)}$ (fm^2)	$M_{20,\alpha\beta}^{(uv)}$ (fm^2)
(a)	$\nu[301]1/2$	$\nu[301]1/2$	2.69	0.130	-3.457	1.710
(b)	$\nu[431]1/2$	$\nu[431]1/2$	2.82	0.354	8.697	5.104
(c)	$\nu[303]5/2$	$\nu[303]5/2$	3.08	0.107	-3.310	1.705
(d)	$\nu[422]5/2$	$\nu[422]5/2$	3.23	0.181	3.927	1.561
(e)	$\nu[431]3/2$	$\nu[431]3/2$	4.54	0.081	5.762	1.525
(f)	$\nu[431]1/2$	$\nu[440]1/2$	4.60	0.020	-2.856	0.697
(g)	$\nu[440]1/2$	$\nu[440]1/2$	5.94	0.030	4.724	7.046
(g')	$\nu[440]1/2$	$\nu[440]1/2$	6.38	0.010	1.629	0.124

Table 6.6: QRPA amplitudes for the 0^+ state at 1.51 MeV in ^{70}Cr. This mode has $B(E2) = 44.3$ $e^2\text{fm}^4$, $B(Q^\nu 2)$=640 fm^4, $B(Q^\text{IS}2)$=1021 fm^4, and $\sum |g_{\alpha\beta}|^2 = 0.090$. Only components with $|f_{\alpha\beta}^2 - g_{\alpha\beta}^2| > 0.01$ are listed.

	α	β	$E_\alpha + E_\beta$ (MeV)	$f_{\alpha\beta}^2 - g_{\alpha\beta}^2$	$Q_{20,\alpha\beta}^{(uv)}$ (fm^2)	$M_{20,\alpha\beta}^{(uv)}$ (fm^2)
(a)	$\nu[431]1/2$	$\nu[431]1/2$	2.32	0.547	10.73	-8.231
(b)	$\nu[303]5/2$	$\nu[303]5/2$	3.11	0.182	-3.238	-1.844
(c)	$\nu[301]1/2$	$\nu[301]1/2$	3.33	0.068	-2.800	-0.971
(d)	$\nu[422]5/2$	$\nu[422]5/2$	3.67	0.018	3.566	-0.433
(e)	$\nu[420]1/2$	$\nu[431]1/2$	3.68	0.038	-1.670	-0.584
(f)	$\nu[420]1/2$	$\nu[420]1/2$	5.06	0.016	3.444	-0.464
(g)	$\nu[431]3/2$	$\nu[431]3/2$	5.11	0.015	4.734	-0.663

Table 6.7: QRPA amplitudes for the 0^+ state at 0.546 MeV in ^{64}Fe. This mode has $B(E2) = 147$ $e^2\text{fm}^4$, $B(Q^\nu 2)$=978 fm^4, $B(Q^\text{IS}2)$=1881 fm^4, and $\sum |g_{\alpha\beta}|^2 = 0.474$. Only components with $|f_{\alpha\beta}^2 - g_{\alpha\beta}^2| > 0.01$ are listed.

	α	β	$E_\alpha + E_\beta$ (MeV)	$f_{\alpha\beta}^2 - g_{\alpha\beta}^2$	$Q_{20,\alpha\beta}^{(uv)}$ (fm^2)	$M_{20,\alpha\beta}^{(uv)}$ (fm^2)
(a)	$\nu[301]3/2$	$\nu[301]3/2$	1.89	0.474	-2.935	2.813
(b)	$\nu[431]3/2$	$\nu[431]3/2$	2.42	0.137	7.039	5.222
(c)	$\nu[440]1/2$	$\nu[440]1/2$	3.11	0.204	7.980	7.223
(d)	$\nu[301]1/2$	$\nu[301]1/2$	3.55	0.069	-1.718	0.668
(e)	$\nu[303]5/2$	$\nu[303]5/2$	5.30	0.035	-1.318	0.402

Table 6.8: QRPA amplitudes for the 0^+ state at 1.13 MeV in ^{66}Fe. This mode has $B(E2) = 80.2$ $e^2\text{fm}^4$, $B(Q^\nu 2)$=579 fm^4, $B(Q^\text{IS}2)$=1090 fm^4, and $\sum |g_{\alpha\beta}|^2 = 0.207$. Only components with $|f_{\alpha\beta}^2 - g_{\alpha\beta}^2| > 0.01$ are listed.

	α	β	$E_\alpha + E_\beta$ (MeV)	$f_{\alpha\beta}^2 - g_{\alpha\beta}^2$	$Q_{20,\alpha\beta}^{(uv)}$ (fm^2)	$M_{20,\alpha\beta}^{(uv)}$ (fm^2)
(a)	$\nu[301]3/2$	$\nu[301]3/2$	2.27	0.068	-2.765	1.205
(b)	$\nu[301]1/2$	$\nu[301]1/2$	2.62	0.091	-2.620	1.355
(c)	$\nu[431]3/2$	$\nu[431]3/2$	2.81	0.446	6.341	4.664
(d)	$\nu[422]5/2$	$\nu[422]5/2$	2.97	0.070	3.177	0.680
(e)	$\nu[440]1/2$	$\nu[440]1/2$	3.92	0.235	7.473	4.300
(f)	$\nu[303]5/2$	$\nu[303]5/2$	4.06	0.015	-1.915	0.680

Table 6.9: QRPA amplitudes for the 0^+ state at 1.19 MeV in ^{68}Fe. This mode has $B(E2) = 88.6\ e^2\text{fm}^4$, $B(Q^\nu 2)=636\ \text{fm}^4$, $B(Q^{\text{IS}}2)=1199\ \text{fm}^4$, and $\sum |g_{\alpha\beta}|^2 = 0.364$. Only components with $|f_{\alpha\beta}^2 - g_{\alpha\beta}^2| > 0.01$ are listed.

	α	β	$E_\alpha + E_\beta$ (MeV)	$f_{\alpha\beta}^2 - g_{\alpha\beta}^2$	$Q_{20,\alpha\beta}^{(\text{uv})}$ (fm^2)	$M_{20,\alpha\beta}^{(\text{uv})}$ (fm^2)
(a)	$\nu[301]1/2$	$\nu[301]1/2$	2.26	0.039	-3.453	2.162
(b)	$\nu[422]5/2$	$\nu[422]5/2$	2.73	0.469	3.811	2.383
(c)	$\nu[301]3/2$	$\nu[301]3/2$	3.17	-0.022	-2.255	0.375
(d)	$\nu[303]5/2$	$\nu[303]5/2$	3.21	-0.032	-2.696	1.355
(e)	$\nu[431]3/2$	$\nu[431]3/2$	3.67	0.270	5.384	2.747
(f)	$\nu[431]1/2$	$\nu[431]1/2$	3.73	0.112	6.498	1.975
(g)	$\nu[413]7/2$	$\nu[413]7/2$	5.04	-0.011	-0.057	0.003
(h)	$\nu[440]1/2$	$\nu[440]1/2$	5.18	0.073	3.062	0.721
(i)	$\nu[312]3/2$	$\nu[312]3/2$	6.53	0.012	0.426	0.032

Table 6.10: QRPA amplitudes for the 0^+ state at 1.14 MeV in ^{70}Fe. This mode has $B(E2) = 98.4\ e^2\text{fm}^4$, $B(Q^\nu 2)=776\ \text{fm}^4$, $B(Q^{\text{IS}}2)=1428\ \text{fm}^4$, and $\sum |g_{\alpha\beta}|^2 = 0.505$. The columns (g) and (g$'$) are assigned the same configuration, because we obtain two discretized continuum states associated with the $\nu[440]1/2$ level for which $E > |\lambda|$. Only components with $|f_{\alpha\beta}^2 - g_{\alpha\beta}^2| > 0.01$ are listed.

	α	β	$E_\alpha + E_\beta$ (MeV)	$f_{\alpha\beta}^2 - g_{\alpha\beta}^2$	$Q_{20,\alpha\beta}^{(\text{uv})}$ (fm^2)	$M_{20,\alpha\beta}^{(\text{uv})}$ (fm^2)
(a)	$\nu[301]1/2$	$\nu[301]1/2$	2.42	-0.076	-3.361	1.550
(b)	$\nu[303]5/2$	$\nu[303]5/2$	2.77	-0.107	-3.199	1.789
(c)	$\nu[431]1/2$	$\nu[431]1/2$	2.83	0.422	7.504	4.638
(d)	$\nu[422]5/2$	$\nu[422]5/2$	2.92	0.467	3.744	2.242
(e)	$\nu[301]3/2$	$\nu[301]3/2$	4.08	-0.022	-1.841	0.235
(f)	$\nu[431]3/2$	$\nu[431]3/2$	4.58	0.136	4.830	1.534
(g)	$\nu[440]1/2$	$\nu[440]1/2$	6.09	0.052	4.103	0.737
(g$'$)	$\nu[440]1/2$	$\nu[440]1/2$	6.56	0.015	1.242	0.091
(h)	$\nu[404]9/2$	$\nu[404]9/2$	8.63	-0.012	-1.743	0.151

Table 6.11: QRPA amplitudes for the 0^+ state at 0.756 MeV in ^{72}Fe. This mode has $B(E2) = 165\ e^2$fm^4, $B(Q^\nu 2)=1393$ fm^4, $B(Q^{\mathrm{IS}}2)=2516$ fm^4, and $\sum|g_{\alpha\beta}|^2 = 0.672$. The state without label represents a non-resonant continuum state. Only components with $|f^2_{\alpha\beta} - g^2_{\alpha\beta}| > 0.01$ are listed.

|	α	β	$E_\alpha + E_\beta$ (MeV)	$f^2_{\alpha\beta} - g^2_{\alpha\beta}$	$Q^{(\mathrm{uv})}_{20,\alpha\beta}$ (fm^2)	$M^{(\mathrm{uv})}_{20,\alpha\beta}$ (fm^2)
(a)	$\nu[431]1/2$	$\nu[431]1/2$	2.19	0.813	9.771	9.585
(b)	$\nu[303]5/2$	$\nu[303]5/2$	2.80	-0.079	-3.020	2.379
(c)	$\nu[301]1/2$	$\nu[301]1/2$	2.98	-0.055	-2.666	1.344
(d)	$\nu[413]7/2$	$\nu[413]7/2$	3.33	-0.028	-0.057	0.005
(e)	$\nu[422]5/2$	$\nu[422]5/2$	3.47	0.079	3.201	0.629
(f)	$\nu[420]1/2$	$\nu[431]1/2$	3.70	0.044	-1.413	0.666
(g)	$\nu[301]3/2$	$\nu[301]3/2$	5.02	-0.022	-1.475	0.289
(h)	$\nu[420]1/2$	$\nu[420]1/2$	5.21	0.044	2.911	0.582
(i)	$\nu[431]3/2$	$\nu[431]3/2$	5.38	0.058	4.941	1.210
(j)	$\nu[440]1/2$	$\nu[440]1/2$	7.23	0.017	2.882	0.235
(k)	$\nu[404]9/2$	$\nu[404]9/2$	7.36	-0.012	-1.945	0.200
(l)	$\nu 1/2-$	$\nu 1/2-$	8.45	0.015	3.080	0.326
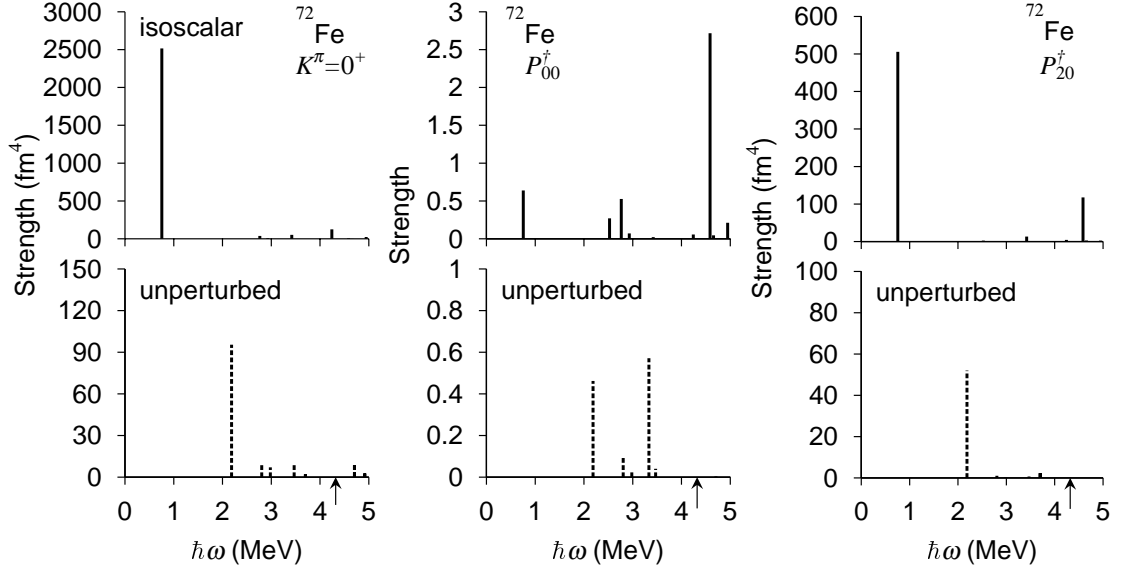
Figure 6.5: Isoscalar quadrupole transition strengths and neutron-pair transition strengths for the $K^\pi = 0^+$ mode are shown together with the unperturbed 2qp transition strengths. The threshold energy is 4.32 MeV as indicated by the arrows. We obtained the self-consistency factors as $f_{pp} = 1.418$ and $f_{ph} = 0.787$.

In the left panel, the isoscalar quadrupole transition strength for $K^\pi = 0^+$ mode in ^{72}Fe and the unperturbed 2qp transition strength are shown. We can see a prominent peak at 0.76 MeV. In the central and right panels, we show strength distributions of monopole- and quadrupole-pair transitions. The strengths for monopole-pair transition are comparable to the unperturbed ones. For the quadrupole-pair transitions, on the other hand, the strengths are quite large, much enhanced compared to the unperturbed ones. It is clear that the quadrupole pairing plays an crucial role in generating coherence among 2qp excitations for $K^\pi = 0^+$ mode.

6.3 Summary

We have studied low-lying vibrational modes in neutron-rich Cr and Fe isotopes around $N = 40$ by means of the deformed QRPA calculation. Neutron-rich ^{62}Cr and ^{64,66}Fe are suggested to be deformed experimentally, and Cr and Fe isotopes around $N = 40$ are expected to be deformed by the theoretical calculation. In these deformed neutron-rich nuclei, we have found that the soft $K^\pi = 0^+$ mode is triggered by the neutron-pair vibration. Furthermore, it is pointed out that the quadrupole pairing plays an important role in the enhancement of the transition strength.

Chapter 7

Single-particle resonances in deformed nuclei

7.1 Introduction

Understanding of single-particle levels in the continuum is essential in describing the nuclear structure close to, and beyond, the drip line, since the shell structure of both bound and continuum levels plays an important role in many-body correlations such as deformation and pairing.

It has been argued recently that, as the binding energy approaches zero, the s-wave component of a bound single-particle wave function behaves uniquely in a deformed potential, and plays a dominant role in Nilsson levels with $\Omega^\pi = 1/2^+$ [116, 117]. Naively, resonant levels can be considered as an extension of bound states into the positive energy regime. Therefore, if the s-wave component keeps dominant in the continuum, the level with $\Omega^\pi = 1/2^+$ might not exist as a physical state. Notice that, for a Nilsson Hamiltonian [149], single-particle levels with $\Omega = 1/2$ belonging to high-j orbit comes down in energy in a prolately deformed potential. These states play an important role in generating the deformed shell structure. It is therefore crucially important to investigate the role of low-l component in a deformed wave function for $\Omega = 1/2$ states and its transition from bound to resonant levels.

The structure of deformed single-particle levels in the continuum has been investigated in a few publications. In Ref. [150], the resonance energy of negative parity states was studied by employing the Gamow wave function. The Analytic Continuation in the Coupling Constant (ACCC) method was applied to study single-particle resonance states in spherical and deformed nuclei [151]. Using the multi-channel scattering approach, Ref. [152] has studied how the single-particle energies change from bound to resonant levels when the depth of the potential is varied. In order to fully understand the structure of deformed single-particle levels in the continuum, however, a detailed study of the wave function components is still necessary, in addition to the resonance energy itself.

In this chapter, we investigate the structure of deformed wave functions around zero energy using the Gamow state representation for a resonant state. To this end, we use a schematic model: a Y_{20} deformed finite square-well potential without spin-orbit force. This enables us to determine the single-particle wave function analytically. To use the Gamow state for resonance has a certain advantage in analyzing the deformed wave function. That is, we are able to treat the bound and the resonant levels on the same footing, because the

Gamow states are normalizable just like the bound states [153]. It is then straightforward to see how the fraction of each component in the deformed wave functions changes when the single-particle level changes its character from bound to resonant. A slight disadvantage of this approach is that the expectation value with the Gamow states, including the probability of wave function components, becomes complex numbers. However, this is not a big defect for our purpose, since the physical quantity of the expectation values can be obtained by taking their real part [154, 155].

This work was reported in Ref. [82].

7.2 Model

Our purpose is to study the structure of wave function in a deformed single-particle potential. To this end, we employ a schematic model for the single-particle potential, that is, a deformed square-well potential without the spin-orbit force,

$$V(\boldsymbol{r}) = -V_0 \, \theta(R(\hat{\boldsymbol{r}}) - r), \tag{7.1}$$

where $R(\hat{\boldsymbol{r}}) = R_0(1 + \beta_2 Y_{20}(\hat{\boldsymbol{r}}))$. For simplicity, we expand this potential up to the first order of deformation parameter β_2 and obtain

$$V(\boldsymbol{r}) \simeq -V_0 \left[\theta(R_0 - r) + R_0\beta_2 Y_{20}(\hat{\boldsymbol{r}})\delta(r - R_0)\right]. \tag{7.2}$$

In order to solve the Schrödinger equation with this potential, we expand the wave function in the multipoles as

$$\Psi_K(\boldsymbol{r}) = \sum_l \frac{u_{lK}(r)}{r} Y_{lK}(\hat{\boldsymbol{r}}), \tag{7.3}$$

where the quantum number $K(=\Lambda)$ is the z-component of the orbital angular momentum l. By projecting out each multipole component, we obtain the coupled equations for the radial wave functions given by

$$\left[-\frac{\hbar^2}{2m}\frac{d^2}{dr^2} - V_0\theta(R_0 - r) + \frac{\hbar^2 l(l+1)}{2mr^2} - E\right]u_{lK}(r)$$
$$= V_0 R_0 \beta_2 \delta(r - R_0) \sum_{l'} \langle lK|Y_{20}|l'K\rangle u_{l'K}(r). \tag{7.4}$$

For the positive energy solution, $E > 0$, we impose the boundary condition corresponding to the Gamow state for resonance. That is, the wave function is regular at the origin and satisfies the out-going boundary condition $u(r) \sim e^{ikr}$ asymptotically. This boundary condition is satisfied only if the energy is complex, $E = \hbar^2 k^2/2m = E_R - i\Gamma/2$, where E_R and Γ are the resonance energy and the width, respectively. In the case for $\Gamma = 0$ and $E_R < 0$, the Gamow state wave function is equivalent to the bound state wave function, which satisfies the decaying asymptotics $u(r) \sim e^{-\alpha r}$, where $\alpha = \sqrt{-2mE_R/\hbar^2}$.

The solutions of the coupled-channels equations (7.4) therefore read (we omit the subscript K for simplicity of notation),

$$u_l(r) = \begin{cases} A_l \, r j_l(k_1 r) & (r < R_0), \\ B_l \, r h_l^{(+)}(kr) & (r \geq R_0), \end{cases} \tag{7.5}$$

where $k_1 = \sqrt{2m(E + V_0)/\hbar^2}$, $k = \sqrt{2mE/\hbar^2}$, and $j_l(x), h_l^{(+)}(x)$ are the spherical Bessel and Hankel functions, respectively. The amplitudes A_l and B_l are determined by the matching condition at $r = R_0$ given by,

$$u_l(R_-) = u_l(R_+), \tag{7.6}$$

$$-\frac{\hbar^2}{2m}\left[u_l'(R_+) - u_l'(R_-)\right] = V_0 R_0 \beta_2 \sum_{l'}\langle lK|Y_{20}|l'K\rangle u_{l'}(R_0), \tag{7.7}$$

where $R_\pm$ represents $\lim_{\varepsilon \to 0} R_0 \pm \varepsilon$.

The bound state wave function is normalized as

$$1 = \int d\boldsymbol{r}\,|\Psi_K(\boldsymbol{r})|^2 = \sum_l N_l, \tag{7.8}$$

where

$$N_l = \int_0^\infty dr|u_l(r)|^2. \tag{7.9}$$

The Gamow state wave function can be also normalized by introducing the regularization factor as Zel'dovich proposed [156]

$$N_l = \lim_{\epsilon \to 0}\int_0^\infty dr e^{-\epsilon r^2}\{u_l(r)\}^2 \tag{7.10}$$

$$= \int_0^{R_0} dr\{A_l\, r j_l(k_1 r)\}^2 + \lim_{\epsilon \to 0}\int_{R_0}^\infty dr e^{-\epsilon r^2}\{B_l\, r h_l^{(+)}(kr)\}^2. \tag{7.11}$$

Using a property of the spherical Bessel function [157], one can evaluate the first term as

$$\int_0^{R_0} dr\,\{A_l\, r j_l(k_1 r)\}^2 = \frac{A_l^2 R_0^3}{2}\Big(\{j_l(k_1 R_0)\}^2 - j_{l-1}(k_1 R_0)j_{l+1}(k_1 R_0)\Big). \tag{7.12}$$

The second term can be also evaluated using the contour integral method or equivalently the Complex Scaling Method (CSM). The result is given by [158],

$$\lim_{\epsilon \to 0}\int_{R_0}^\infty dr e^{-\epsilon r^2}\{B_l\, r h_l^{(+)}(kr)\}^2 = -\frac{B_l^2 R_0^3}{2}\Big(\{h_l^{(+)}(kR_0)\}^2 - h_{l-1}^{(+)}(kR_0)h_{l+1}^{(+)}(kR_0)\Big). \tag{7.13}$$

Note that the fraction of multipole components N_l is in general a complex number for the Gamow state wave function.

7.3 Results and Discussion

Let us now discuss the behavior of the low-l components in deformed wave functions. In §7.3.1, we vary the potential depth for a fixed deformation parameter, while we vary the deformation parameter for a fixed potential depth in §7.3.2.

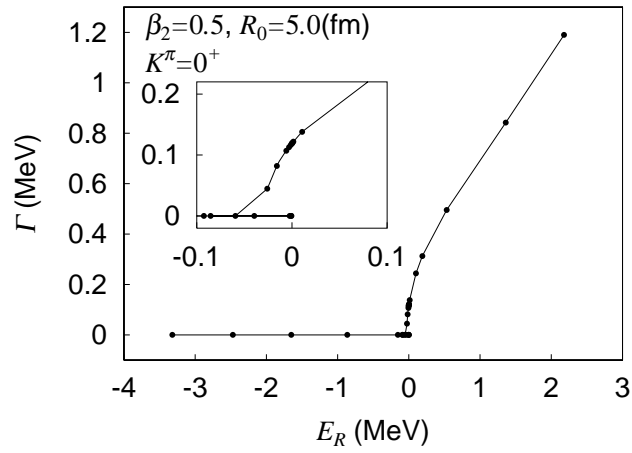Figure 7.1: The real part of the energy and the resonance width for a $K^\pi = 0^+$ state with various potential depths. In the inset, the behavior around zero energy is enlarged. The corresponding potential depths are shown in Fig.7.2.
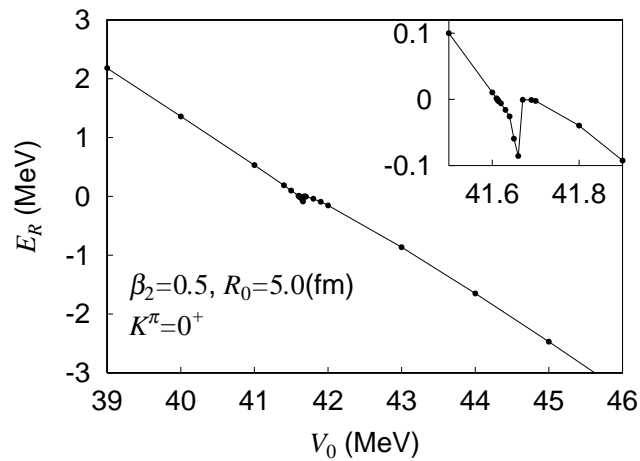

Figure 7.2: The real part of the energy for $K^\pi = 0^+$ state as a function of the potential depth. In the inset, the behavior around zero energy is enlarged.
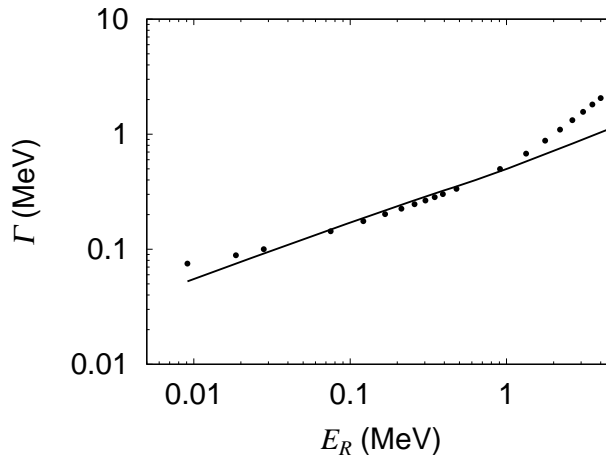
Figure 7.3: Same as Fig.7.1, but in the logarithmic scale. The solid line is an expectation for the pure s-wave configuration given by Eq. (7.14).

7.3.1 Dependence on potential depth

We first study the wave functions at a fixed deformation, $\beta_2 = 0.5$. Figure 7.1 shows the real and imaginary parts of the energy for a $K^\pi = 0^+$ state in varying the potential depth V_0. The correspondence between the potential depth and the real part of the energy is shown in Fig.7.2. We observe that the width is quite large even for a small values of positive energy. This large width is caused by the admixture of the $l = 0$ component in the wave function. Indeed, as shown in Fig.7.3, in the small positive energy region (0.1 MeV $< \Re(E) < 1.0$ MeV), the behavior of the width is consistent with the relation expected for the s-wave resonance state [150, 152, 159],

$$\Gamma \propto \Re(E)^{l+1/2} \times \Re(N_l)\Big|_{l=0}, \tag{7.14}$$

where $\Re(E)$ denotes the real part of E.

Below $E_R = 0.1$ MeV, the width is larger than the solid line, which predicts $\Gamma = 0$ at $E_R = 0$. Also, we found a non-monotonic behavior in the eigen-energy between $V_0 = 41.62$ and 41.68 MeV, where the solution has $E_R < 0$ and $\Gamma > 0$, as is shown in the inset of Fig.7.2. These facts might be related to the possible presence of the anti-bound ($\kappa = 0, \gamma > 0$) and/or 'crazy' resonant ($0 < \kappa < \gamma$) states, where $k = \kappa - i\gamma$, as presented in Ref. [160] for a spherical square-well potential (see Fig.1 of Ref. [160]). In order to study the presence of these states in the present deformed potential, we plot the trajectory for the pole of S-matrix in the complex momentum plane in Fig.7.4. As the potential depth is made shallower, the pole comes down along the imaginary axis. In the present example, the pole goes through $k = 0$ and comes into the anti-bound (virtual) state region. With a shallower potential, the pole begins to have a finite real part, which corresponds to the 'crazy' resonance, and eventually comes into the normal resonance region ($\kappa > \gamma > 0$). It is thus apparent that this state has finite width even in the limit of $E_R \to 0+$.

Above 1.0 MeV also, the width is larger than that expected by Eq.(7.14). This is due to the fact that the relation Eq.(7.14) is valid only for small values of k [159].
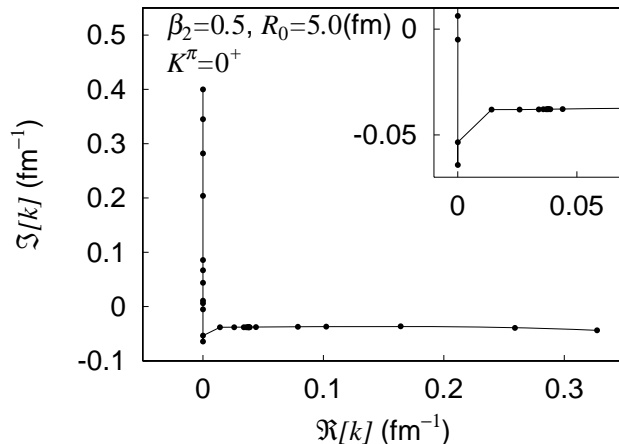
Figure 7.4: The trajectory for the pole of S-matrix in the complex momentum plane. In the inset, the behavior around zero momentum is enlarged.

In Fig.7.2, we see that the slope of the single-particle energy as a function of the potential depth, $\mathrm{d}E/\mathrm{d}V_0$, or equivalently $\mathrm{d}E/\mathrm{d}A$, where A is the mass number, becomes smaller in approaching the zero binding energy. For a spherical square-well potential, it has been shown that $\mathrm{d}E_l/\mathrm{d}A \to 0$ for $l = 0$ in the limit of zero binding [161]. This is due to the fact that the s-wave function can be easily extended outside the nuclear potential and also the kinetic energy is reduced due to the absence of the centrifugal barrier [161]. This property implies that the $l = 0$ component becomes dominant in a deformed wave function around the zero-binding region. On the other hand, the slope has a finite value in the positive energy region even in the limit of zero energy, thus the slope has a discontinuity around zero energy. Therefore, a care must be taken, as discussed in Ref. [160], when one estimates the energy of a deformed resonant level with $K^\pi = 0^+$ by using the ACCC method [151].

The resonance energy and width can be also estimated using the eigenphase sum $\Delta(E)$ [114]. It is defined in terms of the eigenvalues of the scattering matrix (S-matrix) as

$$(U^\dagger S U)_{aa'} = e^{2i\delta_a(E)}\delta_{a,a'}, \quad \Delta(E) = \sum_a \delta_a(E). \tag{7.15}$$

The resonance energy and width are identified with the peak energy of $\mathrm{d}\Delta(E)/\mathrm{d}E$ and its FWHM, respectively [128]. Figure 7.5 shows the eigenphase sum for the $K^\pi = 0^+$ state with two different potential depths. Comparing Figs.7.1, 7.2 and 7.5, we see a good correspondence between the two definitions of resonance state, i.e., the Gamow state representation and the approach with the eigenphase sum.

We now discuss the energy dependence of the fraction of the multipole components in the deformed wave function. Figure 7.6 shows the real part of the fraction for each multipole component in the Gamow state wave function with $K^\pi = 0^+$. When the binding energy approaches zero, the s-wave component in the deformed wave function becomes dominant. In contrast, in the positive energy region, all the multipole components have a finite value even in the zero energy limit and show similarity with the well bound cases. As we will discuss in the next subsection, the state shown in Fig. 7.6 originates from the $2d$ orbit in the spherical limit. This state couples with the lower-lying $2s$, $1g$ and the higher-lying $3s$
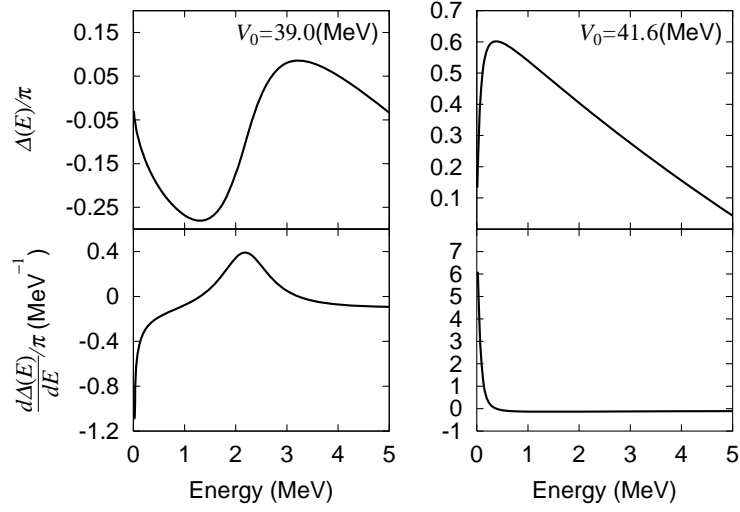
Figure 7.5: The eigenphase sum and its energy derivative for $K^{\pi} = 0^+$ state with potential depth $V_0 = 39.0$ MeV (the left panel), and $V_0 = 41.6$ MeV (the right panel).
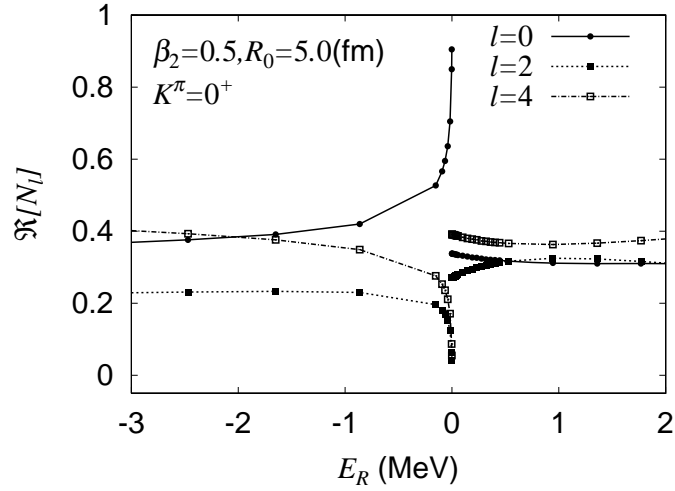
Figure 7.6: The real part of the fraction for each multipole component N_l for the $K^{\pi} = 0^+$ state. The solid, dotted, and dot-dashed lines indicate the $l = 0, 2$ and $l = 4$ components, respectively.
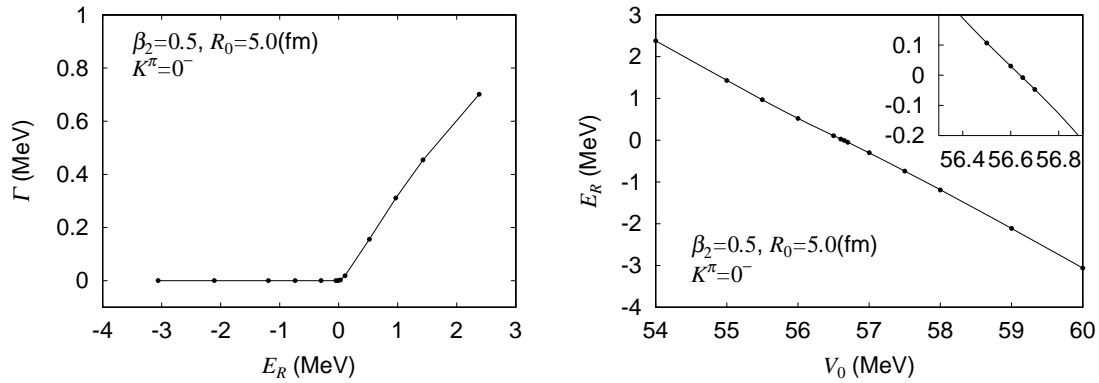
Figure 7.7: *Left*:Same as Fig.7.1, but for a $K^\pi = 0^-$ state. *Right*: Same as Fig.7.2, but for the $K^\pi = 0^-$ state.
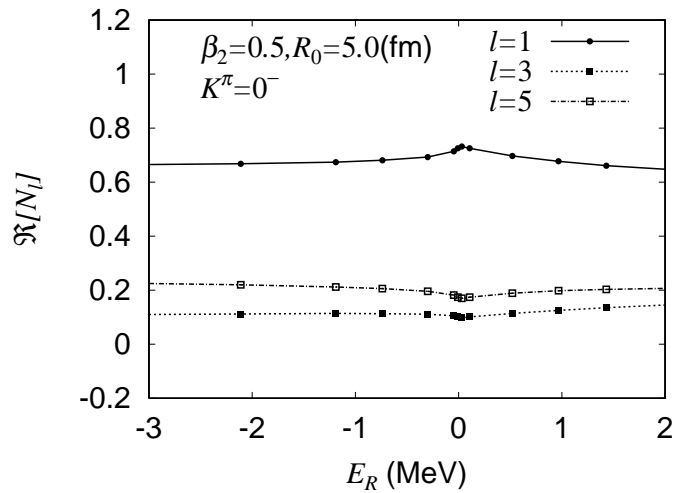
Figure 7.8: The real part of the fraction for each multipole components N_l for the $K^\pi = 0^-$ state. The solid, dotted, and dot-dashed lines indicate the $l = 1, 3$ and $l = 5$ components, respectively.

98

states. The dominant component is $l = 4$ both in well bound and in resonant levels, as one sees in Fig.7.6. This suggests that both the well bound and the resonant levels have a similar property to each other and the intuitive picture that the resonant level is an extension of a bound level into the continuum is valid.

Only at the limit of zero binding, the singular behavior of the $l = 0$ component appears. This is entirely due to the property of the normalization integral, Eq.(7.13). Since the Gamow state wave function is equivalent to the bound state wave function for $E_R < 0, \Gamma = 0$, Eq.(7.13) holds both for the resonance and the bound states. For small values of k, Eq.(7.13) is proportional to k^{2l-1} as discussed in Refs. [117, 162], that diverges only for $l = 0$ as $k \to 0$. When the total wave function Ψ_K is normalized according to Eq.(7.8), then only the s-wave component is allowed in the wave function [117]. This condition is always met for the bound state when the binding energy approaches the threshold. In principle, the same consideration can apply also to the resonance state when the resonance energy approaches zero from the positive energy side. However, as we show in Fig.7.1, the resonance state acquires a relatively large width even when the real part of the energy is infinitesimally small. Since k is defined as $k = \sqrt{2m(E_R - i\Gamma/2)/\hbar^2}$, it remains a constant even if E_R itself approaches zero. This leads to the disappearance of the "s-wave dominance" in the positive energy side.

We next study the case for $K^\pi = 0^-$. In Fig. 7.7, we show the dependence of the single-particle energy on the potential depth. In contrast to the case for $K^\pi = 0^+$, due to the presence of the centrifugal barrier, we do not see any singular behavior around zero energy. Single-particle energies are connected smoothly when changing the potential depth, and the width increases gradually in the small positive energy region. Figure 7.8 shows the fraction of each multipole component in the Gamow state wave function. As the binding energy approaches zero, the p-wave component becomes relatively large, that is consistent with the dominance of low-l component in the limit of zero binding energy discussed in Ref. [116]. The fractions are connected smoothly and asymptotically in the bound and resonant regions.

7.3.2 Deformation dependence

In this subsection, we study the deformation dependence of the low-l component in deformed wave functions for a fixed potential depth. In the realistic situation, the location of single-particle levels changes as a function of nuclear deformation. Especially, the levels of $\Omega = 1/2$ ($K = 0$) with (without) spin-orbit force belonging to high-j (high-l) orbit in the spherical limit play an important role in nuclear deformation.

Figure 7.9 shows the resonance energy and width when the deformation parameter is varied from $\beta_2 = 0.0$ to 0.5. The potential depth V_0 and the radius R_0 are set to be 45.0 MeV and 5.0 fm, respectively. This state belongs to the $2d$ orbit at $\beta_2 = 0.0$ as shown in Fig.7.10. At around zero energy, we see the similar behavior as in Fig.7.1: the width is quite large even for the small values of positive energy, which implies that the $l = 0$ component is responsible for the width of the resonant level.

The corresponding wave function components for this state are shown in Fig.7.11. As in Fig.7.6, we see the singular behavior for the s-wave component at around zero-binding energy, corresponding to the "s-wave dominance" in the limit of zero binding. Except for the zero-energy region, however, we see that the fraction of each multipole components is linked asymptotically and is smoothly connected to the d-state resonant level in the spherical limit. From this calculation, it is evident that the singular behavior of the $l = 0$ component for the $K^\pi = 0^+$ state occurs only just below the continuum threshold and this state is connected to
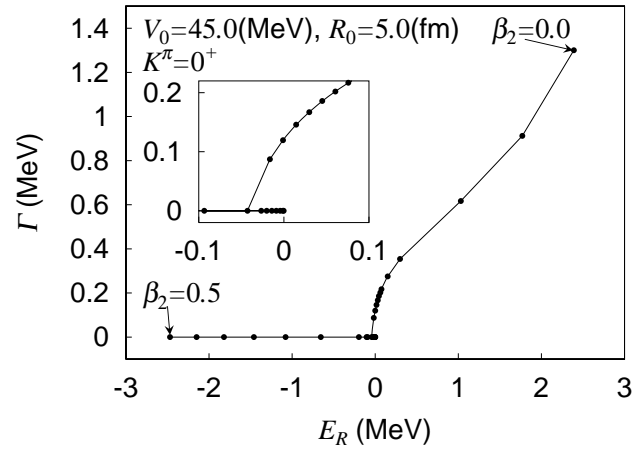
Figure 7.9: Same as Fig.7.1 except for varying the deformation. This level corresponds to the one originating from the $2d$ orbit in the spherical limit. The deformation dependence of the single-particle energies is shown in Fig.7.10.
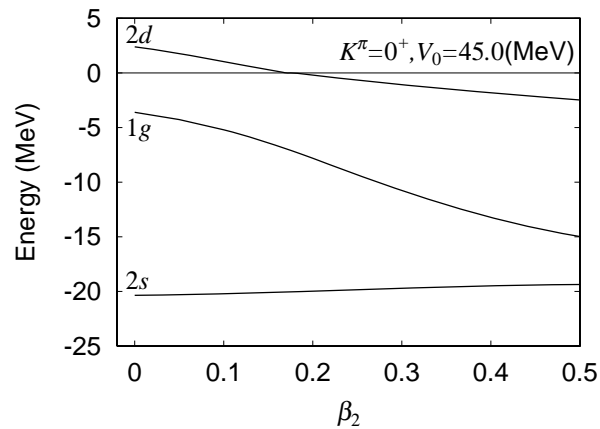
Figure 7.10: Single-particle energies for the $K^\pi = 0^+$ state as a function of deformation parameter β_2. The potential depth is $V_0 = 45.0$ (MeV), and the potential radius $R_0 = 5.0$ (fm).
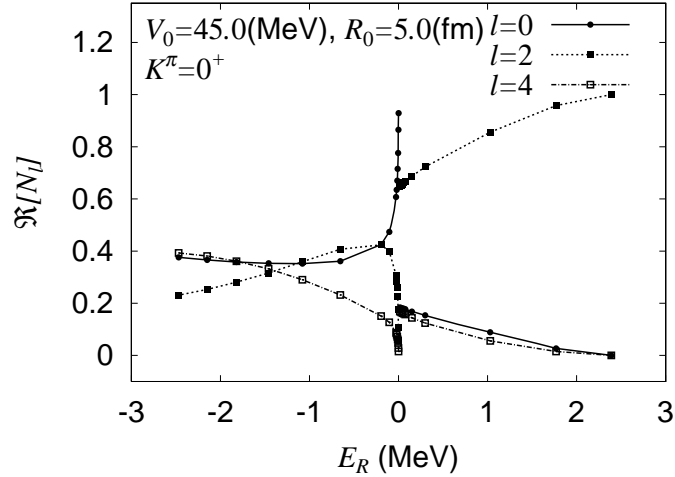
Figure 7.11: Same as Fig.7.6 except for varying the deformation.

the physical resonant level in the continuum. Furthermore, the fraction of each-l components in the deformed wave function is connected smoothly from the bound to the resonant levels except for the region near the threshold.

7.4 Summary

We have analyzed the structure of the deformed wave functions around zero energy using the Gamow state wave function for resonance, with which one can treat the resonant and bound levels on the same footing and thus analyze the wave function continuously from the negative to the positive energy regions. For this purpose, we developed a schematic model with a deformed square-well potential. Since the wave functions can be obtained analytically with this model, detailed analyses of the deformed wave functions were possible. For a $K^\pi = 0^+$ state, we have found a singularity in the resonance width as well as in the s-wave component in the deformed wave function at around zero energy. That is, the width becomes considerably large even in the small positive energy region and the $l = 0$ component approaches unity in the limit of zero binding. We have shown that the "$s-$wave dominance" occurs only at the threshold of continuum. Far from the zero energy region, the probability of each-l components is connected asymptotically. This implies that the $K^\pi = 0^+$ resonant level exists unless the $l = 0$ component is large inherently when extrapolated to the well bound region. In contrast, for the $K^\pi = 0^-$ state, we did not find any singular behavior even in the zero-energy limit. The single-particle energies are connected smoothly when changing the potential depth, and the width increases gradually in the small positive energy region. The probability of each-l component in the wave function is also connected smoothly and asymptotically between the bound and the resonant regions.

Chapter 8

Towards self-consistent calculation based on the nuclear density-functional theory

8.1 Introduction

In 1956, one monumental paper was written by Hohenberg and Kohn [163]. This was the dawn of the density-functional approach in investigating the many-body system. They showed two theorems in their paper:

1. The ground state electron density of a many electron system in the presence of an external potential uniquely determines the external potential: There is a one-to-one mapping between the external potential and the electron density.

2. The functional for the ground state energy is minimized by the ground state electron density.

This theorem says that the ground state energy of $N-$particle systems can be determined by minimization of the universal functional of the density. We do not need to solve Schrödinger equation for the $N-$particle system. This theorem, however, does not provide any functionals; i.e., this is only the existence theorem.

In 1965, Kohn and Sham provided a prescription for constructing the density functional introducing the single-particle orbit [164]. In this approach, we have only to solve single-particle Schrödinger equation. At present, the determination of the effective potential including exchange-correlation effects is the remaining problem. For the nuclear system, the Skyrme interaction is often used as an effective interaction in constructing the nuclear density functional.

8.2 Skyrme energy functional

As shown in Appendix B, one of the most important features of the Skyrme effective interaction is that its mathematical form, which contains $\delta-$functions, simplifies calculation in coordinate-mesh representation. Namely, the Skyrme energy functional can be written using the local density and current.

The total energy E of the system consists of the kinetic energy E_{kin}, the Skyrme energy E_{Sky}, the Coulomb energy E_{Coul}, the pairing energy E_{pair} and the correction of center-of-mass motion and rotational motion E_{corr};

$$E = E_{\text{kin}} + E_{\text{Sky}} + E_{\text{Coul}} + E_{\text{pair}} + E_{\text{corr}}, \tag{8.1}$$

where the kinetic energy is given by

$$E_{\text{kin}} = \int d\boldsymbol{r} \frac{\hbar^2}{2m} \tau. \tag{8.2}$$

The Skyrme energy is given as:

$$E_{\text{Sky}} = \int d\boldsymbol{r} \, \mathscr{H}_{\text{Sky}}(\boldsymbol{r}), \tag{8.3}$$

$$\mathscr{H}_{\text{Sky}} = \sum_{t=0,1} \left\{ C_t^\rho[\varrho_{00}]\varrho_{t0}^2 + C_t^s[\varrho_{00}]\boldsymbol{s}_{t0}^2 + C_t^{\triangle\rho}\varrho_{t0}\triangle\varrho_{t0} + C_t^{\triangle s}\boldsymbol{s}_{t0} \cdot \triangle\boldsymbol{s}_{t0} \right.$$
$$\left. + C_t^\tau(\varrho_{t0}\tau_{t0} - \boldsymbol{j}_{t0}^2) + C_t^T(\boldsymbol{s}_{t0} \cdot \boldsymbol{T}_{t0} - \overleftrightarrow{J}_{t0}^2) + C_t^{\nabla J}(\varrho_{t0}\nabla \cdot \boldsymbol{J}_{t0} + \boldsymbol{s}_{t0} \cdot \nabla \times \boldsymbol{j}_{t0}) \right\}, \tag{8.4}$$

where $\boldsymbol{s}$ denotes the spin density, τ the kinetic density, $\boldsymbol{T}$ the kinetic spin density, $\boldsymbol{j}$ the current tensor, $\overleftrightarrow{J}$ the spin-current tensor and $\boldsymbol{J}$ the spin-orbit current. All densities are labeled by isospin indices $t\, t_z$, where t takes value zero and one and t_z is always assumed to be zero; i.e., we assume no isospin mixing. A more general theory could violate isospin at the single-quasiparticle level, which leads additional densities $\varrho_{1\pm1}$ [71].

The particle density is defined as

$$\varrho(\boldsymbol{r}\sigma, \boldsymbol{r}'\sigma') = \langle\psi^\dagger(\boldsymbol{r}'\sigma')\psi(\boldsymbol{r}\sigma)\rangle, \tag{8.5}$$

where $\psi(\boldsymbol{r}\sigma)$ and $\psi^\dagger(\boldsymbol{r}\sigma)$ are nucleon annihilation and creation operators, and $|\ \ \rangle$ denotes the ground state of the many-body system. The isoscalar and isovector densities are

$$\varrho_{00}(\boldsymbol{r}\sigma, \boldsymbol{r}'\sigma') = \varrho_\nu(\boldsymbol{r}\sigma, \boldsymbol{r}'\sigma') + \varrho_\pi(\boldsymbol{r}\sigma, \boldsymbol{r}'\sigma'), \tag{8.6}$$
$$\varrho_{10}(\boldsymbol{r}\sigma, \boldsymbol{r}'\sigma') = \varrho_\nu(\boldsymbol{r}\sigma, \boldsymbol{r}'\sigma') - \varrho_\pi(\boldsymbol{r}\sigma, \boldsymbol{r}'\sigma'), \tag{8.7}$$

where $\sigma = \pm\frac{1}{2}$ labels the spin component. Defining

$$\varrho_{t0}(\boldsymbol{r}, \boldsymbol{r}') = \sum_\sigma \varrho_{t0}(\boldsymbol{r}\sigma, \boldsymbol{r}'\sigma), \tag{8.8}$$

$$\boldsymbol{s}_{t0}(\boldsymbol{r}, \boldsymbol{r}') = \sum_{\sigma,\sigma'} \varrho_{t0}(\boldsymbol{r}\sigma, \boldsymbol{r}\sigma')\langle\sigma'|\boldsymbol{\sigma}|\sigma\rangle, \tag{8.9}$$

we can write the local densities and currents as

$$\varrho_{t0}(\boldsymbol{r}) = \varrho_{t0}(\boldsymbol{r},\boldsymbol{r}), \tag{8.10}$$

$$\boldsymbol{s}_{t0}(\boldsymbol{r}) = \boldsymbol{s}_{t0}(\boldsymbol{r},\boldsymbol{r}), \tag{8.11}$$

$$\tau_{t0}(\boldsymbol{r}) = \nabla \cdot \nabla' \varrho_{t0}(\boldsymbol{r},\boldsymbol{r}')|_{\boldsymbol{r}=\boldsymbol{r}'}, \tag{8.12}$$

$$\boldsymbol{T}_{t0}(\boldsymbol{r}) = \nabla \cdot \nabla' \boldsymbol{s}_{t0}(\boldsymbol{r},\boldsymbol{r}')|_{\boldsymbol{r}=\boldsymbol{r}'}, \tag{8.13}$$

$$\boldsymbol{j}_{t0}(\boldsymbol{r}) = -\frac{i}{2}(\nabla - \nabla')\varrho_{t0}(\boldsymbol{r},\boldsymbol{r}')|_{\boldsymbol{r}=\boldsymbol{r}'}, \tag{8.14}$$

$$J_{t0,ij}(\boldsymbol{r}) = -\frac{i}{2}(\nabla - \nabla')_i s_{t0,j}(\boldsymbol{r},\boldsymbol{r}')|_{\boldsymbol{r}=\boldsymbol{r}'}, \tag{8.15}$$

$$\overleftrightarrow{J}_{t0}^{2}(\boldsymbol{r}) = \sum_{ij=xyz} J_{t0,ij}^{2}, \tag{8.16}$$

$$\boldsymbol{J}_{t0}(\boldsymbol{r}) = -\frac{i}{2}(\nabla - \nabla') \times \boldsymbol{s}_{t0}(\boldsymbol{r},\boldsymbol{r}')|_{\boldsymbol{r}=\boldsymbol{r}'}. \tag{8.17}$$

Using the parameters of t_0 through t_3, W_0, x_0 through x_3 and α, the Skyrme energy functional (8.4) can be explicitly written as;

$$\begin{aligned}
\mathscr{H}_{\text{Sky}} =& \frac{t_0(2+x_0)}{4}\varrho^2 - \frac{t_0(1+2x_0)}{4}(\varrho_\nu^2 + \varrho_\pi^2) + \frac{t_3(2+x_3)}{24}\varrho^{\alpha+2} - \frac{t_3(1+2x_3)}{24}\varrho^\alpha(\varrho_\nu^2 + \varrho_\pi^2) \\
&+ \frac{t_0 x_0}{4}\boldsymbol{s}^2 + \frac{t_3 x_3}{24}\varrho^\alpha \boldsymbol{s}^2 - \frac{t_0}{4}(\boldsymbol{s}_\nu^2 + \boldsymbol{s}_\pi^2) - \frac{t_3}{24}\varrho^\alpha(\boldsymbol{s}_\nu^2 + \boldsymbol{s}_\pi^2) \\
&- \frac{3t_1(2+x_1) - t_2(2+x_2)}{32}\varrho\triangle\varrho + \frac{3t_1(1+2x_1) + t_2(1+2x_2)}{32}(\varrho_\nu\triangle\varrho_\nu + \varrho_\pi\triangle\varrho_\pi) \\
&- \frac{3t_1 x_1 - t_2 x_2}{32}\boldsymbol{s}\cdot\triangle\boldsymbol{s} + \frac{3t_1 + t_2}{32}(\boldsymbol{s}_\nu\cdot\triangle\boldsymbol{s}_\nu + \boldsymbol{s}_\pi\cdot\triangle\boldsymbol{s}_\pi) \\
&+ \frac{t_1(2+x_1) + t_2(2+x_2)}{8}(\varrho\tau - \boldsymbol{j}^2) - \frac{t_1(1+2x_1) - t_2(1+2x_2)}{8}(\varrho_\nu\tau_\nu - \boldsymbol{j}_\nu^2 + \varrho_\pi\tau_\pi - \boldsymbol{j}_\pi^2) \\
&+ \frac{t_1 x_1 + t_2 x_2}{8}(\boldsymbol{s}\cdot\boldsymbol{T} - \overleftrightarrow{J}^2) - \frac{t_1 - t_2}{8}(\boldsymbol{s}_\nu\cdot\boldsymbol{T}_\nu - \overleftrightarrow{J}_\nu^2 + \boldsymbol{s}_\pi\cdot\boldsymbol{T}_\pi - \overleftrightarrow{J}_\pi^2) \\
&- \frac{W_0}{2}(\varrho\nabla\cdot\boldsymbol{J} + \boldsymbol{s}\cdot\nabla\times\boldsymbol{j} + \varrho_\nu\nabla\cdot\boldsymbol{J}_\nu + \boldsymbol{s}_\nu\cdot\nabla\times\boldsymbol{j}_\nu + \varrho_\pi\nabla\cdot\boldsymbol{J}_\pi + \boldsymbol{s}_\pi\cdot\nabla\times\boldsymbol{j}_\pi).
\end{aligned} \tag{8.18}$$

The Coulomb energy is given as

$$E_{\text{Coul}} = \frac{e^2}{2}\int d\boldsymbol{r}d\boldsymbol{r}'\varrho_\pi(\boldsymbol{r})\frac{\varrho_\pi(\boldsymbol{r}')}{|\boldsymbol{r}-\boldsymbol{r}'|} - \frac{3e^2}{4}\int d\boldsymbol{r}\varrho_\pi^{4/3}(\boldsymbol{r}), \tag{8.19}$$

where the exchange term in the Coulomb energy is treated in the Slater approximation [167], and the higher order correction was found to be small [168].

When we use for the pairing interaction the following form

$$v_{\text{pair}}(\boldsymbol{r},\boldsymbol{r}') = V_0^{(q)}\frac{1-P_\sigma}{2}F(\boldsymbol{r})\delta(\boldsymbol{r}-\boldsymbol{r}'), \tag{8.20}$$

$$F(\boldsymbol{r}) = 1 - \left(\frac{\varrho(\boldsymbol{r})}{\varrho_0}\right)^\gamma, \tag{8.21}$$

the pairing energy is given as

$$E_{\text{pair}} = \int d\boldsymbol{r}\left[\frac{V_0^{(\nu)}}{4}\tilde{\varrho}_\nu^{\,2} + \frac{V_0^{(\pi)}}{4}\tilde{\varrho}_\pi^{\,2}\right]F(\boldsymbol{r}), \tag{8.22}$$

where $\tilde{\varrho}$ denotes the pairing density;

$$\tilde{\varrho}(\boldsymbol{r}\sigma, \boldsymbol{r}'\sigma') = \langle \psi(\boldsymbol{r}'\bar{\sigma}')\psi(\boldsymbol{r}\sigma) \rangle = (-2\sigma')\langle \psi(\boldsymbol{r}' - \sigma')\psi(\boldsymbol{r}\sigma) \rangle, \tag{8.23}$$

$$\tilde{\varrho}(\boldsymbol{r}) = \sum_{\sigma=\pm} \tilde{\varrho}(\boldsymbol{r}\sigma, \boldsymbol{r}\sigma) \tag{8.24}$$

For the correction energy E_{corr}, we only consider in this thesis the correction of center-of-mass motion with the simplest prescription

$$E_{\text{corr}} = -\frac{\hbar^2}{2mA} \int d\boldsymbol{r}\tau. \tag{8.25}$$

8.3 Ground state

When we consider the ground states of even-even nuclei, the 0^+ states, the time-odd components in Eq.(8.4) vanish thanks to the time-reversal invariance. In this case, the expression for the Skyrme energy becomes simpler using the b parameters as;

$$\mathscr{H}_{\text{Sky}} = \frac{b_0}{2}\varrho^2 - \frac{b_0'}{2}(\varrho_\nu^2 + \varrho_\pi^2) + \frac{b_3}{3}\varrho^{\alpha+2} - \frac{b_3'}{3}\varrho^\alpha(\varrho_\nu^2 + \varrho_\pi^2) + b_1\varrho\tau - b_1'(\varrho_\nu\tau_\nu + \varrho_\pi\tau_\pi)$$
$$- \frac{b_2}{2}\varrho\triangle\varrho + \frac{b_2'}{2}(\varrho_\nu\triangle\varrho_\nu + \varrho_\pi\triangle\varrho_\pi) - b_4\varrho\nabla\cdot\boldsymbol{J} - b_4'(\varrho_\nu\nabla\cdot\boldsymbol{J}_\nu + \varrho_\pi\nabla\cdot\boldsymbol{J}_\pi), \tag{8.26}$$

where we neglect the $\overleftrightarrow{J}^2$ term [165, 166], and transformation from the t and x parameters to the b parameters are explained in Appendix C.

8.3.1 Single-particle Hamiltonian

The ground state is obtained by the variational principle

$$\delta E[\varrho, \tilde{\varrho}, \tau, \boldsymbol{J}] = 0, \tag{8.27}$$

and the Skyrme-HFB equation is written as

$$\sum_{\sigma'} \begin{pmatrix} h^q(\boldsymbol{r},\sigma,\sigma') - \lambda^q & \tilde{h}^q(\boldsymbol{r},\sigma,\sigma') \\ \tilde{h}^q(\boldsymbol{r},\sigma,\sigma') & -(h^q(\boldsymbol{r},\sigma,\sigma') - \lambda^q) \end{pmatrix} \begin{pmatrix} \varphi_{1,\alpha}^q(\boldsymbol{r},\sigma') \\ \varphi_{2,\alpha}^q(\boldsymbol{r},\sigma') \end{pmatrix} = E_\alpha \begin{pmatrix} \varphi_{1,\alpha}^q(\boldsymbol{r},\sigma) \\ \varphi_{2,\alpha}^q(\boldsymbol{r},\sigma) \end{pmatrix}, \tag{8.28}$$

where the local fields $h(\boldsymbol{r},\sigma,\sigma')$ and $\tilde{h}(\boldsymbol{r},\sigma,\sigma')$ can be calculated in the coordinate space by the following explicit expressions;

$$h^q = -\nabla\cdot\frac{\hbar^2}{2m_q^*}\nabla + U_q + U_C\delta_{q,\pi} - i\boldsymbol{B}_q\cdot(\nabla\times\boldsymbol{\sigma}), \tag{8.29a}$$

$$\tilde{h}_q = \frac{V_0^{(q)}}{2}F(\boldsymbol{r})\tilde{\varrho}_q. \tag{8.29b}$$

Here the first term in (8.29a) corresponds to the kinetic energy, U_q to the central potential, U_C to the Coulomb potential for protons and the last term to the spin-orbit potential. They

Table 8.1: Calculated properties of ^{16}O obtained by the Skyrme HFB calculation with the SLy4 and SkM* interactions and the density dependent surface-type delta pairing interaction with $V_0 = -418$ MeV·fm^3, using box size of about 10 fm × 10 fm. The quasiparticle energy is cut off at 50 MeV. Calculated energies are compared with the ones obtained by the `HFBTHO` code [138].

	SLy4		SkM*			
	THO	0.8 fm	THO	0.8 fm	0.8 fm	0.4 fm
Energy (MeV)					(Simpson)	
Kinetic	222.00	214.81	220.00	212.75	210.52	211.07
Volume	−423.87	−414.70	−414.18	−403.65	-403.78	−400.99
Surface	60.75	55.49	53.30	48.13	49.03	49.10
Spin-orbit	−0.959	−1.28	−1.21	−1.52	−1.29	−1.02
Coulomb (direct)	16.48	15.71	16.44	15.63	14.48	14.70
Coulomb (exchange)	−2.81	−2.77	−2.81	−2.76	−2.76	−2.75
Pairing	0	0	0	0	0	0
Total biding	−128.41	−132.74	−127.65	−131.42	−133.80	−129.88

are given by

$$\frac{\hbar^2}{2m_q^*} = \frac{\hbar^2}{2m} + b_1\varrho - b_1'\varrho_q \tag{8.30a}$$

$$U_q = b_0\varrho - b_0'\varrho_q + b_1\tau - b_1'\tau_q + \frac{b_3}{3}(\alpha+2)\varrho^{\alpha+1} - \frac{b_3'}{3}\left[\alpha\varrho^{\alpha-1}\sum_q \varrho_q^2 + 2\varrho^\alpha\varrho_q\right]$$

$$-b_4\nabla\cdot\boldsymbol{J} - b_4'\nabla\cdot\boldsymbol{J}_q - b_2\nabla^2\varrho + b_2'\nabla^2\varrho_q + \frac{\delta F}{\delta\varrho}\sum_q \tilde{\varrho}_q^2 \tag{8.30b}$$

$$\boldsymbol{B}_q = b_1'\boldsymbol{J}_q + b_4\nabla + b_4'\nabla\varrho_q. \tag{8.30c}$$

8.3.2 Numerical results

We solve the coordinate-space HFB equation (8.28) by diagonalizing the HFB Hamiltonian on the cylindrical grid points. We use the finite difference method for the derivative and the Bode's rule for the numerical quadrature as explained in Appendix A. In calculating the Coulomb potential, we use the method in Ref. [169].

In Tables 8.1 and 8.2, we show properties of ^{16}O and ^{40}Ca calculated by using the coordinate-space HFB with the Skyrme interaction for the particle-hole channel and the surface-type delta interaction for the particle-particle channel. We compare the calculated results with those obtained by using the `HFBTHO` code [138], in which the coordinate-space HFB equation is solved in the harmonic oscillator basis and the local scale transformation is employed in order to express the proper tail structure.

For both cases of ^{16}O and ^{40}Ca, the calculated binding energies are overestimated. This overestimation is due to the finite mesh size. Namely, accuracy of the derivative and the integration in the present calculation is not enough in comparison with the result of `HFBTHO`. In order to see this finite mesh-size effect, in Table 8.1, we show results obtained by using

Table 8.2: The same as Table 8.1 except for ^{40}Ca.

Energy (MeV)	SLy4		SkM*	
	THO	0.8 fm	THO	0.8 fm
Kinetic	634.94	620.27	632.96	616.42
Volume	−1161.02	−1150.33	−1142.28	−1128.18
Surface	111.02	108.19	97.86	94.85
Spin-orbit	−1.32	−1.23	−1.62	−1.44
Coulomb (direct)	79.41	77.63	79.59	77.76
Coulomb (exchange)	−7.49	−7.42	−7.48	−7.39
Pairing	0	0	0	0
Total biding	−344.17	−352.89	−341.03	−347.98

the smaller mesh size and another technique for the numerical integration called the Simpson method. As we explain in Appendix A, the Bode's rule that we use in the present calculation has higher accuracy than the Simpson method. Comparing two results with mesh size of 0.8 fm using the Bode's rule and the Simpson method, the result with the Simpson method is worse. When we use smaller mesh size of 0.4 fm, the calculated binding energy becomes better.

Table 8.3 lists single-particle energies of occupied states in ^{40}Ca. They are compared with the result of the `HFBTHO` calculation. Though the total binding energy is overestimated in comparison with that of `HFBTHO` as shown in Table 8.2, single-particle energies are reproduced rather well. Because the ground state of ^{40}Ca is spherical, single-particle energies with different m belonging to the same j should be identical. In the `HFBTHO` calculation, this degeneracy is perfect whereas the present calculation shows 0.9 MeV deviation at worst. This shortcoming would come from the finite mesh size, and it might be improved by employing smaller mesh size.

Next we show our results for a superfluid system, the spherical ^{22}O. In Table 8.4, we show properties of ^{22}O. We use two different model spaces for the cut off of Ω, the $z-$component of the angular momentum j. The calculated binding energy is overestimated as in ^{16}O and ^{40}Ca, although it is converged with respect to Ω_{max}. This overestimation is also due to the finite mesh-size artifact.

8.4 Summary

We have performed the coordinate-space HFB calculation using the cylindrical coordinates and the Skyrme effective interaction, in order to construct the energy density functional with which we are going to describe the excited states self-consistently. We made numerical checks for several isotopes in comparison to the other HFB calculations [26, 138]. Although the total binding energies are overestimated, the single-particle energies are well reproduced. This shortcoming would be due to the poor accuracy of the numerical integration and the finite mesh size. This limitation will be overcome in the near future thanks to the development of the supercomputer power. Because the low-lying excitation modes are sensitive to the single-particle levels around the Fermi level not to the binding energy, it will be meaningful to proceed to study excited states based on the density functional obtained in this chapter.

Table 8.3: Single-particle energies (in MeV) in ^{40}Ca in comparison with those of `HFBTHO`.

	SLy4		SkM*	
	THO	0.8fm	THO	0.8fm
$\nu 1s_{1/2}(m=1/2)$	-48.3	-48.2	-43.8	-43.5
$\nu 1p_{3/2}(m=1/2)$	-35.0	-35.1	-32.7	-32.6
$\nu 1p_{1/2}(m=3/2)$	-35.0	-34.7	-32.7	-32.3
$\nu 1p_{1/2}(m=1/2)$	-31.1	-30.9	-28.6	-28.4
$\nu 1d_{5/2}(m=1/2)$	-22.0	-22.1	-21.4	-21.3
$\nu 1d_{5/2}(m=3/2)$	-22.0	-21.9	-21.4	-21.2
$\nu 1d_{5/2}(m=5/2)$	-22.0	-21.5	-21.4	-20.8
$\nu 2s_{1/2}(m=1/2)$	-17.3	-17.1	-16.7	-16.5
$\nu 1d_{3/2}(m=1/2)$	-15.3	-15.4	-14.3	-14.4
$\nu 1d_{3/2}(m=3/2)$	-15.3	-15.0	-14.3	-14.0
$\pi 1s_{1/2}(m=1/2)$	-40.3	-40.2	-36.3	-36.2
$\pi 1p_{3/2}(m=1/2)$	-27.5	-27.8	-25.4	-25.6
$\pi 1p_{1/2}(m=3/2)$	-27.5	-27.3	-25.4	-25.2
$\pi 1p_{1/2}(m=1/2)$	-23.7	-23.7	-21.4	-21.4
$\pi 1d_{5/2}(m=1/2)$	-14.9	-15.4	-14.3	-14.7
$\pi 1d_{5/2}(m=3/2)$	-14.9	-15.1	-14.3	-14.5
$\pi 1d_{5/2}(m=5/2)$	-14.9	-14.5	-14.3	-13.9
$\pi 2s_{1/2}(m=1/2)$	-10.2	-10.4	-9.74	-9.84
$\pi 1d_{3/2}(m=1/2)$	-8.35	-8.82	-7.47	-7.95
$\pi 1d_{3/2}(m=3/2)$	-8.35	-8.82	-7.47	-7.95

Table 8.4: The same as Table 8.1 except for ^{22}O. The cut off for Ω is 9/2 and 13/2.

	SLy4			SkM*		
	THO	0.8 fm		THO	0.8 fm	
Energy (MeV)		$\Omega_{max}=9/2$	$\Omega_{max}=13/2$		9/2	13/2
Kinetic	344.86	334.37	334.11	348.04	334.96	334.81
Volume	-573.98	-567.15	-566.48	-570.00	-560.36	-559.62
Surface	73.52	69.51	69.28	65.21	61.07	60.84
Spin-orbit	-18.44	-17.28	-17.11	-19.47	-18.19	-18.00
Coulomb (direct)	16.17	15.32	15.32	16.21	15.45	15.46
Coulomb (exchange)	-2.77	-2.74	-2.74	-2.78	-2.75	-2.74
Pairing	-3.87	-2.20	-2.55	-6.46	-3.93	-4.49
Total biding	-164.51	-170.17	-170.17	-169.25	-173.75	-173.74

Chapter 9

Concluding remarks

We have studied excitation modes in neutron-rich nuclei, taking account of the effects of nuclear deformation, pairing correlations and continuum coupling simultaneously. Although there have been many attempts to explore collective motions unique in neutron-rich nuclei, the effect of the nuclear deformation on low-lying excitation modes have not been well investigated so far. Thus we first studied the deformation effect on low-frequency modes of excitation built on the superdeformed states in sulfur isotopes close to the neutron drip line, in the limit of large deformation and high isospin, by use of the deformed RPA method. We found that the low-lying state created by the excitation of a single neutron from a loosely bound low-Ω state, which has a spatially extended structure to a high-Ω resonance state trapped in a pocket of centrifugal barrier, acquires an extremely large transition strength. We also found in this calculation that it becomes increasingly difficult to generate collective modes of excitation by coherent superpositions of many particle-hole excitations as we approach the drip line. This is because the bound particle states disappear and individual resonance wave functions possess different spatial structures.

It is well known that the pair correlation plays an important role in the low-lying states as well as the ground states of stable nuclei. Furthermore, novel features of the pair correlation in neutron-rich nuclei have been actively investigated in the spherical system. We extended, therefore, the previous work to take into account the pair correlation, and investigated low-frequency modes of excitation in magnesium isotopes close to the neutron drip line. We performed for the first time the deformed QRPA calculation based on the coordinate-space HFB formalism. We showed the possible emergence of collective motion unique in neutron drip-line nuclei in the presence of the pair correlation. New type of this excitation mode is generated by the superposition of two-quasiparticle excitations near the Fermi level whose wave functions have spatially extended structure. It is found that the dynamical pairing correlation, the pairing vibration, enhances its collectivity.

We furthermore found that the coupling between the pairing vibration and the neutron-skin vibration brings forth the soft $K^\pi = 0^+$ modes in deformed ^{34}Mg region. Appearance of low-lying $K^\pi = 0^+$ modes in deformed neutron-rich nuclei is not restricted to the neutron-rich Mg isotopes. We showed similar examples in ^{32}Ne and neutron-rich Cr and Fe isotopes around $N = 40$. In these cases, the quadrupole pairing plays a crucial role in generating coherence among 2qp excitations. The coherent coupling between the quadrupole-pairing vibration and the beta vibration of neutron skin brings about the striking enhancement of the transition strength.

A major theoretical challenge in description of neutron-rich nuclei, especially weakly

bound nuclei, is the rigorous treatment of both the many-body correlations and the continuum of positive-energy states and decay channels simultaneously. One possible strategy of tackling this challenge is by use of the resonant state expansion, e.g., the Berggren ensemble that consists of the Gamow states and the complex non-resonant continuum. Since this theory incorporates continuum states into the single-particle basis, they can be used for a microscopic description of many-body correlations such as pairing correlation in the "Gamow-HFB" method and collective motions in the "Gamow-QRPA" method. As a first step to apply the Gamow basis to the mean-field model and in order to understand the shell structure of deformed nuclei in the continuum, we investigated a structure of resonance wave functions in a deformed potential in the coupled-channels method. We revealed that the low-angular-momentum component in deformed wave functions behaves uniquely in the vicinity of the continuum threshold, where the virtual or the anti-resonance states play an important role. This result indicates that the novel picture of single-particle motion emerges and might affect the collective motions in weakly-bound deformed nuclei. We plan to attack the subject of "Gamow-QRPA" in order to study the novel features of collective motion embedded in the continuum.

Appendix A

Numearical derivative and integration

A.1 Finite difference method

For the wave functions of the form $\Phi(\rho, \varphi, z) = \phi(\rho, z)e^{i\Lambda\varphi}$, we have

$$\nabla^2 \phi(\rho, z)e^{i\Lambda\varphi} = \left(\frac{1}{\rho}\frac{\partial}{\partial\rho} + \frac{\partial^2}{\partial\rho^2} - \frac{\Lambda^2}{\rho^2} + \frac{\partial^2}{\partial z^2}\right)\phi(\rho, z)e^{i\Lambda\varphi}. \tag{A.1}$$

Using the coordinate-mesh representation and the 9-points formula, the derivative parts can be written as

$$\left(\frac{1}{\rho}\frac{\partial}{\partial\rho} + \frac{\partial^2}{\partial\rho^2} + \frac{\partial^2}{\partial z^2}\right)\phi_{i,j}$$

$$= \frac{1}{\Delta^2}\left[\frac{287000}{5040}\phi_{i,j} + \left(\frac{8064}{5040} + \frac{672}{840(i-1/2)}\right)\phi_{i+1,j} + \left(\frac{8064}{5040} - \frac{672}{840(i-1/2)}\right)\phi_{i-1,j}\right.$$

$$- \left(\frac{1008}{5040} + \frac{168}{840(i-1/2)}\right)\phi_{i+2,j} - \left(\frac{1008}{5040} - \frac{168}{840(i-1/2)}\right)\phi_{i-2,j}$$

$$+ \left(\frac{128}{5040} + \frac{32}{840(i-1/2)}\right)\phi_{i+3,j} + \left(\frac{128}{5040} - \frac{32}{840(i-1/2)}\right)\phi_{i-3,j}$$

$$- \left(\frac{9}{5040} + \frac{3}{840(i-1/2)}\right)\phi_{i+4,j} - \left(\frac{9}{5040} - \frac{3}{840(i-1/2)}\right)\phi_{i-4,j}$$

$$+ \frac{8064}{5040}(\phi_{i,j+1} + \phi_{i,j-1}) - \frac{1008}{5040}(\phi_{i,j+2} + \phi_{i,j-2})$$

$$\left. + \frac{128}{5040}(\phi_{i,j+3} + \phi_{i,j-3}) - \frac{9}{5040}(\phi_{i,j+4} + \phi_{i,j-4})\right]. \tag{A.2}$$

A.2 Numerical quadrature

For numerical integration, we use the Bode's rule given by

$$\int_{x_i}^{x_{i+4}} f(x)\mathrm{d}x = \frac{2\Delta}{45}(7f_i + 32f_{i+1} + 12f_{i+2} + 32f_{i+3} + 7f_{i+4}) + O(\Delta^7). \tag{A.3}$$

This formula is a generalization of the well-known Simpson's rule, and it is derived by taking into account polynomials up to quartic order in the Taylor expansion for interpolation between the mesh points [170].

Appendix B

Matrix elements

B.1 Matrix elements for one-body operators

Let us first consider matrix elements for one-body operators

$$\langle ab|\hat{O}_K^{(\mathrm{uv})}|\mathrm{HFB}\rangle, \tag{B.1}$$

where

$$\hat{O}_K^{(\mathrm{uv})} = \sum_{\sigma\sigma'} \int d\boldsymbol{r} d\boldsymbol{r}' \delta_{\sigma,\sigma'} \delta(\boldsymbol{r} - \boldsymbol{r}') O_K^{(\mathrm{uv})}(\boldsymbol{r}) \hat{\psi}^\dagger(\boldsymbol{r}'\sigma') \hat{\psi}(\boldsymbol{r}\sigma), \tag{B.2}$$

and the HFB ground state and the 2qp excited states

$$\beta_i|\mathrm{HFB}\rangle = 0, \tag{B.3a}$$

$$|ab\rangle = \beta_a^\dagger \beta_b^\dagger |\mathrm{HFB}\rangle \tag{B.3b}$$

are described by the quasiparticle operators. These operators are defined by the generalized Bogoliubov transformation

$$\psi^\dagger(\boldsymbol{r}\sigma) = \sum_k \varphi_{1,k}(\boldsymbol{r}\bar\sigma)\beta_k^\dagger + \varphi_{2,k}^*(\boldsymbol{r}\sigma)\beta_k, \tag{B.4a}$$

$$\psi(\boldsymbol{r}\sigma) = \sum_k \varphi_{1,k}^*(\boldsymbol{r}\bar\sigma)\beta_k + \varphi_{2,k}(\boldsymbol{r}\sigma)\beta_k^\dagger, \tag{B.4b}$$

as explained in Chapter 2.

The matrix elements are calculated as

$$
\begin{aligned}
\langle ab|\hat{O}_K^{(\mathrm{uv})}|\mathrm{HFB}\rangle &= \langle \mathrm{HFB}|\beta_b\beta_a\hat{O}_K^{(\mathrm{uv})}|\mathrm{HFB}\rangle \\
&= \sum_{kk'}\sum_{\sigma\sigma'} \int d\boldsymbol{r} d\boldsymbol{r}' \delta_{\sigma,\sigma'}\delta(\boldsymbol{r}-\boldsymbol{r}') O_K^{(\mathrm{uv})}(\boldsymbol{r})\varphi_{1,k}(\boldsymbol{r}'\bar\sigma')\varphi_{2,k'}(\boldsymbol{r}\sigma)\langle \mathrm{HFB}|\beta_b\beta_a\beta_k^\dagger\beta_{k'}^\dagger|\mathrm{HFB}\rangle \\
&= \int d\boldsymbol{r} O_K^{(\mathrm{uv})}(\boldsymbol{r})\{-\varphi_{1,a}(\boldsymbol{r}\downarrow)\varphi_{2,b}(\boldsymbol{r}\uparrow) + \varphi_{1,a}(\boldsymbol{r}\uparrow)\varphi_{2,b}(\boldsymbol{r}\downarrow) \\
&\qquad\qquad + \varphi_{1,b}(\boldsymbol{r}\downarrow)\varphi_{2,a}(\boldsymbol{r}\uparrow) - \varphi_{1,b}(\boldsymbol{r}\uparrow)\varphi_{2,a}(\boldsymbol{r}\downarrow)\}
\end{aligned} \tag{B.5}
$$

using the quasiparticle wave functions, and we employed the Wick's theorem. In the cylindrical coordinate representation, we can rewrite as

$$\langle ab|\hat{O}_K^{(\mathrm{uv})}|\mathrm{HFB}\rangle = 2\pi\delta_{K,\Omega_a+\Omega_b}\int\rho d\rho dz O_K^{(\mathrm{uv})}(\rho,z)\{\varphi_{1,a}(\rho,z,\uparrow)\varphi_{2,b}(\rho,z,\downarrow) - \varphi_{1,a}(\rho,z,\downarrow)\varphi_{2,b}(\rho,z,\uparrow)$$
$$- \varphi_{1,b}(\rho,z,\uparrow)\varphi_{2,a}(\rho,z,\downarrow) + \varphi_{1,b}(\rho,z,\downarrow)\varphi_{2,a}(\rho,z,\uparrow)\},$$

$$(B.6)$$

where

$$O_K^{(\mathrm{uv})}(\rho,z) = O_K^{(\mathrm{uv})}(\boldsymbol{r})e^{iK\phi}. \tag{B.7}$$

Next we consider the pair creation operators consisting of nucleons with opposite direction of spins

$$\hat{O}_K^{(\mathrm{uu})} = \int d\boldsymbol{r}d\boldsymbol{r}'\delta(\boldsymbol{r}-\boldsymbol{r}')O_K^{(\mathrm{uu})}(\boldsymbol{r})\hat{\psi}^\dagger(\boldsymbol{r}'\uparrow)\hat{\psi}^\dagger(\boldsymbol{r}\downarrow). \tag{B.8}$$

The matrix elements read

$$\langle ab|\hat{O}_K^{(\mathrm{uu})}|\mathrm{HFB}\rangle = \langle \mathrm{HFB}|\beta_b\beta_a\hat{O}_K^{(\mathrm{uu})}|\mathrm{HFB}\rangle$$
$$= \sum_{\sigma'=\uparrow}\sum_{kk'}\delta_{\sigma,-\sigma'}\int d\boldsymbol{r}d\boldsymbol{r}'\delta(\boldsymbol{r}-\boldsymbol{r}')O_K^{(\mathrm{uu})}(\boldsymbol{r})\varphi_{1,k}(\boldsymbol{r}'\bar{\sigma}')\varphi_{1,k'}(\boldsymbol{r}\bar{\sigma})\langle \mathrm{HFB}|\beta_b\beta_a\beta_k^\dagger\beta_{k'}^\dagger|\mathrm{HFB}\rangle$$
$$= \int d\boldsymbol{r}O_K^{(\mathrm{uu})}(\boldsymbol{r})\{-\varphi_{1,a}(\boldsymbol{r}\downarrow)\varphi_{1,b}(\boldsymbol{r}\uparrow) + \varphi_{1,b}(\boldsymbol{r}\downarrow)\varphi_{1,a}(\boldsymbol{r}\uparrow)\}$$
$$= 2\pi\delta_{K,\Omega_a+\Omega_b}\int\rho d\rho dz O_K^{(\mathrm{uu})}(\rho,z)\{\varphi_{1,a}(\rho,z,\uparrow)\varphi_{1,b}(\rho,z,\downarrow) - \varphi_{1,a}(\rho,z,\downarrow)\varphi_{1,b}(\rho,z,\uparrow)\},$$

$$(B.9)$$

where

$$O_K^{(\mathrm{uu})}(\rho,z) = O_K^{(\mathrm{uu})}(\boldsymbol{r})e^{iK\phi}. \tag{B.10}$$

B.2   Matrix elements for two-body interactions

We show some examples of matrix elements appearing in the A, B matrices in the QRPA equation. The two-body residual interaction can be written in a from of

$$\bar{v}(1,2) = [f(\boldsymbol{r}_1) + \boldsymbol{\sigma}_1\cdot\boldsymbol{\sigma}_2 g(\boldsymbol{r}_1)]\delta(\boldsymbol{r}_1-\boldsymbol{r}_2) \tag{B.11}$$

as in Eq.(2.104) unless we take into account the momentum dependent terms in the Skyrme interaction.

As an example of matrix elements in the QRPA, let us consider the term

$$\sum_{\sigma_1,\sigma_2,\sigma_1',\sigma_2'}\int d\boldsymbol{r}_1 d\boldsymbol{r}_2 d\boldsymbol{r}_1'd\boldsymbol{r}_2'\varphi_{1,\alpha}(\boldsymbol{r}_1\bar{\sigma}_1)\varphi_{2,\delta}^*(\boldsymbol{r}_2\sigma_2)\bar{v}_{ph}(\boldsymbol{r}_1\sigma_1,\boldsymbol{r}_2\sigma_2;\boldsymbol{r}_1'\sigma_1',\boldsymbol{r}_2'\sigma_2')\varphi_{2,\beta}(\boldsymbol{r}_1'\sigma_1')\varphi_{1,\gamma}^*(\boldsymbol{r}_2'\bar{\sigma}_2')$$

$$(B.12)$$

in Eq.(2.98). Let us first consider the spin-independent term $f(\boldsymbol{r})$ in Eq.(B.11). Eq.(B.12) reads

$$
\begin{aligned}
\int d\boldsymbol{r} \{ & \varphi_{1,\alpha}(\boldsymbol{r}\downarrow)\varphi_{2,\delta}^{*}(\boldsymbol{r}\uparrow)\varphi_{2,\beta}(\boldsymbol{r}\uparrow)\varphi_{1,\gamma}^{*}(\boldsymbol{r}\downarrow) + \varphi_{1,\alpha}(\boldsymbol{r}\uparrow)\varphi_{2,\delta}^{*}(\boldsymbol{r}\downarrow)\varphi_{2,\beta}(\boldsymbol{r}\downarrow)\varphi_{1,\gamma}^{*}(\boldsymbol{r}\uparrow) \\
& - \varphi_{1,\alpha}(\boldsymbol{r}\downarrow)\varphi_{2,\delta}^{*}(\boldsymbol{r}\downarrow)\varphi_{2,\beta}(\boldsymbol{r}\uparrow)\varphi_{1,\gamma}^{*}(\boldsymbol{r}\uparrow) - \varphi_{1,\alpha}(\boldsymbol{r}\uparrow)\varphi_{2,\delta}^{*}(\boldsymbol{r}\uparrow)\varphi_{2,\beta}(\boldsymbol{r}\downarrow)\varphi_{1,\gamma}^{*}(\boldsymbol{r}\downarrow) \} f(\boldsymbol{r}).
\end{aligned}
$$
(B.13)

In the cylindrical coordinate this becomes

$$
\begin{aligned}
2\pi\delta_{\Omega_\alpha+\Omega_\beta,\Omega_\gamma+\Omega_\delta} \int \rho d\rho dz \{ & \varphi_{1,\alpha}(\rho,z,\downarrow)\varphi_{2,\delta}(\rho,z,\uparrow)\varphi_{2,\beta}(\rho,z,\uparrow)\varphi_{1,\gamma}(\rho,z,\downarrow) \\
& + \varphi_{1,\alpha}(\rho,z,\uparrow)\varphi_{2,\delta}(\rho,z,\downarrow)\varphi_{2,\beta}(\rho,z,\downarrow)\varphi_{1,\gamma}(\rho,z,\uparrow) \\
& - \varphi_{1,\alpha}(\rho,z,\downarrow)\varphi_{2,\delta}(\rho,z,\downarrow)\varphi_{2,\beta}(\rho,z,\uparrow)\varphi_{1,\gamma}(\rho,z,\uparrow) \\
& - \varphi_{1,\alpha}(\rho,z,\uparrow)\varphi_{2,\delta}(\rho,z,\uparrow)\varphi_{2,\beta}(\rho,z,\downarrow)\varphi_{1,\gamma}(\rho,z,\downarrow) \} f(\rho,z). \quad \text{(B.14)}
\end{aligned}
$$

Next we consider the spin-dependent term $\boldsymbol{\sigma}_1 \cdot \boldsymbol{\sigma}_2 g(\boldsymbol{r})$. Eq.(B.12) reads

$$
\begin{aligned}
\int d\boldsymbol{r} \{ & \varphi_{1,\alpha}(\boldsymbol{r}\downarrow)\varphi_{2,\delta}^{*}(\boldsymbol{r}\uparrow)\varphi_{2,\beta}(\boldsymbol{r}\uparrow)\varphi_{1,\gamma}^{*}(\boldsymbol{r}\downarrow) + \varphi_{1,\alpha}(\boldsymbol{r}\uparrow)\varphi_{2,\delta}^{*}(\boldsymbol{r}\downarrow)\varphi_{2,\beta}(\boldsymbol{r}\downarrow)\varphi_{1,\gamma}^{*}(\boldsymbol{r}\uparrow) \\
& + \varphi_{1,\alpha}(\boldsymbol{r}\downarrow)\varphi_{2,\delta}^{*}(\boldsymbol{r}\downarrow)\varphi_{2,\beta}(\boldsymbol{r}\uparrow)\varphi_{1,\gamma}^{*}(\boldsymbol{r}\uparrow) + \varphi_{1,\alpha}(\boldsymbol{r}\uparrow)\varphi_{2,\delta}^{*}(\boldsymbol{r}\uparrow)\varphi_{2,\beta}(\boldsymbol{r}\downarrow)\varphi_{1,\gamma}^{*}(\boldsymbol{r}\downarrow) \\
& + 2\varphi_{1,\alpha}(\boldsymbol{r}\downarrow)\varphi_{2,\delta}^{*}(\boldsymbol{r}\downarrow)\varphi_{2,\beta}(\boldsymbol{r}\downarrow)\varphi_{1,\gamma}^{*}(\boldsymbol{r}\downarrow) + 2\varphi_{1,\alpha}(\boldsymbol{r}\uparrow)\varphi_{2,\delta}^{*}(\boldsymbol{r}\uparrow)\varphi_{2,\beta}(\boldsymbol{r}\uparrow)\varphi_{1,\gamma}^{*}(\boldsymbol{r}\uparrow) \} g(\boldsymbol{r}),
\end{aligned}
$$
(B.15)

and in the cylindrical coordinate, we obtain the expression

$$
\begin{aligned}
2\pi\delta_{\Omega_\alpha+\Omega_\beta,\Omega_\gamma+\Omega_\delta} \int \rho d\rho dz \{ & \varphi_{1,\alpha}(\rho,z,\downarrow)\varphi_{2,\delta}(\rho,z,\uparrow)\varphi_{2,\beta}(\rho,z,\uparrow)\varphi_{1,\gamma}(\rho,z,\downarrow) \\
& + \varphi_{1,\alpha}(\rho,z,\uparrow)\varphi_{2,\delta}(\rho,z,\downarrow)\varphi_{2,\beta}(\rho,z,\downarrow)\varphi_{1,\gamma}(\rho,z,\uparrow) \\
& + \varphi_{1,\alpha}(\rho,z,\downarrow)\varphi_{2,\delta}(\rho,z,\downarrow)\varphi_{2,\beta}(\rho,z,\uparrow)\varphi_{1,\gamma}(\rho,z,\uparrow) \\
& + \varphi_{1,\alpha}(\rho,z,\uparrow)\varphi_{2,\delta}(\rho,z,\uparrow)\varphi_{2,\beta}(\rho,z,\downarrow)\varphi_{1,\gamma}(\rho,z,\downarrow) \\
& + 2\varphi_{1,\alpha}(\rho,z,\downarrow)\varphi_{2,\delta}(\rho,z,\downarrow)\varphi_{2,\beta}(\rho,z,\downarrow)\varphi_{1,\gamma}(\rho,z,\downarrow) \\
& + 2\varphi_{1,\alpha}(\rho,z,\uparrow)\varphi_{2,\delta}(\rho,z,\uparrow)\varphi_{2,\beta}(\rho,z,\uparrow)\varphi_{1,\gamma}(\rho,z,\uparrow) \} g(\rho,z). \quad \text{(B.16)}
\end{aligned}
$$

Here we use the following relations. The Pauli spin matrix $\boldsymbol{\sigma}$ is written in the cylindrical coordinate

$$
\boldsymbol{\sigma} = \boldsymbol{i}_\rho \sigma_\rho + \boldsymbol{i}_\phi \sigma_\phi + \boldsymbol{i}_z \sigma_z \tag{B.17}
$$

with the components

$$
\sigma_\rho = \boldsymbol{\sigma} \cdot \boldsymbol{i}_\rho = \cos\phi\,\sigma_x + \sin\phi\,\sigma_y = \begin{pmatrix} 0 & e^{-i\phi} \\ e^{i\phi} & 0 \end{pmatrix}, \tag{B.18a}
$$

$$
\sigma_\phi = \boldsymbol{\sigma} \cdot \boldsymbol{i}_\phi = -\sin\phi\,\sigma_x + \cos\phi\,\sigma_y = \begin{pmatrix} 0 & -ie^{-i\phi} \\ ie^{i\phi} & 0 \end{pmatrix}, \tag{B.18b}
$$

$$
\sigma_z = \begin{pmatrix} 1 & 0 \\ 0 & -1 \end{pmatrix}. \tag{B.18c}
$$

Then the matrix elements of the spin part become

$$
\langle \sigma' | \boldsymbol{\sigma} | \sigma \rangle =
\begin{cases}
\boldsymbol{i}_z & \text{for} \quad \sigma' = \sigma = \frac{1}{2} \\
-\boldsymbol{i}_z & \text{for} \quad \sigma' = \sigma = -\frac{1}{2} \\
\boldsymbol{i}_\rho e^{-i\phi} + \boldsymbol{i}_\phi(-ie^{-i\phi}) & \text{for} \quad \sigma' = \frac{1}{2}, \sigma = -\frac{1}{2} \\
\boldsymbol{i}_\rho e^{i\phi} + \boldsymbol{i}_\phi(ie^{i\phi}) & \text{for} \quad \sigma' = -\frac{1}{2}, \sigma = \frac{1}{2}.
\end{cases}
\tag{B.19}
$$

Appendix C

Skyrme interaction

C.1 Parameter of the Skyrme interaction

The Skyrme effective interaction is one of the most widely used force in calculations of nuclear structure. It was originally proposed in 1956 by Skyrme [171, 172] and first applied to the Hartree-Fock method in 1972 by Vautherin and Brink [173].

The density-dependent two-body effective nucleon-nucleon interaction under the Skyrme parameterization is given by

$$
\begin{aligned}
v(\boldsymbol{r}, \boldsymbol{r}') =& t_0(1 + x_0 P_\sigma)\delta(\boldsymbol{r} - \boldsymbol{r}') + \frac{t_1}{2}(1 + x_1 P_\sigma)\left[\delta(\boldsymbol{r} - \boldsymbol{r}')\boldsymbol{k}^2 + \boldsymbol{k}'^2\delta(\boldsymbol{r} - \boldsymbol{r}')\right] \\
&+ t_2(1 + x_2 P_\sigma)\boldsymbol{k}' \cdot \delta(\boldsymbol{r} - \boldsymbol{r}')\boldsymbol{k} + \frac{t_3}{6}(1 + x_3 P_\sigma)\delta(\boldsymbol{r} - \boldsymbol{r}')\varrho^\alpha\left(\frac{\boldsymbol{r} + \boldsymbol{r}'}{2}\right) \\
&+ iW_0(\boldsymbol{\sigma}_1 + \boldsymbol{\sigma}_2) \cdot \left[\boldsymbol{k}' \times \delta(\boldsymbol{r} - \boldsymbol{r}')\boldsymbol{k}\right],
\end{aligned}
\tag{C.1}
$$

where $\boldsymbol{k} = \frac{1}{2i}(\nabla_1 - \nabla_2)$ acting on the ket $|\quad\rangle$, $\boldsymbol{k}' = -\frac{1}{2i}(\nabla_1 - \nabla_2)$ acting on the bra $\langle\quad|$, and $P_\sigma = \frac{1}{2}(1 + \boldsymbol{\sigma}_1 \cdot \boldsymbol{\sigma}_2)$ being the spin exchange operator. The t_0 and t_1 terms corresponds to the $S-$wave interaction, the t_2 term the $P-$wave interaction, and the t_3 term represents the phenomenological many-body effects, the W_0 term the spin-orbit interaction. There are many parameter sets for $t_0, t_1, t_2, t_3, W_0, x_0, x_1, x_2$, and α, and they are parameterized in order to reproduces various fundamental properties such as binding energies, charge radii, and single-particle energies of some spherical nuclei. In this thesis we use mainly the SkM* [165] and SLy4 [166] parameter sets. The former was adjusted to reproduce the the fission barrier height of ^{240}Pu in addition to the above observables. The latter was designed to reproduce properties of neutron-rich nuclei and the neutron matter. The values in these two parameterizations are shown in Table. C.1. Parameterization in b, b' [119] is equivalent through the following transformation.

$$
b_0 = t_0\left(1 + \frac{1}{2}x_0\right),
\tag{C.2}
$$

$$
b_0' = t_0\left(\frac{1}{2} + x_0\right),
\tag{C.3}
$$

$$
b_1 = \frac{1}{4}\left[t_1\left(1 + \frac{1}{2}x_1\right) + t_2\left(1 + \frac{1}{2}x_2\right)\right],
\tag{C.4}
$$

Table C.1: Parameters of the Skyrme interactions. Units for t_0 is MeV·fm³, t_1, t_2 and W_0 are MeV·fm⁵, t_3 is MeV·fm$^{3(1+\alpha)}$, $\hbar^2/2m$ is MeV·fm², and remaining terms are dimensionless.

	SkM*	SLy4
t_0	−2645.0	−2488.913
t_1	410.0	486.818
t_2	−135.0	−546.395
t_3	15595.0	13777.0
W_0	130	123
x_0	0.090	0.8340
x_1	0.0	−0.3438
x_2	0.0	−1.0
x_3	0.0	1.3540
α	1/6	1/6
$\frac{\hbar^2}{2m}$	20.73398	20.73553

	SkM*	SLy4
b_0	−2764.025	−3526.790
b_0'	−1560.55	−3320.210
b_1	68.75	32.484
b_1'	68.125	−49.289
b_2	170.625	185.325
b_2'	68.437	62.665
b_3	3898.75	5776.007
b_3'	1949.375	6385.639
b_4	65.0	61.5
b_4'	65.0	61.5

$$b_1' = \frac{1}{4}\left[t_1\left(\frac{1}{2}+x_1\right) - t_2\left(\frac{1}{2}+x_2\right)\right], \tag{C.5}$$

$$b_2 = \frac{1}{8}\left[3t_1(1+\frac{1}{2}x_1) - t_2(1+\frac{1}{2}x_2)\right], \tag{C.6}$$

$$b_2' = \frac{1}{8}\left[3t_1(\frac{1}{2}+x_1) + t_2(\frac{1}{2}+x_2)\right], \tag{C.7}$$

$$b_3 = \frac{1}{4}t_3\left(1+\frac{1}{2}x_3\right), \tag{C.8}$$

$$b_3' = \frac{1}{4}t_3\left(\frac{1}{2}+x_3\right), \tag{C.9}$$

$$b_4 = \frac{1}{2}W_0, \tag{C.10}$$

$$b_4' = \frac{1}{2}W_0. \tag{C.11}$$

In some parameter sets like the SkI [175], SkP [71], SkO [119, 49] interactions, the constants b_4 and b_4' take different values.

Acknowledgements

Bibliography

[1] http://ie.lbl.gov/systematics.html.

[2] E. M. Burbidge, G. R. Burbidge, W. A. Fowler, and F. Hoyle, Rev. Mod. Phys. **29** (1957) 547.

[3] Ed. I. Tanihata, Nucl. Phys. **A693** (2001), Nos. 1, 2.

[4] Ed. H. Horiuchi, T. Otsuka and Y. Suzuki, Prog. Theor. Phys. Suppl. No.142 (2001).

[5] Ed. K. Hagino, H. Horiuchi, M. Matsuo and I. Tanihata, Prog. Theor. Phys. Suppl. No.146 (2002).

[6] I. Tanihata, J. Phys. G: Nucl. Part. Phys. **22** (1996) 157.

[7] A. S. Jensen, K. Riisager, D. V. Fedorov and E. Garrido, Rev. Mod. Phys. **76** (2004) 215.

[8] I. Tanihata et al., Phys. Rev. Lett. **55** (1985) 2676.

[9] I. Tanihata et al., Phys. Lett. **B160** (1985) 380.

[10] G. F. Bertsch, H. Esbensen, Ann. Phys. **209** (1991) 327.

[11] M. V. Zhukov, B. V. Danilin, D. V. Fedorov, J. M. Bang, I. J. Thompson and J. S. Vaagen, Phys. Rep. **231** (1993) 151.

[12] T. Myo, S. Aoyama, K. Katō, and K. Ikeda, Phys. Lett. **B576** (2003) 281.

[13] K. Hagino and H. Sagawa, Phys. Rev. C **72** (2005) 044321.

[14] http://www.nishina.riken.jp/UsersGuide/index.html

[15] M. G. Mayer, Phys. Rev. **75** (1949) 1969; ibid. **78** (1950) 16.

[16] O. Haxel, J. H. D. Jensen and H. E. Suess, Phys. Rev. **75** (1949) 1766; Z. Phys. **128** (1950) 295.

[17] H. Iwasaki *et al.*, Phys. Lett. **B481** (2000) 7; ibid. **B491** (2000) 8.

[18] A. Navin *et al.*, Phys. Rev. Lett. **85** (2000) 266.

[19] Y. Yanagisawa *et al.*, Phys. Lett. **B566** (2003) 84.

[20] D. Guillemaud-Müller *et al.*, Nucl. Phys. **A426** (1984) 37.

[21] T. Motobayashi *et al.*, Phys. Lett. **B346** (1995) 9.

[22] A. Ozawa *et al.*, Phys. Rev. Lett. **84** (2000) 5493.

[23] A. Bohr, B. R. Motteleson, *Nuclear Structure*, vol. I (Benjamin, 1969; World Scientific 1998).

[24] I. Hamamoto, Eur. Phys. J. A **13** (2002) 21.

[25] J. Dobaczewski, I. Hamamoto, W. Nazarewicz, J. A. Sheikh, Phys. Rev. Lett. **72** (1994) 981.

[26] M. V. Stoitsov, J. Dobaczewski, W. Nazarewicz, S. Pittel and D. J. Dean, Phys. Rev. C **68** (2003) 054312.

[27] T. R. Werner, J. A. Sheikh, W. Nazarewicz, M. R. Strayer, A. S. Umar and M. Misu, Phys. Lett. **B333** (1994) 303.

[28] T. R. Werner, J. A. Sheikh, M. Misu, W. Nazarewicz, J. Rikovska, K. Heeger, A. S. Umar and M. R. Strayer, Nucl. Phys. **A597** (1996) 327.

[29] J. Terasaki, H. Flocard, P. -H. Heenen and P. Bonche, Nucl. Phys. **A621** (1997) 706.

[30] G. A. Lalazissis, A. R. Farhan, and M. M. Sharma, Nucl. Phys. **A628** (1998) 221.

[31] G. A. Lalazissis, D. Vretener, P. Ring, M. Stoitsov, and L. M. Robledo, Phys. Rev. C **60** (1999) 014310.

[32] S. Peru, M. Girod, and J, F. Berger, Eur. Phys. J. A **9** (2000) 35.

[33] R. Rodoríguez-Guzmán, J. L. Egido, L. M. Robledo, Nucl. Phys. **A709** (2002) 201.

[34] S. Grevy *et al.*, Phys. Lett. **B594** (2004) 252.

[35] M. Notani *et al.*, Phys. Lett. **B542** (2002) 49.

[36] H. Savajols *et al.*, Eur. Phys. J. A **25**, Suppl. 1 (2005) 23.

[37] C. M. Campbell *et al.*, Phys. Rev. Lett. **97** (2006) 112501.

[38] P. D. Cottle and K. W. Kemper, Phys. Rev. C **58** (1998) 3761.

[39] E. Caurier, F. Nowacki and A. Poves, Nucl. Phys. **A742** (2004) 14.

[40] J. Fridmann *et al.*, Nature **435** (2005) 922.

[41] J. Fridmann *et al.*, Phys. Rev. C **74** (2006) 034313.

[42] T. Suzuki *et al.*, Phys. Rev. Lett. **75** (1995) 3241.

[43] P. Ring and P. Schuck, *The Nuclear Many-Body Problem* (Springer, 1980).

[44] I. Hamamoto, H. Sagawa and X. Z. Zhang, Phys. Rev. C **53** (1996) 765; ibid. **55** (1997) 2361; ibid. **56** (1997) 3121; ibid. **57** (1998) R1064; ibid. **64** (2001) 024313.

[45] I. Hamamoto and H. Sagawa, Phys. Rev. C **60** (1999) 064314; ibid. **62** (2000) 024319; ibid. **66** (2002) 044315.

[46] S. Shlomo and B. Agrawal, Nucl. Phys. **A722** (2003) 98c.

[47] M. Matsuo, Nucl. Phys. **A696** (2001) 371.

[48] K. Hagino, H. Sagawa, Nucl. Phys. **A695** (2001) 82.

[49] M. Bender, J. Dobaczewski, J. Engel, W. Nazarewicz, Phys. Rev. C **65** (2002) 054322.

[50] E. Khan, N. Sandulescu, M. Grasso, N. Van Giai, Phys. Rev. C **66** (2002) 024309.

[51] M. Yamagami, N. Van Giai, Phys. Rev. C **69** (2004) 034301.

[52] J. Terasaki, J. Engel, M. Bender, J. Dobaczewski, W. Nazarewicz, M. Stoitsov, Phys. Rev. C **71** (2005) 034310.

[53] D. Vretenar, N. Paar, P. Ring, G. A. Lalazissis, Nucl. Phys. **A692** (2001) 496.

[54] N. Paar, P. Ring, T. Nikšić, D. Vretenar, Phys. Rev. C **67** (2003) 034312.

[55] N. Paar, T. Nikšić, D. Vretenar, P. Ring, Phys. Rev. C **69** (2004) 054303.

[56] N. Paar, T. Nikšić, D. Vretenar, P. Ring, Phys. Lett. **B606** (2005) 288.

[57] L. G. Cao, Z. Y. Ma, Phys. Rev. C **71** (2005) 034305.

[58] D. Vretenar, A. V. Afanasjev, G. A. Lalazissis, P. Ring, Phys. Rep. **409** (2005) 101.

[59] G. Giambrone, S. Scheit, F. Barranco, P. F. Bortignon, G. Colò, D. Sarchi, E. Vigezzi, Nucl. Phys. **A726** (2003) 3.

[60] S. Péru, J. F. Berger, P. F. Bortignon, Eur. Phys. J. A **26** (2005) 25.

[61] D. Sarchi, P. F. Bortignon, G. Coló, Phys. Lett. **B601** (2004) 27.

[62] M. Bender, P-H. Heenen, P-G. Reinhard, Rev. Mod. Phys. **75** (2003) 121.

[63] T. Nakatsukasa and K. Yabana, Phys. Rev. C **71** (2005) 024301.

[64] T. Inakura, H. Imagawa, Y. Hashimoto, S. Mizutori, M. Yamagami and K. Matsuyanagi, Nucl. Phys. **A768** (2006) 61.

[65] R. H. Lemmer and M. Vénéroni, Phys. Rev. **170** (1968) 883.

[66] A. Muta, J-I. Iwata, Y. Hashimoto, and K. Yabana, Prog. Theor. Phys. **108** (2002) 1065.

[67] H. Imagawa and Y. Hashimoto, Phys. Rev. C **67** (2003) 037302.

[68] P. Urkedal, X. Z. Zhang and I. Hamamoto, Phys. Rev. C **64** (2001) 054304.

[69] R. Álvarez-Rodríguez, P. Sarriguren, E. Moya de Guerra, L. Pacearescu, A. Faessler, F. Šimkovic, Phys. Rev. C **70** (2004) 064309, and references therein.

[70] K. Hagino, N. Van Giai and H. Sagawa, Nucl. Phys. **A731** (2004) 264.

[71] J. Dobaczewski, H. Flocard and J. Treiner, Nucl. Phys. **A422** (1984) 103.

[72] A. Bulgac, Preprint No. FT-194-1980, Institute of Atomic Physics, Bucharest, 1980. [arXiv:nucl-th/9907088]

[73] R. Smolańczuk, J. Dobaczewski, Phys. Rev. C **48** (1993) R2166.

[74] J. Dobaczewski, W. Nazarewicz, T. R. Werner, J. F. Berger, C. R. Chinn, and J. Dechargé, Phys. Rev. C **53** (1996) 2809.

[75] K. Bennacuer, J. Dobaczewski, and M. Ploszajczak, Phys. Rev. C **60** (1999) 034308.

[76] M. Yamagami, Phys. Rev. C **72** (2005) 064308.

[77] M. Matsuo, K. Mizuyama, Y. Serizawa, Phys. Rev. C **71** (2005) 064326.

[78] K. Yoshida, M. Yamagami and K. Matsuyanagi, Prog. Theor. Phys. **113** (2005) 1251.

[79] K. Yoshida, T. Inakura, M. Yamagami, S. Mizutori and K. Matsuyanagi, *Proc. the 4th Int. Conference on Exotic Nuclei and Atomic Masses*, Pine Mountain, Georgia, USA, 12-16 September, 2004, Eur. Phys. J. A **25**, Suppl. 1 (2005) 557.

[80] K. Yoshida, M. Yamagami, K. Matsuyanagi, Nucl. Phys. **A779** (2006) 99.

[81] K. Yoshida, M. Yamagami and K. Matsuyanagi, *Proc. Int. Conference on Finite Fermionic Systems -Nilsson Model 50 Years*, Lund, Sweden, 14-18 June, 2005, Phys. Scr. **T125** (2006) 45.

[82] K. Yoshida, K. Hagino, Phys. Rev. C **72** (2005) 064311.

[83] J.-P. Blaizot and G. Ripka, *Quantum Theory of Finite Systems* (The MIT press, 1986).

[84] E. Terán, V. E. Oberacker and A. S. Umar, Phys. Rev. C **67** (2003) 064314.

[85] V. E. Oberacker, A. S. Umar, E. Terán and A. Blazkiewicz, Phys. Rev. C **68** (2003) 064302.

[86] A. Blazkiewicz, V. E. Oberacker, A. S. Umar and M. Stoitsov, Phys. Rev. C **71** (2005) 054321.

[87] K. Sawada, Phys. Rev. **106** (1957) 372.

[88] S. Takagi, Prog. Theor. Phys. **21** (1959) 174.

[89] K. Ikeda, M. Kobayasi, T. Marumori, T. Shiozaki and S. Takagi, Prog. Theor. Phys. **22** (1959) 663.

[90] M. Kobayasi and T. Marumori, Prog. Theor. Phys. **23** (1960) 387.

[91] T. Marumori, Prog. Theor. Phys. **24** (1960) 331.

[92] R. Arvieu and M. Vénéroni, Compt. Rend. **250** (1960) 992.

[93] M. Baranger, Phys. Rev. **120** (1960) 957.

[94] E. R. Marshalek and J. Weneser, Ann. Phys. **53** (1969) 569.

[95] D. J. Rowe, Rev. Mod. Phys. **40** (1968) 153.

[96] D. J. Rowe, *Nuclear Collective Motion*, (Methuen and Co. Ltd., 1970)

[97] N. Ullah and D. J. Rowe, Nucl. Phys. **A163** (1971) 257.

[98] S. Shlomo and G. F. Bertsch, Nucl. Phys. **A243** (1975) 507.

[99] J.-P. Blaizot and D. Gogny, Nucl. Phys. **A284** (1977), 429.

[100] T. Inakura, M. Yamagami, S. Mizutori and K. Matsuyanagi, Nucl. Phys. **A728** (2003) 52.

[101] E. Ideguchi *et al.*, Phys. Rev. Lett. **87** (2001) 222501.

[102] C. J. Chiara *et al.*, Phys. Rev. C **67** (2003) R041303.

[103] H. C. Pauli, Phys. Rep. **7** (1973) 35.

[104] S. Cwiok, J. Dudek, W. Nazarewicz, J. Skalski and T. Werner, Comput. Phys. Commun. **46** (1987) 379.

[105] I. Ragnarsson, S. G. Nilsson and R. K. Sheline, Phys. Rep. **45** (1978) 1.

[106] J. Dobaczewski, *Proc. Int. Conf. on Nuclear Structure '98*, ed. C. Baktash (AIP conference proceedings **481**, 1999), p. 315.

[107] M. Yamagami and K. Matsuyanagi, Nucl. Phys. A **672** (2000) 123.

[108] H. Molique, J. Dobaczewski and J. Dudek, Phys. Rev. C **61** (2000) 044304.

[109] R. R. Rodriguez-Guzmán, J. L. Egido and L. M Robeldo, Phys. Rev. C **62** (2000) 054308.

[110] T. Tanaka, R. G. Nazmitdinov and K. Iwasawa, Phys. Rev. C **63** (2001) 034309.

[111] S. Mizutori, T .Nakatsukasa, K. Arita, Y. R. Shimizu and K. Matsuyanagi, Nucl. Phys. **A557** (1993) 125c.

[112] T. Nakatsukasa, K. Matsuyanagi, S. Mizutori and Y. R. Shimizu, Phys. Rev. C **53** (1996) 2213.

[113] T. Nakatsukasa, K. Matsuyanagi, S. Mizutori and W. Nazarewicz, Phys, Lett. **B343** (1995) 19.

[114] K. Hagino and Nguyen Van Giai, Nucl. Phys. **A735** (2004) 55.

[115] A. U. Hazi, Phys. Rev. A **19** (1979) 920.

[116] I. Hamamoto, Phys. Rev. C **69** (2004) R041306.

[117] T. Misu, W. Nazarewicz and S. Åberg, Nucl. Phys. **A614** (1997) 44.

[118] F. Catara, E. G. Lanza, M. A. Nagarajan and A. Vitturi, Nucl. Phys. **A624** (1997) 449.

[119] P.-G. Reinhard, D. J. Dean, W. Nazarewicz, J. Dobaczewski, J. A. Maruhn, M. R. Strayer, Phys. Rev. C **60** (1999) 014316 and references therein.

[120] J. Terasaki, P.-H. Heenen, P. Bonche, J. Dobaczewski, H. Flocard, Nucl. Phys. **A593** (1995) 1.

[121] J. Sauvage-Letessier, P. Quentin, H. Flocard, Nucl. Phys. **A370** (1981) 231.

[122] M. Bender, K. Rutz, P.-G. Reinhard, J. A. Maruhn, Eur. Phys. J. A **8** (2000) 59.

[123] T. Duguet, P. Bonche, P.-H. Heenen, Nucl. Phys. **A679** (2001) 427.

[124] M. Yamagami, K. Matsuyanagi, M. Matsuo, Nucl. Phys. **A693** (2001) 579.

[125] E. Khan, N. Sandulescu, and N. Van Giai, Phys. Rev. C **71** (2005) R042801.

[126] A. Bohr, B. R. Motteleson, *Nuclear Structure*, vol. II (Benjamin, 1975; World Scientific 1998).

[127] M. Grasso, N. Sandulescu, Nguyen Van Giai, R. J. Liotta, Phys. Rev. C **64** (2001) 064321.

[128] A. Muta, T. Otsuka, Prog. Theor. Phys. Suppl. No.142 (2001) 355.

[129] T. Vertse, P. Curutchet, O. Civitarese, L. S. Ferreira, and R. J. Liotta, Phys. Rev. C **37** (1988) 876.

[130] P. Curutchet, T. Vertse, R. J. Liotta, Phys. Rev. C **39** (1989) 1020.

[131] T. Vertse, P. Curutchet, and R. J. Liotta, Phys. Rev. C **42** (1990) 2605.

[132] T. Vertse, R. J. Liotta, E. Maglione, Nucl. Phys. **A584** (1995) 13.

[133] J. A. Church *et al.*, Phys. Rev. C **72** (2005) 054320.

[134] Z. Elekes *et al.*, Phys. Rev. C **73** (2006) 044314.

[135] K. Yoneda *et al.*, Phys. Lett. **B499** (2001) 223.

[136] X. Liang *et al.*, Phys. Rev. C **74** (2006) 014311.

[137] P. M. Endt, Nucl. Phys. **A633** (1998) 1.

[138] M. V. Stoitsov, J. Dobaczewski, W. Nazarewicz, P. Ring, Comp. Phys. Comm. **167** (2005) 43.

[139] L. M. Eisenberg and W. Greiner, *Nuclear Models*, vol. I (North Holland, 1970).

[140] T. Otsuka, Eur. Phys. J. A **20** (2004) 69.

[141] T. Otsuka, M. Honma, T. Mizusaki, N. Shimizu, Y. Ustuno, Prog. Part. Nucl. Phys. **47** (2001) 319.

[142] C. D. O'Leary *et al.*, Phys. Rev. C **67** (2000) 064314.

[143] W. Nazarewicz, J. Dudek, R. Bengtsson, T. Bengtsson, and I. Ragnarsson, Nucl. Phys. **A435** (1985) 397.

[144] R. Broda *et al.*, Phys. Rev. Lett. **74** (1995) 868.

[145] O. Sorlin *et al.*, Nucl. Phys. **A660** (1999) 3.

[146] M. Hannawald *et al.*, Phys. Rev. Lett. **82** (1999) 1391.

[147] O. Sorlin *et al.*, Eur. Phys. J. A **16** (2003) 55.

[148] E. Caurier, F. Nowacki and A. Poves, Eur. Phys. J. A **15** (2002) 145.

[149] S. G. Nilsson, Mat. Fys. Medd. Dan. Vid. Selsk. **29** (1955) No.16.

[150] L. S. Ferreira, E. Maglione and R. J. Liotta, Phys. Rev. Lett. **78** (1997) 1640.

[151] G. Cattapan and E. Maglione, Phys. Rev. C **61** (2000) 067301.

[152] I. Hamamoto, Phys. Rev. C **72** (2005) 024301.

[153] W. J. Romo, Nucl. Phys. **A116** (1968) 618.

[154] T. Berggren, Phys. Lett. **B33** (1970) 547; ibid. **B373** (1996) 1.

[155] S. Aoyama, K. Katō and K. Ikeda, Prog. Theor. Phys. **99** (1998) 623.

[156] Y. B. Zel'dovich, Sov. Phys. JETP **12** (1961) 542.

[157] P. M. Morse and H. Feshbach, *Methods of theoretical physics* (McGrow-Hill, 1953), p.1574.

[158] B. Gyarmati and T. Vertse, Nucl. Phys. **A160** (1971) 523.

[159] K. W. McVoy, *Fundamentals in Nuclear Theory*, edited by A. De-Shalit and C. Villi (IAEA, Vienna, 1967),p.419.

[160] N. Tanaka, Y. Suzuki, K. Varga and R. G. Lovas, Phys. Rev. C **59** (1999) 1391.

[161] I. Hamamoto, S. V. Lukyanov and X. Z. Zhang, Nucl. Phys. **A683** (2001) 255.

[162] K. Riisager, A. S. Jensen, P. Møller, Nucl. Phys. **A548** (1992) 393.

[163] P. Hohenberg and W. Kohn, Phys. Rev. **136** (1956) B864.

[164] W. Kohn and L. Sham, Phys. Rev. **140** (1965) A1133.

[165] J. Bartel, P. Quentin, M. Brack, C. Guet and H. B. Håkansson, Nucl. Phys. **A386** (1982) 79.

[166] E. Chanbanat, P. Bonche, P. Haensel, J. Mayer and R. Schaeffer, Nucl. Phys. **A627** (1997) 710.

[167] J. Slater, Phys. Rev. **81** (1951) 385.

[168] C. Titin-Schnaider and P. Quentin, Phys. Lett. **74** (1974) 397.

[169] D. Vautherin, Phys. Rev. C **7** (1973) 296.

[170] S. E. Koonin, *Computational Physics* (Addison-Wesley, 1986).

[171] T. H. R. Skyrme, Phil. Mag. **1** (1956) 1048.

[172] T. H. R. Skyrme, Nucl. Phys. **9** (1959) 615.

[173] D. Vautherin and D. Brink, Phys. Rev. C **5** (1972) 626.

[174] M. Beiner, H. Flocard, N. Van Gai and P. Quentin, Nucl. Phys. **A386** (1975) 29.

[175] P. -G. Reinhard and H. Flocard, Nucl. Phys. **A584** (1995) 467.